



## City Research Online

### City, University of London Institutional Repository

---

**Citation:** Musaj, M (2010). Computational and Experimental Investigation of the Aerodynamics of a W-shaped leading edge reversed delta plan-form wing. (Unpublished Doctoral thesis, City, University of London)

This is the accepted version of the paper.

This version of the publication may differ from the final published version.

---

**Permanent repository link:** <https://openaccess.city.ac.uk/id/eprint/18110/>

**Link to published version:**

**Copyright:** City Research Online aims to make research outputs of City, University of London available to a wider audience. Copyright and Moral Rights remain with the author(s) and/or copyright holders. URLs from City Research Online may be freely distributed and linked to.

**Reuse:** Copies of full items can be used for personal research or study, educational, or not-for-profit purposes without prior permission or charge. Provided that the authors, title and full bibliographic details are credited, a hyperlink and/or URL is given for the original metadata page and the content is not changed in any way.

---

---

---

City Research Online:

<http://openaccess.city.ac.uk/>

[publications@city.ac.uk](mailto:publications@city.ac.uk)

---

**Computational and Experimental Investigation  
of the Aerodynamics of a W-shaped leading  
edge reversed delta plan-form wing**

By

**Mimoza Musaj**

Thesis submitted as part of the requirements for the degree of  
Doctor of Philosophy

Centre for Aeronautics, School of Engineering  
City University, Northampton Square  
London EC1V 0HB

January 2010

# Contents

Contents .....	i
List of Tables .....	iv
List of Figures .....	iv
Declaration .....	xvi
Acknowledgments .....	xviii
Abstract .....	xix
Nomenclature .....	xx
1. Introduction .....	1
1.1 Background .....	1
1.2 Project Overview and Objectives .....	8
1.3 Wing Specification .....	10
1.4 Thesis Overview .....	13
2. Literature Review (Wing aerodynamics) .....	15
2.1 Background History .....	15
2.2 Ground Effect .....	28
3. Literature Review (Numerical methods for predicting Flows) .....	44
3.1 Governing Equations of Fluid Motion .....	44
3.2 Finite Volume Discretisation .....	47
3.2.1 Finite Volume Method .....	47
3.2.1.1 Convection Differencing Scheme .....	48
3.2.1.2 Diffusion Term .....	49
3.2.2 Errors .....	51
3.2.3 Convergence Acceleration .....	51
3.4 Pressure-Velocity Coupling .....	54
3.4.1 Pressure Correction .....	54
3.5 Turbulence Modeling Methodology .....	55
3.6 Numerical Algorithms- Review .....	62
3.6.1 Numerical Simulations and Differencing Schemes .....	63

3.6.2	Turbulence Modelling.....	66
3.7	Full-Potential Equations.....	79
3.8	Grid Generation Methodologies-Review.....	81
3.9	Grid Generation (W-wing).....	94
3.10	Preview of CFD Codes .....	96
4.	Validation of Numerical Methods .....	101
4.1	The Onera M6 wing.....	101
4.2	Methods.....	103
4.3.1	High-Speed Study .....	105
4.4	Low-speed Results .....	110
5.	Experimental Arrangements .....	113
5.1	The T2 Wind Tunnel.....	113
5.2	The T3 Wind Tunnel.....	115
5.3	Wing Model .....	116
5.4	Ground Board.....	119
5.5	Data Measurement and Analysis .....	121
5.5.1	T2 Testing .....	121
5.5.2	T3 Testing .....	123
5.5.3	Wake Measurement .....	125
5.5.4	Force and Moment Processing.....	128
5.5.5	Wake Analysis .....	129
5.6	Visualization .....	130
5.6.1	Laser Smoke visualisation .....	130
5.7	Wind Tunnel Boundary Corrections.....	130
5.7.1	Solid Blockage.....	131
5.7.2	Wake Blockage .....	132
5.7.3	Corrections for the Angle of Attack.....	133
6.	Low-Speed Experimental and Numerical Wind Tunnel Test Results.....	135
6.1	Experimental Reynolds Number Effect Study.....	136
6.2	Wind-tunnel Numerical Simulations .....	139
6.3	Results-Forces and Moments.....	143
6.4	Results Near-Wake Analysis .....	147
7.	Full-scale High-speed Numerical Analyses of W-shaped-leading-edge wing Aerodynamics in Cruise Flight .....	156

7.1 Grid Dependency Analyses.....	158
7.2 Convergence Monitoring .....	162
7.3 Turbulence models.....	163
7.4 Results of Full-Scale High-Speed Numerical Analyses .....	164
7.5 Results Near-Wake Analysis .....	180
8. Experimental and Numerical Test Results for the W-wing in Ground Effect...	188
8.1 Grid Dependency Analyses.....	190
8.2 Convergence Monitoring .....	191
8.3 Results of Low-Speed Experimental and Numerical Analyses .....	192
8.3.1 Near-Wake Analysis .....	201
8.4 Results of Full-Scale Numerical Analyses .....	209
9. Assessment of the Aerodynamic Performance Improvement of the W-Shaped Leading-Edge Wing .....	226
9.1 Numerical examination of un-swept mid-wing and forward-swept tip of the W-shaped leading-edge wing.....	227
9.2 Numerical Full-Potential investigation on variations of the sweeps on the original wing.....	241
10. Concluding Remarks.....	249
11. Recommendations for Further Work .....	253
References.....	255
Appendix.....	272
Parasite Drag Calculations.....	272

# List of Tables

Table 1-1: Jetpod Total Wing Specifications.....	11
Table 9-1. Variations of the original wing investigated with FP method.....	241

# List of Figures

Figure 1-1: PAR Lift Concept in Ground Vicinity (Lange 1998) .....	2
Figure 1-2: Possible Configuration for a Green-Aircraft a) upper surface blowing engines, b) fan shielded by wings (high wings), c) fan shielded by wings (low wings) and d) buried engines (low wings) (Hepperle 2004) .....	3
Figure 1-3. The light aircraft-Eclipse 500 (Eclipse Aviation).....	4
Figure 1-4: AVCEN Jetpod (www.avcen.com).....	5
Figure 1-5: Jetpod in Take-off (www.avcen.com).....	6
Figure 1-6. Total Lift vs. Ground Roll Distance.....	7
Figure 1-7: Jetpod Wing Specifications.....	12
Figure 1-8: NACA 2412 Section Characteristics (Abbott and Von Doenhoff 1959)..	12
Figure 2-1: Leading Edge Angle Effect on the Pressure Distribution (Jones 1947) ...	16
Figure 2-2: Stream-tube on Upper Surface of Aft-Swept Wing (Jones 1947) .....	16
Figure 2-3: Stall Progression on an Aft-Swept Wing (Furlong and McHugh 1952)...	17
Figure 2-4: Flow Pattern on a Aft-swept wing with $\Lambda_{c/4} = 60^\circ$ , AR = 1.5 and NACA 0012 (Purser and Spearman 1951).....	19
Figure 2-5: Flow Pattern on a Forward-swept wing with $\Lambda_{c/4} = 46.6^\circ$ , AR = 2.1 and NACA 23012 (Purser and Spearman 1951).....	19

Figure 2-6: The X-29A Aircraft (Saltzman and Hicks 1994).....	21
Figure 2-7: Span-wise Lift Distribution Comparison between FSX and Un-swept- Wing (Lombardi 1993).....	22
Figure 2-8: The M-Wing Employed by Lemme.....	24
Figure 2-9: Vickers Project X (left) and Whitworth AWP22001 M-wing (right) (Payne 2004).....	24
Figure 2-10: Purser and Spearman study results: a) W-wing geometry, b) Pitching moment comparison between W-wing and an aft-swept wing and c) aerodynamic center shift comparison for three planforms.....	26
Figure 2-11: The W-wing employed by Jing et al.....	27
Figure 2-12: Streamlines Around an Aerofoil at Various Ground Heights (Staufenbiel and Schlichting 1988).....	29
Figure 2-13: Lift Coefficient versus $h/c$ for a Rectangular Wing with $AR = 6$ (Fink and Lastinger 1961).....	29
Figure 2-14: Horseshoe Vortex Distribution in Ground Effect.....	31
Figure 2-15: Wieselsberger's Image Method.....	31
Figure 2-16: Criteria for Determining the Need for Moving Ground Belt (Thomas et al 1979).....	35
Figure 2-17: Experimental Method Devised by Sowdon and Hori (Sowdon and Hori 1996).....	36
Figure 2-18: Wakes of Wings at a) out of Ground Effect and b) in Ground Effect (Nuhait 1995).....	39
Figure 3-1: Discretised Control Volume (Anderson 1995).....	47
Figure 3-2: Face Interpolation.....	49
Figure 3-3: Vector $a$ on non-orthogonal mesh.....	50
Figure 3-4: V-Cycle Multigrid Method (STARCCM+ UM #236).....	52
Figure 3-5: Turbulent Boundary Layer on a Flat Plate (Thwaites 1960).....	61
Figure 3-6: Pressure Coefficient Prediction Comparison with Experimental results a) one-equation algebraic models and $k-\omega$ SST and b) low-Reynolds Number $k-\epsilon$ models (Kral 1998).....	69
Figure 3-7: Inner Skin Friction Prediction for a U duct (Rumsey et al 1999).....	71
Figure 3-8: Tip Vortex Numerical Prediction comparison between $k-\omega$ SST and Experimental Results (Kandil et al 1995).....	72

Figure 3-9: Multi-element Aerofoil Velocity Profile Predictions with two Turbulence Models (Rumsey et al 2000) .....	75
Figure 3-10: DLR-F6 Configuration and Predicted Lift Coefficients from Rumsey et al with EASM, k- $\omega$ SST and SA (Rumsey et al 2004) .....	77
Figure 3-11: Pitching Moment Prediction with k- $\omega$ SST for the 2 <sup>nd</sup> Drag Prediction Workshop (Langtry 2003).....	78
Figure 3-12: Observed Speed-Up for ONERA M6 wing (Mavriplis and Pirzadeh 1999) .....	79
Figure 3-13: Example of Structured and Unstructured grid for ONERA M6 (Frink 1994) .....	83
Figure 3-14: Example of a mixed Tetra/Prism Grid on a Multi-Element Aerofoil (Marcum 1995) .....	86
Figure 3-15: Unstructured Advancing Layer generated Mesh for the F-16 aircraft (Frink and Pirzadeh 1998) .....	88
Figure 3-16: Structured and Unstructured Grid Results for the DLR-F4 Drag Prediction Workshop (Rakowitz and Eisfeld 2003) .....	92
Figure 3-17: Grid and Surface Pressures on an ONERA M6 wing, a) initial, b) adapted and c) finely adapted (Pirzadeh 1999).....	94
Figure 3-18: Octree Mesh Generation Process (Yerry and Shephard 1984) .....	96
Figure 4-1. The ONERA M6 wing (Schmitt and Charpin 1979). .....	102
Figure 4-2. ONERA M6 wing specification and pressure taps locations (Schmitt and Charpin 1979). .....	102
Figure 4-3. $Y^+$ distribution for numerical predictions on Onera M6 fine grid at $Re = 1.2 \times 10^7$ , $M = 0.84$ and $\alpha = 3.06^\circ$ .....	104
Figure 4-4. Planform view of Onera M6 final unstructured grid.....	104
Figure 4-5. The Onera M6 computational grid in the near surface region. ....	104
Figure 4-6. Pressure Distribution over Onera M6 wing at $Re = 1.2 \times 10^7$ , $M = 0.84$ , $\eta = 0.2$ and $\alpha = 3.06^\circ$ . ....	107
Figure 4-7. Experimental, numerical (STARCCM+ N-S k- $\omega$ SST) and Full-Potential Pressure Distribution over Onera M6 wing at $Re = 1.2 \times 10^7$ , $M = 0.84$ , $\eta = 0.44$ and $\alpha = 3.06^\circ$ . ....	107
Figure 4-8. Experimental, numerical (STARCCM+ N-S k- $\omega$ SST) and Full-Potential Pressure Distribution over Onera M6 wing at $Re = 1.2 \times 10^7$ , $M = 0.84$ , $\eta = 0.65$ and $\alpha = 3.06^\circ$ .....	108

Figure 4-9. Experimental, numerical (STARCCM+ N-S k- $\omega$ SST) and Full-Potential Pressure Distribution over Onera M6 wing at $Re = 1.2 \times 10^7$ , $M = 0.84$ , $\eta = 0.8$ and $\alpha = 3.06^\circ$ .....	108
Figure 4-10. Experimental, numerical (STARCCM+ N-S k- $\omega$ SST) and Full-Potential Pressure Distribution over Onera M6 wing at $Re = 1.2 \times 10^7$ , $M = 0.84$ , $\eta = 0.9$ and $\alpha = 3.06^\circ$ .....	109
Figure 4-11. Experimental, numerical (STARCCM+ N-S k- $\omega$ SST) and Full-Potential Pressure Distribution over Onera M6 wing at $Re = 1.2 \times 10^7$ , $M = 0.84$ , $\eta = 0.99$ and $\alpha = 3.06^\circ$ .....	109
Figure 4-12. Numerical (STARCCM+ N-S k- $\omega$ SST) and Full-Potential Pressure Distribution over upper-surface Onera M6 wing at $Re = 2.3 \times 10^6$ , $M = 0.2$ , $\eta = 0$ and $\alpha = 0^\circ$ .....	110
Figure 4-13. Numerical (STARCCM+ N-S k- $\omega$ SST) and Full-Potential Pressure Distribution over upper-surface Onera M6 wing at $Re = 2.3 \times 10^6$ , $M = 0.2$ , $\eta = 0.483$ and $\alpha = 0^\circ$ .....	111
Figure 4-14. Numerical (STARCCM+ N-S k- $\omega$ SST) and Full-Potential Pressure Distribution over upper-surface Onera M6 wing at $Re = 2.3 \times 10^6$ , $M = 0.84$ , $\eta = 0.987$ and $\alpha = 0^\circ$ .....	111
Figure 5-1: T2 Wind Tunnel .....	114
Figure 5-2: T3 Wind Tunnel .....	115
Figure 5-3: Wooden Wing Model Utilized in T2 and T3 Wind Tunnels .....	116
Figure 5-4: Downstream View of the Model Mounted in T2 .....	117
Figure 5-5: Shielded Strut in T2 Wind Tunnel .....	118
Figure 5-6: T3 Strut System (wing model at $\alpha = 6^\circ$ ) .....	119
Figure 5-7: Schematic of the Wing Model Set-up with Respect to the Ground Board .....	120
Figure 5-8: Downstream View of the Model and Ground Board Installed in T3 .....	120
Figure 5-9. Tunnel-to-tunnel repeatability test at $V=35\text{m/s}$ (Lift Coefficient).....	123
Figure 5-10. Tunnel-to-tunnel repeatability test at $V=35\text{m/s}$ (Drag Coefficient).....	124
Figure 5-11: Wake Rake .....	126
Figure 5-12: Schematic View of the Wake Rake Utilized in T2 and T3 Tests .....	126
Figure 5-13: Wake Rake Positioning for the T2 tests.....	127
Figure 5-14: Wake Rake Positioning for the T3 Tests .....	128

Figure 6-1. Experimentally measured lift coefficient at $M = 0.1$ and $Re = 4.1 \times 10^5$ ( $v = 40\text{m/s}$ ), $Re = 3.6 \times 10^5$ ( $v = 35\text{m/s}$ ), $Re = 2.1 \times 10^5$ ( $v = 20\text{m/s}$ ), and $Re = 1.5 \times 10^5$ ( $v = 15\text{m/s}$ ). .....	137
Figure 6-2. Experimentally measured drag coefficient at $M = 0.1$ and $Re = 4.1 \times 10^5$ ( $v = 40\text{m/s}$ ), $Re = 3.6 \times 10^5$ ( $v = 35\text{m/s}$ ), $Re = 2.1 \times 10^5$ ( $v = 20\text{m/s}$ ), and $Re = 1.5 \times 10^5$ ( $v = 15\text{m/s}$ ) .....	138
Figure 6-3. Experimentally measured lift-to-drag ratio at $M = 0.1$ and $Re = 4.1 \times 10^5$ ( $v = 40\text{m/s}$ ), $Re = 3.6 \times 10^5$ ( $v = 35\text{m/s}$ ), $Re = 2.1 \times 10^5$ ( $v = 20\text{m/s}$ ), and $Re = 1.5 \times 10^5$ ( $v = 15\text{m/s}$ ).....	139
Figure 6-4. Experimentally measured moment coefficient at $M = 0.1$ and $Re = 4.1 \times 10^5$ ( $v = 40\text{m/s}$ ), $Re = 3.6 \times 10^5$ ( $v = 35\text{m/s}$ ), $Re = 2.1 \times 10^5$ ( $v = 20\text{m/s}$ ), and $Re = 1.5 \times 10^5$ ( $v = 15\text{m/s}$ ).....	139
Figure 6-5. W-leading-edge-wing unstructured computational grid-planform view.	141
Figure 6-6. Computational grid in the near-surface region.....	141
Figure 6-7. Complete computational unstructured grid domain and fine grid density box around the wing (inset). .....	142
Figure 6-8. Predicted $Y^+$ distribution on the wing at $M = 0.1$ and $Re = 3.5 \times 10^5$ and $\alpha = 12^\circ$ .....	142
Figure 6-9. Comparison of numerically predicted (fine and medium grid) and experimentally measured lift coefficient at $M = 0.1$ and $Re = 3.6 \times 10^5$ .....	145
Figure 6-10. Comparison of numerically predicted (fine and medium grid) and experimentally measured drag coefficient at $M = 0.1$ and $Re = 3.6 \times 10^5$ .....	146
Figure 6-11. Comparison of numerically predicted (fine and medium grid) and experimentally measured moment coefficient at $M = 0.1$ and $Re = 3.6 \times 10^5$ .....	146
Figure 6-12. Comparison of numerically predicted (fine and medium grid) and experimentally measured lift-to-drag ratio at $M = 0.1$ and $Re = 3.6 \times 10^5$ .....	147
Figure 6-13. Near-Wake grid example at $M = 0.1$ and $Re = 3.6 \times 10^5$ and $\alpha = 10^\circ$ for a) experimental results from the T2 tunnel and b) numerical tests.....	148
Figure 6-14. Experimental strut wake effects comparison at $M = 0.1$ and $Re = 3.6 \times 10^5$ and $\alpha = 0^\circ$ for a) struts without fairings and b) struts with fairings .....	149
Figure 6-15. Experimental strut wake effects comparison at $M = 0.1$ and $Re = 3.6 \times 10^5$ and $\alpha = 24^\circ$ for a) struts without fairings and b) struts with fairings .....	150
Figure 6-16. Near-wake total pressure coefficients at $\alpha = 0^\circ$ a) experimental and b) numerical.....	151

Figure 6-17. Near-wake total pressure coefficients at $\alpha = 6^\circ$ a) experimental and b) numerical.....	152
Figure 6-18. Near-wake total pressure coefficients at $\alpha = 10^\circ$ a) experimental and b) numerical.....	152
Figure 6-19. Near-wake total pressure coefficients at $\alpha = 14^\circ$ a) experimental and b) numerical.....	152
Figure 6-20. Near-wake total pressure coefficients at $\alpha = 16^\circ$ a) experimental and b) numerical.....	153
Figure 6-21. Near-wake total pressure coefficients at $\alpha = 18^\circ$ a) experimental and b) numerical.....	153
Figure 6-22. Numerically predicted upper-surface pressure distribution at $M = 0.1$ and $Re = 3.6 \times 10^5$ for a) $\alpha = 14^\circ$ and b) $\alpha = 18^\circ$ .....	154
Figure 6-23. Numerically predicted upper-surface wall shear-stress streamlines at $M = 0.1$ and $Re = 3.6 \times 10^5$ for a) $\alpha = 14^\circ$ and b) $\alpha = 18^\circ$ .....	154
Figure 7-1. Boundary layer state at separation, together with dominant transition mechanism as a function of incidence and Reynolds Number (Poll 1985).....	157
Figure 7-2a. Predicted $Y^+$ distribution on the wing at $M = 0.45$ and $Re = 3 \times 10^7$ and $\alpha = 10^\circ$ (fine grid).....	159
Figure 7-3. Numerically predicted lift coefficients, with three different grids at $M = 0.45$ and $Re = 3 \times 10^7$ .....	160
Figure 7-4. Numerically predicted drag coefficients, with three different grids at $M = 0.45$ and $Re = 3 \times 10^7$ .....	161
Figure 7-5. Turbulence model sensitivity analyses; numerically predicted a) lift coefficient and b) drag coefficient at $M = 0.45$ and $Re = 3 \times 10^7$ .....	164
Figure 7-6. Numerically predicted lift coefficients, with two numerical methods at $M = 0.45$ and $Re = 3 \times 10^7$ .....	165
Figure 7-8. Numerically predicted drag vs lift coefficients, with two numerical methods at $M = 0.45$ and $Re = 3 \times 10^7$ .....	166
Figure 7-9. Numerically predicted pitching moment coefficients, with two grids at $M = 0.45$ and $Re = 3 \times 10^7$ .....	166
Figure 7-10. Predicted pressure distributions on the upper (on the left) and lower (on the right) surfaces at $\alpha = 0^\circ$ , $M = 0.45$ and $Re = 3 \times 10^7$ .....	169
Figure 7-11. Predicted pressure distributions on the upper (on the left) and lower (on the right) surfaces at $\alpha = 10^\circ$ , $M = 0.45$ and $Re = 3 \times 10^7$ .....	169

Figure 7-12. Predicted pressure distributions on the upper (on the left) and lower (on the right) surfaces at $\alpha = 12^\circ$ , $M = 0.45$ and $Re = 3 \times 10^7$ .....	169
Figure 7-13. Predicted pressure distributions on the upper (on the left) and lower (on the right) surfaces at $\alpha = 14^\circ$ , $M = 0.45$ and $Re = 3 \times 10^7$ .....	170
Figure 7-14. Predicted pressure distributions on the upper (on the left) and lower (on the right) surfaces at $\alpha = 16^\circ$ , $M = 0.45$ and $Re = 3 \times 10^7$ .....	170
Figure 7-15. Predicted pressure distributions on the upper (on the left) and lower (on the right) surfaces at $\alpha = 18^\circ$ , $M = 0.45$ and $Re = 3 \times 10^7$ .....	170
Figure 7-16. Predicted wall shear stress streamlines at $\alpha = 10^\circ$ and $\alpha = 14^\circ$ , at $M = 0.45$ and $Re = 3 \times 10^7$ .....	171
Figure 7-17. Predicted wall shear-stress streamlines at $\alpha = 16^\circ$ and $\alpha = 18^\circ$ , at $M = 0.45$ and $Re = 3 \times 10^7$ .....	171
Figure 7-18. Predicted wall shear stress contours at $\alpha = 16^\circ$ and $\alpha = 18^\circ$ , at $M = 0.45$ and $Re = 3 \times 10^7$ .....	174
Figure 7-19. Predicted Mach number distributions at $\alpha = 12^\circ$ , $\alpha = 14^\circ$ and $\alpha = 18^\circ$ , at $M = 0.45$ and $Re = 3 \times 10^7$ .....	176
Figure 7-20. Leading-edge refined grid. ....	177
Figure 7-21. Predicted total pressure distributions at $\alpha = 6^\circ$ , $\alpha = 12^\circ$ , at $M = 0.45$ and $Re = 3 \times 10^7$ .....	179
Figure 7-22. Predicted total pressure distributions at $\alpha = 6^\circ$ , $\alpha = 12^\circ$ , $\alpha = 14^\circ$ and $\alpha = 14^\circ$ , at $M = 0.45$ and $Re = 3 \times 10^7$ .....	179
Figure 7-23. Wing spanwise lift distribution at $L/D_{max}$ at $M=0.45$ and $Re = 3 \times 10^7$ .	180
Figure 7-24. Near-wake total pressure coefficient plots at $x/c_r = 1.5$ , $\alpha = 10^\circ$ and $\alpha = 14^\circ$ , at $M = 0.45$ and $Re = 3 \times 10^7$ .....	182
Figure 7-25. Near-wake total pressure coefficient plots at $x/c_r = 1.5$ , $\alpha = 16^\circ$ and $\alpha = 18^\circ$ , at $M = 0.45$ and $Re = 3 \times 10^7$ .....	183
Figure 7-26. Off-surface particle traces at $\alpha = 14^\circ$ , at $M = 0.45$ and $Re = 3 \times 10^7$ .....	184
Figure 7-27. Off-surface investigations of the source of the vortical structure at $\alpha = 16^\circ$ , at $M = 0.45$ and $Re = 3 \times 10^7$ .....	185
Figure 7-28. Off-surface particle traces at $\alpha = 18^\circ$ , at $M = 0.45$ and $Re = 3 \times 10^7$ .....	185
Figure 8-1. Ground effect- domain grid layout with a close-up view of the near wing grid clustering (inset). ....	191

Figure 8-2. Convergence residuals for ground effect numerical predictions, at $h/b = 0.145$ , $M = 0.09$ , $Re = 3 \times 10^5$ and $\alpha = 10^\circ$ with a) image and b) fixed ground method.	192
Figure 8-3. Convergence residuals for ground effect numerical predictions, at $M = 0.11$ , $Re = 6.9 \times 10^6$ and $\alpha = 0^\circ$ for a) $h/b = 0.145$ and b) $h/b = 0.27$ .	192
Figure 8-4: Experimental variation of lift coefficient with changing angle of attack at different ground clearances, $Re = 3 \times 10^5$ and $M = 0.09$ .	195
Figure 8-5. Experimental variation of drag coefficient with changing angle of attack at different ground clearances, $Re = 3 \times 10^5$ and $M = 0.09$ .	196
Figure 8-6. Experimental variation of lift coefficient with changing $h/b$ at various $\alpha$ , $Re = 3 \times 10^5$ and $M = 0.09$ .	197
Figure 8-7. Experimental variation of drag coefficient with changing angle of attack at different ground clearances, $Re = 3 \times 10^5$ and $M = 0.09$ .	197
Figure 8-8. Numerical lift coefficient with changing angle of attack at different ground clearances, $Re = 3 \times 10^5$ and $M = 0.09$ .	199
Figure 8-9. Numerical drag coefficient with changing angle of attack at different ground clearances, $Re = 3 \times 10^5$ and $M = 0.09$ .	199
Figure 8-10. Numerical variation of lift coefficient with changing angle of attack at different ground clearances, $Re = 3 \times 10^5$ and $M = 0.09$ .	200
Figure 8-11. Numerical variation of drag coefficient with changing angle of attack at different ground clearances, $Re = 3 \times 10^5$ and $M = 0.09$ .	200
Figure 8-12. Experimental near-wake total pressure distribution for the ground-alone case at $Re = 3 \times 10^5$ and $M = 0.09$ .	202
Figure 8-13. Experimental near-wake total pressure distribution at $\alpha = 0^\circ$ , $Re = 3 \times 10^5$ and $M = 0.09$ .	203
Figure 8-14. Experimental near-wake total pressure distribution at $\alpha = 6^\circ$ , $Re = 3 \times 10^5$ and $M = 0.09$ .	203
Figure 8-15. Near-wake total pressure distribution at $\alpha = 6^\circ$ , $h/b = 0.09$ , $Re = 3 \times 10^5$ and $M = 0.09$ a) experimental and b) numerical results.	205
Figure 8-16. Near-wake total pressure distribution at $\alpha = 10^\circ$ , $h/b = 0.09$ , $Re = 3 \times 10^5$ and $M = 0.09$ a) experimental and b) numerical results.	205
Figure 8-17. Numerical fixed-ground results of the near-wake total pressure distribution at $\alpha = 10^\circ$ , $h/b = 0.09$ , $Re = 3 \times 10^5$ and $M = 0.09$ .	206

Figure 8-18. Near-wake total pressure distribution at $\alpha = 10^\circ$ , $h/b = 0.145$ , $Re = 3 \times 10^5$ and $M = 0.09$ a) experimental and b) numerical results. ....	206
Figure 8-19. Near-wake total pressure distribution at $\alpha = 16^\circ$ , $h/b = 0.145$ , $Re = 3 \times 10^5$ and $M = 0.09$ a) experimental and b) numerical results. ....	206
Figure 8-20. Numerical fixed-ground results of the near-wake total pressure distribution at $\alpha = 16^\circ$ , $h/b = 0.145$ , $Re = 3 \times 10^5$ and $M = 0.09$ .....	207
Figure 8-21. Plan-view of the tip vortex performance when the wing is in ground effect at $h/b = 0.145$ and $h/b = 0.09$ .....	207
Figure 8-22. Plan-view of the tip vortex performance when the wing is in ground effect at $h/b = 0.45$ and $h/b = 0.09$ .....	208
Figure 8-23. Full-scale numerical variation of lift coefficient with angle of attack at various $h/b$ , $Re = 6.9 \times 10^6$ and $M = 0.11$ . ....	211
Figure 8-24. Full-scale numerical variation of drag coefficient with angle of attack at various $h/b$ , $Re = 6.9 \times 10^6$ and $M = 0.11$ .....	211
Figure 8-25. Full-scale numerical variation of lift-to-drag ratio with angle of attack at various $h/b$ , $Re = 6.9 \times 10^6$ and $M = 0.11$ . ....	212
Figure 8-26. Full-scale numerical variation of $C_D - C_{D0}$ with angle of attack at various $h/b$ , $Re = 6.9 \times 10^6$ and $M = 0.11$ . ....	212
Figure 8-27. Full-scale numerical variation of pressure and shear drag coefficient with angle of attack at various $h/b$ , $Re = 6.9 \times 10^6$ and $M = 0.11$ .....	213
Figure 8-28. Full-scale numerical variation of pitching moment coefficient with angle of attack at various $h/b$ , $Re = 6.9 \times 10^6$ and $M = 0.11$ .....	213
Figure 8-29. Full-scale numerical variation of lift coefficient with $h/b$ , at various $\alpha$ $Re = 6.9 \times 10^6$ and $M = 0.11$ .....	214
Figure 8-30. Full-scale numerical variation of drag coefficient with $h/b$ , at various $\alpha$ $Re = 6.9 \times 10^6$ and $M = 0.11$ .....	214
Figure 8-31. Predicted pressure distributions on the upper and lower surfaces at ground free, $\alpha = 6^\circ$ , $Re = 6.9 \times 10^6$ and $M = 0.11$ . ....	215
Figure 8-32. Predicted pressure distributions on the upper and lower surfaces at ground free, $\alpha = 12^\circ$ , $Re = 6.9 \times 10^6$ and $M = 0.11$ . ....	216
Figure 8-33. Predicted pressure distributions on the upper and lower surfaces at ground free, $\alpha = 16^\circ$ , $Re = 6.9 \times 10^6$ and $M = 0.11$ . ....	216
Figure 8-34. Predicted pressure distributions on the upper and lower surfaces at $h/b = 0.09$ , $\alpha = 6^\circ$ , $Re = 6.9 \times 10^6$ and $M = 0.11$ .....	216

Figure 8-35. Predicted pressure distributions on the upper and lower surfaces at $h/b = 0.09$ , $\alpha = 12^\circ$ , $Re = 6.9 \times 10^6$ and $M = 0.11$ .....	217
Figure 8-36. Predicted pressure distributions on the upper and lower surfaces at $h/b = 0.145$ , $\alpha = 12^\circ$ , $Re = 6.9 \times 10^6$ and $M = 0.11$ .....	217
Figure 8-37. Predicted pressure distributions on the upper and lower surfaces at $h/b = 0.145$ , $\alpha = 14^\circ$ , $Re = 6.9 \times 10^6$ and $M = 0.11$ .....	217
Figure 8-38. Predicted pressure distributions on the upper and lower surfaces at $h/b = 0.145$ , $\alpha = 16^\circ$ , $Re = 6.9 \times 10^6$ and $M = 0.11$ .....	218
Figure 8-39. Ground Mach distribution contours at $\alpha = 12^\circ$ , $h/b = 0.09$ , $Re = 6.9 \times 10^6$ and $M = 0.11$ .....	219
Figure 8-40. Ground Mach distribution contours at $\alpha = 12^\circ$ , $h/b = 0.145$ , $Re = 6.9 \times 10^6$ and $M = 0.11$ .....	219
Figure 8-41. Ground Mach distribution contours at $\alpha = 12^\circ$ , $h/b = 0.45$ , $Re = 6.9 \times 10^6$ and $M = 0.11$ .....	219
Figure 8-42. Wall shear-stress streamline distribution for $h/b = 0.09$ (left) and $h/b = 0.145$ (right) at $\alpha = 12^\circ$ , $Re = 6.9 \times 10^6$ and $M = 0.11$ .....	220
Figure 8-43. Wall shear-stress streamline distribution for $h/b = 0.145$ (left) and $h/b = 0.27$ (right) at $\alpha = 16^\circ$ , $Re = 6.9 \times 10^6$ and $M = 0.11$ .....	220
Figure 8-44. Off-surface streamlines and near-wake at $h/b = 0.09$ , $\alpha = 12^\circ$ , $Re = 6.9 \times 10^6$ and $M = 0.11$ .....	222
Figure 8-45. Off-surface streamlines and near-wake at $h/b = 0.145$ , $\alpha = 12^\circ$ , $Re = 6.9 \times 10^6$ and $M = 0.11$ .....	222
Figure 8-46. Off-surface streamlines and near-wake at $h/b = 0.09$ , $\alpha = 16^\circ$ , $Re = 6.9 \times 10^6$ and $M = 0.11$ .....	223
Figure 8-47. Off-surface streamlines and near-wake at $h/b = 0.09$ , $\alpha = 18^\circ$ , $Re = 6.9 \times 10^6$ and $M = 0.11$ .....	223
Figure 8-48. Numerical results of the near-wake total pressure distribution at $\alpha = 16^\circ$ , $Re = 6.9 \times 10^6$ and $M = 0.11$ at a) $h/b = 0.145$ and b) $h/b = 0.45$ .....	224
Figure 9-1. Un-swept mid-wing geometry.....	228
Figure 9-2. Forward-swept tip wing geometry.....	228
Figure 9-3. Numerically (Navier-Stokes) predicted lift coefficients for the three design variations at $M = 0.45$ and $Re = 3 \times 10^7$ .....	229

Figure 9-4. Numerically (Navier-Stokes) predicted drag coefficients for the three design variations at $M = 0.45$ and $Re = 3 \times 10^7$ .....	230
Figure 9-5. Numerically (Navier-Stokes) predicted lift-to-drag ratio for the three design variations at $M = 0.45$ and $Re = 3 \times 10^7$ .....	230
Figure 9-6. Numerically (Navier-Stokes) predicted lift-to-drag ratio for the three design variations at $M = 0.45$ and $Re = 3 \times 10^7$ .....	231
Figure 9-7. Predicted pressure distributions on the upper (on the left) and lower (on the right) surfaces of the W-wing Variant A at $\alpha = 16^\circ$ , $M = 0.45$ and $Re = 3 \times 10^7$ ..	232
Figure 9-8. Predicted pressure distributions on the upper (on the left) and lower (on the right) surfaces of the W-wing Variant A at $\alpha = 18^\circ$ , $M = 0.45$ and $Re = 3 \times 10^7$ ..	232
Figure 9-9. Predicted wall shear stress streamlines of the W-wing Variant A at $\alpha = 16^\circ$ and $\alpha = 18^\circ$ , at $M = 0.45$ and $Re = 3 \times 10^7$ .....	233
Figure 9-10. Predicted total pressure distributions of the W-wing Variant A at $\alpha = 16^\circ$ , $\alpha = 18^\circ$ , at $M = 0.45$ and $Re = 3 \times 10^7$ .....	233
Figure 9-11. Predicted wall shear stress contours of the W-wing Variant A wing at $\alpha = 16^\circ$ and $\alpha = 18^\circ$ , at $M = 0.45$ and $Re = 3 \times 10^7$ .....	234
Figure 9-12. Near-wake total pressure coefficient plots for the W-wing Variant A at $x/c_r = 1.5$ , $\alpha = 16^\circ$ at $M = 0.45$ and $Re = 3 \times 10^7$ .....	235
Figure 9-13. Predicted pressure distributions on the upper (on the left) and lower (on the right) surfaces of the W-wing Variant B at $\alpha = 14^\circ$ , $M = 0.45$ and $Re = 3 \times 10^7$ ...	236
Figure 9-14. Predicted pressure distributions on the upper (on the left) and lower (on the right) surfaces of the W-wing Variant B at $\alpha = 14^\circ$ , $M = 0.45$ and $Re = 3 \times 10^7$ ...	236
Figure 9-15. Predicted wall shear stress contours of the W-wing Variant B wing at $\alpha = 14^\circ$ and $\alpha = 16^\circ$ , at $M = 0.45$ and $Re = 3 \times 10^7$ .....	237
Figure 9-16. Predicted Mach number distributions of the W-wing Variant B at $\alpha = 14^\circ$ , $M = 0.45$ and $Re = 3 \times 10^7$ .....	238
Figure 9-17. Predicted total pressure distributions of the W-wing Variant B at $\alpha = 14^\circ$ , $\alpha = 16^\circ$ , at $M = 0.45$ and $Re = 3 \times 10^7$ .....	239
Figure 9-18. Near-wake total pressure coefficient plots for the W-wing Variant B at $x/c_r = 1.5$ , $\alpha = 14^\circ$ at $M = 0.45$ and $Re = 3 \times 10^7$ .....	240
Figure 9-19. Near-wake total pressure coefficient plots for the W-wing Variant B at $x/c_r = 1.5$ , $\alpha = 16^\circ$ at $M = 0.45$ and $Re = 3 \times 10^7$ .....	240
Figure 9-20. Geometry diagram for all wing variations.....	242

Figure 9-21. Lift coefficient results for a range of design variations to the original wing, at $M = 0.45$ and $Re = 3 \times 10^7$ .....	244
Figure 9-22. Drag coefficient results for a range of design variations to the original wing, at $M = 0.45$ and $Re = 3 \times 10^7$ .....	245
Figure 9-23. Lift-to-drag ratio results for a range of design variations to the original wing, at $M = 0.45$ and $Re = 3 \times 10^7$ .....	245
Figure 9-24. Drag Coefficient versus $C_L^2$ for a range of design variations to the original wing, at $M = 0.45$ and $Re = 3 \times 10^7$ .....	246
Figure 9-25. Span-wise lift distribution for a range of design variations to the original wing, at $\alpha = 6^\circ$ , $M = 0.45$ and $Re = 3 \times 10^7$ .....	247

**THE FOLLOWING PARTS OF THIS THESIS HAVE BEEN REDACTED  
FOR COPYRIGHT REASONS:**

Figure 1-3. The light aircraft-Eclipse 500 (Eclipse Aviation) .....	4
Figure 1-4: AVCEN Jetpod (www.avcen.com) .....	5
Figure 1-5: Jetpod in Take-off (www.avcen.com) .....	6

## **Declaration**

I grant powers of the discretion to the University Librarian to allow my thesis to be copied in whole or in part without further reference to the author. This permission covers only single copies made for study purposes, subject to normal conditions of acknowledgment.

*Dedicated to my Father*

*For not giving up on me, even when I did.*

# Acknowledgments

This thesis is an evidence of great support I have had from my family, friends and colleagues throughout the study.

I would like to thank my supervisors Dr. Simon A. Prince and Dr. Chak W. Cheung for their invaluable support, guidance and encouragement throughout my research for this project. I would also like to use this opportunity to express my greatest gratitude to Prof. Dinos Arcoumanis, for the continuous support and for giving me the opportunity to complete this work.

I am most grateful and would like to give my solemn thanks to Mr. Mike Smith, Mr. Chris Barber, Mr. Tim Barnes and Mr. Carmine Badalamenti for the never-ending guidance and encouragement in greatly assisting me throughout the research and without whom I would not be able to realise this work.

My deepest thanks also go to my family, my parents Mr. and Mrs. Muse and Emine Musaj, my brother Mr. Mentor Musaj and my husband Mr. Naim Maqedonci, to whom I am eternally grateful as their limitless love, encouragement and assistance has helped me through the toughest times, to reach the long-awaited finish line. Above all, I would like to thank my little son Jon for understanding during demanding stages. Faleminderit!

## Abstract

A feasibility analysis for an unconventional W-shaped leading edge, reversed delta plan-form wing has been carried out. The wing is believed to aid the Vertical/Short Take-off and Landing (V/STOL) capabilities of small aircraft. The main focus of the research was to carry out computational investigations of the flow phenomena associated with this unique shaped wing at cruise, take-off, and landing configurations. An interactive numerical and experimental method was used to baseline the important flow-field structures associated with this wing, and to identify the necessary areas for further comprehensive full-scale numerical investigations carried out herein.

Numerical simulations solved the explicit quasi-steady compressible Navier-Stokes equations for the cruise conditions (run at a Reynolds Number of  $3 \times 10^7$ ), while segregated quasi-steady incompressible Navier-Stokes equations were solved for the ground-effect analyses and low-speed wind tunnel simulations on a 5% scale of the wing (run at Reynolds Number of  $3 \times 10^5$  and  $3.6 \times 10^5$ ). Numerically, the ground was accounted for with the image method, and the static ground board method.

The fuselage was not modelled in the numerical or experimental investigations. Hence, it needs to be noted that the additional lift-dependant drag caused by the modification of the span loading due to fuselage has not been accounted for. Also, there are limitations on the ground height limited by the inclusion of the fuselage.

In general, the wing was found to have a highly three-dimensional flow field. Both low-speed and high-speed free-flight results revealed that the wing exhibits soft stall and a good lift-to-drag ratio, as well as statically stable pitching moment response up to stall conditions. Maximum lift was reached at  $14^\circ < \alpha < 16^\circ$ , giving a lift-to-drag ratio of 18. On-surface streamline observations showed that the effect of the forward sweep assists in terminating the propagation of the flow separation along the entire part of the wing. High-speed numerical investigations showed regions of local supersonic flow, but with no detrimental effects on the performance of the wing. Near-wake results by both means of study revealed inboard vortex phenomena at higher angle of attack.

The ground-effect results showed a great increase of the lift coefficient and lift-to-drag ratio for the W-wing in ground effect. Values of  $L/D=30$  were achieved for  $h/b = 0.09$ , a 90 % increase as compared to the free-flight case. Regions of very low velocity and high pressure underneath the wing were resolved, suggesting a very strong “air cushion” effect being induced by the wing.

Modification of the wing design suggested that in absence of the forward-sweep, the un-swept wing struggles to maintain attached flow, or indeed prevent further separation on the rest of the wing.

# Nomenclature

<b>Abbreviations</b>	<b>Definition</b>
AR	Wing Aspect Ratio
ASW	Aft Swept Wing
BB	Baldwin Barth
BL	Baldwin Lomax
CFD	Computational Fluid Dynamics
CV	Control Volume
DNS	Direct Numerical Simulation
EASM	Explicit Algebraic Stress Model
FD	Finite Difference
FE	Finite Element
FSW	Forward Swept Wing
FV	Finite Volume
LES	Large Eddy Simulation
MAC	Mean Aerodynamic Chord
MTOW	Maximum Take Off Weight
PAR	Power Augmented Ram
RANS	Reynolds Averaged Navier Stokes
RSM	Reynolds Stress Model
SA	Spalart-Allmaras
SIMPLE	Semi Implicit Method for Pressure Linked Equations
SST	Shear stress transport
STOL	Short Take Off and Landing
VLJ	Very Light Jets
VSTOL	Vertical Short Take Off and Landing
VQSTOL	Very Quiet Short Take Off and Landing
WB	Wing Body
WBNP	Wing Body Nacelle Pylon

<b>Symbol</b>	<b>Definition</b>
a	Speed of sound, Area vector
A, S	Wing area
b	Wing span
B	Tunnel working section width, Dimensionless constant
C	Tunnel frontal cross-sectional area
$C_f$	Skin friction coefficient
$C_L = \frac{L}{\frac{1}{2}\rho V^2 S}$	Lift coefficient
$C_l$	Sectional lift coefficient
$C_D = \frac{D}{\frac{1}{2}\rho V^2 S}$	Drag coefficient
$C_{Dtotal}$	Total drag coefficient
$C_{Dstrut}$	Strut drag coefficient
$C_{DWS}$	Interference of the wing on the strut
$C_{DSW}$	Interference of the strut on the wing
$C_M = \frac{M_{w-on} - M_{w-off}}{\frac{1}{2}\rho V^2 S \bar{c}}$	Moment coefficient
$C_\mu$	Closure coefficient
$c_r$	Root chord
$c_t$	Tip chord
$C_p = \frac{p - p_\infty}{1/2\rho U^2}$	Static pressure coefficient
$C_p$	Specific heat
$C_{p0} = \frac{p - p_{ref}}{1/2\rho_{ref} U_{ref}^2}$	Total pressure coefficient defined
D	Discrete form of the diffusion term
e	Total specific energy
E	Total energy per unit mass
F,G	Flux vectors, defined in Equations 3.11-3.13

$f_r, f_p, f_u$	Source terms
$g$	Body force
$H$	Total pressure, Total enthalpy
$h$	Tunnel height, Internal energy
$h/b$	Ground-height-to-span ratio
$h/c$	Ground-height-to-chord ratio
$k$	Turbulence kinetic energy
$K$	Body shape factor
$L/D$	Lift-to-drag ratio
$l_{mix}$	Turbulence mixing length
$l$	Turbulence length
$m$	Mass flux
$M$	Mach number, Pitching Moment
$P$	Pressure
$q''$	Heat flux vector
$Q$	Volume energy source
$r$	Residual
$R$	Universal gas constant
$Re$	Reynolds Number based on the mean aerodynamic chord
$s$	Specific entropy
$S$	Sutherland's constant
$T$	Temperature, viscous stress tensor
$t$	Time
$T_l, T_t$	Laminar stress tensor and turbulent stress tensor
$T_o$	Reference temperature
$u^*$	Wall shear stress
$u, v, w$	Velocity components in x, y and z direction
$u_\tau = \sqrt{\frac{\tau_w}{\rho}}$	Friction velocity
$U, v$	Velocity
$U$	Dimensionless velocity
$W$	Dependant variables vector, defined in Equation (3.10),
Multigrid cycle	

x	Distance from the wing trailing edge to the rake
y	Normal distance from the wall to the centroid of the first cell
$Y^+ = \frac{u_\tau y}{\nu}$	Dimensionless sub-layer scaled distance
z	Spanwise coordinate

### Subscripts

$\infty$	Free-stream
c/4	Quarter chord
le	Leading-edge
te	Trailing-edge
r	Root
t	Tip
max	Maximum value
s	Specific / Stall
w-on	Wind-on values
w-off	Wind-off values
ref	Reference

### Superscripts

*	Initial guess of a property
'	Corrected value of a property
-	Mean value of a property
°	Degrees
k	Iteration number

### Greek Symbols

$\alpha$	Angle of attack measured in degrees with respect to the free-stream direction, Under-relaxation factor
$\beta, \Lambda$	Wing sweep angle
$\beta^*$	Closure coefficient
$\delta$	Prandtl interference coefficient

$\delta_{ij}$	Kronecker delta
$\varepsilon$	Turbulence dissipation per unit mass, Blockage correction factor
$\kappa$	von Karman's constant
$\mu$	Dynamic molecular viscosity
$\eta$	Ratio of span-wise distance to total
$\rho$	Fluid density
$\sigma$	Shear stress tensor
$\sigma^*$	Closure coefficient
$\tau$	Shear stress, Tunnel working section dependant factor
$\tau_{ij}$	Reynolds stress tensor
$\tau_{ij}$	Surface stress tensor
$\nu = \frac{\mu}{\rho}$	Kinematic molecular viscosity
$\nu_t$	Eddy viscosity
$\Phi$	Flow variable
$\chi$	Wing taper ratio, Heat conductivity
$\Psi$	Yaw angle
$\omega$	Specific dissipation rate

# 1. Introduction

## 1.1 Background

Aerodynamicists are always motivated to consider unconventional aircraft design concepts in order to achieve better performance, improved stall capability, and enhance short take-off and landing potential. One of the main purposes of the search into alternative concepts is the reduction of drag, and the increase of lift-to-drag ratio. Therefore, methods to reduce the induced drag, which constitutes approximately one third of the total drag in cruise and as much as one half of the total drag in climb, are always desirable (Campbell 1998). Enhanced take-off and landing capabilities which would assist in reducing the required runway length and acoustic signature are also considered as a vital design prerequisite.

In addition, the application of power augmented ram (PAR) lift or vertical thrust concepts have been proposed so as to provide lift enhancement during take off and landing whilst allowing the wing loading to be optimized for cruise conditions ( see Figure 1-1).

A range of vehicles have made use of advanced technologies such as composite materials, advanced propulsion systems, laminar flow control and so forth for designs of unconventional concepts.

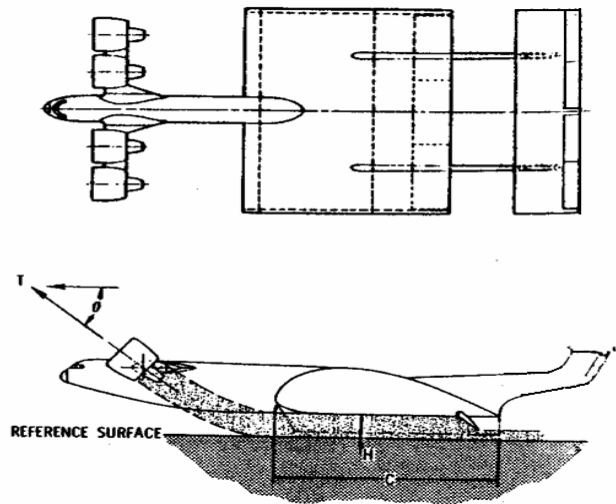


Figure 1-1: PAR Lift Concept in Ground Vicinity (Lange 1998)

On the other hand, environmental issues and sustainable air transportation, able to meet society's demands for minimal environmental impact, will be an ever present and growing motivation for aviation (Hepperle 2004). It is well recognized that environmental issues are an increasing concern for aviation, in terms of emissions and noise propagation, which is particularly significant near airports. Consequently, studies on over-wing-engine placement (Figure 1-2), full span flaps and alternative fuels are of increased interest. These challenges have made new designs more cautious, as it is now not sufficient to only consider the current market environment. It is also necessary to consider possible future environments that will dictate the desired design characteristics.

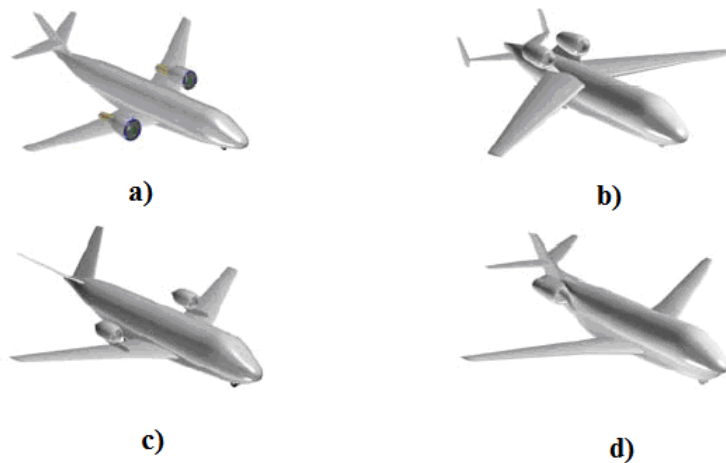


Figure 1-2: Possible Configuration for a Green-Aircraft a) upper surface blowing engines, b) fan shielded by wings (high wings), c) fan shielded by wings (low wings) and d) buried engines (low wings) (Hepperle 2004)

Furthermore, as road transportation across larger cities will continue to be a serious problem, alternative transportation routes have been assessed. Amongst others, “air-taxis” have been proposed as an option. They have been suggested as one way of off-setting road and rail congestion, with on-demand and affordable travel. These vehicles would operate at lower cruise heights and would possess greater agility. Increasing interest for the so-called Very Light Jets (VLJ) to be used as taxi-style aircraft has been reported recently in the US. These vehicles can operate from shorter runways than commercial airliners and this means that they can utilize the available satellite airports. The first aircraft of such kind is the Eclipse 500 (Figure 1-3), which has been designed to take-off within 700m; it comprises of four seats and can reach maximum speeds of 370 knots.

Other vehicles of such purpose are currently being built by Embraer and Cessna. These vehicles, however similar to the regional jets, which have been heavily employed, have to use the already congested airports. The Federal Administration Aviation (FAA) estimated that up to 500 VLJs will be added to the US skies next year, whilst the number of private jets including VLJs, will double to 22,800 by 2020

(Peake 2007). Interest in these vehicles has also been shown in the UK; around 200 of the Eclipse 500 have already been ordered by companies based in the UK.



Figure 1-3. The light aircraft-Eclipse 500 (Eclipse Aviation)

Companies such as Linear and DayJet have been establishing the transportation routes for VLJs as orders for 30 (by Linear) and 239 (by DayJet) Eclipse 500, have been placed. Although, the air-taxi as another transportation system has shown increased interest the idea has also been criticized by others. These aircraft will fly at 40,000 ft and critics are already sceptical about having more aircraft in the airspace of commercial aircraft ([www.shortlist.com](http://www.shortlist.com)).

A disadvantage of such vehicles is the fact that VLJs still require longer runways, as they are designed to avoid the airport congestion rather than the transportation problem in general such as road and rail. Therefore VLJs that would take-off at shorter distances, for greater flexibility in avoiding congestion in general, would be in high demand. One such configuration of such kind is the Jetpod air-taxi design proposed by AVCEN. The AVCEN designed Jetpod (Figure 1-4) is based on the idea that air taxis should shuttle between an outer ring of park-and-fly sites and several city-centre STOL strips (Figure 1-5) or between countryside and suburban sites that do not require long runways.

The Jetpod is a VQSTOL (Very Quiet Short Take off and Landing) aircraft, featuring two over-the-wing mounted jet-engines; vertical under-wing thrust nozzles (with

carefully designed aeronautical components) and a thrust management system. The Jetpod aircraft is designed to take-off and land within 125m, loiter at around 45knots and reach cruise speeds of 300knots. The aircraft has been designed to carry out multiple daily flights, between 5 to 7 passengers. AVCEN has reported that the Jetpod will produce 50% less noise and 35% less pollution than its counterparts.

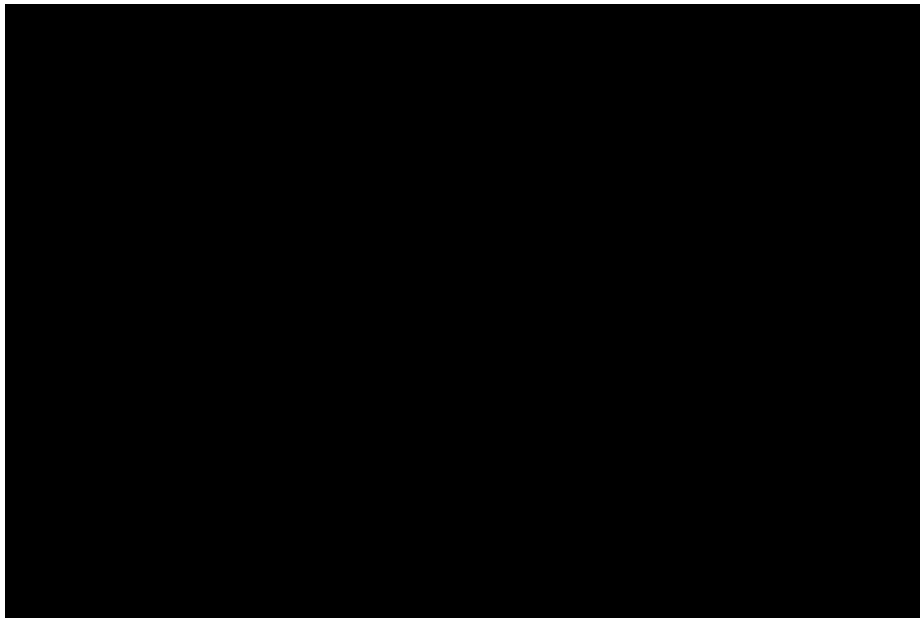


Figure 1-4: AVCEN Jetpod ([www.avcen.com](http://www.avcen.com))

Three proposed utility designs have been developed; civil or air-taxi, military and ambulance. The Jetpod uses an unconventional wing is that has a W-shaped-leading-edge reversed delta planform wing, hereafter referred as the W-shaped leading-edge wing. This wing comprises of combined backward-forward sweep (further details of the wing is given in sub-section 1.3 below).

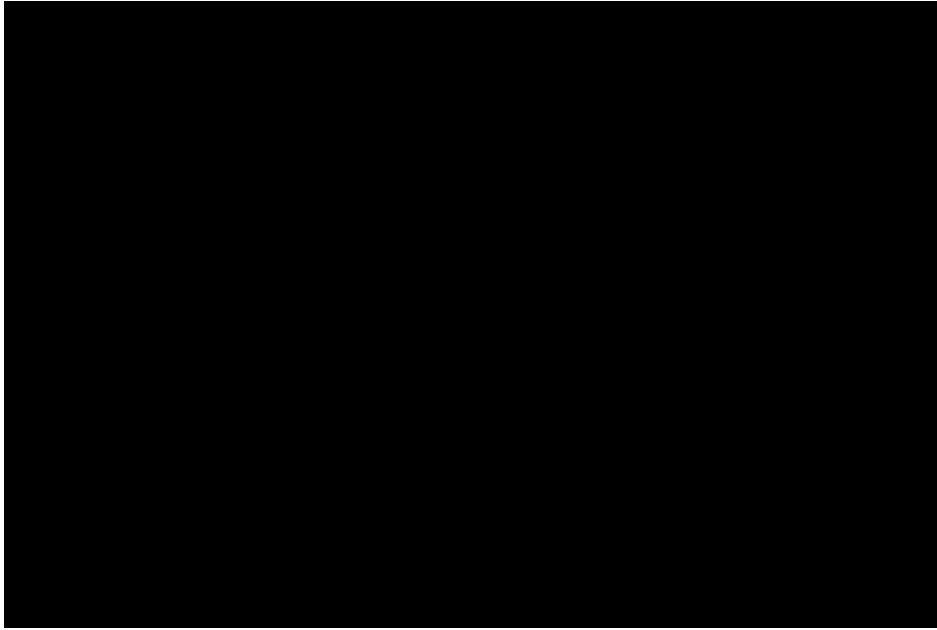


Figure 1-5: Jetpod in Take-off ([www.avcen.com](http://www.avcen.com))

The purpose of the current work by the author is to carry out feasibility analyses for the new Jetpod (air-taxi) aircraft designed by AVCEN.

A preliminary design investigation carried out at City University with an estimated  $C_L=1$  showed that the required runways length could be met with the current specifications of the aircraft. This characteristic would be attained with an augmentation upward thrust that increases as engines with decreasing maximum thrust are considered. For 4,750lbf of maximum engine thrust, 41.3% of this thrust must be deflected downwards; for 5,000lbf of forward thrust (see Figure 1-6), only 31.4% of this thrust should be directed down, for 6,000lbf of forward thrust just 5% of this thrust directed down is sufficient for Jetpod to lift off with 125m. These studies were based on Maximum take-off weight of 6500 lbs; this specification was later changed to 6000 lbs which relaxes the downward thrust deflections even further. Nevertheless, no thorough investigations have been carried out on the take-off and landing runway length as this work is beyond the scope of this study.

### Jetpod Total Lift, Max. Thrust=5,000 Lbf

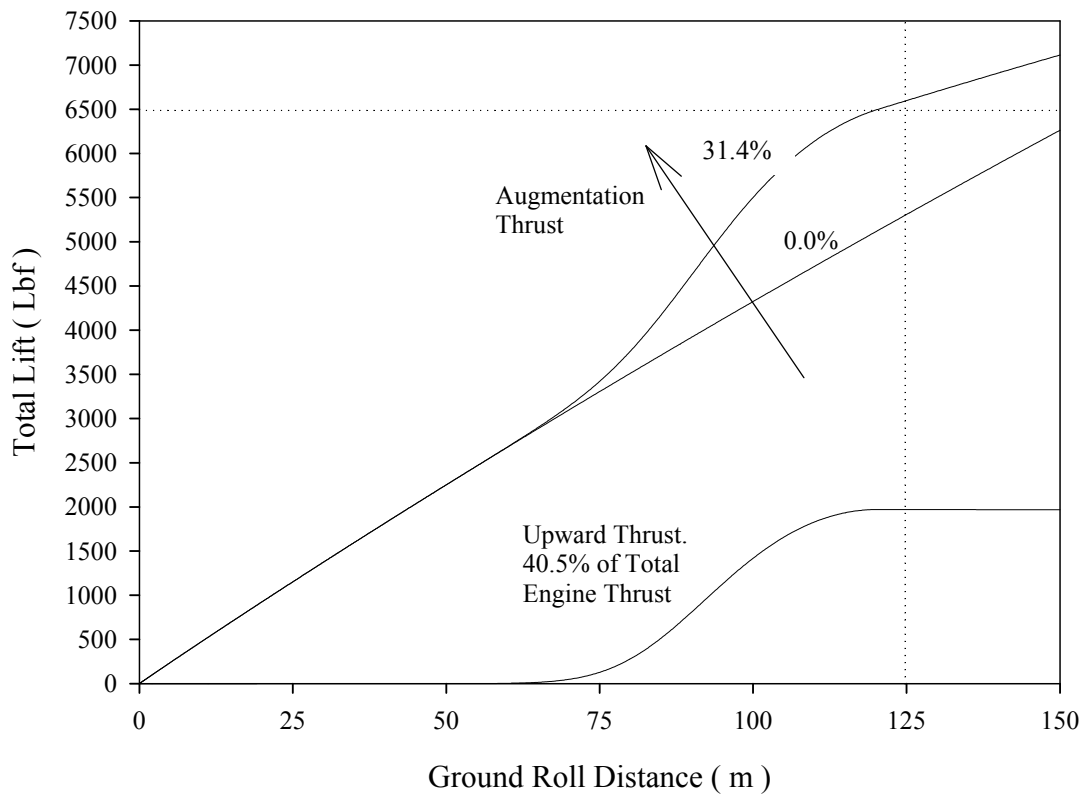


Figure 1-6. Total Lift vs. Ground Roll Distance

Initial requirements of the Jetpod aircraft are to take-off and land within 125m strips with other speed characteristics as presented in below.

- Cruise speed 300kts i.e Mach=0.455
- Initial approach speed 82 knots
- Stall speed ( $V_s$ ) clean of 80 knots, no vertical thrust component at MTOW 6000 lbs
- $V_s$  clean of 70 with 45 degree vertical thrust component at MTOW 60 % power

The above lead to top level requirements of  $C_{L_{cruise}} = 0.18$ ,  $C_{L_{max}} = 1.07$  and  $C_{L_{TO,CLIMB}} = 0.73$ . Hence if the requirements ought to be met the lift characteristics of the wing should fall within these values.

## 1.2 Project Overview and Objectives

The main purpose of this study was to carry out extensive aerodynamics investigations in assessing and refining the performance of the Jetpod aircraft wing components. Primarily, a study on the choice of the most appropriate methods to be exercised, in order to carry out these investigations has been performed.

Theoretical aerodynamics has always provided insights to aerodynamicists in the preliminary stages of aircraft/ wing design. However, the traditional approach to aircraft design relies on experimental data. Whilst this approach has been very successful, it has its drawbacks because it is very expensive and time consuming. With the recent technological improvements in computer speed and memory size there are opportunities to apply Computational Fluid Dynamics (CFD) investigations to much more complex geometries such as the three-dimensional wing designs seen in unconventional aircraft. CFD applies specific solutions of the governing equations of fluid dynamics to the design and analysis of vehicle systems. The potential of CFD in solving a wide variety of fluid flow problems is well recognized and it is rapidly becoming an important tool in the design of aerospace systems. Studies suggest that incorporating the high fidelity of CFD into the conceptual design stage, where the most freedom is available in the design, allows the use of CFD to make a greater impact (Jameson 1997). While CFD has not replaced the wind tunnel it has certainly become an important enhancement to the use of the wind tunnel. Nevertheless, blind acceptance of computed results will lead to problems; therefore coupling of the computational and experimental techniques is both necessary and beneficial. This CFD-experimental design method can achieve successful and less expensive results, as compared to experimental alone. Therefore, this research employed a coupled experimental and numerical approach. The research examines lift, drag and pitch behavior, stall, and flow separation conditions. The focus involved CFD and experimental investigations of several low-speed tests over the wing configuration, which was then followed by extensive complete viscous-flow high-speed numerical only analyses using commercial CFD packages.

During loiter, the Jetpod aerodynamic flow remains fundamentally incompressible. In typical air-taxi applications the cruise Mach number exceeds the accepted incompressibility threshold of Mach = 0.3. Consequently, compressibility effects become sizable and must be incorporated in the analyses. Also, as expected with this type of flow, turbulence modelling will have to be included in the investigation. For every computation a grid will be established and then refined, smoothed and updated as the simulations progress to increase the accuracy of the investigation.

As one of the most critical phases of powered flight, take-off, where weight is at its largest and speeds are low, should be assessed for every system at the initial new design stage. Complete incompressible analyses of the flow field phenomena of the wing in ground-effect for various ground heights have been carried out.

The numerical method was validated, for these low speed conditions, by comparison with data from a wind-tunnel test program of single element wing geometry similar to the AVCEN wing, undertaken by the author. Free-flight and ground tests have been carried out in two different wind tunnels available at the Handley Page Laboratory at City University. Reynolds Numbers, sting, ground boundary layer and wall effects have been assessed to optimise the results.

In addition a systematic design study has been performed using an industry standard full-potential equation flow solver, to investigate a series of design variations based on the AVCEN wing etc.

The specific objectives of this Dissertation are:

- Selection of a three-dimensional numerical model which reasonably reflects the physical and geometric conditions of the flow in the vicinity of the wings.
- Design of the appropriate numerical set-up for the high and low-speed analyses to be performed on the W-shaped-leading-edge wing.
- Asses the suitability of the numerical algorithm for full-scale and scaled (5%) model of the wing, by assessing the boundary condition requirements,

geometry and mesh generation as well as the use of the appropriate models that will correctly account for the turbulence features.

- Develop an experimental procedure for preliminary analyses of the flow around a replica scaled (5%) wing model. Moreover, employ the experimental procedure to verify and validate the numerical algorithm employed for the study.
- Assess the ground effect capabilities of the W-shaped-leading-edge wing, by investigation of the take-off/landing configurations by both numerical and experimental methods on a full-scale and scaled wing model.
- Thorough investigation of wing's performance: detailed drag, lift and moment analysis, wake profile, surface shear-stress data and off-surface particle trace investigations.

### **1.3 Wing Specification**

The Jetpod wing is an unconventional W-shaped-leading-edge wing, which comprises a combined backward-forward sweep, which is believed to provide the beneficial qualities of both sweep options in a single design. The use of aft-sweep has long been recognized; together with its disadvantage. The use of forward sweep can provide several advantages, such as increased leading edge suction and “soft” stall without the detrimental effects of aft-sweep. Past research has shown that poor wing root design can negate many of the advantages of forward sweep. The use of backward sweep on the inboard wing may reduce such detrimental side effects. It is believed that the properties of this type wing make it suitable to the performance requirements of such Short Take-off and Landing (STOL) type aircraft. The wing is similar in shape to the so-called Lippich wing, which is known to be highly effective in ground effect and is the only ground effect –planform design that can also perform out of ground effect. A further review in these matters is given in section 2 of this dissertation.

This study is dedicated to assessing the aerodynamic performance capabilities of a combined sweep wing of the AVCEN planform type. The wing has no twist, and comprises of three segments (see Figure 1-7); the inboard segment has an anhedral of 12 degrees, whilst the central and outboard segments both have an anhedral of zero degrees. The NACA 2412 aerofoil section was used throughout, the choice which was based on the attractiveness of the section, as it possesses relatively high  $C_{L_{max}}$  and linear pitching moment characteristics. The wing has been employed on numerous conventional wing configurations until now. This cambered airfoil is 12 % thick with maximum lift coefficient of 1.65 for  $Re = 3.1 \times 10^6$ . Details and a sketch of the airfoil characteristics are presented in Figure 1-8.

Given the shallow nature of the sweep, its inversion relative to the M-wing concept, and the inverted delta planform this type of wing has been termed a W-shaped leading-edge reversed delta planform wing.

Total Wing Area	23.98	m <sup>2</sup>
Wing Aspect Ratio	5.50	
Mean Aerodynamic Chord (MAC)	2.86	m
MAC Location for main root chord	0.71	m
Wing Span	11.46	m

Table 1-1: Jetpod Total Wing Specifications

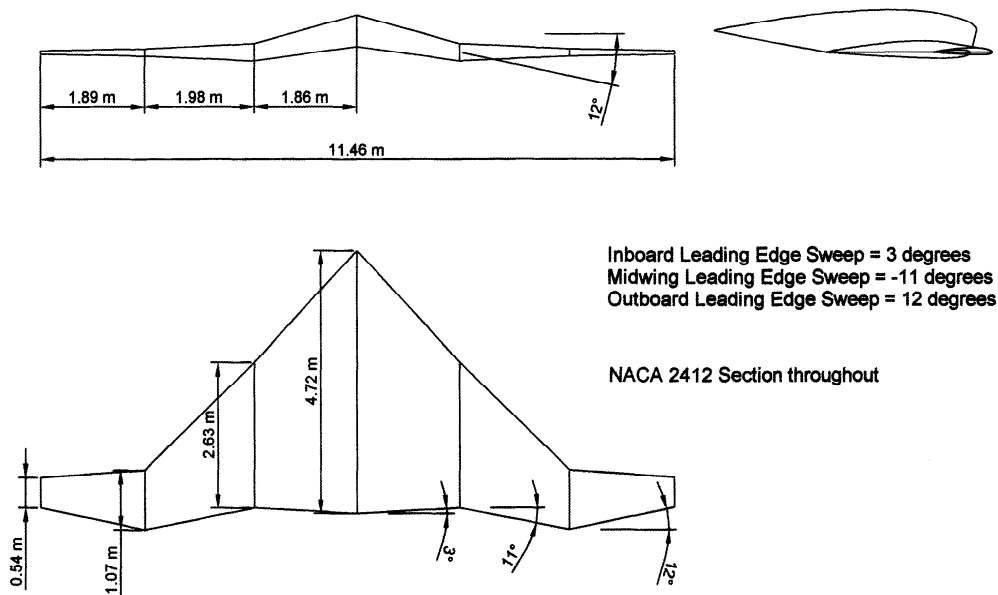


Figure 1-7: Jetpod Wing Specifications

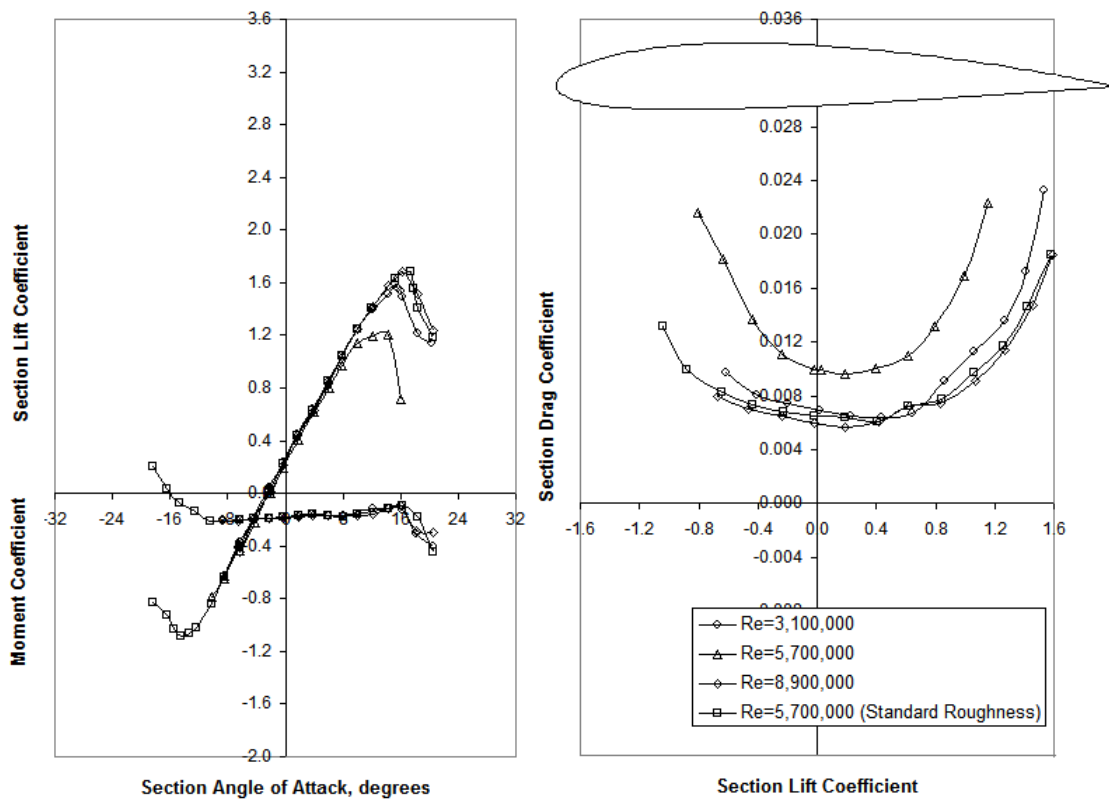


Figure 1-8: NACA 2412 Section Characteristics (Abbott and Von Doenhoff 1959)

## 1.4 Thesis Overview

The remaining seven sections of this dissertation are organized as follows:

Section 2 gives a brief overview on the wing aerodynamics both conventional and unconventional. A background history on the aft and forward swept as well as available data of combined sweep wings is given. This section also illustrates ground effect methods for experimental and numerical analyses are examined and key specific concerns related to their application have been addressed.

In Section 3 the governing equations of continuum fluid dynamics (Navier-Stokes and Full-Potential) are summarized together with their applicability to model and predict flow-field phenomena. Computational methods for solving these equations are described. Discretisation schemes are presented, as well as error sources from the discretised computational model. Section 3 also illustrates practical application of computational methods in wing design. A literature survey of some of the requirements for practical use of CFD in the design process is followed by a description of different CFD design algorithms, along with their relative strengths and weaknesses. Issues that need to be addressed, with regards to which algorithm would be most properly suited for the current wing design analysis, have been evaluated from a large body of literature of complex configurations. The choice of grid generation methodology and turbulence modelling most appropriate for three-dimensional wings have also been reviewed. A short overview of the turbulence modeling technology is presented, together with the pressure correction methods applied to this study. A description of the CFD packages employed is also given.

Section 4 includes derived results from the study performed to assess the applicability of the CFD codes and algorithms employed herein. The codes were verified against available experimental data for the Onera M6 wing. For the purposes of the current study, validation of both the Navier-Stokes (compressible and incompressible) CFD code and full-potential code were carried out. Both high-speed and low-speed validation studies were performed to inspect the capability of the codes.

Section 5 describes the experimental set-up used in obtaining data applied to validate the numerical predictions. The two wind tunnels employed for the study are described together with the flow measurement and visualization tools employed. The equations employed for the calculations of the force and moment coefficients and near wake pressure coefficients are given. A description of the routine of the tests carried out and the apparatus employed for the ground effect studies are specified.

Section 6 provides detailed results obtained with two different low-speed studies; experimental and wind tunnel numerical simulations. Both low-speed studies of the exact scale model of the wing in free-flight are given. This section gives preliminary aerodynamic analysis of the wing configuration to provide additional data for further investigations in the subsequent section.

Section 7 explains the results of the numerical study of the wing for the cruise conditions. Convergence and grid sensitivity studies are presented, together with the final choice of the turbulence model and grid. Broad results on the force coefficients and near-wake phenomena are presented.

Results of the ground simulation of the full-scale and wind-tunnel model wing are presented in section 8. Two methods of simulating the ground are assessed: the image method and the fixed ground board method (description of the methods is given in section 2 of this dissertation). Near-wake analyses are presented for various rake locations in both numerical and experimental investigations. Systematic results and discussion follow.

Section 9 gives a brief design synthesis carried out to investigate a series of design variations based on the AVCEN wing. This includes results and discussion on the design variation effect on flow phenomena in comparison with the original wings as well as suggestions towards possible improvement towards the best configuration.

Section 10 presents a summary of the key results of this study, conclusions, and suggestions for future work.

## 2. Literature Review (Wing Aerodynamics)

### 2.1 Background History

The effect of aft-sweep on the flight characteristics of aircraft wings has long been recognized. Swept wing use has arisen because of the desire to increase the cruise Mach number (Munk 1924). With the increase in cruise speed aircraft wings began to experience the effects of local shock waves. Jones recommended the use of sweepback as means of reducing transonic drag (Jones 1947). Jones suggested that for aerodynamic efficiency, wings should be swept back at an angle greater than the free-stream Mach angle and that the angle of sweepback should be such that the component of velocity normal to the leading edge is less than the critical velocity of the aerofoil section. For swept back wings the velocity components normal to the leading edge appear to contract as they flow over the upper surface (see Figure 2-1). It is seen that they pass over the wing in such a way as to increase the stream-tube area (Figure 2-2).

Furlong and McHugh gave a comprehensive summary of the behavior of swept-back wings (Furlong and McHugh 1952). Furlong and McHugh explain that pressures on an un-swept wing indicate an outflow of the boundary layer on the lower surface and inflow on the upper surface. With sweepback, the respective chord-wise pressure distributions are staggered, so on any line perpendicular to the plane of symmetry the pressures on the upper surface become more negative with distance from the symmetry plane. A pressure gradient therefore exists from root to tip which induces a boundary layer flow in that direction. This causes the change in the span-wise distribution of induced angle of attack, which causes the lift distribution to move outward. Flow separation and lift loss at the tip would consequently precede that of the inboard section. The combined influence of these two effects is to make the root sections of swept wings highly resistant to separation.

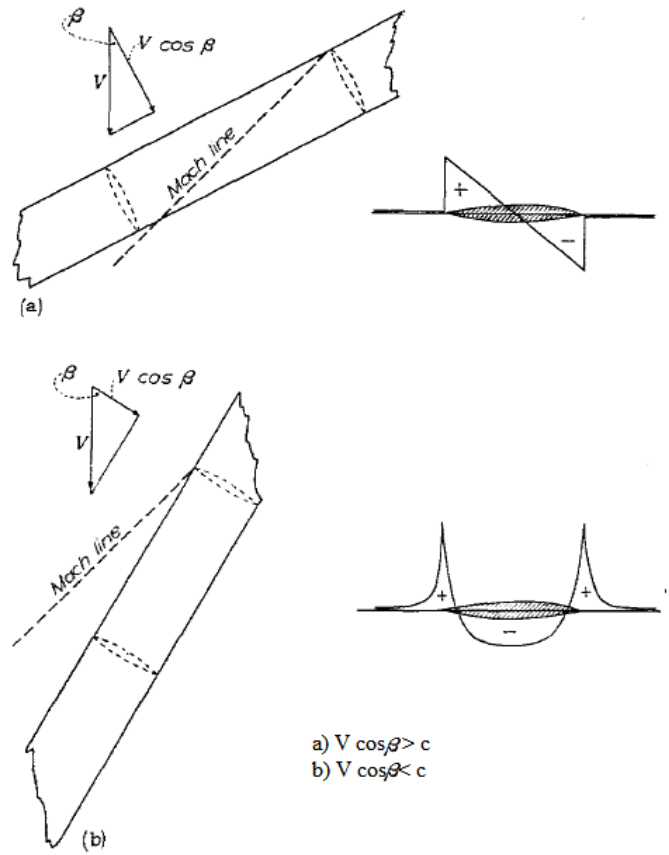


Figure 2-1: Leading Edge Angle Effect on the Pressure Distribution (Jones 1947)

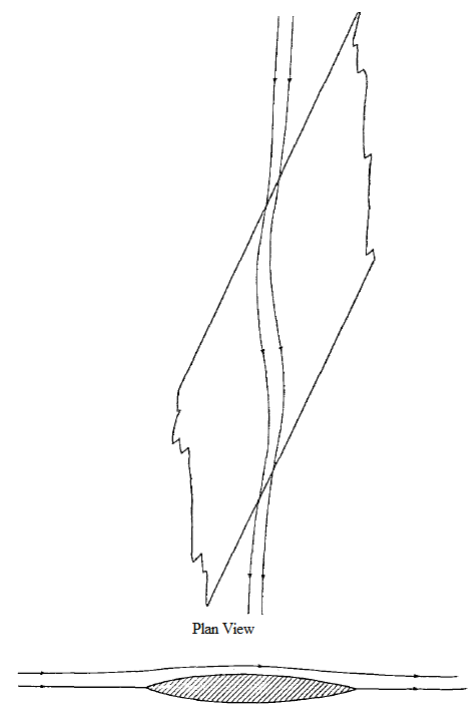


Figure 2-2: Stream-tube on Upper Surface of Aft-Swept Wing (Jones 1947)

Therefore, as soon as sweepback was introduced it was realized that at subsonic speed the induced angle of attack distribution and boundary layer growth would promote tip stall, and the maximum lift coefficient of the tip will fall short of the maximum lift coefficient of the root sections as illustrated in Figure 2-3. It has also been shown that pitching moment curves become increasingly nonlinear as the sweep angle is increased and the wing tends to become more unstable near stall (Letko 1946), as tip stall could result in a loss of lift behind the moment center of such magnitude to cause a nose-up pitching moment. Other disadvantages noted for swept back wings are the difficulty of accommodating the engines, the undesirable displacement of the centre of pressure in the area of undisturbed flow, the decrease of lateral and directional stability before reaching  $C_{L,max}$  and the decrease of aileron effectiveness at large angles of attack (Furlong and McHugh 1952).

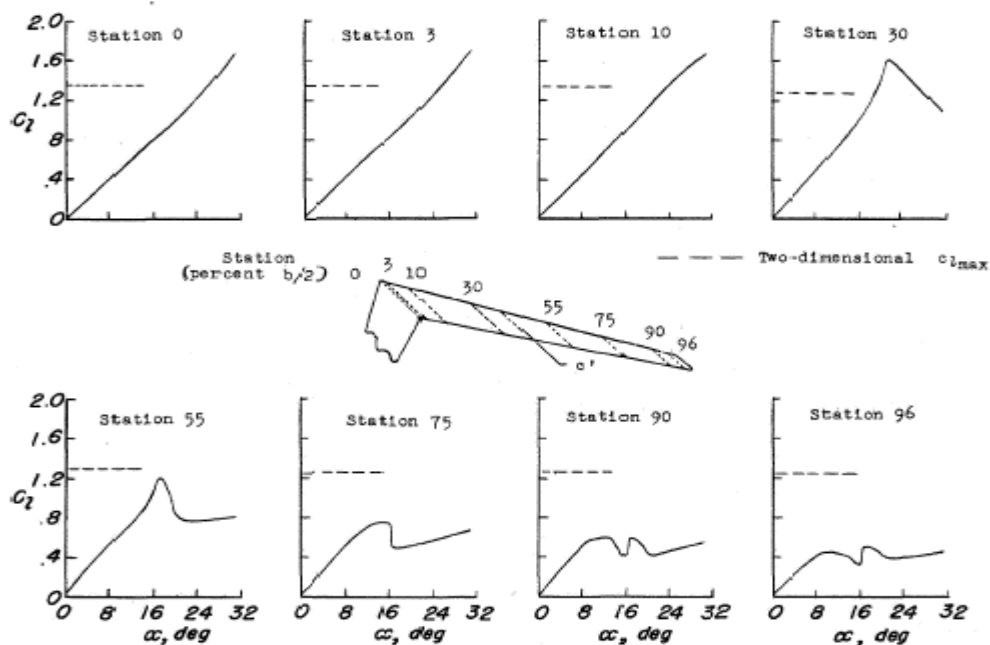


Figure 2-3: Stall Progression on an Aft-Swept Wing (Furlong and McHugh 1952).

As a result of the disadvantages associated with the employment of highly swept back wings, there have been many studies to avoid these effects by alteration of the wing contour. This is done by employment of various stall control methods to delay or prevent separation, such as devices attached or built into the wing. These devices include fences, vanes, and extensible leading-edge flaps amongst others. As aft-swept

wings (ASW) are handicapped by the fact that the maximum lift is limited by the occurrence of tip stall, if premature boundary layer separation in the wing's root area is prevented, (i.e by using leading edge extensions ) the relocation of the lift from the tip region to the root area provides further aerodynamic advantage. A further review of this subject is given in (Furlong and McHugh 1952). Others have also suggested the use of forward sweep and a limited number of authors have suggested the use of combined sweep, such as "M" or "W" wings.

Forward swept wings (FSW) are not seen very often on aircraft. However, the use of forward sweep can provide several advantages. Forward-swept wing designs appear to offer aerodynamic performance improvements over conventional aft-swept wings. This includes reduced drag, increased leading edge suction, a soft stall and a higher lift-to-drag ratio (Owens 1996). These benefits may have been a consideration in the design of the Junkers prototype bomber, the Ju-287, the first forward swept wing aircraft, which flew briefly in early 1945 (Bowers 1990).

Lademann gives a further review of early experiments that employed forward-sweep (Lademann 1932). Until recently serious consideration had not been given to forward-swept wing designs because forward sweep led to an unfavorable static aero-elastic characteristic, namely, static divergence (Diederich 1948). Through the development of advanced composite materials and using specially oriented laminates, the aeroelastic divergence problem was alleviated (Ricketts 1980) and many feasibility studies were initiated.

Differences between forward sweep and aft sweep arise when three-dimensional effects are considered, particularly at the root. The curved streamlines typical of the sheared flow for the FSW cannot persist into the centre or up to the tip; in these regions the streamlines are straightened out. These features cause the forward swept wing to have an upwash at the wing root and normally a downwash at the tip. As the sweep is reduced the aerodynamic lift of the inner wing is exploited to an increasing degree (Lombardi 1993). Purser and Spearman illustrated the behavior of tuft studies for various planforms (Purser and Spearman 1951). Fig 2-4 and 2-5 present the results for an aft-swept wing and a forward-swept wing, respectively.

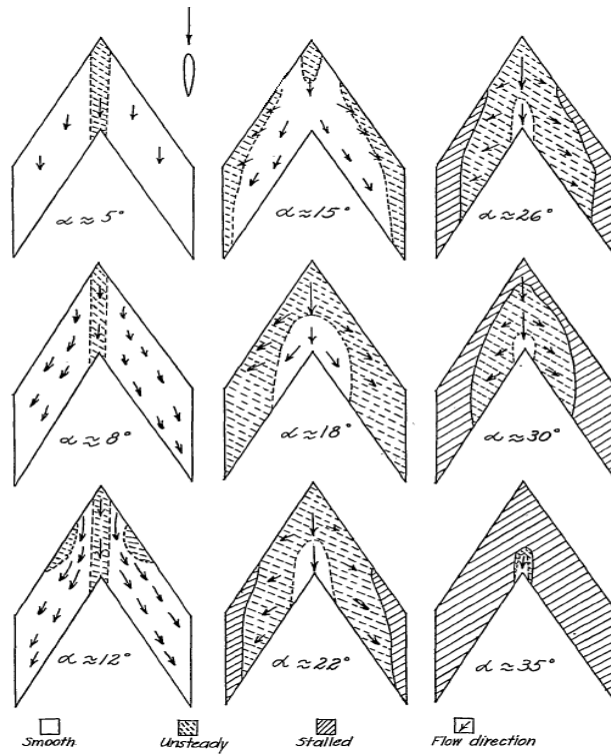


Figure 2-4: Flow Pattern on a Aft-swept wing with  $\Lambda_{c/4} = 60^\circ$ , AR = 1.5 and NACA 0012 (Purser and Spearman 1951).

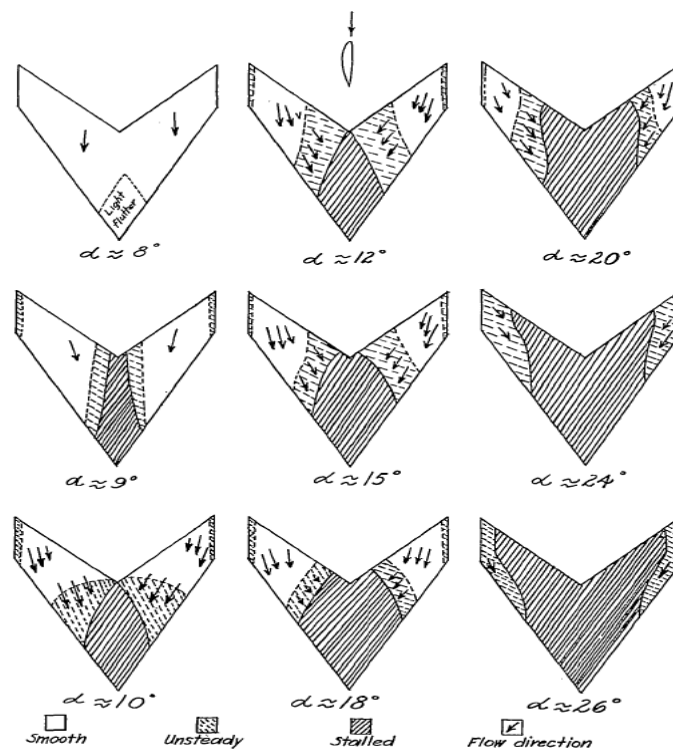


Figure 2-5: Flow Pattern on a Forward-swept wing with  $\Lambda_{c/4} = 46.6^\circ$ , AR = 2.1 and NACA 23012 (Purser and Spearman 1951).

Redeker and Wichmann showed that forward sweep results in a more stable laminar boundary layer (Redeker and Wichmann 1991). Directional lateral control over higher angles of attack is also retained. Forward sweep is also known to reduce the approach speed. Of particular interest is higher lift at take-off and landing conditions, which could be very influential in VSTOL design (Putnam 1994).

FSW configurations are stable in yaw and roll up to the maximum angles of the attack. Knight and Noyles suggested the use of forward sweep provided a greater useful angle of attack than the aft swept wings (Knight and Noyles 1931).

In addition to a reduction in wing profile drag, flexibilities on aft placement of the wing box, resulting in a decrease in wing structural box weight have been noted as further advantage of the FSWs. Furthermore, increased fuselage design freedom and reduced trim drag owing to less wing twist required have been reported. Results have shown that the use of FSWs can provide aircraft weight reductions of 5% to 30% depending on the design and mission requirements (Putnam 1994) which is a favorable feature, in this case, for air-taxi designs.

Knight and Noyles reported the benefits of forward-sweep in the early 1930's. They carried out pressure distribution measurements for the purpose of studying the effects on lateral stability of changing span-wise load distribution on a rectangular monoplane wing model of fairly thick section. Twist from  $+5^\circ$  to  $-15^\circ$  at the tip and leading-edge sweep from  $+20^\circ$  to  $-20^\circ$  were employed.

It was noted that increasing the tip twist reduces lateral instability but also decreases wing effectiveness. It was observed that transition from forward sweep to aft sweep gradually reduces the useful angle-of-attack range, but has no clearly defined effect on maximum lateral instability. Relative to the angle for the un-swept wing, forward sweep was seen to raise the angle of attack of neutral stability, aft-sweep to lower it. In the forward-sweep case because the tips, which affect lateral stability more than any other part of the wing, stall later than on the aft-swept wings, the angle of attack of neutral stability is raised. Thus, for FWS wings the slopes of the normal-force curves for the tip sections are increased and their maxima delayed, both of which tend to maintain lateral stability to a higher angle of attack. When the wing is swept back the slopes decrease and their maximum points occur at lower angles, which have the opposite effect upon the angle of neutral lateral stability. It was shown that forward

sweep of up to  $20^\circ$  has no effect on maximum angle of attack whilst sweepback up to  $20^\circ$  reduces it about 10%.

The X-29 aircraft was the first manned, experimental forward swept wing high-performance aircraft manufactured and flown in many years. Extensive analyses and studies of the forward swept wing design of the X-29 were conducted.

(Hicks and Huckabone 1989) carried out flight tests for the X-29A aircraft. The most notable feature of the aircraft was the forward-swept wing with a  $29.3^\circ$  leading edge sweep and an aspect ratio of 4 (see Figure 2-6). Preliminary investigation of the subsonic lift and drag characteristics of the X-29A aircraft was conducted and compared with predictions. The configuration gave favorable results in the application of forward sweep and several tests of the configuration have been conducted.

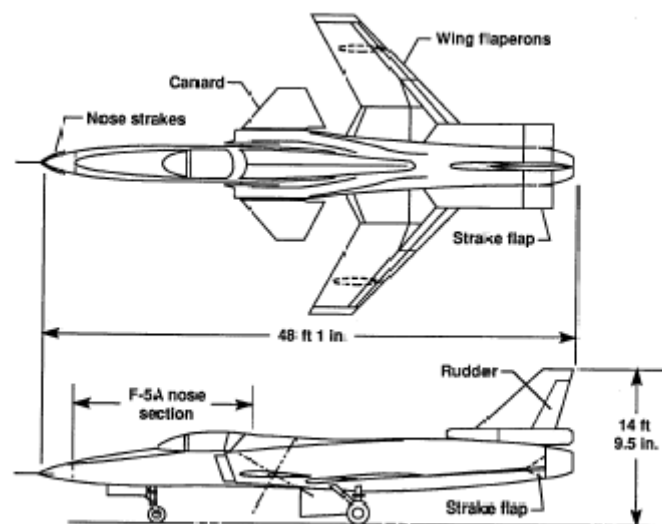


Figure 2-6: The X-29A Aircraft (Saltzman and Hicks 1994)

Saltzman and Hicks obtained in-flight lift and drag characteristics for the X-29 airplane for Mach = 0.4-1.3. The data were then compared with three high performance fighter aircraft: the F-15C, F-16C, and F/A-18. The X-29 was seen to have a better overall aircraft aerodynamic  $e$  (Oswald) efficiency factor for the same aspect ratio, when compared against aft-swept wings counterparts (Saltzman and Hicks 1994).

An experimental study of the comparison of forward-swept wings to un-swept wings was performed by Lombardi (1993). Pressure distributions on two wing models with different sweep angles,  $\Lambda = 0^\circ$  and  $\Lambda = -25^\circ$ , were evaluated. Two flow regimes were tested, at Mach = 0.3 and Mach = 0.7. The forward swept wings gave a maximum lift coefficient that was slightly lower but close to that of an equivalent un-swept wing, however this value is reached at much higher angles of attack. The usual trend of stall initiating at the root and moving from the root to tip was noticed at higher angles of attack of approximately  $24^\circ$  (see Figure 2-7). However, forward sweep gave a much sharper decline of the force coefficients post stall, which disagrees with previous findings (Owens 1996). The difference, as described by Lombardi, was attributed to the fact that in un-swept wings all sections have the same local angle of attack whereas for the forward swept wing at max lift a large part of the wing has already stalled so that beyond this angle the flow is almost fully separated.

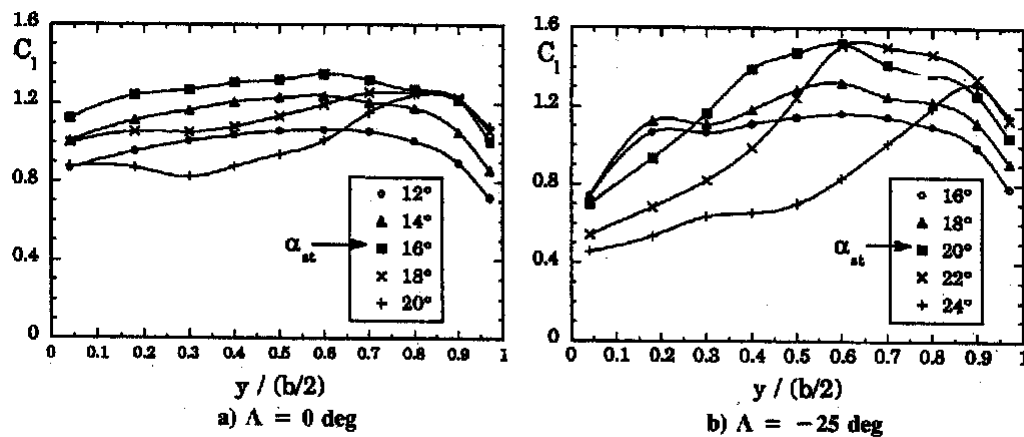


Figure 2-7: Span-wise Lift Distribution Comparison between FSX and Un-swept-Wing (Lombardi 1993)

From an aerodynamic view point, the lift distribution on a forward-swept wing particularly at higher angles of attack can be turned to a real advantage when coupled with a canard surface. Under these conditions the canard wake induces a downwash at the wing root as well as an upwash at the wing tip, so that more uniform stall conditions along the span are obtained (Lombardi et al 1996).

Lombardi et al (Lombardi et al 1998; Lombardi 1998) also assessed the capabilities of different numerical models in evaluating the aerodynamic characteristics of a forward-swept wing in subsonic and transonic flow. Navier-Stokes computations have been shown to give better agreement with experimental data than potential and Euler calculations. However, at lower angles of attack all models showed discrepancies when compared with experimental data.

One feature that is very sensitive when considering the use of forward sweep in wing configurations is the wing root design. Several researchers have noted that poor root design may cause the loss of many of the advantages of the forward sweep design.

In the search for a wing planform which would incorporate the benefits to be derived from sweep and yet possess acceptable low-speed characteristics, Lemme in 1946 investigated the behavior of aft-swept, blunt aft-swept and “M” planform wings, with aileron and flap deflection (Lemme 1946). All the tests were run at a Reynolds Number of  $Re = 4.6 \times 10^5$ . The drag of the three wings in the range of small angles of incidence was found to be practically the same for the Reynolds Number tested. The swept back and M wings possessed the same  $C_{L,max}$  whereas the blunt wing possessed the highest  $C_L$  and lift curve slope. Lemme concluded that in comparison with the aft-swept wing, the M wing (illustrated in Figure 2-8) has the advantage of the engine placement and favorable longitudinal moment, as with increase in angle of attack it becomes nose heavy instead of tail heavy. Using flow visualization Lemme noted that the middle part of the M wing was found to separate first. The M wing, however, was noticed to not have any advantage over the swept back wing with split flap deflection. M wings, also do not exhibit the aerodynamic centre shift, resulting from twisting, a feature seen with aft-swept wings.

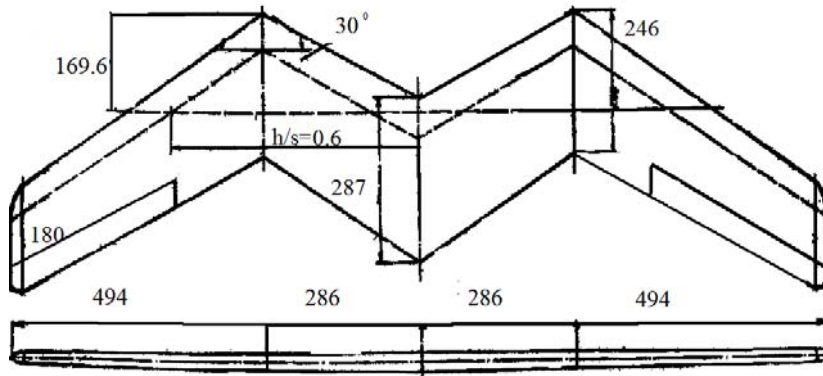


Figure 2-8: The M-Wing Employed by Lemme.

The concept of the M wing has been also studied by Whitworth, Vickers and Bristol (Payne 2004) (see Figure 2-9). These experimental aircraft were designed to fly at supersonic speeds, however these designs have never been taken any further and no results of these projects are available. The high drag due to junction associated with M wings caused the projects to be shelved before any low speed work had been done.

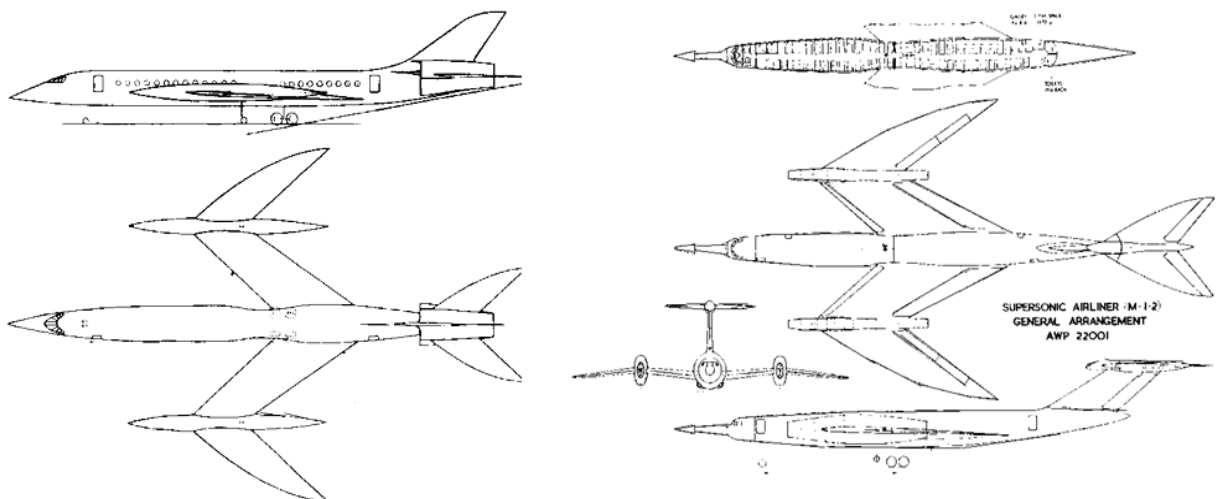


Figure 2-9: Vickers Project X (left) and Whitworth AWP22001 M-wing (right) (Payne 2004)

Purser and Spearman carried out wind tunnel tests of an exploratory nature on various small-scale models of aft-swept, forward swept and yawed wings (Purser and

Spearman 1951). The tests were run at Reynolds Numbers varying between  $6.2 \times 10^5$  and  $1.2 \times 10^6$  and various tip modifications were carried out in pursuit of stall delay. In general, reducing the aspect ratio and the ratio of root chord to tip chord resulted in increases in drag and effective dihedral and increased the longitudinal stability near the stall.

Cutting off the tip normal to the leading edge on an un-tapered  $60^\circ$  aft-swept wing had little effect on either the nonlinearity of the pitching-moment curve or the stability near the stall but did move the aerodynamic center back at low lift coefficients. By sweeping forward a part of the outer panel of an aft-swept wing an improvement in the longitudinal stability and a decrease in the effective dihedral were observed. When the outer 40% of the wing panels were swept-forward the wing resembles a W-wing shape, as shown in Figure 2-10. For this type planform the pitching-moment curve became nearly linear and indicated stability near the stall. However, this configuration slightly decreased the maximum lift coefficient and increased the drag at high lift coefficients. Purser and Spearman explain that this effect may be due to the increased interference between the forward-swept and the aft-swept panels.

It was also noticed that the aileron effectiveness at a lift coefficient of  $C_L = 0.2$  for the  $45^\circ$  untapered swept forward wing was about 10 % greater than the value obtained for the  $45^\circ$  untapered aft-swept wings. This result was caused by the thinner boundary layer and the less turbulent flow existing on the tips of swept forward wings.

A form of combined sweep wing has more recently been proposed as an efficient configuration for tailless aircraft. Jing et al studied an innovative aerodynamic configuration of a form of so-called “W”<sup>1</sup> shaped tailless aircraft (Jing et al 2004; Jing 2004). They note that favorable outboard stalling performance of the forward wing affords great potential in yaw and roll control ability which makes up for the control deficiency of tailless aircraft. Tests were run at Mach = 0.3 and Reynolds Number of  $Re = 2.85 \times 10^6$ . Excellent lift to drag characteristics were reported with  $L/D_{\max} = 30$  and favorable pitching moment characteristics. The results however to seem to be

---

<sup>1</sup> It needs to be noted, however that the W shape proposed by Jing et al, is not the same as the one tested by the author (see figure 2-11 for comparison).

rather optimistic, with a rather high L/D ratio being reported. The study is unclear on the drag data used to calculate the ratio.

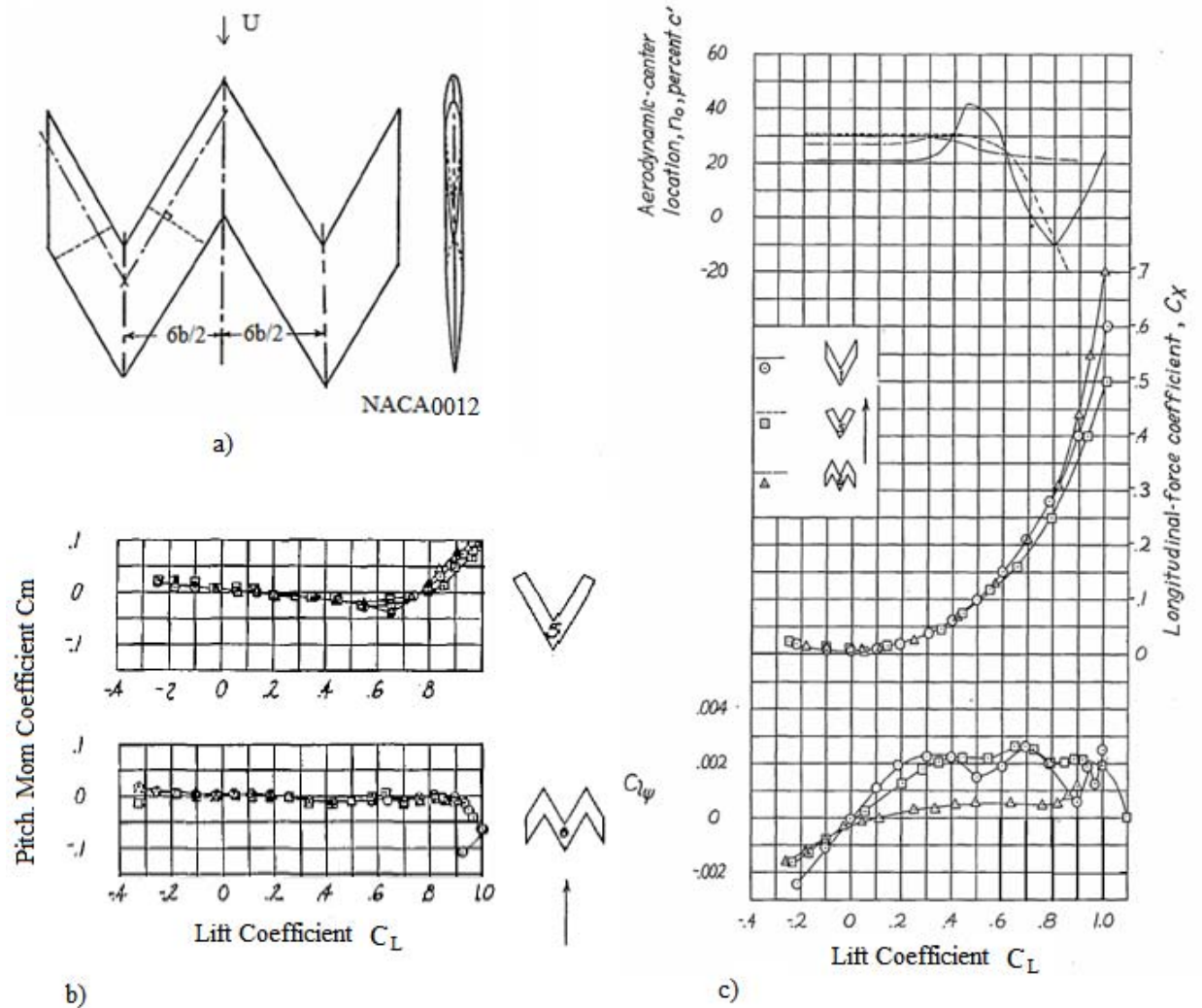


Figure 2-10: Purser and Spearman study results: a) W-wing geometry, b) Pitching moment comparison between W-wing and an aft-swept wing and c) aerodynamic center shift comparison for three planforms.

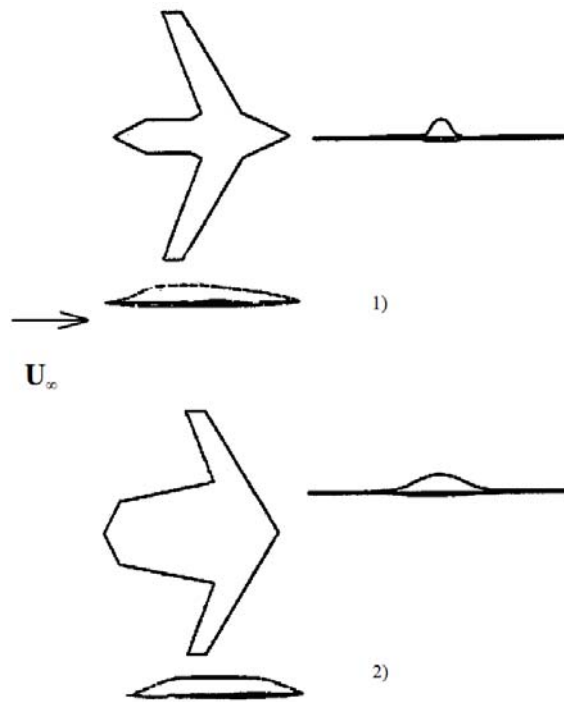


Figure 2-11: The W-wing employed by Jing et al.

## 2.2 Ground Effect

As one of the most critical phases of aircraft flight, take-off and landing flow characteristics need to be addressed at the beginning of the wing design process. During take-off and landing, aircraft move close to the ground, and the ground distance is therefore relatively small in comparison with the dimensions of the vehicle. Hence, during these phases of flight the proximity of the ground is expected to influence the aerodynamic characteristics considerably. As a result, ground effect analyses should be carried out for accurate interpretations of flying vehicle qualities (Staufenbiel and Schlichting 1988). This phenomenon, of the wing flying in the vicinity of the ground is also known as wing-in-ground (WIG) effect. In ground effect, a body tends to float and this phenomenon, also known as the “air cushion” effect, develops in the cavity between the underside of the vehicle and the ground.

Extensive research has been carried out over the past 90 years in order to understand and predict the effect of ground interference on the aerodynamic characteristics of the wing. The general effect of proximity to the ground is a trend of increasing lift-curve slope and decreasing induced drag (but not necessarily total drag), as the distance between the wing and the ground is reduced (Suh and Ostowari 1988). Ground effect is also known to increase the suction pressure on the upper wing, leading to an increase in nose-up pitching moment (Bagley 1961). Studies have shown that some of the downwash caused by trailing vortices when aircraft fly near the ground is suppressed; this reduction leads to an increase in the effective angle of attack and a decrease in the induced drag. On the lower side of the aerofoil the streamlines become increasingly modified and density is reduced, the stagnation point moves down, hence more air flows above the wing. This leads to a decrease of velocity and an increase in the pressure on the lower surface; the so-called “ram effect” (Staufenbiel and Schlichting 1988). Generally, the data indicate that the decrease in height causes losses in lift at negative angles of attack, no difference at zero angle of attack and an increase at positive angles of attack. The wing appears to be out of ground effect at a height of one chord length above the ground as depicted in Figure 2-13 (Fink and Lastinger 1961).

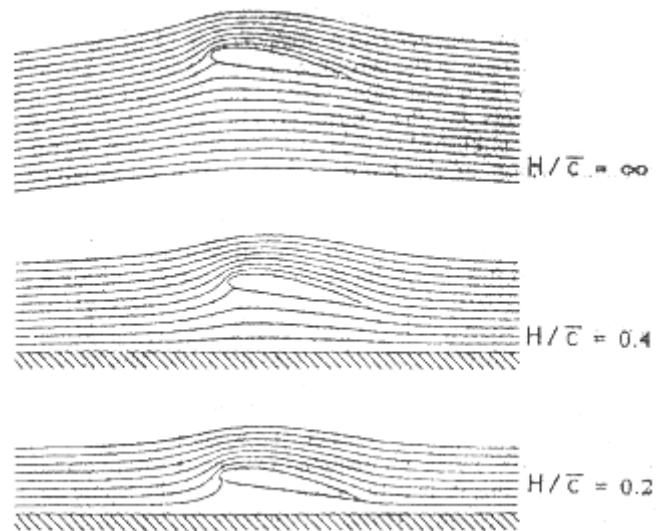


Figure 2-12: Streamlines Around an Aerofoil at Various Ground Heights (Staufenbiel and Schlichting 1988)

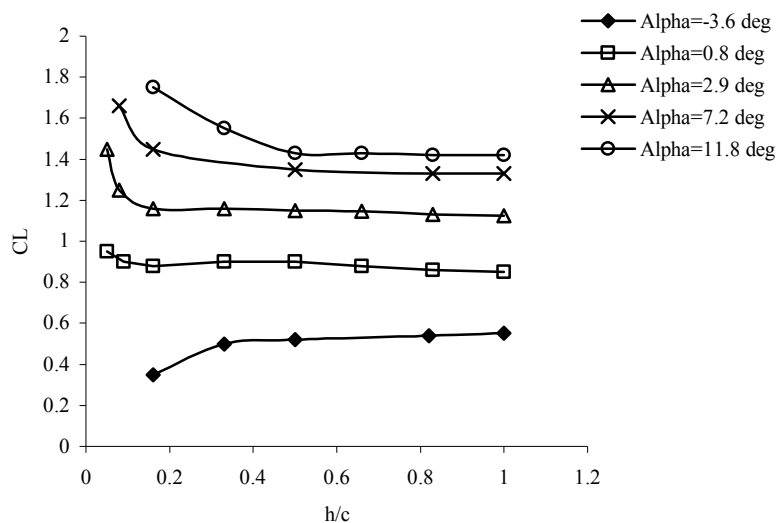


Figure 2-13: Lift Coefficient versus  $h/c$  for a Rectangular Wing with  $AR = 6$  (Fink and Lastinger 1961)

Some studies have found conflicting behaviour: Hooker, suggested that there is no reduction in drag in ground effect (Hooker 1995). Tuck observed that both lift and induced drag increased with ground proximity (Tuck 1983). Other studies have shown that at lower Reynolds Numbers ( $Re = 10^5$ ) and higher angles of attack, the flow

separation phenomena for an aerofoil in ground effect is stronger than that without ground effect (Hayashi 1978). The effect of endplates is also noticed to increase in ground effect (Chawla et al 1990).

Aircraft stability and longitudinal motion in ground effect is also remarkably different from out of ground characteristics. Staufenbiel and Schlichting used the panel method to calculate the aerodynamic coefficients of a rectangular wing with flapped trailing edge (Staufenbiel and Schlichting 1988). As expected, in ground effect an adverse nose-down pitching moment was observed accompanied by a decrease in the induced angle of attack. A reduction in downwash effects at the tail, hence giving favorable tail efficiency were noticed as well.

There are many theoretical, experimental and numerical investigations of the phenomenon, with one of the first being by Wieselsberger (1922). Wieselsberger developed an analytical method which determines the drag polar curve of an aircraft at short distances from the ground. In addition he used the basic concepts of Prandtl's lifting-line theory to calculate a correction, which was used to modify the classical induced drag and induced angle of attack. According to this theory, the airflow about a wing can be calculated on the assumption that the lift is distributed over the wing span in the form of a half ellipse. Wieselsberger then used the theoretical consideration that a vortex band, of width equal to the wing span, goes out from the trailing edge of each wing. In order to investigate the change in resistance near the ground, he used the principle of reflection, where the image of the wing is placed below a ground plane as illustrated in (see Figure 2-14 and Figure 2-15). In this manner the wing flow will be affected by its image.

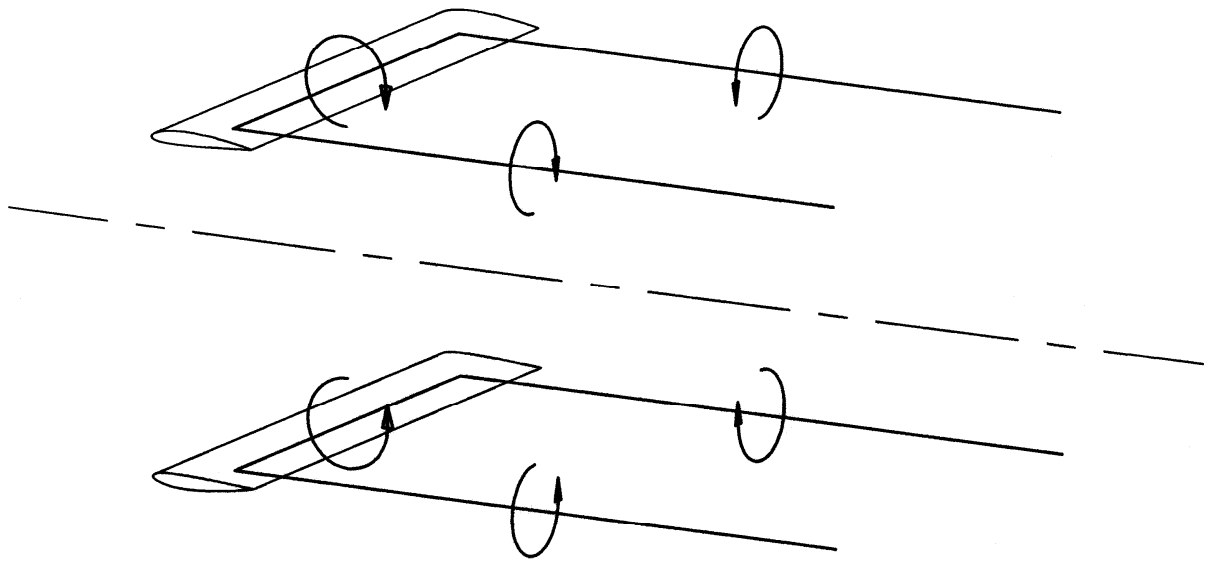


Figure 2-14: Horseshoe Vortex Distribution in Ground Effect

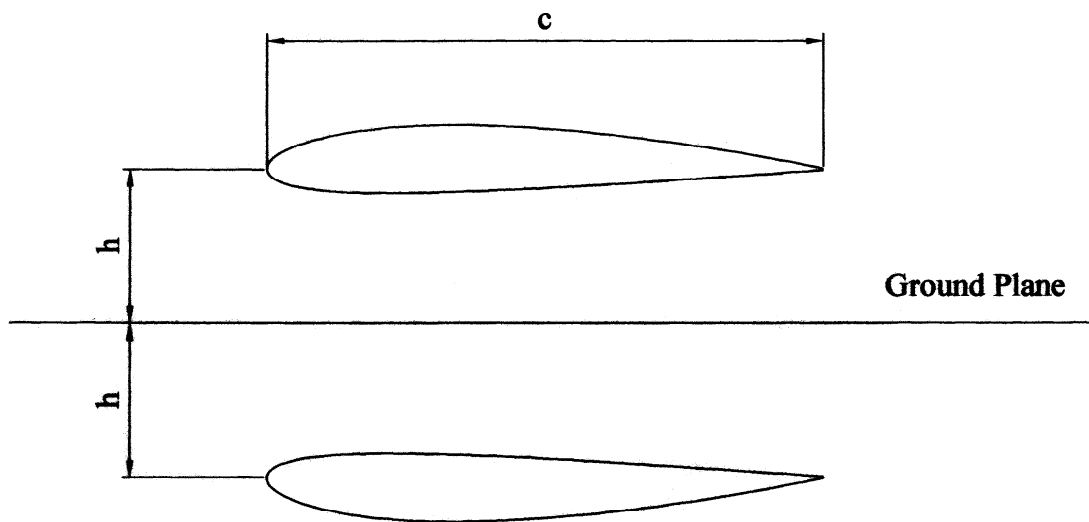


Figure 2-15: Wieselsberger's Image Method

According to Wieselsberger's method the induced drag near the ground must be smaller than out of ground. Since, with decreasing distance between wing and image, the disturbing velocity increases from zero to maximum.

The resulting changes in angle of attack and drag coefficient at a constant lift are expressed by the equations:

$$\Delta\alpha = -57.3 \frac{C_L}{\pi A} \delta \text{ deg} \quad (2.1)$$

and

$$\Delta C_D = -\frac{C_L^2}{\pi A} \delta \quad (2.2)$$

where A is the aspect ratio and  $\delta$  is Prandtl's interference coefficient from multi-plane theory, given by the expression:

$$\delta = e^{-2.48(2h/b)^{0.768}} \quad (2.3)$$

The effective aspect ratio with the wing influenced by the ground is given by:

$$A_G = \frac{A}{1 - \delta} \quad (2.4)$$

Other analytical methods have been developed, such as Tani et al (1937) where the effect of the tail is incorporated into the study as well; however Wieselsberger's method still remains the most popular. Many other researchers have employed the Wieselsberger image concept to simulate wings-in-ground effect, with the height fixed in time. Others have used the method for comparison with experimental and numerical analyses. Some of these findings are discussed throughout this subsection.

Most of the experimental studies employ the fixed ground plane, the image method, the moving belt, or the moving model technique to simulate the ground. The use of a stationary ground board has proven to be satisfactory and considerably less complex, especially for cases where particularly low ground heights are avoided (Lockwood and Phillips 1968; Thomas et al 1979). For these extreme cases, the fixed ground plane is considered not to be sufficiently accurate, as the boundary layer of the board

affects the aerodynamics of the model, a phenomenon that is not present in real-flight (Katz 1985). George conducted experimental investigations of bluff bodies in ground effect and found that for clearances where  $h/c$  (the distance from the ground board,  $h$ , non-dimensionalised by the reference chord,  $c$ ) is less than 0.1, the moving ground plane should be used (George 1981). Sowdon and Hori suggested that while Wieselsberger's image method will adequately represent the velocity field, the turbulence field will not be represented well, nor will flow separation (Sowdon and Hori 1996). Other ground effect tests by Baker et al have suggested that there are certain transient elements associated with the ground effects that are not properly modelled with the typical static ground boards (Baker et al 1970). These elements are especially important for military and STOL applications where the ground clearance changes rapidly. However, most of the studies still treat this problem in a quasi-steady fashion.

Early experimental studies on the subject (Fink and Lastinger 1961), employed the image method for wind tunnel investigations of the ground proximity effect on the aerodynamic characteristics of thick, highly cambered rectangular wings with aspect ratios of 1, 2, 4 and 6. The image method technique involves the use of an identical model mounted inverted with respect to the test wing. This method does not present the boundary layer problem associated with the fixed ground board methods. The results showed that for all the aspect ratios considered, the lift-curve slope increased and the induced drag decreased, as the ground was approached, with no relative change in the profile drag. This was accompanied by a reduction in negative pitching moment. For  $0^\circ$  angle of attack the lift coefficient was found to be approximately the same for all the values of  $h/c$ . The drag reduction was reflected in the lift-to-drag ratio plot, which showed that the maximum lift-to-drag ratio is obtained at progressively higher lift coefficients as  $h/c$  is reduced. These experimental results were compared with Wieselsberger's method, with general agreement being noted. Fink and Lastinger noted that, in ground effect, the improvement in the lift-to-drag ratio of thinner wings is much more prominent. The results also showed that the ground presence resulted in an increase in static longitudinal stability at positive angles of attack, and instability at negative angles of attack.

Lockwood and Phillips carried out an investigation to determine the ground effect on a 0.15-scale model of a fighter-type aircraft having an ogee-wing planform (Lockwood and Phillips 1968). The ground was simulated by using a level moving-belt facility both with and without ground-plane boundary-layer removal. The increases in lift-curve slope and longitudinal stability and the reduction in induced drag usually encountered by an aircraft entering ground effect were noted. Some additional tests were made with the belt inoperative to determine any influence that the boundary layer might have on the characteristics. The results showed no differences in the characteristics obtained with the ground-plane belt stationary or with the ground-plane belt operating at a speed equivalent to free-stream velocity. Based on their findings Lockwood and Phillips indicated that the moving-ground technique is unnecessary for wings operating at relatively low lift coefficients. A similar method was also applied more recently (Ahmed et al 2006). Ahmed et al investigated flow characteristics over a NACA 4412 wing in a low turbulence wind tunnel with a moving ground belt at a Reynolds Number of  $Re = 3 \times 10^5$  and by varying the angle of attack in the range of  $0^\circ < \alpha < 10^\circ$ . Up to  $\alpha = 4^\circ$  it was found that the lift decreased with reducing ground clearance whilst an increase in the lift was noticed at higher angles of attack. The drag was found to be higher close to the ground for all angles investigated; this was due to modification of the lower surface pressures. A loss of suction on the upper side was noticed at very low  $h/c$  ratios, which induced a laminar separation well ahead of the trailing edge.

Er-EI and Weihs investigated the effect of the ground on a  $60^\circ$  sweep delta wing. Tests were carried out at free-stream velocity  $V = 30\text{m/s}$  and angles of attack from  $10^\circ < \alpha < 31^\circ$  (Er-EI 1986). Non-dimensionalised heights of  $h/c = 0.365$  to  $h/c = 2.336$  (ground free conditions) were assessed. Ground proximity was simulated by a steady flat board spanning the width of the tunnel. The general behaviour associated with ground effect was obtained, and no effect of the ground boundary layer was seen. However, Chen and Schweikhard in their tests with a flat plate, found that the increase in lift for the unsteady case is even higher than the steady one (Chen and Schweikhard 1985). This effect reverses when the model is very close to the ground as the influence of the shed vortices becomes more prominent.

Kemmerly and Paulson devised a new experimental method involving a moving model (Kemmerly and Paulson 1989). The technique utilizes a model moving horizontally over an upwardly inclined ground plane to simulate rate of descent. The moving model technique involves measuring the aerodynamics while the model is in motion and the flow field is in dynamic state. Results were obtained for a generic  $60^\circ$  delta wing and an F-18 configuration both with and without thrust reversing at forward speeds of about 100ft/sec. The same models were also tested with and without the moving belt ground plane to obtain data for comparison. The un-powered case responded to the ground as expected, i.e. increased lift, slight drag reduction, and nose-down pitching moment. Whereas the powered case clearly began to show ground effect at larger than expected  $h/c$ . Simulations of normal approaches without the thrust reversers have indicated only small negligible differences between the static and dynamic tests. When thrust reversers were operated the results were quite different, at  $\alpha = 14^\circ$  ground effects were noticed for  $h/b > 1$ . One of the shortcomings of this method was found to be due to model motion caused by vibrations of the cart and strut. The balance force data were contaminated with inertial loads, which had to be correctly removed from the balance for accurate results.

Similarly, Thomas et al ran tests on a powered wing with both a stationary and moving belt and found that below stall, lift and drag coefficients for the power-off case were not affected by the moving belt (Thomas et al 1979). The criteria developed for the need of a moving ground belt is presented in Figure 2-16.

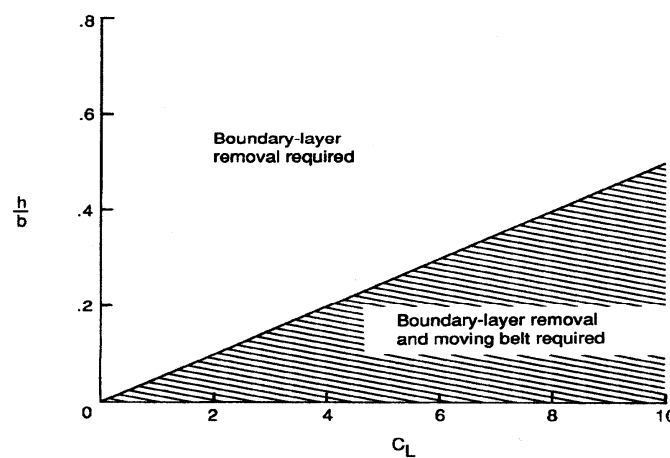


Figure 2-16: Criteria for Determining the Need for Moving Ground Belt (Thomas et al 1979).



effect problem with a vortex-lattice method (Nuhait 1993; Nuhait 1995). Hsiun and Chen solved the steady incompressible N-S equations for an aerofoil in ground effect in laminar flow (Hsiun and Chen 1996).

For a more realistic comparison with experimental studies many researchers also simulate the presence of the ground board. In terms of boundary conditions for this case most apply the no-slip condition. Hsiun and Chen and Steinbach suggested a slip condition ( $u = 1, v = 0$ ) although this means a condition of zero shear (Hsiun and Chen 1996; Steinbach 1997). Morishita and Tezuka suggested that the ground should be moving at the free-stream velocity, otherwise a boundary condition of symmetry for the ground would also be appropriate (Morishita and Tezuka 1994).

Studies by Nuhait and Mook and Nuhait suggested that employing the image method is not accurate as this approach ignores the effect of the bound vortex (Nuhait 1989; Nuhait 1995). Nuhait and Mook conducted a numerical simulation of steady and unsteady ground effect on the wing of an F-104A, a delta wing (70 deg sweep with  $AR = 1.456$ ) and a plain rectangular wing. The simulation was based on the general unsteady vortex-lattice method, which was unrestricted by any of the geometrical constraints such as planform area, dihedral, AR, twist etc. For the unsteady simulations, they initially located the wing far from the ground, to allow the flow to reach steady state, later the wing was made to descend along a flight path so as to experience ground effect. They noticed that at  $h/c = 1.5$  the ground effect became apparent. The study showed that the lift increase is greater for the unsteady ground effect as compared to steady. For the F-104A, lift and drag coefficients were compared with the experimental data, showing good agreement up to  $10^\circ$  where stall occurs. Similar trends were noticed for the delta wing, as well. The drag results however, show discrepancies between the experimental and numerical studies. It was also noticed that the ground effect together with the general behavior of increasing  $C_L$  and  $C_M$  increases the rolling moment and side force.

However, a study by Gallington et al (1990), suggested that the use of vortex lattice methods was inappropriate for three-dimensional flows due to the geometry assumed for the wake sheet and the exclusion of vorticity in the assessment. Katz also

suggested that in real flow the lift will be affected by viscous effects, occurring at approximately  $h/c = 0.3$ , hence only viscous calculations apply for these conditions (Katz 1985).

Hsiun and Chen (Hsiun and Chen 1996) studied the effect of the Reynolds Number on the aerodynamic characteristics of an aerofoil with ground effect, in viscous flow. Hsiun and Chen solved the steady incompressible Navier-Stokes equations with a  $k-\epsilon$  turbulence model for a NACA 4412 aerofoil at  $\alpha = 8^\circ$ . The ground was simulated by the fixed ground plane method, where no-slip boundary conditions were assigned to the ground plane.

The results clearly showed that the lift coefficient increased with increasing Reynolds Number, with the strongest Reynolds Number effect being at lower ground heights. However, for very small clearances, there is a large loss of lift due to the effect of the ground boundary layer. Ground effect was noticed to decrease the drag coefficient for all Reynolds Numbers; this being mainly due to a decrease in the pressure drag.

Viscous Navier-Stokes calculations on the same model were also carried out by Wu and Rozhdestvensky. It was noted that in extreme ground effect the main contribution to the increase in the lift-to-drag ratio is from the increase in  $C_L$  (Wu and Rozhdestvensky 2005). For a constant lift-to-drag ratio, the required AR of the wing is reduced significantly for clearances of  $h/c = 0.1$ .

In contrast to the quantity of experimental and numerical analyses only moderately few flight test investigations have been carried out. Wetmore and Turner performed an investigation to find the effect of the ground on the aerodynamic characteristics of a Franklin PS-2 Glider (Wetmore and Turner 1940). Two wing arrangements were tested; a plain wing and a wing with a nearly full-span flap deflected at  $45^\circ$ . They used a glider towed by an automobile, tested at  $Re = 1.4 \times 10^6$  and  $2.5 \times 10^6$ . The tests were made on a concrete runway of about one and a half miles long. The results showed that within the range of the angle of attack investigated, the drag coefficient and the angle of attack for a given lift coefficient was reduced when the wing was influenced by the ground. This reduction was larger for the flapped wing. Ground effect at  $h/b =$

0.14 was found to increase the lift by about 15%. The experimental results were in good agreement with the theoretical values calculated with Wieselsberger's method.

Curry carried out flight investigations of the ground characteristics of an X-29, having a forward swept wing and variable incidence canards (Curry 1990). An optical tracking system was used to determine aircraft position with respect to a fixed ground reference system. The optical data were obtained at 4 samples per second, for  $6.5^\circ < \alpha < 8.5^\circ$ , and at indicated airspeeds from 145 knots to 160 knots.

The data indicated that ground effect was negligible for heights above 15 ft, or  $h/b > 0.55$ . From the measured normal forces, it was concluded that the maximum normal force is about 17% greater than that out of ground. The flight tests and wind tunnel data agree poorly, as the increases predicted by the wind tunnel and CFD results were substantially greater than those in flight test. The discrepancies may be due to the dynamic nature of flight maneuver, or the use of a fixed ground board in the wind tunnel tests. The measured angle of attack was found to be insensitive to ground effect.

Although there is no definitive agreement on the behavior of wings in ground effect as the ground effect is very configuration dependant most of the researchers in this area agree that the trailing vortices behind the aircraft do change with proximity of the ground, which increases the effective aspect ratio of the wing and leads to a reduction in the induced drag (see Figure 2-18). Therefore, the behavior of the wake and trailing vortices in ground effect is of paramount importance. This is especially true when all take-off clearances between aircraft take place.

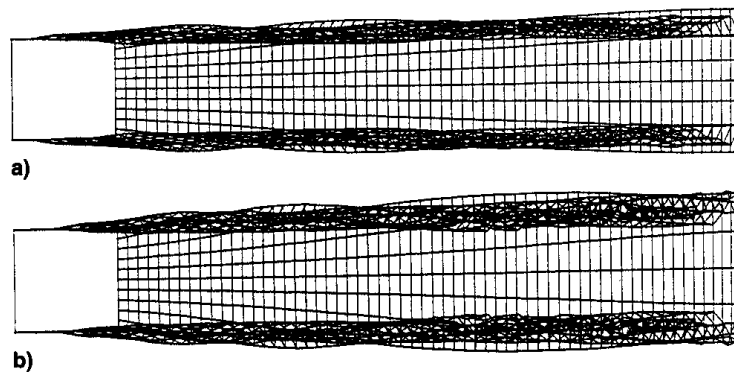


Figure 2-18: Wakes of Wings at a) out of Ground Effect and b) in Ground Effect (Nuhait 1995).

It is known that the powerful trailing vortex pair produces rotational forces that can override the direct controllability of many aircraft (Zheng 1996). Those vortices have circulation levels that scale directly with the size and speed of the generating aircraft and persist for extensive distances. Most of the studies in this matter are concerned with increasing throughput of runways, in order to safely decrease spacing between arriving and departing aircraft, and increase airport capacity.

Fonseca 2003 employed the Numerical Inviscid Vortex method to study the unsteady two-dimensional incompressible flow that occurs during aerofoil vortex interaction in the vicinity of the ground (Fonseca 2003). The NACA 0012 aerofoil bound vorticity was modelled using a panel method with piecewise-continuous distribution, whilst the ground effect was simulated using the method of images. The study showed that the aerofoil in ground effect suffers a strong temporal variation of its loading as the vortex moves past the aerofoil from far upstream. This occurs because the vortex induces a time-dependant local angle of attack and generates a time varying lift effect. Also, the ground was subjected to a strong pressure variation, which depending on the strength and direction of the vortex may cause separation on the ground.

Hamilton and Proctor conducted a compressible numerical simulation with LES for wake vortex transport in proximity of the ground in order to increase airport capacity (Hamilton and Proctor 2000). The simulation assumed an environment with no ambient turbulence. The results showed that the vortex transport is primarily influenced by the magnitude of the cross-wind and is insensitive to aircraft type. It was noted that the ground effect extends the lateral position of the downwind vortex by about one initial vortex spacing.

Vertical gradients in the ambient cross wind have been shown to affect the wake vortex descent. A study by Schilling concluded that a minimum crosswind of 2.5 m/s was necessary to transport vortices on the parallel runway at Frankfurt international airport (Schilling 1992).

Zhu and Takami, investigated the wake roll-up behind a lifting-surface in ground effect, by employing a vortex-lattice method (Zhu and Takami 1987).

Han modelled the unsteady evolution of trailing vortex sheets in ground effect by the use of a discrete vortex method (Han 2005). Both the elliptic loading and a fuselage-flap-wing configuration were simulated. The wake vortices behind a wing-in-ground effect were not fully developed due to insufficient distance between the wing and the ground, therefore, the strength of the wingtip vortex was weaker compared to the case out of ground effect. Han observed that the vortex strength increases proportionally with the aircrafts weight. The position of the tip vortex behind a wing with greater wing loading moves more laterally outward in the span-wise direction, whereas its position from the ground and size are similar to those of wing tip vortices of a smaller aircraft. Furthermore, the position of the tip vortex from a larger aircraft moves further downward as compared with that of a smaller aircraft. Han also described the consecutive roll-up of the wing-tip, flap and fuselage vortices, one after another. Out of ground effect the tip vortex and flap vortex roll around each other because their circulation has the same sense of rotation. In ground effect however, the ground prevents the rolling up of the tip vortex and flap vortex, and this reduces the strength of the flap vortex. Nevertheless, Barber et al, in an earlier Navier-Stokes numerical study concluded that no weakness of the trailing vortices is apparent as the clearance is decreased (Barber et al 2002). They conclude that the outboard movement of the vortex core suggests that their influence on the wing would be reduced.

## **Summary**

The literature in the wing aerodynamics illustrates an ongoing research on the aerodynamics of unconventional wing concepts designed to achieve improved performance such as increase lift to drag ratio, improved stall capability, and enhance short take-off and landing potential. It is well known that at subsonic speeds for the conventional aft-swept wings the pressure gradient between the root and tip of the wing promotes boundary layer flow in that direction. This therefore causes the lift distribution to move outward and as a consequence promotes tip stall before the maximum lift is reached. In search for improvement the forward swept wings were designed.

In general the use of forward sweep can provide several advantages, such as increased leading edge suction and soft stall. Subsonic experimental investigations of forward

swept wings have also shown induced drag reduction, and a higher lift-to-drag ratio. Past research has shown that poor wing root design can negate many of the advantages of forward sweep. The use of backward sweep on the inboard wing may reduce such detrimental side effects. Wings of similar nature as in the current study have been studied previously and those experimental designs were intended for supersonic flight, however those projects have never been taken to completion and very limited results are available (Payne 2004). Furthermore, other studies by Lemme ( Lemme 1946) and Purser and Spearman (Purser and Spearman 1951) on so called M wings have shown that the wings have a lower  $C_L$  in comparison with conventional aft-swept wings however do possess better lateral stability and stall characteristics.

Another part of the survey involved the experimental and analytical methods for studies of wings in ground effect. Extensive research over the years has shown that in ground the general effect is a reduction of drag, particularly induced drag and evidently an increase of lift-to-drag ratio, as well as increased leading-edge suction leading to an increase on the nose-down pitching moment. In ground effect the body tends to float and this feature, also known as the “air cushion” effect, develops in the cavity between the vehicle and the ground. Many studies have found conflicting behavior on the subject, where suggestions of no drag reduction in ground-effect have been reported. Others detail that increase in lift and drag is noted when the wing is under the ground influence. It has also been reported that the flow separation phenomenon is increased with ground proximity.

As far as accounting for the ground is concerned, of the most successful analytical methods is that of Wieselsberger. This theory uses the principle of reflection, where the image of the wing is placed below a ground plane to investigate the change in resistance near the ground. In this manner the wing will be affected by its image. Experimental methods, on the other hand, range from the fixed ground board use to the moving-belt method, where the ground boundary layer is removed. The fixed ground method is the least complex method, and although it has some shortcomings the method has been proven to be an acceptable method, as long as small clearance areas and very high angles of attack are avoided.

Despite the great number of studies on the effect of the ground there are still many recent theoretical and experimental studies that report significant differences between computational and experimental results (Barber et al 2002). There are many possible causes for discrepancies in the published work, between different techniques used in ground effect studies. Overall this may be due to the limitations of the techniques involved. Experimental methods often require complex configurations and thus simplifying methods have to be introduced. Analytical methods are often limited in their application and computational methods use assumptions that may not be applicable. These also include the inappropriate specification of the boundary conditions and the neglect of viscosity on some computations.

### **3. Literature Review (Numerical Methods for Predicting Flows)**

Fluid flows are governed by the physical phenomena of the conservation of mass, momentum and energy. CFD describes these phenomena by numerically solving the mathematical expressions for the appropriate physical quantities.

In this section together with a literature survey on the current numerical methods a brief description of the numerical algorithm employed in this study is presented, together with the discretisation schemes, turbulence models, boundary conditions and grid generation. This section is meant to be for preliminary descriptive reasons; therefore, it is not exhaustive in terms of all the applications and the methods available. Further details on the methods, equations and their step-by-step derivations can be found in (Anderson 1994; Versteeg and Malalasekera 1995; Demirdzic and Muzaferija 1997).

#### **3.1 Governing Equations of Fluid Motion**

The numerical procedure presented in this study deals with continuum mechanics (i.e. it assumes that flow fills the space continuously), where a system of a certain number of physical quantities is conserved. The governing equations for fluid motion describe the flow-field as a continuum and therefore quantities related to the flow, such as pressure and velocity, can be determined at any time or location. The characteristic length and time scales of such problems are considerably larger than the scale of the discrete structure of the flow. Therefore the macroscopic properties of the flow can be described as a continuous function in microscopic coordinates in time and space. The

concept of a continuum allows for mathematical equations to express these physical quantities.

The governing equations are a coupled system of non-linear equations that would be very difficult to solve. Consequently, alternative numerical methods are necessitated. Employing an iterative method is typically the procedure applied. In this manner, in order for analysis of the flow field to take place, the differential or integral equations are approximated via algebraic equations at discrete points throughout the domain.

The most common form of CFD code solves the governing equations using the finite volume method which was chosen for this study. The fundamental fluid flow partial differential (or integral) equations mentioned previously can be formulated in two different methods (Anderson, 1994). The first method is the ‘conservative’ method, which considers a finite volume in space with fluid flowing in and out of it. The second method is the ‘non-conservative method where the finite mass moves in a streamline with the main flow. See Anderson 1994 for the derivations of the partial differential forms of the governing equations.

The conservative integral Navier-Stokes equations describe the balance of some quantity within an arbitrary control volume or “cell”, and take the form:

*rate of change + net outward flux = source*

or

$$\frac{\partial}{\partial t} \int W dV + \oint [F - G] dV = \int M dV \quad (3.1)$$

Where

$$W = \begin{bmatrix} \rho \\ \rho U \\ \rho e \end{bmatrix} \quad (3.2)$$

$$F = \begin{bmatrix} \rho U \\ \rho U \otimes U + pI \\ \rho UH + pU \end{bmatrix} \quad (3.3)$$

$$G = \begin{bmatrix} 0 \\ \sigma \\ \sigma \cdot v + q \end{bmatrix} \quad (3.4)$$

$$M = \begin{bmatrix} 0 \\ f_r + f_g + f_p + f_u \\ 0 \end{bmatrix} \quad (3.5)$$

Where

- ⇒  $\rho$  is the density
- ⇒  $\sigma$  ( $\sigma = \sigma^T$ ) is the stress tensor
- ⇒  $e$  is the total specific energy
- ⇒  $Q$  is the volume energy source
- ⇒  $s$  is the specific entropy
- ⇒  $T$  is the temperature
- ⇒  $q$  is the heat flux and
- ⇒  $U$  is the velocity vector and
- ⇒  $g$  is the body force
- ⇒  $M$  is the vector of body forces

The coefficient of molecular viscosity is calculated using Sutherland's law, which is defined as:

$$\frac{\mu}{\mu_0} = \frac{(T_0 + S)}{(T + S)} \left( \frac{T}{T_0} \right)^{\frac{3}{2}} \quad (3.6)$$

where

- ⇒  $\mu_0 = 1.716 \times 10^{-5} \text{ kg/ms}$
- ⇒  $T_0 = 273.15K$  and
- ⇒  $S$  (the Sutherland's constant) = 111K.

### 3.2 Finite Volume Discretisation

The method of transforming one or more of the integral (or partial differential) equations into a corresponding system of algebraic equations is then called Discretisation. The most common methods were discussed briefly in section 2; however, the numerical solver employed for this study utilises the finite volume method, hence in the following section the finite volume discretisation method (FVM) is addressed. FVM is perhaps the simplest to understand and apply due to the fact that all the terms approximated having a physical meaning, thus making it the most popular amongst physicist and engineers.

#### 3.2.1 Finite Volume Method

FVM is a discretisation method where the solution domain is divided into a finite number of discrete regions, known as control volumes (CV). CVs do not overlap; they completely fill the solution domain and are bounded by a surface, which consist of a number of boundary cell faces. The finite volume procedure is divided into two main steps: the discretisation of the solution domain and equation discretisation. For transient simulations the given time interval is also discretised into smaller time steps. The integration of the governing equations over the control volume gives the discretised equations at the nodal points. Three non-linear and coupled algebraic equations will be available for each control volume. However, there are four unknowns, so a general parameter has to be evaluated for the control volume and the pressure, obtained from the continuity equation. The accuracy of the numerical approximations depends on the number of CVs, consequently the greater the number of CVs the smaller the errors.

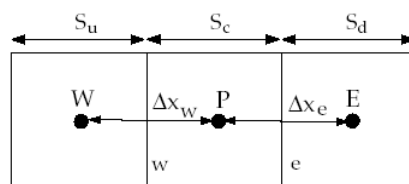


Figure 3-1: Discretised Control Volume (Anderson 1995)

To illustrate the discretisation procedure a simple control volume is shown in *Figure 3-1*. Point P is located at the centroid of the control volume, and the cell is bound by a set of faces which are shared with the neighbouring cells. The faces are then divided into two groups the internal and the boundary faces.

The governing equations integrated over all control volumes are defined by the equation:

$$\int \underbrace{\frac{\partial \rho \phi}{\partial t}}_{\text{temporal term}} + \int \underbrace{\nabla \circ (\rho U \phi)}_{\text{convection term}} ndA - \int \underbrace{\nabla \circ (\Gamma \nabla \phi)}_{\text{diffusion term}} ndA = \int \underbrace{S_\phi}_{\text{source term}} ndV \quad (3.7)$$

The accuracy of the discretisation then depends on the assumed variation of the variable  $\phi = \phi(x, t)$  in time and space around point P. Each of the terms above is discretised using appropriate methods. For example the first derivative of the property variable can be approximated by:

$$\int \frac{\partial \phi}{\partial x} dx = \phi_e - \phi_w \quad (3.8)$$

### 3.2.1.1 Convection Differencing Scheme

The role of the convection differencing scheme is to determine the values of the variable  $\phi$  at the face from the values at the cell centers. A number of choices of differencing schemes of the convection term are available depending on how the grid is aligned with the flow. When the flow is aligned with the grid then first-order upwind schemes are acceptable. In those cases when flow is not aligned, with triangular grids for example, more accurate solutions can be obtained by employing second-order upwind differencing.

Hence, for unstructured meshes, higher order discretisation schemes lead to more accurate results.

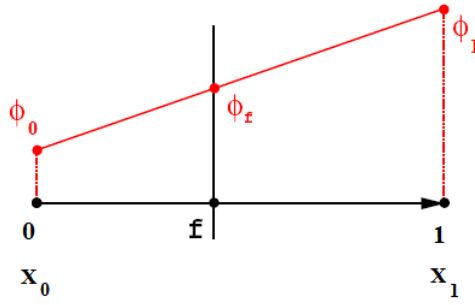


Figure 3-2: Face Interpolation

For an arbitrary unstructured mesh (see *Figure 3-2*), if the values for the flow variable at each side are called  $\phi_0$  and  $\phi_1$ , and assuming linear variation of  $\phi$  between 0 and 1. For upwind schemes then, the value of the variable at the face is obtained from cell values as follows:

$$\phi_{f,0} = \phi_0 + (x_f - x_0)\nabla\phi_0 \quad (3.9)$$

$$\phi_{f,1} = \phi_1 + (x_f - x_1)\nabla\phi_1 \quad (3.10)$$

The choice of the values is dependent on the direction of the flow such as

$$\phi_f = \begin{cases} \phi_{f,1} & \text{for } F < 0 \\ \phi_{f,0} & \text{for } F \geq 0 \end{cases} \quad (3.11)$$

### 3.2.1.2 Diffusion Term

Similarly for the diffusion term, if  $D$  is the discrete form of the diffusion term then:

$$D = \sum_f (\Gamma \nabla \phi \mathbf{a})_f \quad (3.12)$$

Where

$\Rightarrow \Gamma$  is the face diffusivity

$\Rightarrow \mathbf{a}$  is the area vector (see *Figure 3-3*)

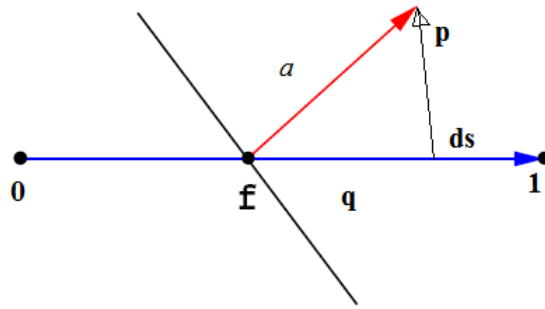


Figure 3-3: Vector a on non-orthogonal mesh

A second order expression for an interior face gradient can then be obtained from

$$\nabla \phi_f = (\phi_1 - \phi_0)\alpha + \overline{\nabla \phi} + (\overline{\nabla \phi} + ds) \quad (3.13)$$

Where

$$\alpha = \frac{a}{a ds} \quad (3.14)$$

$$ds = x_1 - x_0 \quad (3.15)$$

$$\overline{\nabla \phi} = \frac{(\nabla \phi_0 + \nabla \phi_1)}{2} \quad (3.16)$$

For in-depth information on the derivation of all of the above equations see (Demirdzic and Muzaferija 1997)

The structure of the algebraic equations resulting from discretisation depends on the time integral method employed - the explicit and implicit techniques. In the former the variables are explicitly expressed in terms of known variables, whereas in the latter a solution of the equations is required, as more than one variable is unknown at the same time level.

The explicit method has the disadvantage of a restricted admissible time step, whereas the implicit method does not possess the time restrictions of its counterpart, but imposes higher demands on computer resources, requiring large matrix transformations.

### 3.2.2 Errors

Numerical solutions of the discretised equations are prone to two main errors; the round-off error and the truncation error. The former is a result of computer architecture and not much can be done by the user to eliminate it. The latter is a discretisation error and may be reduced by grid refinement. The truncation error can be observed in two form, dissipation or dispersion. Dissipation tends to smooth out sharp gradients and is manifested if the lowest order term in the truncation is an odd derivative. Dispersion is usually expressed in form of oscillations and is manifested when lowest order term is an even derivative.

### 3.2.3 Convergence Acceleration

To provide an efficient solution to either compressible or incompressible flows, the solver employed for this study was a preconditioning matrix. Preconditioning is particularly necessary for lower Mach number flows, in order for the algorithm to have the correct behaviour at low speeds. Furthermore, it assists with acceleration of convergence to a steady-state. The method is necessary to be used with multi-grid methods (to be defined below). Further review on the subject can be found in (Demirdzic and Muzaferija 1997). The matrix is incorporated into the integral form of the Navier- Stokes equations as follows:

$$\Gamma \frac{\partial}{\partial t} \int W dV + \oint [F - G] dV = \int_V M dV \quad (3.17)$$

Where

$$\Gamma = \begin{bmatrix} \theta & 0 & \rho_{,T} \\ \theta v & \rho I & \rho_{,T}^v \\ \theta H - \delta & \rho v & \rho_{,T}^H + \rho_{,T} C_p \end{bmatrix} \quad (3.18)$$

and  $Q = [\rho v T]^T$  is the dependant vector of the primary variables.

The above method is applied as it removes the stiffness of the system of equations caused by the spread in wave speeds, thus improving the convergence rate of any

marching scheme. Since the rate of convergence for most iterative linear solvers degrades as the condition number of a matrix increases. Instead of solving the original linear system above, one may solve either the left preconditioned system and it causes a system of equations to behave more like a scalar equation, facilitating the design of concomitant techniques. In addition, preconditioners decouple the system of equations into purely elliptic and hyperbolic parts.

Another method to increase convergence acceleration is the multigrid method. The multigrid procedure can greatly reduce the number of iterations required to obtain a converged solution. The basic concept of multigrid is performing relaxation or smoothing steps on a coarser level of the mesh then using the corrections for finer levels. For example, for the simplest cycle, known as V cycle, multigrid in the first leg (see *Figure 3-4*) performs smoothing at the finest level, then repeats the operation until the coarsest level is reached. The information then on the second leg is corrected from the coarsest level to the finest one.



Figure 3-4: V-Cycle Multigrid Method (STARCCM+ UM #236)

### 3.3 Boundary Condition Implementation

As the computational mesh consists of a series of faces, these faces are then coincident with the boundaries of the physical domain. Boundary conditions are then used to impose the settings of numerical simulations. For well-posed numerical predictions, correct implementation of the boundary conditions is required to complete the mathematical model. There are two forms of boundary conditions: the numerical and physical form. Furthermore, numerical boundary conditions, are divided into two groups; the Dirichlet (fixed value) type and the Neumann type

(prescribes the value of the gradient normal to the boundary). Physical form of the boundary conditions is when prescribed values of the variables are given at inlet, outlet, symmetry of the computational domain and so forth.

For incompressible flow they are as follows

**Inlet Boundary-** Velocity components are prescribed at this point together with turbulence properties across the faces. Many specifications may be used to prescribe the turbulence conditions, depending on the nature of the flow. Amongst most convenient are turbulence viscosity ratio, turbulence intensity, turbulence kinetic energy, turbulence length scales etc.

For the current study for cruise conditions turbulence properties were assigned in terms of the turbulence intensity and turbulent viscosity ratio. Best practice guidelines in aerospace external flow applications suggest that the turbulence intensity,  $I$ , defined as the ratio of the root-mean-square of the velocity fluctuations,  $u'$ , to the mean free stream velocity,  $u$  to be set for free stream values as 0.1%. The turbulent viscosity ratio which is the ratio of turbulent to laminar (molecular) viscosity for external flows is in the order of 0.1 – 0.2 (ERCOFTAC 2000).

For numerical validations the estimate of the turbulence intensity at the free stream boundary from was set from experimentally measured data.

**Outlet Boundary-** These boundaries should be prescribed in such form that the total mass balance for the domain is satisfied. Usually the outlet pressure is given. Also, turbulence properties are assigned.

**Symmetry Plane Boundary Condition-**For this boundary condition the velocity normal to the plane and all other gradient components are set to zero. The components parallel to it are then projected to the boundary face inside the domain.

**No-Slip Wall-** The velocity of the fluid (i.e  $u, v$  and  $w$ ) on the wall are set to zero. Turbulence properties are also defined with various methods, depending on the

turbulence model chosen; wall functions such as those described in section may be imposed.

For compressible flow at a lower range of Mach numbers the same methods as above may be applied, the rules however, differ for transonic and supersonic cases.

### **3.4 Pressure-Velocity Coupling**

There are two approaches to solving the discretised Navier-Stokes equation, the first is known as the coupled approach and the second is the segregated approach.

These two approaches differ in the way the continuity and momentum, and where applicable, energy equations are solved. The coupled method solves these equations simultaneously, whereas the segregated method solves the equation sequentially (segregated from each other). The segregated solver is usually used for incompressible calculations; the coupled method is more applicable for high speed compressible flow. However, because of computer resource requirements, the coupled solver is more expensive to run; therefore if possible, the segregated solver may be used for low Mach number cases.

#### **3.4.1 Pressure Correction**

An important matter when solving the discretised Navier-Stokes equations is to consider the pressure. Pressure is not a conserved property and does not have its own governing transport equation; therefore an adjustment of pressure is to be performed. Fluid pressure does not feature explicitly in the continuity equation, which consequently can not be considered as 'an equation for pressure'. Hence, the continuity equation acts just as an additional constraint on the velocity field. The Navier-Stokes equations show linear dependence of velocity on pressure and vice-versa. For the coupled simulation this is done via inter-equation coupling. For the segregated solver, due to the nature of the decoupled system, a pressure-velocity coupling has to be made.

The SIMPLE (Semi Implicit Method for Pressure Linked Equations) algorithm, which is incorporated by the solver employed in this study, uses a relationship between the

pressure and velocity to enforce mass conservation and obtain the pressure field. The algorithm uses a guessed pressure correction to adjust the velocities. The pressure correction is substituted into the continuity equation and the correction is updated until the continuity equation satisfies the velocity.

With the SIMPLE method the velocity field is obtained from solving the momentum equations. Pressure gradients are then calculated using the pressure distribution from an initial guess or previous iteration.

The following is applied for the velocity and pressure variables

$$u = u^* + u' \quad (3.19)$$

$$p = p^* + p' \quad (3.20)$$

Where  $u^*$ ,  $p^*$  are the guessed values and  $u'$ ,  $p'$  are the correction of velocity and pressure.

The pressure correction methodology is prone to divergence, hence under-relaxation need to be applied such as

$$p = p^* + \alpha p' \quad (3.21)$$

Where

-  $\alpha$  is the under-relaxation factor for pressure ( $0 < \alpha < 1$ ).

After the velocities and pressures have been corrected mass fluxes are then corrected as well, by obtaining the following;

$$m_f = m_f^* + m_f' \quad (3.22)$$

### 3.5 Turbulence Modeling Methodology

Since most of the flows occurring in engineering applications are turbulent, modelling of turbulence and understanding of the nature of turbulence is very important.

“Turbulence is a three-dimensional time dependant motion in which vortex stretching causes velocity fluctuations to spread to all wavelengths between a minimum determined by viscous forces and a maximum determined by the boundary conditions of the flow”(Bradshaw 1971). Turbulence is neither constant in time nor in space, and is therefore the most difficult phenomenon to describe and model. Turbulent

flows always occur at high Reynolds Number and it requires sophisticated techniques to achieve correct predicted data. No general solutions to turbulent flows are available.

Turbulence always has three directions of motion, even if the mean velocity has only one or two components. The main characteristics of turbulent flow are that the rotation and the vorticity vectors of the vortex elements are aligned and highly unsteady. For this reason vorticity dynamics plays a very important role in the description of turbulent flows. The range of scales in turbulent flows is very large; from the smallest turbulent eddies occurring at microscales up to flow features comparable with the size of geometry. Consequently, the larger scale turbulent motion carries most of the energy and is therefore responsible for the enhanced diffusivity. Turbulence cannot maintain itself; a common source of energy is required as it otherwise decays. One of these energy sources is shear in the mean flow.

The diffusivity of the turbulent flows that causes rapid mixing, increased rates of momentum, heat and mass transfer is another important feature of turbulence. For turbulence as a continuous instability in flow, it is still possible to separate the fluctuations from the mean flow properties. Since randomness is the essential characteristic of turbulence, complete computation of the description of fluid motion in all scales is not possible. Instead the velocity is decomposed into a steady mean value with a fluctuating component.

If no chosen direction of the fluctuating velocity occurs, and the flow is in complete disorder, then the turbulence is considered to be isotropic, which is easier to model. On the other hand, if an average shear stress occurs the turbulence is considered anisotropic. This type of turbulence is more difficult to model but it is the most common case encountered in real fluid flows.

There are three main approaches to modelling turbulent flows. The first is the so-called Direct Numerical Simulation (DNS) method, which requires solving the Navier-Stokes equation in every perturbation of the flow. The mesh resolution and time-step requirements for such methods put a very high demand on computer resources. Therefore, this approach is both time consuming and highly expensive. The

second approach is the Large Eddy Simulation (LES), where a spatial filter is applied. Large-scale structures are resolved by the numerical method on a given mesh called the super-grid scales. Then the influence of the other sub-grid scales on the super-scales is modelled. As the mesh gets finer, the number of scales necessary becomes smaller, thus approaching the DNS method, and hence demanding large computer resources. This third approach is the Reynolds Averaged Navier- Stokes (RANS) method. The method solves the mean and fluctuating components of the Navier-Stokes equations and then takes a time-average.

(Examples of the models)

The RANS averaging method applies as follows

$$\tilde{u}_x = u_x + u'_x \quad (3.23)$$

Where  $u_x$  denotes the mean values defined as:

$$u_x = \frac{1}{\Delta t} \int_{t_0}^{t_0 + \Delta t} \tilde{u}_x dt \quad (3.24)$$

Reynolds averaged turbulence modelling then needs to express the Reynolds stress tensor  $\overline{u_i u_j}$  in terms of known quantities. There are two general acceptable methods to do so; the first method solves the transport equations for the Reynolds stress tensor term, and the second, more popular approach, prescribes a relationship between Reynolds stresses and mean velocity gradient. Examples of such methods can be found in Launder et al (Launder et al 1975). One alternative such approach to predicting turbulent flows was devised by Boussinesq, The so-called ‘eddy viscosity’ model; where the turbulence was described by Boussinesq as an increase in viscosity, and gives a linear relation of the form:

$$\overline{u_i u_j} = -\nu_t (\overline{U_{i,j}} + \overline{U_{j,i}}) + \frac{2}{3} k \delta_{ij} \quad (3.25)$$

Equation (3.25) is the general eddy viscosity equation, where  $\nu_t$  is the eddy viscosity,  $\delta_{ij}$  is the Kronecker delta and  $k$  is the turbulent kinetic energy and is given as:

$$k = \frac{1}{2}(\overline{u_i u_j}) \quad (3.26)$$

The kinematic eddy viscosity  $\nu_t$ , can be evaluated in many ways, ranging from algebraic relations and local equilibrium assumptions to the solution of the transport equations.

The development of computers with sufficient power was followed by implementing several turbulence modelling techniques, which have been devised to predict the turbulence phenomena. The purpose of turbulence models is to estimate the main effect of fluctuations on scales which are resolvable. Some of the main models used in most CFD packages are:

1. The Algebraic model is a one-equation model, used to compute the turbulent viscosity, often called eddy viscosity. The Reynolds stress is computed with an approximation which relates the stress tensor to the velocity gradients and the turbulent viscosity. This model is not as accurate compared to the others. In this model for boundary type flow the viscosity is defined as

$$\nu_t = l_{mix}^2 \left| \frac{\partial U}{\partial y} \right| \quad (3.27)$$

$$l_{mix} = \kappa y \quad (3.28)$$

Where  $l_{mix}$  is the mixing length,  $\kappa$  is von Karman's constant and  $y$  is the coordinate normal to the wall. This model is called the mixing length model.

2. The one-equation models: In these equations the transport equation is solved for a turbulent quantity; often the turbulent kinetic energy  $k$  derived from  $k = \frac{1}{2}(\overline{u' u'})$ ,

and a turbulent length scale which is obtained from an algebraic expression. i.e Spallart-Allmaras model.

3. Two-equation models belong to the group of eddy viscosity models. In these cases two transport equations are solved, for example the turbulent kinetic energy  $k$  and its dissipation  $\varepsilon$ . The Reynolds stress is then computed from the assumption which relates the Reynolds stress to the velocity gradients and eddy viscosity. For the  $k$ - $\varepsilon$  model, for example, the equations for the kinetic energy and the dissipation rate are used and the turbulence length is obtained as follows:

$$l = \frac{k^{\frac{2}{3}}}{\varepsilon} \quad (3.29)$$

The eddy viscosity is then found from

$$\nu_t = C_\mu \frac{k^2}{\varepsilon} \quad (3.30)$$

where  $C_\mu$  is a closure coefficient.

A wide variety of the  $k$ - $\varepsilon$  models exist, the most noteworthy is the one devised by Launder and Spalding (Launder and Spalding 1974).

For this study the  $k$ - $\varepsilon$  Realisable version devised by Shih et al (Shih et al 1994) was utilised for performance comparison with the SST  $k$ - $\omega$ . The choice was based on the proven record to be one of the most successful recent developments of the  $k$ - $\varepsilon$  family.

Another two-equation model which is becoming more popular is the  $k$ - $\omega$  model. Here, the kinetic energy is used together with another term,  $\omega$ , which is the specific dissipation derived as  $\omega \propto \varepsilon / k$ . This model works better in those regions where  $k$  tends to zero. In the  $k$ - $\varepsilon$  model,  $\varepsilon$  is directly proportional to  $k$ , therefore for the model to work both have to tend to zero at the same time, which is not always the case;  $\omega$  on the other hand is not proportional to  $k$  therefore in these regions the  $k$ - $\omega$  model would perform better. As such, this model is very useful when predicting rotational flow.

The modelled  $k$  and  $\omega$  equations devised by Wilcox (Wilcox 1993):

- Turbulence Kinetic Energy

$$\rho \frac{\partial k}{\partial t} + \rho U_j \frac{\partial k}{\partial x_j} = \tau_{i,j} \frac{\partial U}{\partial x_j} - \beta^* \rho k \omega + \frac{\partial}{\partial x_j} \left[ (\mu + \sigma^* \mu_T) \frac{\partial k}{\partial x_j} \right] \quad (3.31)$$

- Specific Dissipation Rate

$$\rho \frac{\partial \omega}{\partial t} + \rho U_j \frac{\partial \omega}{\partial x_j} = \alpha \frac{\omega}{k} \tau_{i,j} \frac{\partial U}{\partial x_j} - \beta^* \rho \omega^2 + \frac{\partial}{\partial x_j} \left[ (\mu + \sigma \mu_T) \frac{\partial \omega}{\partial x_j} \right] \quad (3.32)$$

- Eddy Viscosity

$$\mu_t = \rho \frac{k}{\omega} \quad (3.33)$$

- Auxiliary Relations

$$\varepsilon = \beta^* \omega k \text{ and } l = \frac{k^{1/2}}{\omega} \quad (3.34)$$

The constants are determined as  $\alpha = 5/9$ ,  $\beta = 3/40$ ,  $\beta^* = 9/100$ ,  $\sigma = 1/2$  and  $\sigma^* = 1/2$

One of the modified versions of the  $k$ - $\omega$  turbulence models includes Menter's  $k$ - $\omega$  SST, which is largely employed in this study, for reasons discussed at section 2 of this dissertation.

Several comparisons and investigation of the different models developed and presently available have been assessed by numerous researchers, (see section 3.6.2).

An essential feature of any turbulence model is the accurate and rigorous near-wall treatment. When dealing with turbulent flow it is important to have very fine grids near the wall for the boundary layer treatment, because of the anisotropy of the turbulence. Alternatively, it is possible to compensate for the existence of the wall without resolving the near-wall region. This way considerable approximation can be made where wall-functions are used to prescribe boundary conditions near the wall.

Wall functions represent simplified turbulence models, used to bridge the near-wall region with the distant region where the turbulence models are used. Wall functions

mimic the behaviour of the velocity, and turbulence quantities, i.e  $k$  and  $\epsilon$  in the vicinity of the wall (Launder and Spalding 1974). Assumptions are made that the region near the wall behaves like a fully developed turbulent boundary layer.

The turbulent profile near the wall is divided into three main regions as depicted in *Figure 3-5*. Immediate with the wall is the ‘viscous sub-layer’ where the turbulent fluctuations are dominated by the viscous force. The middle region is the ‘buffer region’ where the viscous effects reduce and the last region, the ‘log law region’, is the fully turbulent region governed by turbulent fluctuations. Near-wall treatments require that the first cell is always located in the viscous sub-layer, whereas wall-functions require that the first cell is located in the log layer.

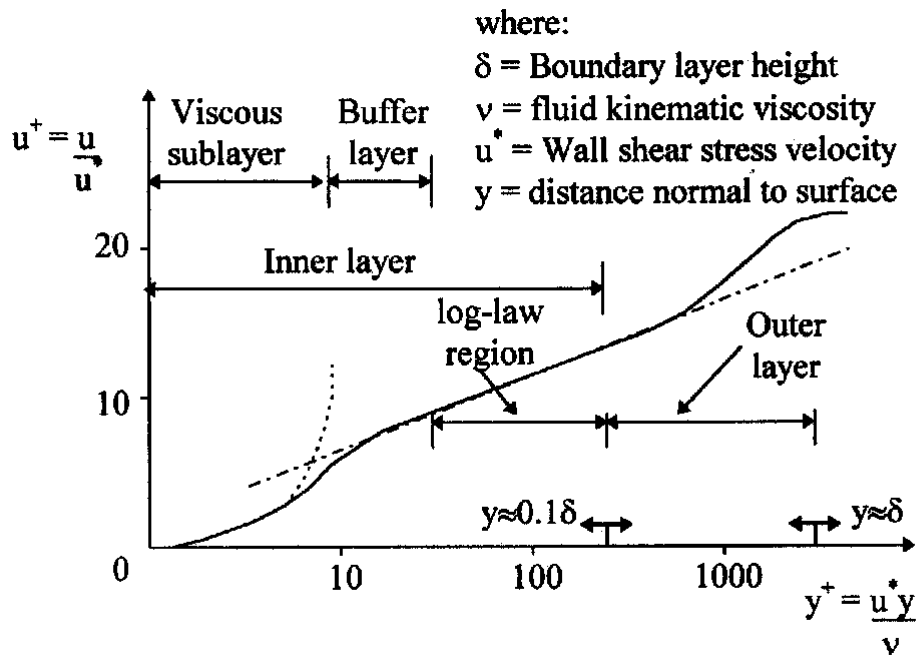


Figure 3-5: Turbulent Boundary Layer on a Flat Plate (Thwaites 1960)

To assess the performance of the first cell near the wall, dimensionless velocity and normal distance are defined as follows:

$$U^+ = \frac{U}{u_\tau} \tag{3.35}$$

$$Y^+ = \frac{u_\tau y}{\nu} \quad (3.36)$$

Where

$$\Rightarrow u_\tau \text{ is the friction velocity defined as } u_\tau = \sqrt{\frac{\tau_w}{\rho}}$$

$\Rightarrow \tau_w$  is the surface shear stress

$\Rightarrow \nu$  is the kinematic molecular viscosity

The equation then takes the form

$$U^+ = \frac{1}{\kappa} \ln Y^+ + B \quad (3.37)$$

Where

$\Rightarrow \kappa$  is the Karman constant

$\Rightarrow B$  is a dimensionless constant

The dimensionless quantity  $Y^+$  is generally employed for the near wall treatment. Close to the wall the velocity varies approximately linearly with  $Y^+$ . For values of  $Y^+ < 1$ , no wall functions need to be employed. The region of the log layer usually lies within the  $Y^+ = 30$  region, where wall functions are then employed.

### 3.6 Numerical Algorithms- Review

The choice of the algorithm, as discussed by Anderson, has to be based on all the important flow features the user wants to assess (Anderson 1994). A large body of literature is available on different methods used to simulate or examine flow behavior in the vicinity of aircraft wings. A considerable number of these studies have been focused on the design and optimization of rectangular, swept and delta wings. However, there are no numerical analyses for “W” or “M” shaped wings. Consequently, a survey of the literature concerning several other complex cases of investigations, i.e two and three-dimensional high-lift cases and delta wings has been carried out.

In the case of a single aerofoil, the boundary layer on the aerofoil's suction side is subjected to a large adverse pressure gradient. As a consequence of high incidence, and thus thickens rapidly, eventually leading to separation. High-lift flows, in contrast, are dominated by viscous effects (such as boundary layer transition, flow separation, viscous wakes and confluent boundary layers), whereas delta wings at higher angles of attack are complicated by the presence of the fixed primary separation and secondary vortices. Each of these complex phenomena are difficult to calculate accurately.

For aerodynamic flows when the boundary layer is attached, viscous effects have only a small influence on the level of lift generated by the aerofoil but when the boundary layer separates from the aerofoil surface there can be catastrophic loss in lift accompanied by an increase in drag. Regions of separated flow can readily form at many different sections the aircraft body configurations and they significantly affect the aerodynamic performance. In fact, separation can be induced or suppressed by seemingly insignificant variations in conditions well upstream of the critical region in which separation might occur. This can occur even at low angles of attack due to geometric discontinuities at highly swept wings (Flores 1990). When attention to all these details is added, critical decisions have to be made in the discretization of the flow field. Also, great care has to be taken when the choice of the algorithm to predict the behaviour of these types of flows.

### 3.6.1 Numerical Simulations and Differencing Schemes

The numerical calculations or approximations of fluid flow are based on the fundamental governing conservation equations of fluid dynamics; continuity, momentum and energy equations. Generally, two main forms of the governing equations are solved: the viscous flow equations (Navier-Stokes), where the transport phenomena of friction, thermal conduction and mass diffusion are included and the inviscid flow equations (Euler) where the above phenomena are excluded. The decision on which of the methods is to be employed is down to the user's selection.

Studies have proven that Euler calculations can be reliable in numerically resolving many aerodynamic phenomena including shockwave and the convection of vortices once they have been formed (van Dam et al 1995). For wake analysis, for example, although an inviscid analysis cannot describe the formation of wake diffusion, it is still capable of representing the wake convection and its dynamics. On the other hand, for wing aerodynamics the use of Euler calculations limits its use to evaluation of only induced drag and wave drag where applicable. Although the Euler calculations may prove to be significant for cruise calculations where there is negligible effects of the separation, considerable differences have been reported with flight comparison with the high-lift conditions. If there is any development in the boundary layer than the Euler calculations are deemed inappropriate, as this has an effect on the pressures even if the flow is not separated.. Because fluid dynamics is dominated by viscous effects, only a high-fidelity simulation using Navier-Stokes equations can provide the accuracy necessary to assist in aircraft design (Rogers et al 2001). As a result, many wing numerical calculations, at present are performed by employing the Navier-Stokes Equations. Hence, further review on Navier-Stokes solutions for various flight configurations is now presented.

There are three methods of numerical solution techniques, finite difference (FD), finite element (FE) and finite volume (FV) methods (Versteeg and Malalasekera 1995). These numerical methods all follow the same basic rules, where approximation of flow variables is made by employing simple functions. The approximations of the governing flow equations are then substituted with mathematical operation and finally a solution of the algebraic equations is carried out.

The main difference between these models lies in the method of solving the approximated equations. The finite difference method describes the unknown variable  $\Phi$  of the flow problem by means of point samples at the node points of grid coordinate lines. Truncated Taylor series expansions are often used to generate finite difference approximations to the flow variable  $\Phi$ . The Finite Element method uses simple piecewise functions valid on elements to describe the local variation of flow variables  $\Phi$ . The finite-volume approach is based on the physical concept of using macroscopic control volumes to numerically solve the conservation laws of fluid motion; the equations are then discretised by approximating the governing flow

equations, which are then solved iteratively. Further, the finite-volume Navier-Stokes methodology is maturing along two tracks: node-centered and cell-centered schemes, each with their relative merits. Node-centered schemes exploit an efficient edge-based data structure and more readily facilitate general polyhedral cell volumes. Cell-centered schemes exploit geometric features of tetrahedra to construct accurate spatial reconstructions and provide comparable accuracy with fewer tetrahedra.

Comparisons between the results obtained by the FD method versus the FV method have reached contradictory conclusions. Rumsey and Vatsa have suggested that the use of the FD method and the FV method can alter significantly the character of three-dimensional separated flow solutions (Rumsey and Vatsa 1995). On the other hand Van Dam et al have found that both FD and FV methods gave accurate results for lift predicted by the trailing vortex (van Dam et al 1995). The results were compared to the lift computed from experimental pressure distribution around an Onera M6 wing (Schmitt and Charpin 1979).

For every numerical simulation, associated initial and final boundary conditions need to be defined. Also, the initial start-up values of the flow variables need to be specified, in order to achieve accurate results (see section 4 for further details on the matter). Attention needs to be placed to the boundary conditions when attempting to compare numerical results with experimental data. Careful attention needs to be placed on the selection of the inflow and outflow boundary conditions for CFD simulations of flow within a wind tunnel to achieve similarity with solutions generated by different methods (Baker et al 2002).

Jameson gives a methodical review on incorporating CFD into the early stages of design. Jameson explains that as far as the complex geometry and flow is concerned there are still challenges remaining with regards to simulation of turbulence and viscous flow at the high Reynolds Numbers associated with full-scale flight (Jameson 2003). He notes that several challenges related to the complexity of flow simulations lead to challenges for algorithm design; the non-linearity of the fluid flow equations at the inviscid level of modelling can lead to the formation of singularities such as shock waves and discontinuities; sharp edges can lead to shedding of vortex sheets and extreme gradients near wing tips may lead to numerical errors.

### 3.6.2 Turbulence Modelling

To avoid the difficulty of describing every discrete turbulent motion possible, some type of averaging can be employed to eliminate some of the details (such as instantaneous fluctuations) concerning the state of the flow. Of the many possible averaging schemes, Reynolds time-averaging has proved the most successful so far. However, time-averaging results in more unknowns than governing equations through the introduction of apparent Reynolds stresses for the actual transfer of momentum by velocity fluctuations. Deriving additional equations for those Reynolds stresses only results in the introduction of additional unknowns. Subsequently, these extra unknowns must be represented by physically plausible combinations of quantities for which transport equations are expressed in terms of functions considered as known or expressible in terms of the mean variables. The problem of reducing the unknowns to equal the number of equations is referred to as the closure problem. "Turbulence modelling" is then defined as the process of developing computational procedures to predict the Reynolds stresses (Marvin 1977).

Over the last few years many different turbulence models have been developed for use with Reynolds-Averaged-Navier-Stokes (RANS). There are many advanced turbulence models available but the choice of the most appropriate for the specific flow phenomena is left to the user's expertise. Many researchers do not agree on the reliability of different turbulence models as the search for the model that accurately predicts both attached and separated three dimensional flow-fields is complicated by the fact that it is difficult to assess the capabilities of new or refined turbulence models because of inherent limitations in the CFD codes that use them. It is therefore very important that new as well as existing models be thoroughly validated in all the CFD codes into which they are implemented. Nonetheless, most turbulence models are derived and calibrated for flat plate zero pressure gradient boundary layer flows.

Davidson gives an introduction to some of the most popular turbulence models currently being used (Davidson 2003). Most turbulence models for use with Reynolds Averaging Navier- Stokes are linear eddy viscosity models (Menter 1992; Spalart and Allmaras 1994) which assume a Boussinesq relationship between the turbulent stresses and mean strain rate tensor through the use of an isotropic eddy viscosity. The

nonlinear eddy viscosity models assume a higher order tensor representation involving powers of the mean velocity gradient, and are better at predicting differences in the turbulent normal stresses. Explicit Algebraic Stress Models (EASM) belong to the class of nonlinear eddy viscosity (see (Rumsey and Gatski 2003)). Reynolds Stress Models actually solve the six equations for the Reynolds stress tensors, and although they are very time consuming to solve, whenever non-isotropic effects are important, the Reynolds stress models should be used.

There is no generally applicable turbulence model that has satisfactory accuracy in arbitrary flow problems. Therefore, it is necessary to identify the most important features of the flow, before the decision of the appropriate model has been taken. For example; with flat plates where the boundary layers are thin and the outer inviscid flow can be described, adequate turbulence models such as the linear eddy viscosity models may be applied. When pressure gradients are severe, non-linear turbulence models or Reynolds stress models would give more accurate results. Of special interest to most engineering applications is the accurate prediction of adverse pressure gradient flow both with and without separation (Menter 1992). Also, for three dimensional flow, the cross-flow turbulent stress in linear eddy viscosity models lags in response to changes in the cross flow velocity gradient (Marvin 1990).

In external flows, such as the flow around an aircraft, the flow conditions near the boundaries are almost invariably important; therefore near-wall modelling significantly impacts the fidelity of the numerical solution, in as much as the walls are the main source of mean vorticity and turbulence. It is in the near wall region that the solution variables have large gradients and that momentum and other scalar transports occur most vigorously. As the flow approaches separation, the behaviour of the near wall layer departs drastically from any universal law of the wall, and its detailed structure must be resolved, including that of the semi-viscous sub-layer in which viscosity affects turbulence. Wall functions may be employed to bridge the near-wall region with the numerical model, with the assumption that the flow near the wall behaves like a fully turbulent boundary layer. Similarly, if wall functions are not used a sufficiently greater number of cells have to be inserted near the boundaries (but not necessarily away from it). At the computational turbulence workshop held to discuss

the best practices in terms of turbulence modelling, (1993-Workshop on Computational Turbulence Modelling), it was concluded that for wall bounded flows and high turbulent Reynolds Number flows, the use of wall functions as a boundary condition often produces reasonable results even for very complex flows. On the other hand, for low Reynolds Number flows, which are sometimes related with the separation bubbles that occur at  $Y^+ < 40$ , turbulence models that can be extended all the way up to the wall have to be used. The general guide applied by most is to maintain an average value of  $Y^+ \leq 1$ . Otherwise, in high Reynolds number flows in order to capture the boundary layer development this method ( $Y^+ \leq 1$ ) required a great amount of near wall layer which drastically increases the total number of grids. Due to computational limitations wall functions are applied in the near wall region which then relaxes the number of layers required in the near wall region with approximate  $Y^+ > 20$  to avoid the buffer layer.

Despite the great variety of turbulence modelling options available, and the many reported weaknesses of the eddy viscosity models (such as under predicting the post separation, under predicting flow recovery etc), they still remain the most preferred solution (Rizzeta 1993). The  $k-\epsilon$  model as derived by Launder and Spalding (1974) and the Spalart-Allmaras (1994) (SA) model have been the predominant methods employed for aerodynamic computations. Another successful model is the  $k-\omega$  model developed by Wilcox. It has the advantage that it does not require damping functions in the viscous sub-layer and that the equations are less inflexible near the wall (Wilcox 1993). Later it was noticed that when  $k-\omega$  model was applied to free-shear-layer flows, strong dependency on the free-stream values for  $\omega$ , was observed. Menter then suggested additional terms in the  $\omega$  to ensure that solutions are consistent with experiments, resulting in the new  $k-\omega$  Shear Stress Transport (SST) model (Menter 1992). The  $k-\omega$  SST model offered considerable improvement because the SST eliminates the sensitivity of  $\omega$  in free-shear-layer flows by switching to an alternative of the  $k-\epsilon$  model away from the wall region. The starting point for the development of the SST model was the need for the accurate prediction of aeronautical flows with strong adverse pressure gradient and separation. As such the SST model tends to be more accurate in separated flows, while the Spalart-Allmaras performs better in attached flows (Godin et al 1997; Godin 1997).

Kral assessed ten turbulence models (Baldwin-Lomax (BL), Baldwin-Barth (BB), SA,  $k-\omega$  SST,  $k-\epsilon$  among others) for use in complex engineering flows (Kral 1998). He examined a flat plate boundary layer and two RAE 2822 transonic supercritical aerofoil cases, a highly offset three dimensional diffuser and impinging jet among others. All the examined models were able to predict the flow-field for a flat plate boundary layer at  $M = 0.45$  and comparison with experiment gave excellent agreement. For the RAE aerofoil the  $k-\omega$  SST model gave the best predicted lift and drag data. None of the models adequately predicted the wake region. The  $k-\omega$  SST over-predicted the separation on the highly curved diffuser, behaving in the same manner as the other models. Kral, however concludes that calculations using the low-Reynolds Number  $k-\epsilon$  were in best agreement as presented in Figure 3-6. Such research has shown that there is no universal choice of turbulence model for all geometries.

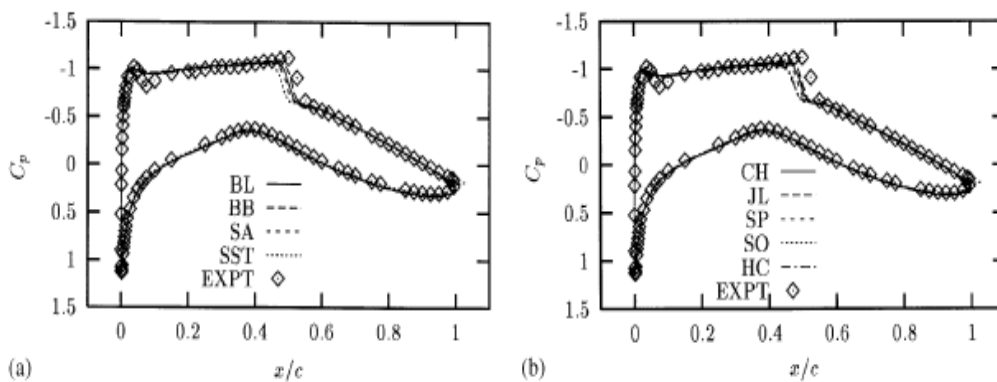


Figure 3-6: Pressure Coefficient Prediction Comparison with Experimental results a) one-equation algebraic models and  $k-\omega$  SST and b) low-Reynolds Number  $k-\epsilon$  models (Kral 1998)

As explained by Leschziner, there are some applications such as a wing-body-fin junction which provoke strong horseshoe vortices (that can induce separation in the junction) or VSTOL flight with vectored jets, where turbulence plays a more influential role (Leschziner 2002). Leschziner's review has shown that eddy viscosity models perform poorly in flows featuring separation, strong shock boundary layer interactions and 3-D vortical structures. The research on this area shows that the

Reynolds Stress Models (RSM) are the most complete and fundamentally secure forms. However, RSMs are time consuming and complex to implement, whereas eddy viscosity models are simpler and have shown to produce acceptable results for most engineering phenomena. Rautaheimo et al suggest that for accurate predictions in external aerodynamics analysis, modified eddy viscosity models or even more advanced modelling has to be used (Rautaheimo et al 2000).

To assess the abilities of three types of turbulence models to accurately predict the effect of curvature of a U duct, Rumsey et al employed the Spalart-Allmaras model, the  $k-\omega$  SST of Menter and an EASM model (Rumsey et al 1999). This type of analysis is important for high-lift flow fields, as strong curvatures of the flow are induced. Rumsey et al concluded that none of the eddy viscosity models captured the full extent of suppressed turbulence near the convex wall or enhanced turbulence at the concave wall as they all exhibited a too slow a recovery from separation. Figure 3-7 illustrates the skin friction prediction from Rumsey et al, all models showed slight discrepancies.

Studies of a similar nature were also carried out by many others, where use of experimental data for various configurations, such as the Onera M6 wing, NACA four-digit series aerofoil and near wake analysis have been made.

Computations of the fluid flow around an Onera M6 wing and RAE2822 aerofoil were carried out by Davidson and Wang et al. A comparison between  $k-\epsilon$  models with the original Spalart-Allmaras model Navier-Stokes calculations were carried out (Davidson 1993; Wang et al 1999). The Spalart –Allmaras model showed the most agreement with the experimental data. All the models missed the location of the first suction peak by about 2%.

Navier-Stokes calculations with Spalart-Allmaras coupled with wall functions were also conducted by Frink, to assess the predictive capabilities of the algorithm for a flat plate boundary layer (Frink 1996). The skin friction coefficient showed spurious behaviour near the plate leading edge, which suggested that Spalart-Allmaras with wall function was insufficient in correctly computing the skin friction.

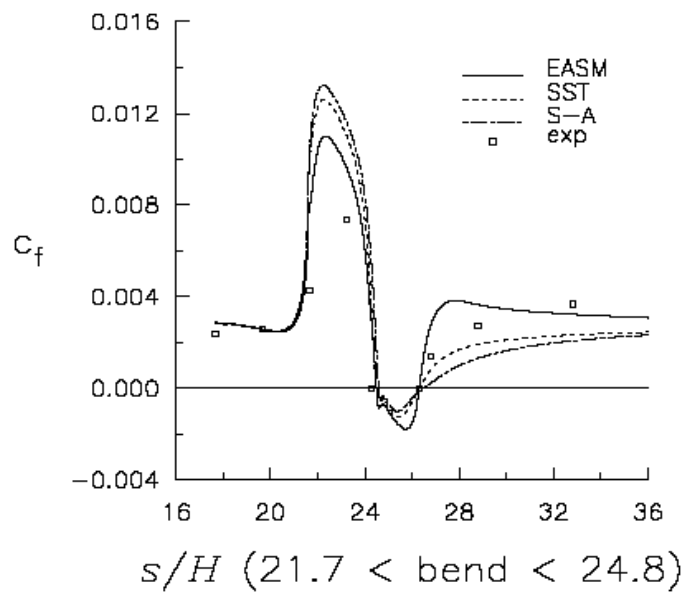


Figure 3-7: Inner Skin Friction Prediction for a U duct (Rumsey et al 1999)

One piece of valuable information coming from the more recent experiments is accurate measurements of the skin friction even in separated flows. These data are extremely useful in assessing near-wall turbulence modelling assumptions. Johnson et al carried out analysis of the equilibrium of the turbulent boundary layer and the caption of wakes, for a NACA 64 A010 and a NACA 4412 aerofoils (Johnson et al 1994). The results show a better agreement with experiment for the  $k-\omega$  SST model as compared to Spalart-Allmaras.

Most of the turbulence modelling studies is based on the performance of the turbulence models in the prediction of skin friction, the displacement thickness of the boundary layer and momentum deficit in the wake analysis. The latter attracted growing interest with the increase in the volume of civil transport. It is particularly important for small aircraft should they encounter high intensity turbulent vortices originating from large aircraft (Spalart 1998).

Prediction of both near and far-field vortex wake turbulent flows are also presented below (Kandil et al 1995; Kandil 1995). Reynolds Averaged Navier Stokes equations were used to compute and analyse vortex-wake flows of isolated and interacting

wings. A two equation  $k-\omega$  SST model was implemented with the solver for the investigation of a NACA 0012 profile with  $AR = 1.5$  at  $\alpha = 10^\circ$ . Overall agreement was achieved with experimental results, the turbulence model showed excellent agreement with the experimental data in the near wake region. However, the tip vortex core showed diffusion in comparison with the experimental data due to the lack of grid resolution in the core region (Figure 3-8).

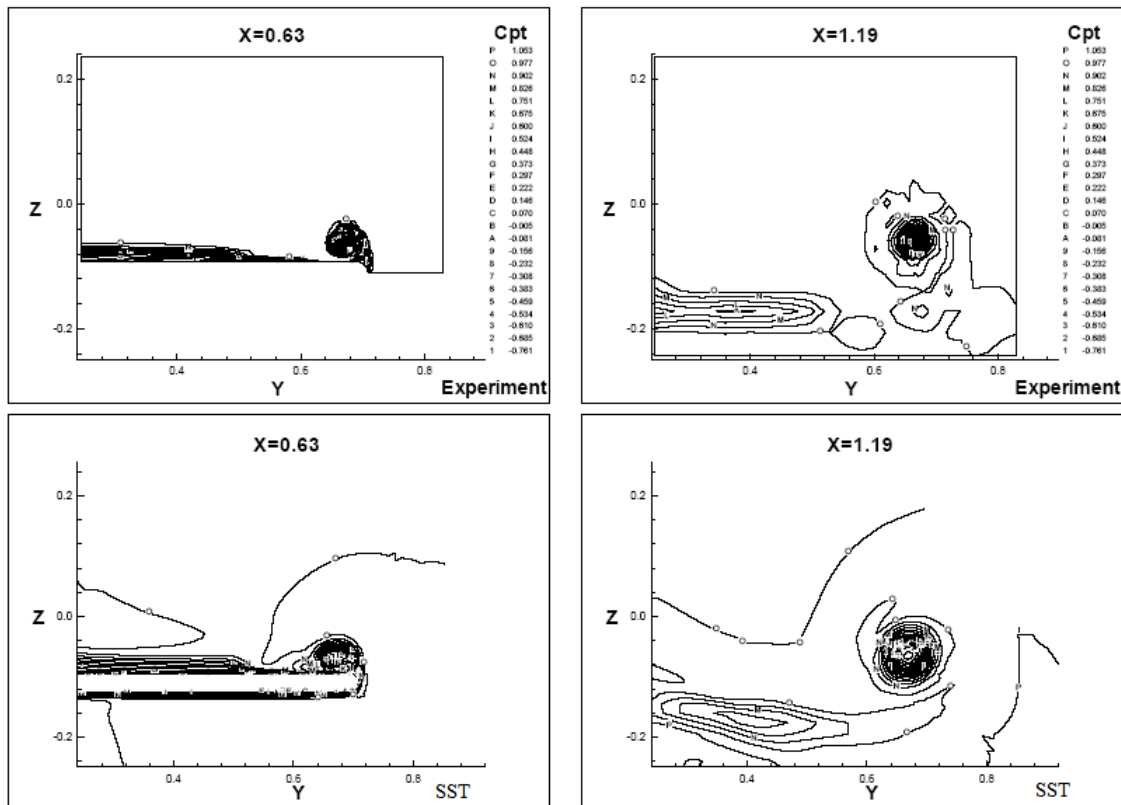


Figure 3-8: Tip Vortex Numerical Prediction comparison between  $k-\omega$  SST and Experimental Results (Kandil et al 1995)

Delta and STOL configurations have also been tested with numerical models, and studies have shown that the choice of turbulence modelling can have an effect on the accuracy of the results.

Ghaffari carried out systematical analysis to predict leading edge flow separation for a  $65^\circ$  delta wing, having either a sharp or blunt leading edge geometry definition (Ghaffari 2005). The computational results were based on a steady state, turbulent, Reynolds-Averaged Navier-Stokes formulation. The numerical analyses were

primarily performed for two angles of attack of approximately  $13^\circ$  and  $20^\circ$ . All computational results were obtained for free-stream Mach number of  $\text{Mach} = 0.40$  and Reynolds Number of  $\text{Re} = 6 \times 10^6$  (based on the wing mean aerodynamic chord). The effects of two widely used turbulence models that of Baldwin-Lomax (BL) (Baldwin and Lomax 1978) and Spalart-Allmaras, have been examined. It was generally concluded that the BL turbulence model coupled with the FV scheme provides the most effective combination for numerical simulation of vortical flows over the sharp leading edge model. Similarly, the SA turbulence model coupled with the FV yields the best combination for simulating the leading-edge flow separation and the off-surface vortical flows over the blunt leading edge configuration. Earlier studies in delta wings have also revealed that although more advanced two-equation models are available, use of them diffuses vertical flows. Hence, one-equation models are better in predicting these flow phenomena (Gordnier 1996; Dol et al 2002).

One of the most challenging issues in external aerodynamics is the accurate turbulence modelling of high lift flows. The following paragraphs present numerous computational studies which examine the performance of the variants of second-moment closure and non-linear eddy viscosity models when used to predict the attached and separated flows over high-lift aerofoils.

A high-lift workshop held in May of 1993 at NASA Langley Research Centre centred on a blind test of various CFD methods in which the flow about a two-dimensional (2D) three-element aerofoil was computed without prior knowledge of the experimental data. Comparisons were made between computation and experiment for (a) lift, drag, and moment, (b) lift and drag increments due to Reynolds Number and flap gap changes, (c) pressure and skin-friction distributions, and (d) mean velocity profiles. Interestingly it was revealed that in general, drag prediction using coupled methods agreed more closely with experiment than the RANS methods. Lift was more accurately predicted than drag for both methods. Pressures and skin friction results compared favourably with experiment for most of the codes. Poor performance of the RANS methods in simulating the far wake was also noted by other studies for high-lift configurations (Lien and Leschziner 1995).

A high-lift study by Gatski concluded that neither type of model employed ( $k-\epsilon$  and EASM) accurately predicted lift and drag characteristics over the Reynolds Number range ( $1.2-6.3 \times 10^6$ ) studied (Gatski 1996). The EASM more closely predicted the  $C_L$  distribution over a wide range of angle of attack, but was unable to accurately predict the distributions near stall.

Mavriplis and Valarezo (1999) employed the  $k-\omega$  turbulence SST model to predict the flow around a multi-element aerofoil. It was established that the  $k-\omega$  SST model performs very well as it accounts for the transport of the principal turbulent shear stresses in adverse pressure gradient flows. In this research it was noticed that predicted velocity profiles show differences in each computation as compared to the experiments, especially in the predicted boundary layer confluence and the velocity deficit from the upstream wakes. Similar results were also reported by Godin et al and Sullivan et al who obtained better agreement with experimental data when using the  $k-\omega$  SST model (Sullivan et al 1996; Godin et al 1997). Rudnik (Rudnik et al 2005) also assessed several models on the single NACA 4412 aerofoil near maximum lift and showed that only the SST model gave accurate results.

Duquesne focused on the effects of various pressure gradients on developing symmetric wakes, for the purpose of getting insight on the wake behaviour of wings in high lift (Duquesne 1999). The  $k-\epsilon$  linear eddy viscosity model and EASM model were used to assess the capabilities of predicting near wake flow.

The results are in good agreement with experimental tests, with slight variations at higher angles of attack. Duquesne notes that the differences between computed and experimental results can not be attributed to turbulence models only, the transition location and numerical differences between the codes can be accountable as well. Duquesne also suggests that turbulence models can easily be differently coded in different CFD packages; thus, small difference can completely alter the results.

Deficiencies in the wake profile configurations are found to be attributable in large part to poor boundary layer prediction on the generating wing element and not necessarily inadequate turbulence modelling in the wake as proved by Rumsey et al (1997, 2000), who also used the eddy viscosity and non-linear algebraic models to predict the flow-field of two high-lift aerofoils. Rumsey et al also concluded that the

difference between turbulence models is generally smaller than the difference between experiment and computations (see Figure 3-9).

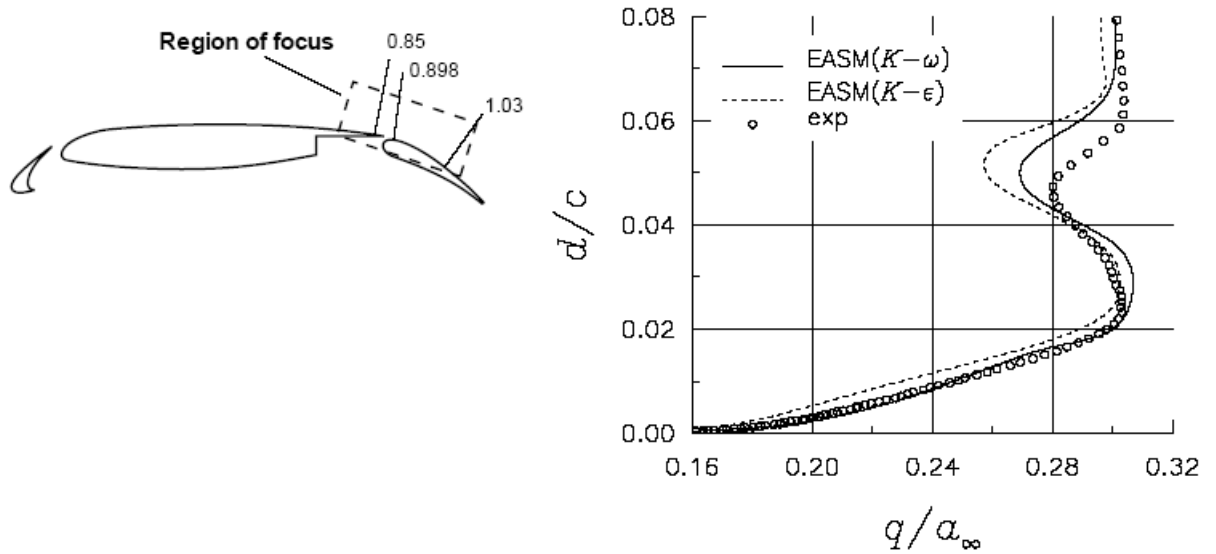


Figure 3-9: Multi-element Aerofoil Velocity Profile Predictions with two Turbulence Models (Rumsey et al 2000)

Similar revelations have also been reported by other studies in direct comparison of numerical and wind tunnel simulations. Discrepancies in both CFD and experimental results show that much needs to be done to reduce the variation not just numerically but experimentally as well. Pao et al carried out a study of the longitudinal forces and moments for a blended wing-body system (Pao et al 2005). Numerical results were compared with experimental investigations at two different wind tunnel facilities. Two different scale wind tunnel models of an early Boeing blended body model were used. One was a 2% scale transonic metal model and the other is a 3% composite subsonic model. It was found that pitching moment behaviour was particularly most sensitive, as the results obtained from CFD were significantly different from experimental values. It was also noticed that the pitching moment was different in the two wind tunnel tests. Whereas the results from the two turbulence models employed (SA and k- $\epsilon$ ) were found to be almost identical.

The latest work on turbulence models has been on addressing the major discrepancies in the drag results. Drag and pitching moment data are found to be the most difficult to predict, it is therefore important to routinely examine CFD capabilities in this area by methodically assessing the influence of various numerical parameters and physical models. Many studies in this area have been carried out in the past few years. Of the most recent ones are the drag prediction workshops held in concurrence with the AIAA. A total of 38 solutions from 18 authors were submitted for the first workshop and nearly 90 CFD test cases were performed as a contribution to the second Drag Prediction Workshop held in 2003, whose combined purpose was to study grid effects using the same code, and turbulence model effects using the same grid. A total of 9 turbulence models were used by different authors to assess the predictive capabilities of the codes. Although from all the solutions submitted a considerable number of the participants employed the same mesh and turbulence model differences between the predictions, have still been reported. There appears not to be a single main effect among the results that were gathered that might explain why these solutions differ. It was reported that the code-to-code scatter was more than an order of magnitude different, and the most significant source of modelling errors is due to incorrect choice of turbulence model (Rumsey et al 2004).

Rumsey et al used the Spalart-Allmaras, EASM and  $k-\omega$  SST models to compute the drag for the DLR-F6 wing-body and wing-body-nacelle-pylon configurations (Rumsey et al 2004). All cases were computed at Mach  $M = 0.75$  and Reynolds Number  $Re = 3 \times 10^6$ . It was observed that the  $k-\omega$  SST turbulence model consistently predicted lower drag than both SA and EASM. The effect on drag was at most 5 drag counts. The pressure drag component was obtained to be roughly the same for all three models, but the viscous drag component was lower for the SST and EASM models by about 18 drag counts. Figure 3-10 represents the DLR-F6 configuration utilised in the 2<sup>nd</sup> drag prediction workshop, together with the predicted results obtained by Rumsey et al with EASM.

Langtry et al employed an automatic wall treatment (automatic shift from low Reynolds model to wall functions based on grid spacing, when compared with experimental tests ) with the  $k-\omega$  SST turbulence model, for the 2<sup>nd</sup> workshop (Langtry 2003). Langtry et al on the other hand observed very good agreement,

particularly for the highly sensitive pitching moment, as depicted in Figure 3-11. Yamamoto et al (2004) noted that the k- $\epsilon$  model gave the most agreeable results for the same model. Nonetheless, from these studies it is easy to see why the drag prediction workshops have shown variations among participants of as much as 25-50 drag counts.

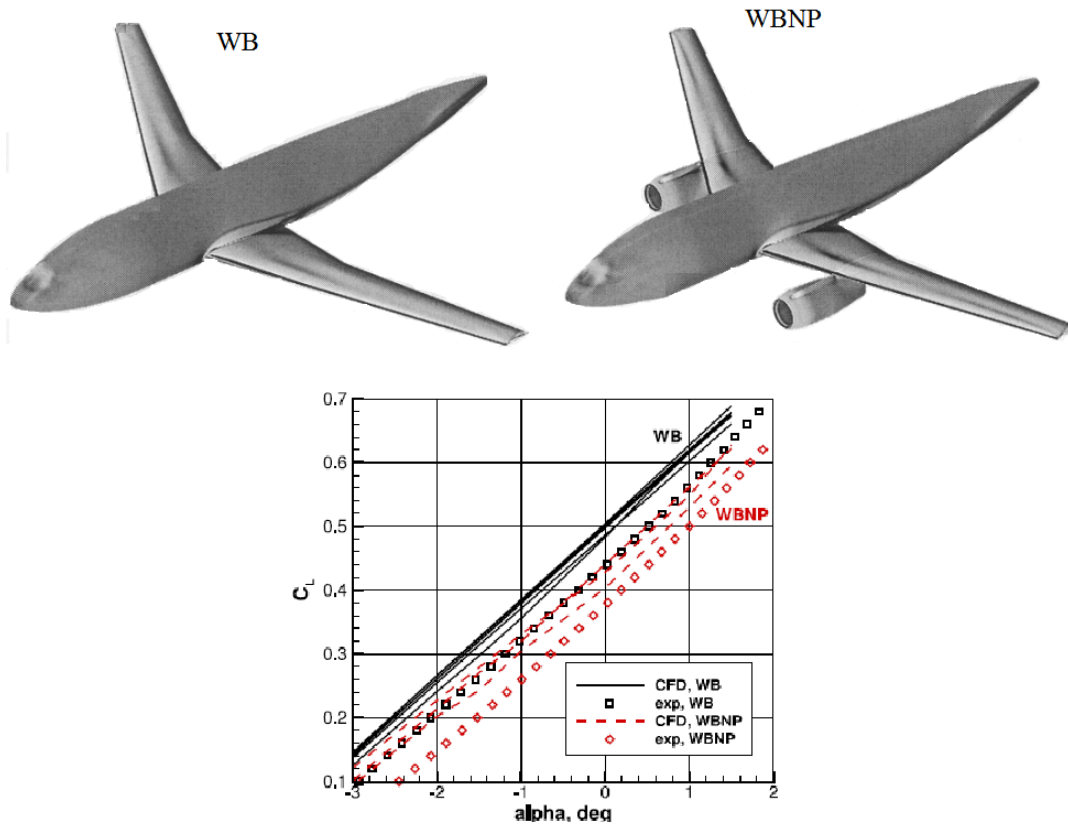


Figure 3-10: DLR-F6 Configuration and Predicted Lift Coefficients from Rumsey et al with EASM, k- $\omega$  SST and SA (Rumsey et al 2004)

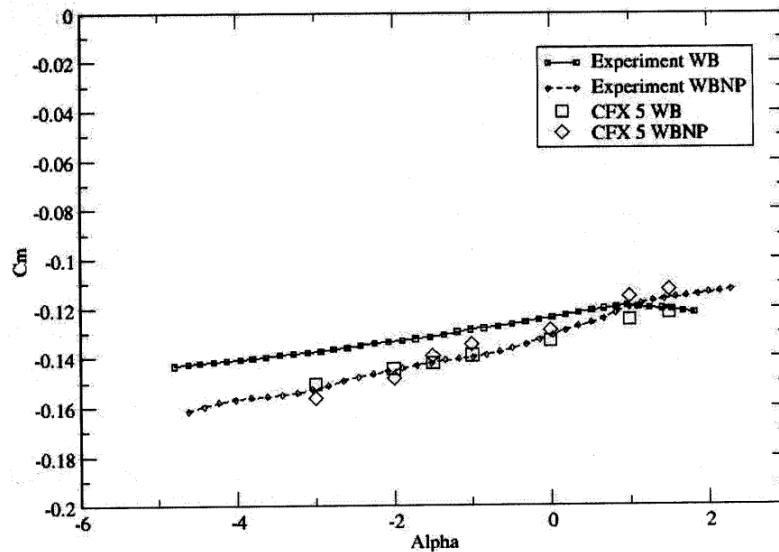


Figure 3-11: Pitching Moment Prediction with  $k-\omega$  SST for the 2<sup>nd</sup> Drag Prediction Workshop (Langtry 2003)

With regards to the acceleration of the steady flow solution and the rate of convergence, several research papers (Mavriplis et al 1999) show the possibilities of using a multigrid approach in the improvement of these matters. The most common multigrid is the W-cycle, where in the 3D case the number of cells is reduced by a factor of eight on each coarser grid. This procedure has shown good results when solving Euler equations, but is less effective in the calculation of viscous turbulent flow. The multigrid method can also be applied to unstructured meshes, with finer grids because of the complex geometry constraints. A multigrid agglomeration method has proven more effective when dealing with complex geometries. For example for the unstructured grid methodology, if the solver is based on a single grid it suffers a degradation of the convergence rate. However, these difficulties can be circumvented by a multigrid methodology (Pandya et al 2004).

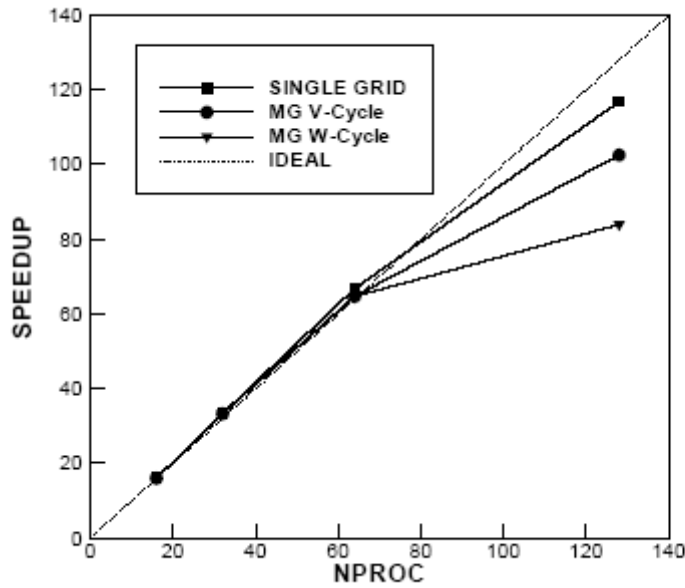


Figure 3-12: Observed Speed-Up for ONERA M6 wing (Mavriplis and Pirzadeh 1999)

### 3.7 Full-Potential Equations

Full potential equations are a part of potential flow methods. These methods involve the solution of the governing equations which are reduced by assuming the flow is inviscid, irrotational and isentropic. By employing these simplifications the continuity equation is then derived in terms of the velocity potential function  $\Phi$ .

The full velocity potential equation, for an irrotational, inviscid, isentropic flow, in terms of Cartesian coordinates  $(x,y,z)$  is written:

$$\begin{aligned}
 & \left(1 - \frac{\overline{\Phi_x^2}}{a^2}\right) \overline{\Phi_{xx}} + \left(1 - \frac{\overline{\Phi_y^2}}{a^2}\right) \overline{\Phi_{yy}} + \left(1 - \frac{\overline{\Phi_z^2}}{a^2}\right) \overline{\Phi_{zz}} - 2 \frac{\overline{\Phi_x \Phi_y}}{a^2} \overline{\Phi_{xy}} - 2 \frac{\overline{\Phi_x \Phi_z}}{a^2} \overline{\Phi_{xz}} - \\
 & - 2 \frac{\overline{\Phi_y \Phi_z}}{a^2} \overline{\Phi_{yz}} - 2 \overline{\Phi_x \Phi_{xt}} - 2 \overline{\Phi_y \Phi_{yt}} - 2 \overline{\Phi_z \Phi_{zt}} - \overline{\Phi_{tt}} = 0
 \end{aligned}
 \tag{3.38}$$

Where the velocity potential  $\Phi$  is defined by:

$$\nabla\Phi = \sqrt{u^2 + v^2 + w^2} = V \quad (3.39)$$

Such that:

$$u = \bar{\Phi}_x = \frac{\partial \bar{\Phi}}{\partial x}$$

$$v = \bar{\Phi}_y = \frac{\partial \bar{\Phi}}{\partial y} \quad (3.40)$$

$$w = \bar{\Phi}_z = \frac{\partial \bar{\Phi}}{\partial z}$$

The time  $t$  are the unsteady terms, which are neglected when the flow is steady.

Similarly, the integral form of the potential equations can be solved iteratively, and vortex methods may be introduced.

The section lift and drag coefficients are determined by integration of computed local  $C_p$  values. The overall lift and drag coefficients are then found by appropriate integrations of the section values.

In the vortex sheet approximation employed in FP, the trailing vortex sheet is effectively assumed to coincide with the grid surface passing through the trailing-edge. The practical significance of this assumption is that no effects of wake roll-up can be accounted for by FP, and so it must be expected to lose accuracy at relatively high lift conditions, where such rolling-up might noticeably influence the flow over the wing.

### 3.8 Grid Generation Methodologies-Review

Crucial to every CFD simulation, in order to achieve accurate results is the generation of a well posed grid, sufficient in capturing the smallest required scales of flow features around a potentially complex geometry. The grid generation methodology is based on creating a smooth variation of the grid characteristics, which are very important for successful progress (Pirzadeh 1999). The rate of growth, spacing and stretching parameters are prescribed through several “point” and “line” sources placed in the domain by the user, which is a common technique in most of the grid generation packages.

There are few different techniques available in grid topology approach: The simplest version of a numerical grid is a single block structured grid, but even if the geometry is relatively simple, the corner grid cells around a curved surface may be distorted in physical space.

Multi-block structured grids are a further development of the single-block grid. In this case, for a more complex geometry, the grid is divided into sub-domains that are called grid blocks and which transfer information across their boundaries.

Overlapping grids employ a similar approach as the multi blocks structured approach except that the grids are not required to match the boundaries.

Unstructured grids allow a great range of cell shapes; a combination of triangular, rectangular or curve-sided cells may be used. The number of cells surrounding any node is not constant throughout the grid.

A suitably fine grid that is consistent with the nature of the flow is required to overcome the difficulties associated with complex geometries and flow-fields such as boundary layer separation in stall conditions. A systematic analysis of the role of a flow consistent grid was carried out by Kumar. He suggests that computational grids play a crucial role in accurate CFD simulations (Kumar 1999). For instance, conventional grids for flow over a sharp leading edge do not solve near-apex flow due

to similar length scales of the flow and grid. A sufficiently fine grid is required not only to give a grid-free solution (independent of grid refinement) but to also solve the fine details of the flow phenomena. Kumar explains that there are still solutions which, in spite of a fine grid, give insufficient results where some features are not only left unresolved but un-captured as well. This suggests that however fine a grid may be, capturing of all phenomena is still a challenge. Hence, a comparison of computations with other forms of data is necessary. This type of validation is usually achieved by comparison with experimental results.

Another study of grid resolution, transition and turbulence models by Bartels discusses the importance of creating a good quality mesh before the simulation (Bartels 2001). Bartels depicts the issues of the choice of grid and turbulence modelling as having a significant effect on the three dimensional flow-field, and so in order to obtain an accurate solution, these issues must not be ignored. Furthermore, Bartels concludes that only a viscous solution will point out the important flow details.

The discussion on the use of a “structured” versus an “unstructured” mesh has been ongoing for the past few decades, and is still unresolved. A structured mesh can be recognised by all interior nodes of the mesh having an equal number of adjacent elements, whereas the unstructured mesh relaxes the node valence requirement, allowing any number of elements to meet at a single node. Structured meshes have been used for aerodynamic analysis in many cases in the past and have shown good results, however the time and the effort required to generate them are enormous. Different from the structured technique, the unstructured methodology possesses local refinement ability, allowing the user more flexibility on the time and computer constraints. Unstructured and semi-structured (hybrid) grid methodologies have proven to be as successful and less expensive compared to the structured grid when solving flows over complex geometries. Aside from the treatment of complex geometries, the second main advantage of unstructured meshes is the ease with which solution-adaptive meshing may be implemented (Mavriplis 1995). Since no inherent structure is assumed in the representation of unstructured meshes, mesh refinement and coarsening may be performed arbitrarily in any region of the mesh.

The benefits of using unstructured grids, especially when dealing with complex geometries, have been highlighted by early research in this area (Leicher et al 1982). The unstructured grid technology offers flexibility of both complex geometry and physics. As such, it can provide a powerful capability for accurately predicting and computing complex flows in aerospace applications (Marcum 1995). Marcum believes that the restrictions of the structured grid approach have to be improved using the approach of the unstructured method, especially in three-dimensional cases.

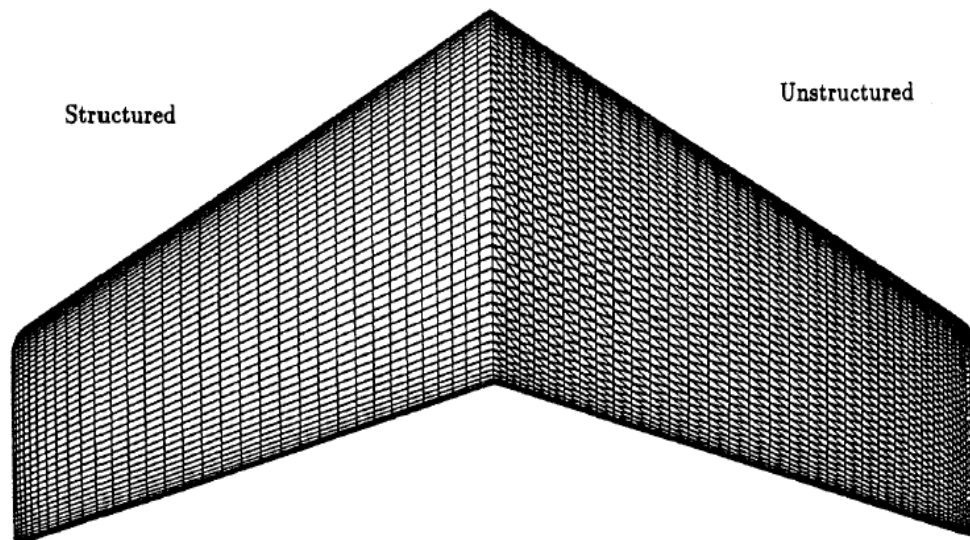


Figure 3-13: Example of Structured and Unstructured grid for ONERA M6 (Frink 1994)

One application that has received interest in the literature is the use of general structured elements positioned locally, in an extruded mesh, to improve mesh quality. Such an extruded mesh is typically employed as a component of a hybrid mesh near viscous boundaries. These highly anisotropic extruded meshes provide an efficient mechanism to resolve gradients that are primarily in the direction normal to the viscous boundary.

Over many years a number of different approaches to the generation of unstructured grids have been investigated. And many unstructured grid generation algorithms have been developed, see (Merriam 1991; Hassan et al 1994; Mavriplis 1995; Frink 1996;

Mavriplis 1997; Frink and Pirzadeh 1998). Automatic unstructured mesh generation algorithms have mostly used triangular and tetrahedral elements. Other alternative mixed tetrahedral, prism and pyramid grids have also been developed by (Ward 1993; Sharov and Nakahashi 1995; Yamamoto et al 2004) etc.

(Owen 1999) gives a brief survey of some of the fundamental algorithms for unstructured mesh generation. Most of the unstructured techniques used at present fit into one of the following three categories:

1. Octree
2. Delaunay
3. Advancing Front

The Octree technique was primarily developed in the 1980s (Shepherd 1991). With this method, cubes containing the geometric model are recursively subdivided until the desired grid resolution is reached. The Octree technique does not match a pre-defined surface mesh, as the other methods do; rather surface facets are formed wherever the internal octree structure intersects the boundary.

The Delaunay method is the most popular method, also known as the “empty sphere” method. In the Delaunay technique any node must not be contained within the circumference of any tetrahedra within the mesh, where a circumference is defined as the sphere passing through all four vertices of a tetrahedron.

In the Advancing front method, the tetrahedra are built progressively inward from the triangulated surface. An active front is maintained where new tetrahedra are formed, and the front will advance to fill the remainder of the area with triangles. Many grid generation algorithms based upon the Advancing Front method have been developed (Lohner 1988; Mavriplis 1997) etc.

Although, the Delaunay method has been successfully applied in many grid generation packages, Barth, on addressing the subject of numerical aspects of computing high Reynolds Number flows on unstructured meshes, reports that from an accuracy point of view, the Delaunay triangulation is not always the method of choice for viscous applications. Barth also questions the application of triangular cells up-

close to surface, suggesting that, although mathematically correct the mesh is still flawed (Barth 1991).

The available unstructured viscous grid generation algorithms can be divided into three groups. One group involves fully unstructured uniform tetrahedra such as the viscous model of Pirzadeh, the second group also produces a tetrahedral grid but directional refinement is used to generate stretched tetra in the viscous region (Pirzadeh 1994; Frink and Pirzadeh 1998). The third group involves a hybrid grid with overlapping viscous and inviscid regions such as prism and tetra. These have been developed by (Sharov and Nakahashi 1998; Yamamoto et al 2004) and others.

In general, the literature reveals no consensus regarding which is the most appropriate method. Pirzadeh suggests that prismatic methods still retain some of the imitations of the structured methodology, and furthermore, to obtain one-to-one connections between prismatic cells and tetra an identical number of prism layers need to be created globally, which impairs flexibility (Pirzadeh 1994).

Marcum, on the other hand, notes that the most common approach of stretching the grid in the viscous region is not realistic for complex geometry (Marcum 1995). A fully unstructured grid with tetra and mixed cells is necessary. This is achieved by firstly generating a fully unstructured grid and then combining elements where appropriate. Several other studies mentioned later in this section have reported that such a grid provides improved efficiency and reduced memory requirements.

Marcum employed the mixed tetra/prism method and applied it to two- and three-dimensional examples (see example in Figure 3-14). Navier-Stokes solutions for a multi-element aerofoil showed good agreement with experimental pressure coefficient data. The F-18 fighter aircraft was used as an example for the three-dimensional case. Although a good quality grid was achieved no comparison of the results is available.

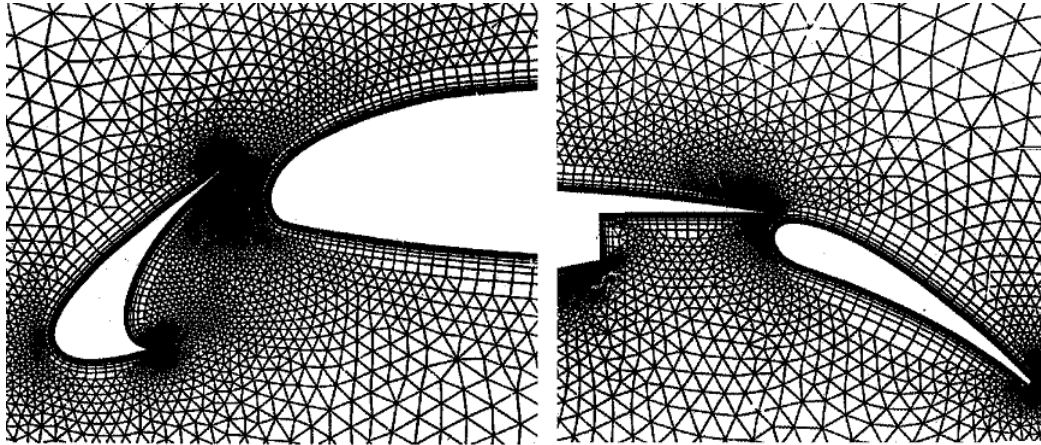


Figure 3-14: Example of a mixed Tetra/Prism Grid on a Multi-Element Aerofoil (Marcum 1995)

To assess the accuracy of the unstructured methodology numerous researchers have compared their numerical results against the available experimental data, such as high-lift flows. Other available validations are for a single element wing aerodynamics such as ONERA M6 (Schmitt and Charpin 1979), and military aircraft, such as the F-16 as large amount of experimental data for these configurations are available.

The computation of three-dimensional high-lift flows constitutes one of the most challenging steady-state aerodynamic analyses. Three-dimensional high-lift is typically characterised by complicated geometries, involving flaps, slats, and hinge fairings, in addition to very complex flow physics which must be captured adequately in order to provide a useful predictive capability for the design process.

Ghaffari carried out inviscid flow analyses with an unstructured grid algorithm. The configuration used in this study was an isolated fuselage wind tunnel model (Ghaffari 1999). The model was tested at a free stream Mach number of  $M_\infty = 0.4$ , Reynolds Number  $Re = 2.4 \times 10^6$  and  $\alpha = 19.8^\circ$  and  $29.8^\circ$ . The results were verified against both experimental data and viscous structured Navier-Stokes computations. Excellent agreement was reported between the structured and unstructured methods, in terms of off-surface flow and surface pressure distributions.

Frink has extensively researched the use of unstructured grids for viscous applications (Frink 1994; Frink 1996; Frink and Pirzadeh 1998). For the purpose of validation, results were compared with the available experimental data on the ONERA M6 wing. Frink confirms the significance of the unstructured methodology by obtaining good and agreeable results with both structured mesh computations and experimental analysis. He suggests however that further investigation on the use of wall functions to keep the 'viscous' overhead down, would be suitable.

Research carried out by Pirzadeh highlights the application of the unstructured Navier-Stokes solver for the all-important case of aircraft performance in landing and take-off (Pirzadeh 1999). As the CFD modelling on these cases has shown to be more difficult, Pirzadeh assesses the grid generation issues against the flow-field issues, which are highly dominated by viscous effects. The unstructured methodology was assessed on an Energy Efficient Transport Aircraft. The algorithm gave good results, in terms of agreement with experimental data.

Hassan et al used unstructured grids, with the stretching tetras method, to assess the turbulent flow for a two-dimensional aerofoil in a high-lift configuration (Hassan et al 1994). Numerical analyses were performed for Mach number,  $M_\infty = 0.2$  and Reynolds Number (based on the chord) of  $Re = 5 \times 10^6$ . For the three-dimensional configuration the ONERA M6 wing was used at Mach number  $M_\infty = 0.5$ ,  $\alpha = 3^\circ$  and  $Re = 1 \times 10^6$ . Ten layers of stretched elements were generated in the boundary layer region, giving a total number of elements of  $3 \times 10^6$ . Reasonable agreement with experimental data is noted; however further improvement of the boundary layer treatment was suggested. Numerical analysis on the same wing (ONERA M6) were also carried out by Chalasani et al with a hybrid grid (Chalasani et al 2005). Results were obtained at free stream Mach number  $M_\infty = 0.84$  and Reynolds Number based on mean aerodynamic chord  $Re = 1.2 \times 10^7$  and  $\alpha = 3.6^\circ$ . The results gave excellent agreement between predicted numerical and experimental results.

A similar method, where tetras are stretched into the boundary layer region, was employed by Frink and Pirzadeh. The Advancing Front method was used for pure tetrahedral grid generation in the inviscid region, whereas the advancing layer method was used for the viscous region (Frink and Pirzadeh 1998; Pirzadeh and Frink 2000).

The algorithm was tested for its ability to predict the lift coefficient, as compared with experiment, for a full F-16 aircraft tested at Mach number  $M_\infty = 0.95$  (see Figure 3-15). They used the Spalart-Allmaras turbulence model with wall functions. The Roe flux-difference splitting approach was used in this case. The best results were obtained at  $0^\circ$  with Navier-Stokes solutions, although difficulties at this angle of attack were reported when Euler modelling was employed. Reasonably good agreement with experimental results was obtained for force predictions. The code achieves excellent accuracy in predicting the turbulent skin friction coefficient on both a flat plate and the F-16 configuration. The results demonstrated the strong potential of the use of tetrahedral based finite volume Navier-Stokes solvers as an aerodynamic tool. Fink and Pirzadeh explain that, while there has been no definitive resolution to the issue of using pure or mixed tetra, most of the researchers are generally pleased with the cell-centered approach.

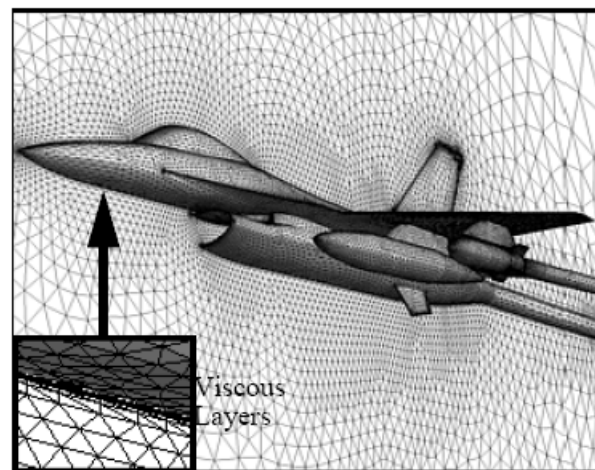


Figure 3-15: Unstructured Advancing Layer generated Mesh for the F-16 aircraft (Frink and Pirzadeh 1998)

Chaffin and Pirzadeh carried out solutions on a trapezoidal three-element high-lift wing model with a single slotted flap and a slat (Chaffin and Pirzadeh 1999). This model was developed in order to provide a database for CFD validation. Chaffin and Pirzadeh utilised an unstructured Reynolds Averaged Navier-Stokes (RANS) code for this study. The code uses a cell-centered, upwind biased, finite volume, implicit/explicit algorithm to solve the compressible Euler and Navier-Stokes equations on unstructured tetrahedral meshes. The viscous region was characterized

by a thin layer of tetrahedral cells. The predicted solutions for the trapezoidal wing showed that force and moment coefficients can be accurately estimated with the unstructured grid method and the general characteristics of the lift curve, particularly near  $C_{Lmax}$ , were captured well by the calculations. The results also showed that insufficient wake grid resolution leads to premature separation and significant errors in the calculated lift and pitching moment when compared to a structured overset grid flow-field investigation for the same geometry by (Rogers et al 2000). The study by Chaffin and Pirzadeh suggests that additional grid refinement and increased grid resolution in the vicinity of the trailing vortices is important.

Kallinderis defined a method for generating hybrid (prism/tetra) grids for complex three-dimensional geometries employed for viscous flow analysis around an aircraft (Kallinderis 1996). The method is an Octree/Advancing Front scheme for the generation of a hybrid grid. The special octree method is conducted via a “divide and conquer” method of the space outside the prism region. The authors suggest that the use of prismatic cells near the surface is the most suitable method, as this technique is able to capture the thin boundary layer. The suitability of hybrid meshes for capturing viscous flow phenomena was demonstrated by simulating viscous flows around a high-speed civil transport type of aircraft configuration. Rudnik et al compared the structured and the hybrid unstructured methodology for numerical predictions of high lift flows (Rudnik et al 2005). They demonstrated that an unstructured hybrid grid with a similar number of cells to the structured one was adequate in predicting good results when compared with experimental data.

Studies on the use of tetras and mixed tetra/prism grids were also conducted by Ghaffari and Mavriplis. Ghaffari presented numerical viscous solutions based on an unstructured grid methodology for a high-speed civil transport configuration, designated the Technology Concept Airplane (TCA) (Ghaffari 1999; Mavriplis et al 1999). Three-dimensional RANS equations were solved to simulate the flow. The numerical results were obtained on a representative TCA high-lift configuration that consisted of the fuselage and the wing, with deflected full-span leading-edge and trailing-edge flaps. Numerical results and experimental data were obtained at free stream Mach number  $M_\infty = 0.25$  and Reynolds Number based on mean aerodynamic chord  $Re = 8 \times 10^6$  for angles of attack of  $\alpha = 9.7^\circ$  and  $\alpha = 13.5^\circ$ . The computational

results indicated an excellent agreement between the predictions and the measured data over the examined angle of attack range. Reasonable surface pressure correlations between the numerical and experimental results were obtained for the above conditions. However, above and below these angles of attack, the correlation between computed and measured pressure distributions deteriorates.

Mavriplis et al carried out a complete geometry to drag-polar analysis capability for three-dimensional high-lift configurations (Mavriplis et al 1999). The approach is based on the use of unstructured meshes in order to enable rapid turnaround for the complicated geometries which arise in high-lift configurations. Mavriplis employed the mixed prism/tetra approach. They explain that there are several reasons why the use of prismatic elements rather than tetrahedral elements in the boundary layer regions is advantageous. Since prismatic elements contain almost half as many edges as tetrahedral elements and up to two thirds of the grid elements are often merged into prisms, the reduction in the computational overhead can be substantial. The geometry used for this study consisted of a twin-engine transport known as the Energy Efficient Transport (EET) configuration, which was tested both as a full-span and semi-span model at a free-stream Mach number,  $M_\infty = 0.2$ , Reynolds Number of  $Re_c = 1.6 \times 10^6$ , and  $-4^\circ < \alpha < 24^\circ$ . A total of 18.2 million tetrahedral were generated. This tetrahedral grid was then merged into a mixed-element grid of 3.9 million prisms, 6.6 million tetrahedra, and 46,899 pyramids. The fine grid was obtained by uniform refinement of this mixed prismatic-tetrahedral grid, resulting in a grid of 24.7 million vertices, with 53 million tetrahedra, 31 million prisms, and 281,000 pyramids. Good agreement between computed and experimental pressure coefficients and force coefficients as a function of angle of attack was shown for the full aircraft configuration.

Other investigations on the behavior and accuracy of the unstructured grid methodology were carried out at three recent drag prediction workshops held in association with the AIAA. A large number of participants have submitted results, on a predefined DLR-F4 configuration as given by the organizers (Redeker 1994). The objective of the study was to assess the accuracy of the unstructured/structured grid solvers for predicting drag in the transonic cruise regime, assess the efficiency of the method in terms of convergence and to determine the effect of the grid resolution on this predictive ability and its computational efficiency. Participants on the study

presented Navier-Stokes formulation based on block structured grids, overset grids and unstructured grids.

The results of the first prediction workshop, held in 2001, are summarised by Mavriplis and Levy. The test case was to produce drag polars and drag rise curves to compare with available experimental data (Mavriplis and Levy 2002). For this case a RANS solver was used with unstructured grids of mixed element types which include tetrahedral, pyramids, prisms and hexahedra. Tetrahedral elements were employed in the regions where the grid is nearly isotropic, which generally corresponds to regions of inviscid flow, whilst prismatic cells were employed in regions close to the wall such as in the boundary layer, and pyramid cells are formed in the regions where quadrilateral prismatic faces are exposed. The final mesh obtained in this study contained a total of 13 million points with 16 million prismatic elements and 28.8 million tetrahedral elements. The drag level was reduced by 4 counts when going from a 1.6 million grid to a 3 million grid. It was noticed that grid refinement appears to have little effect on the induced drag in the attached flow region. The pitching moment was under predicted with larger discrepancies observed for the refined grids. For the higher Mach numbers, the drag was substantially under predicted at the higher lift values. The agreement at lower lift values was improved with grid refinement for all grids considered. The predictive ability of the numerical scheme was found to degrade for flow conditions involving larger amounts of flow separation.

Rakowitz and Eisfeld assessed the accuracy of the structured and unstructured grid against available experimental data (Rakowitz and Eisfeld 2003). They concluded that the unstructured grid gives less agreeable results with experimental ones; however it is significantly less time consuming to generate. The structured grid gives more agreeable results; however the computational predictions are very grid dependent, a 20 % difference in the drag coefficient is noticed on between the two grids (structured and unstructured) with the similar number of cells (see Figure 3-16).

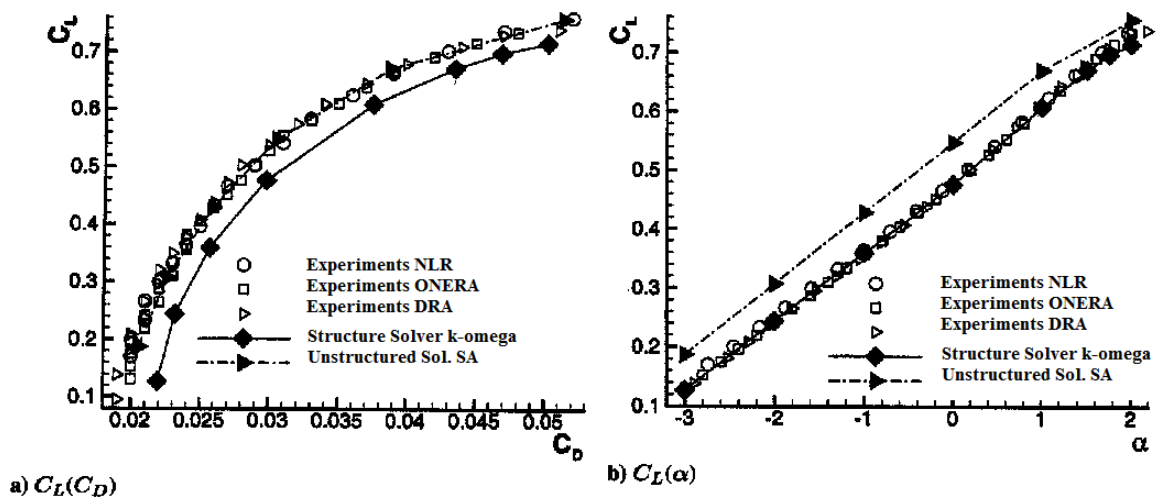


Figure 3-16: Structured and Unstructured Grid Results for the DLR-F4 Drag Prediction Workshop (Rakowitz and Einfeld 2003)

(Yamamoto et al 2004) reported on the second CFD drag prediction validation study for a DLR F6 aircraft model with wing body (WB) and wing-body-nacelle-pylon (WBNP) configuration. Two solvers were used for the study, one using Navier-Stokes and a cell-centered finite volume method on a multi-block structured grid and the other being a finite volume for mixed element grid. A total of 14.8 million grid points were generated for the structured case for the WBNP configuration, and 8.7 million for the WB configuration. The unstructured grid consisted of hexahedral and prism cells with a small number of tetrahedral and pyramid cells. For the unstructured case, the finest grid obtained for the WBNP configuration was 9.5 million with a 5.2 million grid for the WB configuration. A  $Y^+ = 1$  was achieved over almost 85% of the model surface. It was noted that most of the drag variation between grids is caused by the pressure drag. The predicted slopes with both codes compared well with the experimental results. Though for the WBNP case the predicted lift curve slope was considerably smaller than experimental values. Both structured and unstructured results correctly predict the drag at higher angle of attack for the WBNC configuration, but a shift from the experimental curve is noticed at lower angles of attack. The unstructured code predicted the WB drag better than the structured one.

Rumsey et al employed two programs for the drag prediction workshop (Rumsey et al 2004). An overset Chimera structured grid Navier-Stokes flow solver based on the finite difference method and an unstructured finite volume method were utilized. They noted that the unstructured method consistently under predicted lift, drag and moment coefficients compared to the structured one.

Generally, due to the large number of cells for Navier-Stokes computations, the literature recommends several useful techniques to make the unstructured grid methodology more practicable (Beall 2003). For example, utilisation of parallel computers shows considerable time savings for large problems. Another alternative which was found to be useful is the grid adaptation technique (Mavriplis 1995), which produces efficient grids and improves the solution accuracy economically. The principle idea of adaptive meshing is to enable a higher accuracy solution, through a more optimal distribution of grid points for each computed solution (see Figure 3-17).

Grid-post processing was recommended as well, as it was found that with finite volume grids, small isolated pockets of cells were present which would not be accepted by the solver, due to discontinuities. The two main categories of mesh improvement include smoothing and clean-up. Smoothing is a procedure that involves some form of iterative process that repositions individual nodes to improve the local quality of elements. Clean-up generally refers to any process that changes the element connectivity. Also, refinement is a procedure that should always be applied; the reduction of cells size may be required in order to capture a local physical phenomenon.

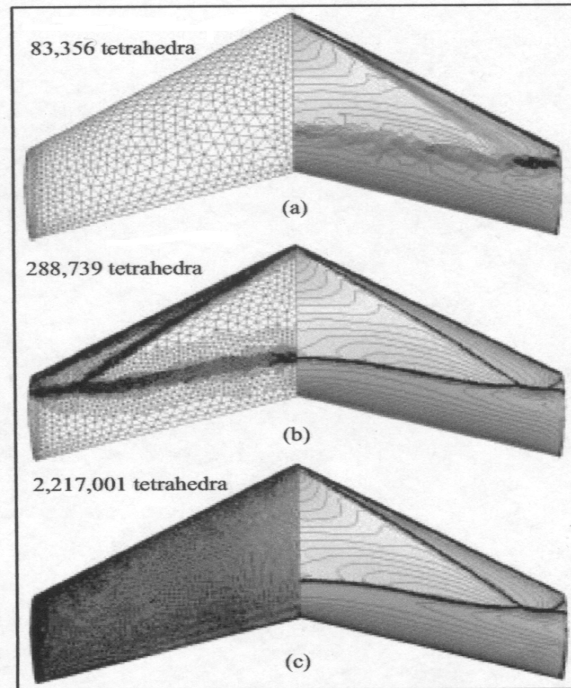


Figure 3-17: Grid and Surface Pressures on an ONERA M6 wing, a) initial, b) adapted and c) finely adapted (Pirzadeh 1999)

### 3.9 Grid Generation (W-wing)

After discretisation numerical solution can be obtained at discrete points which are called grid points.

Prior to generating the grid for the solution domain one has to define the spatial coordinates of any solid surfaces, inlets, outlets and other geometrical boundary features applicable to the problem. A suitable grid of discrete nodes has to be generated so that the algebraic equations can be solved; these algebraic equations are firstly solved in the computational domain and then translated back to the physical domain.

For this project, the grid generator employed allows application of the unstructured grid generation. A literature review on the subject revealed greater flexibility when unstructured grids were employed for complex geometries, as is the case for this

study. It was also concluded that the unstructured method performs the best when dealing with flow fields which are highly dominated by viscous effects.

The choice of the unstructured grid generation technique (i.e Octree, Delaunay or Advancing Front) is already decided by the code developers. The Octree approach is employed in the current code; hence this method will be briefly reviewed in the following.

An important aspect of the unstructured approach is that a local coordinate system is required for each cell. The octree method firstly defines a cube that corresponds to the domain that contains the geometry. The cube then is subdivided into four smaller octants; these are then further divided until a satisfactory solution is reached.

Furthermore, to obtain the tetrahedral the octants are sub-divided into five tetrahedra. If the boundaries are set, the octants may be divided into six pyramids.

The current methodology applies two co-ordinate systems, the first is the solid modeller which defines the entire geometry and the second is the so-called integer co-ordinate system (any point in this is referred to as a set of co-ordinates that are integer). A process is then set-up to create communication between these two co-ordinate systems (see (Yerry and Shephard 1984) for a methodical description on this matter)).

The basic steps octree technique as developed by Yerry and Shepherd are (see Figure 3-18):

1. Set-up of the integer co-ordinate system that contains the geometry to be meshed.
2. Generate the octree representation of the object
3. Break the octree into valid cell elements
4. Pull the nodes of the boundary of the octree to the appropriate vertices, edges and faces of the original geometry.
5. Smooth the location of the node points to create a better mesh.

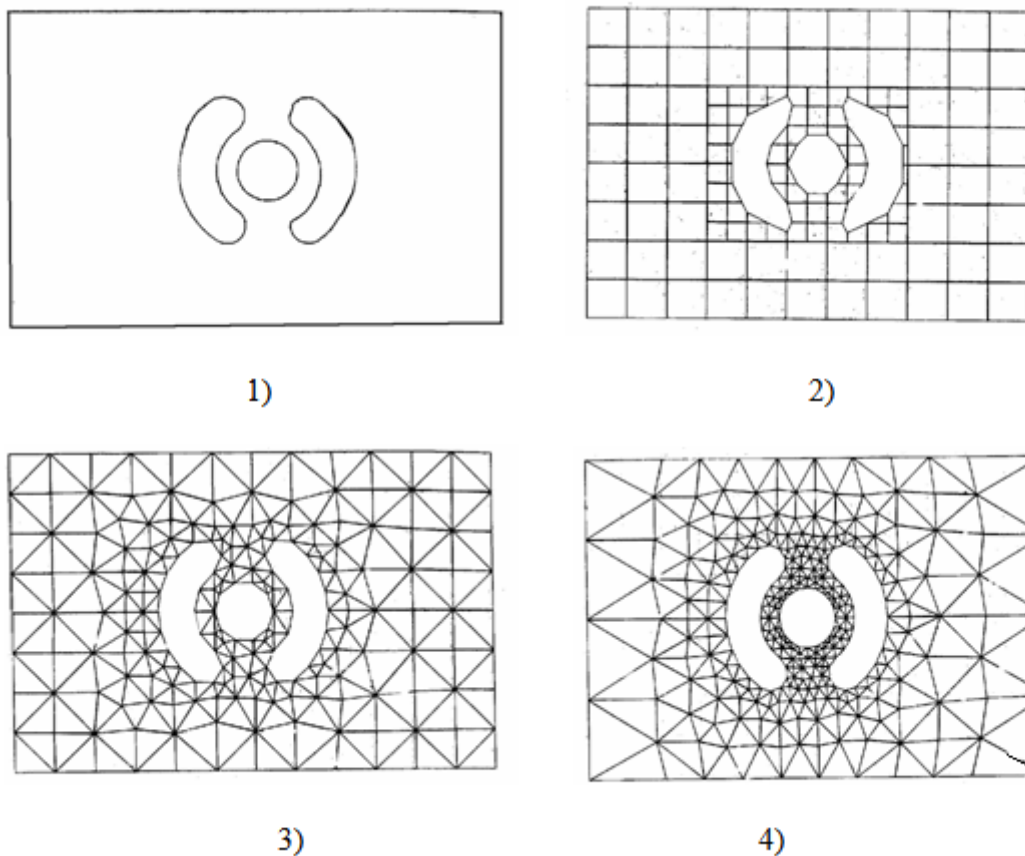


Figure 3-18: Octree Mesh Generation Process (Yerry and Shephard 1984)

### 3.10 Preview of CFD Codes

Many commercial CFD packages are available to solve a wide range of flow phenomena. Most of these codes would provide all the necessary tools, from grid generation to the post processing. Ideally, when dealing with more complex flow a comparative study examining which of these codes performs best for different flow-fields should be carried out.

Not all CFD packages with pre- (provides data for the solver) and post-processing (data are processed and visualized) abilities are sophisticated enough to deal with more complex flows. There are several powerful grid generation only packages that can be used separately to create the grid, which can then be imported into the solver with the best simulation capabilities.

Geometry and mesh generation was achieved using CD-adapco's *SolidWorks* program and ANSYS *ICEM CFD* respectively, whereas simulation codes used for this project were firstly *COMET*, and later *STARCCM+*. *Solidworks* was used to generate the drawing of sophisticated 3-D graphical images. The geometry can then be exported in various formats for the mesh generator.

ANSYS *ICEM CFD* models geometry such that whatever is in the geometry (tetin) file will be modeled in the mesh (domain) file. Therefore, the resulting mesh will be an exact replica of the geometry. The generation method employed in this study is the hybrid tetra and prism. The ANSYS *ICEM* code offers several advantages, including, rapid model set-up, control over cell size inside a volume, volume and surface mesh smoothing, merging nodes and swapping edges, automatic detection of holes etc.

The *ICEM CFD* Tetra mesher includes a prism mesh required for CFD boundary layer meshes. The prism mesher uses the existing volume mesh as a starting point which gives it the ability to detect and mesh intersecting prism layers. The hybrid tetrahedral grids with near-surface prism layers were employed due to previous evidence of more adequate modelling of the close-to-wall physics of the flow field.

*STARCCM+* was used for numerical simulations, as it offers a wide range of modelling physical phenomena including inviscid (Euler) and viscous flow (Navier-Stokes). The code is a finite-volume numerical flow solver; it uses the segregated and coupled explicit/ implicit approach to solve the resulting set of coupled non-linear algebraic equation system.

The full-potential code employed was the one derived at ESDU (ESDU Data Item 02014). FP is a CFD (computational fluid dynamics) method coded in Fortran for calculating the flow field and aerodynamic forces of an isolated wing (denoted usually as a wing-alone) or a wing-body combination (denoted usually as a wing-body) in a subsonic free-stream, including the effects of shock waves. The code uses a relaxation process to solve the finite-difference form of the full, nonlinear velocity-potential equation for the inviscid, compressible flow around the three-dimensional geometry.

Although the method assumes the flow is inviscid and irrotational, the code has been shown to give good agreement with experiments, particularly at low incidence.

## **Summary**

Reviewing the literature in numerical modelling revealed that only a Navier-Stokes solution would be considered accurate enough for the type of configuration assessed in this study. Although, studies have proven that Euler calculations can be reliable in numerically resolving many aerodynamic phenomena including shockwave and the convection of vortices once they have been formed because fluid dynamics is dominated by viscous effects, only a high-fidelity simulation using Navier-Stokes equations can provide the accuracy necessary to assist in aircraft design (Rogers et al 2001).

There are three main approaches to modelling turbulent flows. The first is the so-called Direct Numerical Simulation (DNS) method, which requires solving the Navier-Stokes equation in every perturbation of the flow. The second approach is the Large Eddy Simulation (LES), where a spatial filter is applied. Large-scale structures are resolved by the numerical method on a given mesh called the super-grid scales. Then the influence of the other sub-grid scales on the super-scales is modelled. This third approach is the Reynolds Averaged Navier- Stokes (RANS) method.

Turbulence modelling literature survey gave an insight into the available methods and the most appropriate application in aerospace studies. Interest to most engineering applications is the accurate prediction of adverse pressure gradient flow both with and without separation (Menter 1992). In external flows, such as the flow around an aircraft, the flow conditions near the boundaries are almost invariably important; therefore near-wall modelling significantly impacts the fidelity of the numerical solution, in as much as the walls are the main source of mean vorticity and turbulence.

In general Reynolds time-averaging has proved the most successful so far. Over the last few years many different turbulence models have been developed for use with Reynolds-Averaged-Navier-Stokes (RANS). Despite the great variety of turbulence

modelling options available, and the many reported weaknesses of the eddy viscosity models (such as under predicting the post separation, under predicting flow recovery etc), they still remain the most preferred solution (Rizzeta 1993). The  $k-\epsilon$  model as derived by Launder and Spalding (1974) and the Spalart-Allmaras (1994) (SA) model have been the predominant methods employed for aerodynamic computations. Another successful model is the  $k-\omega$  model developed by Wilcox, later Menter suggested additional terms in the  $\omega$  to ensure that solutions are consistent with experiments, resulting in the new  $k-\omega$  Shear Stress Transport (SST) model (Menter 1992).

Most of the turbulence modelling studies reviewed herein, reveal good agreement between the eddy viscosity models and the available experimental data. Overall it should be noted that the research on this area shows that the Reynolds Stress Models (RSM) are the most complete and fundamentally secure forms (Leschziner 2002), however as due to computer limitations the eddy viscosity models are considered more popular in aerospace applications.

On the whole for wing alone applications the Spalart Almaras model gave the best agreement with experimental results, particularly in two-dimensional analyses, followed by the  $k-\omega$  turbulence SST model. It has also been reported that the  $k-\omega$  SST model tends to be more accurate in separated flows whereas the Spalart-Allmaras performs better in attached flows (Godin et al 1997; Godin 1997). Prediction of both near and far-field vortex wake turbulent flows are also showed the best agreement with the  $k-\omega$  turbulence SST (Kandil et al 1995; Kandil 1995). Turbulence modelling of high lift flows was best represented by the  $k-\omega$  SST model, also it was established that the  $k-\omega$  SST model performs very well as it accounts for the transport of the principal turbulent shear stresses in adverse pressure gradient flows Mavriplis and Valarezo (1999).

Previous studies on grid generation reveal no definitive consensus on the best methods available for the numerical assessment on aerospace application. In general there is an ongoing discussion on the use of a “structured” versus an “unstructured”. Structured meshes have been used for aerodynamic analysis in many cases in the past and have shown good results, however the time and the effort required to generate

them are enormous. Different from the structured technique, the unstructured methodology possesses local refinement ability, allowing the user more flexibility on the time and computer constraints. Unstructured and semi-structured (hybrid) grid methodologies have proven to be as successful and less expensive compared to the structured grid when solving flows over complex geometries. Since no inherent structure is assumed in the representation of unstructured meshes, mesh refinement and coarsening may be performed arbitrarily in any region of the mesh.

In the latest studies on aerospace applications because of the number of grids required mostly unstructured methodologies are being utilised. Those can be divided into three groups. One group involves fully unstructured uniform tetrahedra such as the viscous model of Pirzadeh, the second group also produces a tetrahedral grid but directional refinement is used to generate stretched tetra in the viscous region (Pirzadeh 1994; Frink and Pirzadeh 1998). The third group involves a hybrid grid with overlapping viscous and inviscid regions such as prism and tetra used by (Sharov and Nakahashi 1998; Yamamoto et al 2004) and others. The latest application that has received interest in the literature is the use of general structured elements positioned locally, in an extruded mesh, to improve mesh quality. Such an extruded mesh is typically employed as a component of a hybrid mesh near viscous boundaries.

The above methods have been used to verify experimental data of Onera M6 wings, high lift applications, delta wings, DLR F6 wing etc. These methods have shown good results and agreement with the experimental data with the most success being noted by the hybrid methods where prism layers of more than 10 have been employed in the boundary layer region (Hassan et al 1994, Kallinderis 1996, Chafin and Pirzadeh 1999). The latest method will be used in the current project as well.

In this study the three-dimensional quasi-steady, compressible Navier-Stokes equations supplemented by Sutherland's viscosity law were utilised for the cruise simulation study, whereas incompressible Navier-Stokes equations were utilised for the ground effect study. In both studies the numerical grid utilised was an unstructured hybrid grid with relevant number of prism layer according to the Reynolds number. Turbulence was accounted for by using Menter's  $k-\omega$  SST model.

## 4. Validation of Numerical Methods

The proof of validity of any numerical prediction depends, above all, on experimental comparison. To assess the degree to which a numerical solution is an accurate representation of the real world, CFD codes and algorithms need to be verified against accurate experimental data for the same geometry. For the purposes of the current study, validation of both the Navier-Stokes CFD code and full-potential code used to study the W-shaped leading-edge wing was accomplished using the Onera M6 wing. The simple geometry and transonic phenomena involved with this wing have made it a classic CFD validation case.

The Onera M6 has been employed previously in the verification of a large number of computational algorithms and numerous CFD papers have been published on this case. Studies by (Frink 1994; Hassan et al 1994; Frink 1996; Frink and Pirzadeh 1998; Chalasani et al 2005), have utilized the Onera M6 wing to verify the application of the unstructured grid methodology, with a successful outcome. Other studies (van Dam 1995) have shown that the finite volume and finite difference methods gave good accuracy in predicting the Onera M6 flow-field and others (Davidson 1993; Wang et al 1999) showed that Navier-Stokes computations of the Onera M6 gave very good predictions. The unstructured grid procedure with Navier-Stokes equations solved with a finite volume approach was also employed by the author in this study. The results of the current validation study are presented in this section.

### 4.1 The Onera M6 wing

The experimental data pertaining to the Onera M6 wing were obtained from AGARD Report AR-138 (Schmitt and Charpin 1979). The report provides results from wind tunnel tests on the M6 at a range of transonic Mach numbers (0.7, 0.84, 0.88 and

0.92), various angles-of-attack up to  $\alpha = 6^\circ$  and Reynolds Numbers between  $1.5 \times 10^6 < Re = 1.5 \times 10^7$ .

Figure 4-1 and 4-2 illustrate the wing geometry employed by Schmitt and Charpin. The spanwise location of the pressure tapings used to take the measurements is also shown.

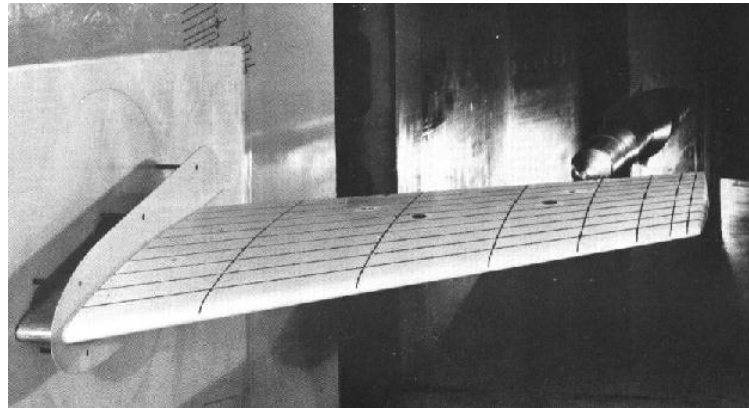


Figure 4-1. The ONERA M6 wing (Schmitt and Charpin 1979).

FIGURE B1-1

SWEPT WING M6

Aspect ratio  $A = 3.8$   
 Taper ratio  $\lambda = 0.56$   
 Sweep angle  $\Lambda_{25\%} = 26.7^\circ$

ROWS OF PRESSURE TAPS

N°	y/b	upper	under
1	0.20	23	11
2*	0.44	23	11
3	0.65	23	11
4	0.80	23	11
5	0.90	31	14
6	0.95	31	14
7	0.99	31	14

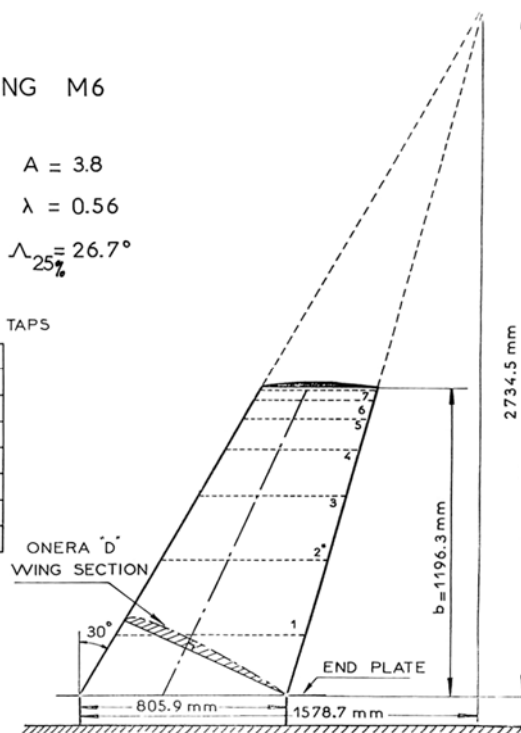


Figure 4-2. ONERA M6 wing specification and pressure taps locations (Schmitt and Charpin 1979).

## 4.2 Methods

An initial set of Navier-Stokes flow-field predictions were carried out with equivalent conditions to those of Schmitt and Charpin test case 2308 ( $Re = 1.2 \times 10^7$ ,  $M = 0.84$  and  $\alpha = 3.06^\circ$ ). These were dubbed the ‘high-speed’ simulations. A second set of simulations, the ‘low-speed’ tests, were carried out for conditions of  $Re = 2.3 \times 10^6$ ,  $M = 0.2$  and  $\alpha = 0^\circ$ . These were used to validate the low-speed portion of the W-wing study. Since no equivalent experimental results were available from the Schmitt and Charpin study, the low-speed validation was accomplished through comparison with the full-potential code.

The Navier-Stokes simulations were carried out using the StarCCM+ Solver on a hybrid tetra/prism mesh, which was generated with ICEM CFD commercial software. The mesh was made to be an exact replica of the M6 geometry, as outlined above. As in the experimental study of Schmitt and Charpin, only half of the wing was modeled. Symmetry boundary conditions were employed to mirror the port side of the wing. Prism cells were clustered in twenty-two layers near the wall, with the first prism layer giving an average  $Y^+ = 10$  on most parts of the wing (see Figure 4-3). No-slip conditions were applied to the wing model and free-stream conditions emulating those employed in the experimental study have been applied to the far-field boundaries. The final mesh obtained for the validation had 2.6 million cells. Figure 4-4 illustrates this final grid. A close up of the near wall grid is depicted in Figure 4-5.

Compressible quasi-steady calculations were carried out for the high-speed Navier-Stokes computations, whereas incompressible quasi-steady calculations were carried out for the low-speed computations. The validation study was performed using the  $k-\omega$  SST turbulence model. This decision was influenced by the fact that the  $k-\omega$  SST was the primary turbulence model employed for the W-shaped leading-edge wing study. Nonetheless, it should be noted that findings of a similar nature have been obtained in the past with the  $k-\epsilon$  model see (Wang et al 1999).

The full-potential code uses a relaxation process to solve the finite-difference form of the full, nonlinear velocity-potential equation for the inviscid, compressible flow

around the three-dimensional geometry. Further details of the code can be found in ESDU Data Item 02013 (ESDU 2002).

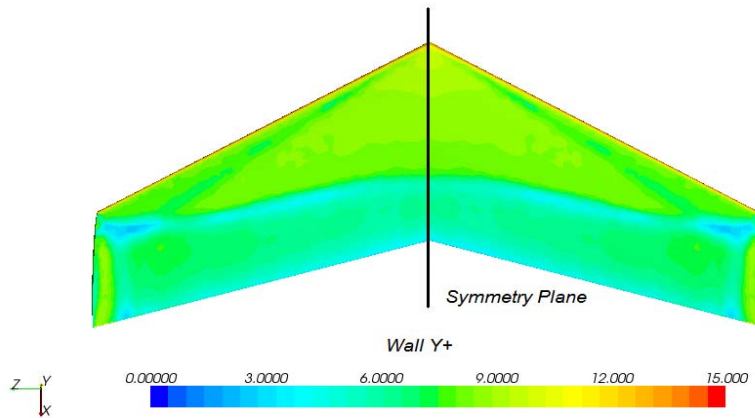


Figure 4-3.  $Y^+$  distribution for numerical predictions on Onera M6 fine grid at  $Re = 1.2 \times 10^7$ ,  $M = 0.84$  and  $\alpha = 3.06^\circ$

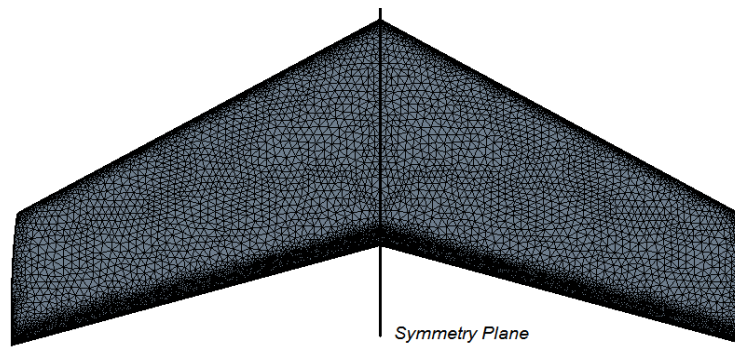


Figure 4-4. Planform view of Onera M6 final unstructured grid.

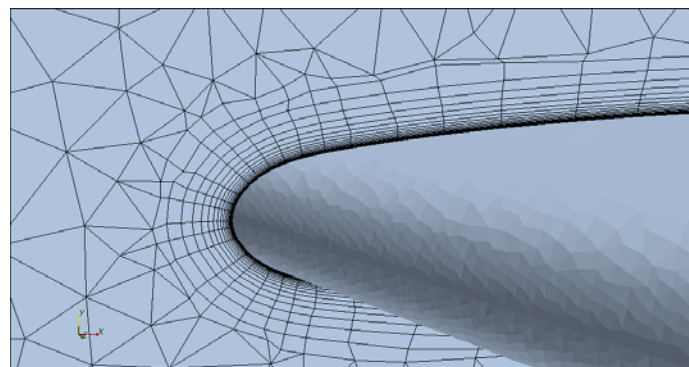


Figure 4-5. The Onera M6 computational grid in the near surface region.

### 4.3 Results

The AGARD wind tunnel tests on the Onera M6 wing produced only pressure coefficient data. Hence, pressure coefficients for the same spanwise locations were assessed numerically. Nevertheless, pressure coefficient plots are of paramount importance and good agreement with the experimental data is imperative.

Numerically predicted pressure coefficients for various  $z/b$  ( $\eta$ ) locations were plotted to examine the relevant pressure loading. These plots were employed as the primary code verification measure and their comparison with the experimental data will be discussed below. Afterwards, a discussion will follow on the comparison between the numerical results from the codes (Navier-Stokes and Full-Potential) employed on the Onera M6 wing.

#### 4.3.1 High-Speed Study

Fig 4-6 to 4-11 represent the pressure distribution at various spanwise locations for the high-speed calculations ( $M = 0.84$  and  $\alpha = 3.06^\circ$ ). In examining the pressure coefficient data, one may conclude that there is generally a good agreement between the numerical data and the published experimental results. At all sections investigated, Navier-Stokes computations were capable of capturing the leading-edge suction pressures, with only a slight over prediction at the farthest outboard spanwise section of  $\eta = 0.99$  (see Figure 4-11). Full-potential predictions of the leading-edge suction peaks also compare remarkably well with experimental results, the solution being very similar to the Navier-Stokes computations at the outermost spanwise locations. The latter are more accurate in shock capturing capabilities in terms of correct pressure distributions and precise predictions of the shock location. At  $\eta = 0.65$ , both Navier-stokes and full-potential results somewhat under-predict the pressure behavior at  $x/c = 0.2$ , whereas for  $\eta = 0.8$  the full-potential code failed to capture the initial shock presence at all.

Trailing edge pressure distributions were generally predicted well by both methods, with differences noted near the root sections. Flow behavior at the wing-tip section ( $\eta = 0.99$ ) were again in more agreement with the Navier-Stokes computations. Lower surface pressure distributions were generally consistently under-predicted by both numerical methods employed. The lower pressure coefficients as observed from all the plots vary albeit very slightly from the experimental data. The difference might be attributed to the grid or the near wall layer resolution being constant throughout the geometry. Although the layer might be sufficient in the upper surface behaviour predictions the difference in the lower surface where no major phenomena such as shocks are taking place should not be present. Further analysis in the grid independence approach might have given better predicted pressures in the lower surface region.

The current validation study performed well in comparison with previous validation methods (Frink 1994; Hassan et al 1994; Frink 1996; Frink and Pirzadeh 1998; Chalasani et al 2005). The offset in the lower surface pressure coefficient were observed in the previous studies conducted by Frink ( Frink 1994, 1996). Also the divergence from the experimental data in trailing edge pressure coefficient at  $\eta = 0.99$  with very similar characteristics has also been reported from previous researches in the area (Chalasani et al 2005). It has to be mentioned that the current study was better in capturing the shock appearance in comparison to the other studies from Hassan et al and Pirzadeh. Nevertheless lower surface pressure coefficient predictions were less accurate than the ones predicted by Frink, Hassan et al and Chalasani et al.

The cause of the differences between the computational studies and experimental results may be due to various factors, ranging from numerical errors to the lack of resolution on the near-surface region and also experimental inaccuracies which can never be avoided. Furthermore, the greater difference with the full-potential method is due to the code not accounting for viscosity and rotational flow. Although, grid refinement for both numerical methods might improve the predictions, no further investigation of such kind was considered necessary as both methods gave sufficiently accurate results as to conclusively validate the capabilities of the numerical algorithms, at the transonic speed range investigated.

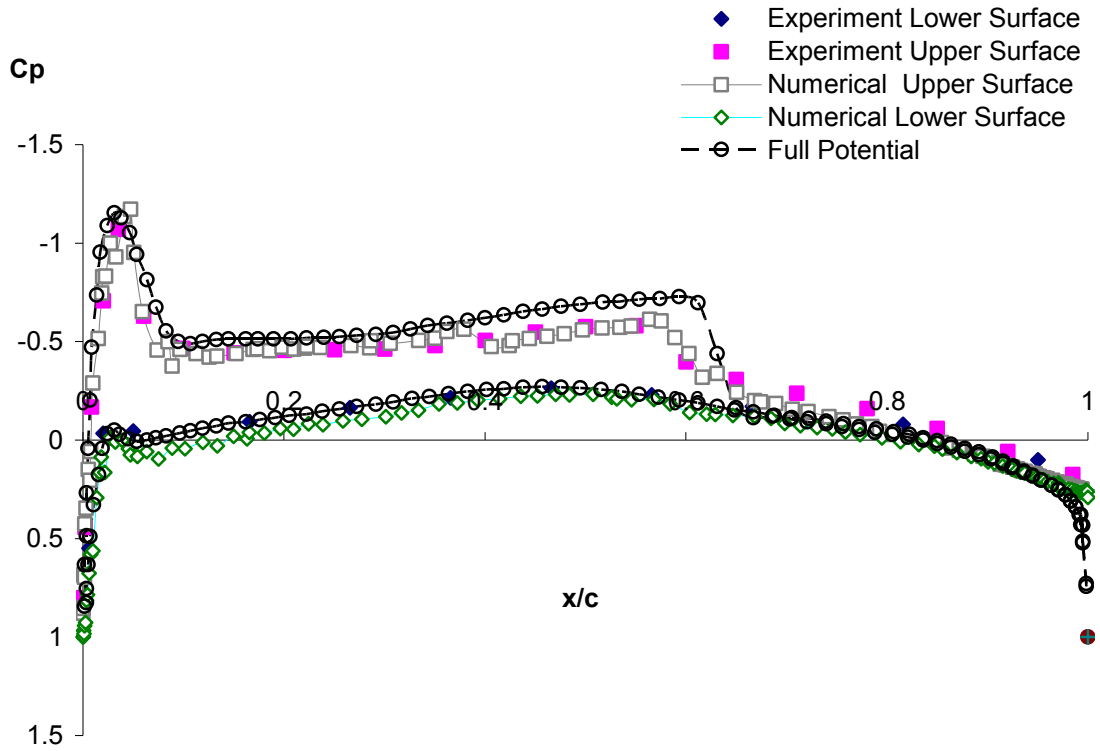


Figure 4-6. Pressure Distribution over Onera M6 wing at  $Re = 1.2 \times 10^7$ ,  $M = 0.84$ ,  $\eta = 0.2$  and  $\alpha = 3.06^\circ$ .

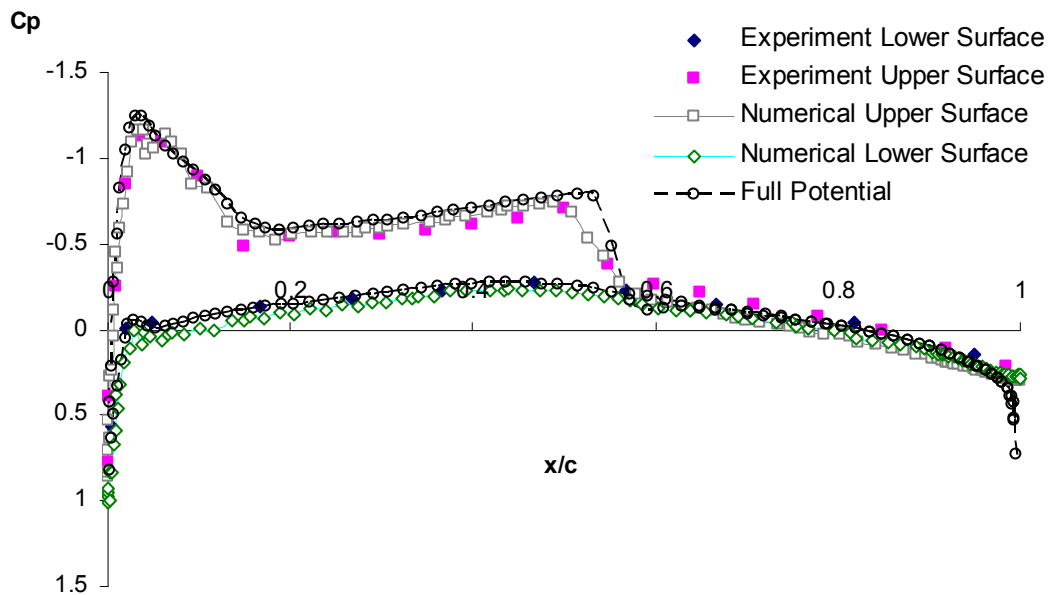


Figure 4-7. Experimental, numerical (STARCCM+ N-S  $k-\omega$  SST) and Full-Potential Pressure Distribution over Onera M6 wing at  $Re = 1.2 \times 10^7$ ,  $M = 0.84$ ,  $\eta = 0.44$  and  $\alpha = 3.06^\circ$ .

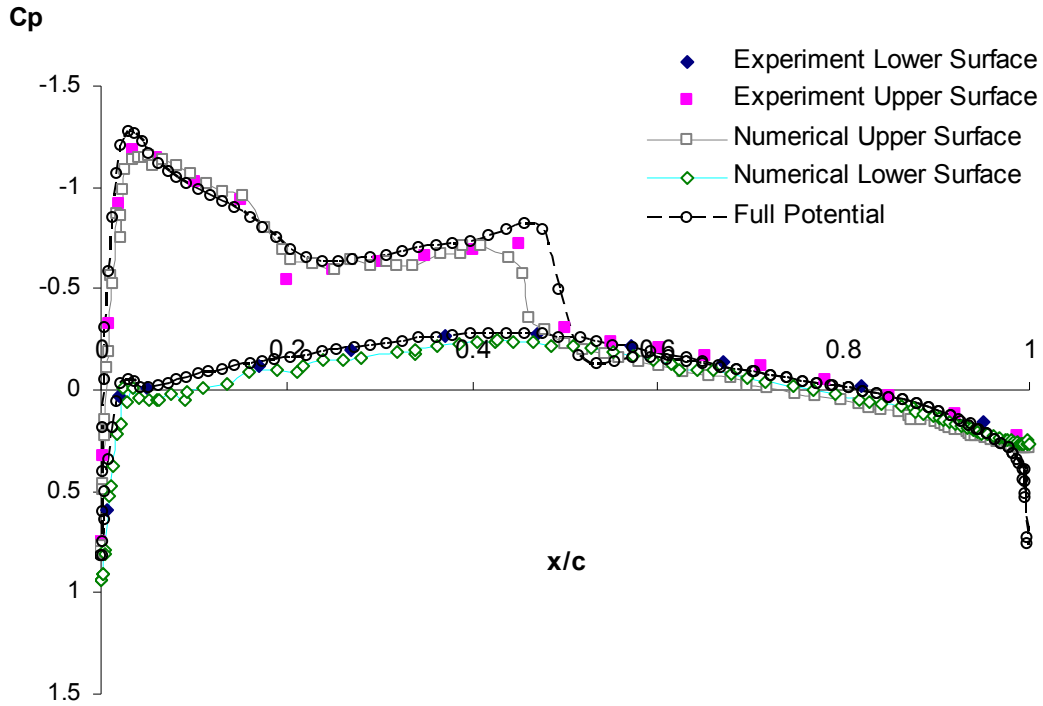


Figure 4-8. Experimental, numerical (STARCCM+ N-S  $k-\omega$  SST) and Full-Potential Pressure Distribution over Onera M6 wing at  $Re = 1.2 \times 10^7$ ,  $M = 0.84$ ,  $\eta = 0.65$  and  $\alpha = 3.06^\circ$

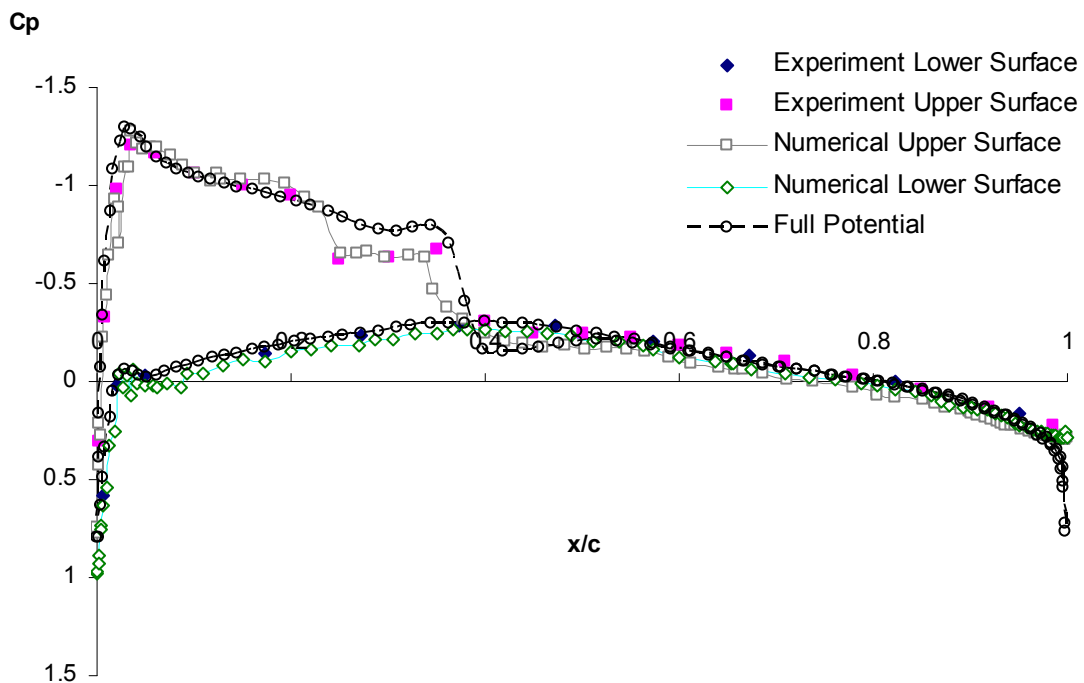


Figure 4-9. Experimental, numerical (STARCCM+ N-S  $k-\omega$  SST) and Full-Potential Pressure Distribution over Onera M6 wing at  $Re = 1.2 \times 10^7$ ,  $M = 0.84$ ,  $\eta = 0.8$  and  $\alpha = 3.06^\circ$

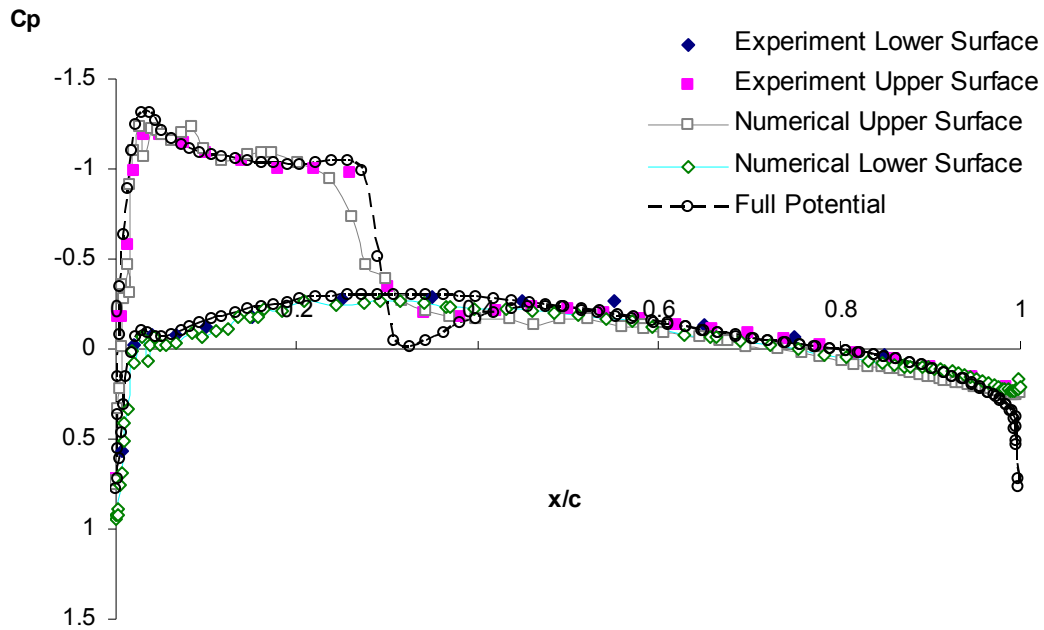


Figure 4-10. Experimental, numerical (STARCCM+ N-S  $k-\omega$  SST) and Full-Potential Pressure Distribution over Onera M6 wing at  $Re = 1.2 \times 10^7$ ,  $M = 0.84$ ,  $\eta = 0.9$  and  $\alpha = 3.06^\circ$ .

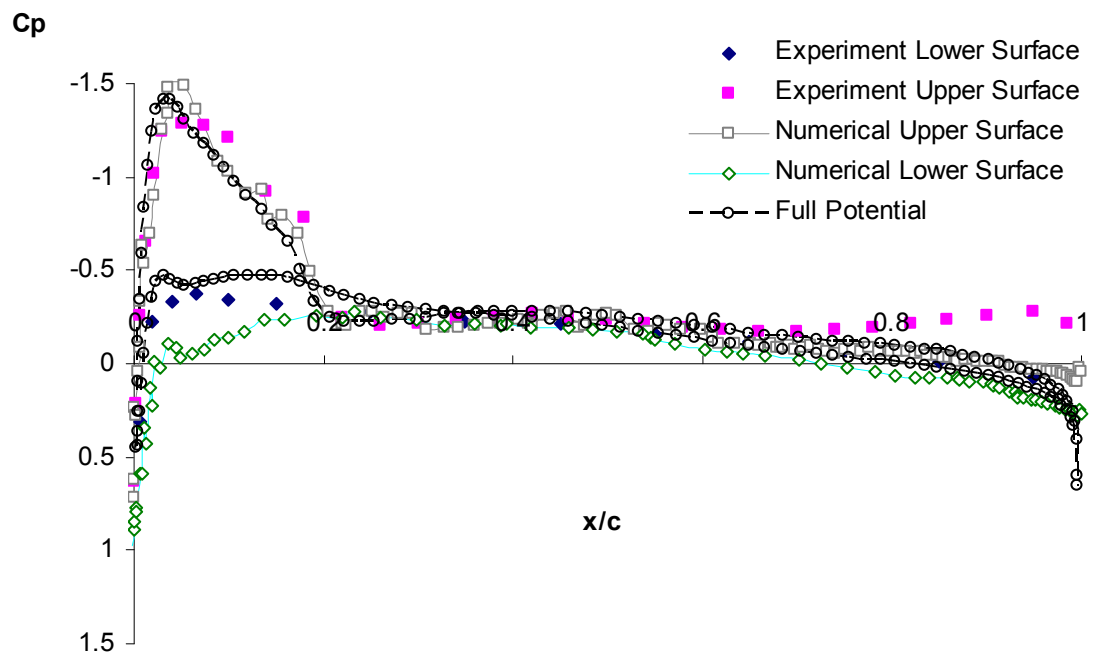


Figure 4-11. Experimental, numerical (STARCCM+ N-S  $k-\omega$  SST) and Full-Potential Pressure Distribution over Onera M6 wing at  $Re = 1.2 \times 10^7$ ,  $M = 0.84$ ,  $\eta = 0.99$  and  $\alpha = 3.06^\circ$ .

#### 4.4 Low-speed Results

Figures 4-12 to 4-14 present the upper surface pressure distribution for three spanwise locations from the low-speed calculations ( $M = 0.2$  and  $\alpha = 0^\circ$ ). The  $\eta = 0$ ,  $\eta = 0.483$  and  $\eta = 0.987$  spanwise locations were examined. Generally, one may conclude that the pressure coefficients predicted by the two studies are in excellent agreement in all three spanwise locations investigated, which furthermore, validated the use of the full-potential method, particularly for the low-speed studies. No further refinement of either numerical study was deemed necessary as the predictions provided the equivalent results for the flow parameters (surface pressure and flow structure) of interest to this study.

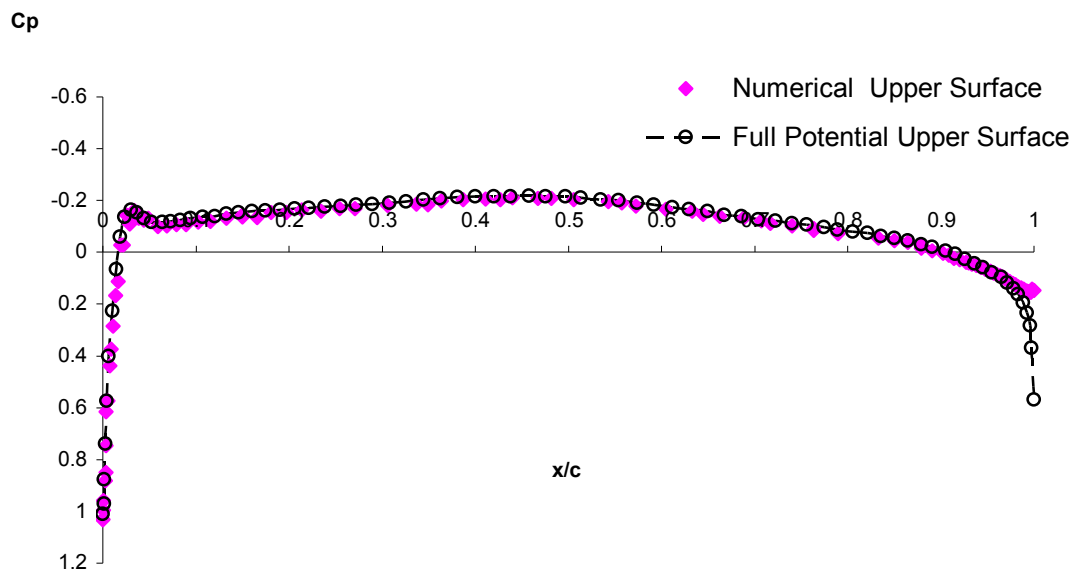


Figure 4-12. Numerical (STARCCM+ N-S  $k-\omega$  SST) and Full-Potential Pressure Distribution over upper-surface Onera M6 wing at  $Re = 2.3 \times 10^6$ ,  $M = 0.2$ ,  $\eta = 0$  and  $\alpha = 0^\circ$ .

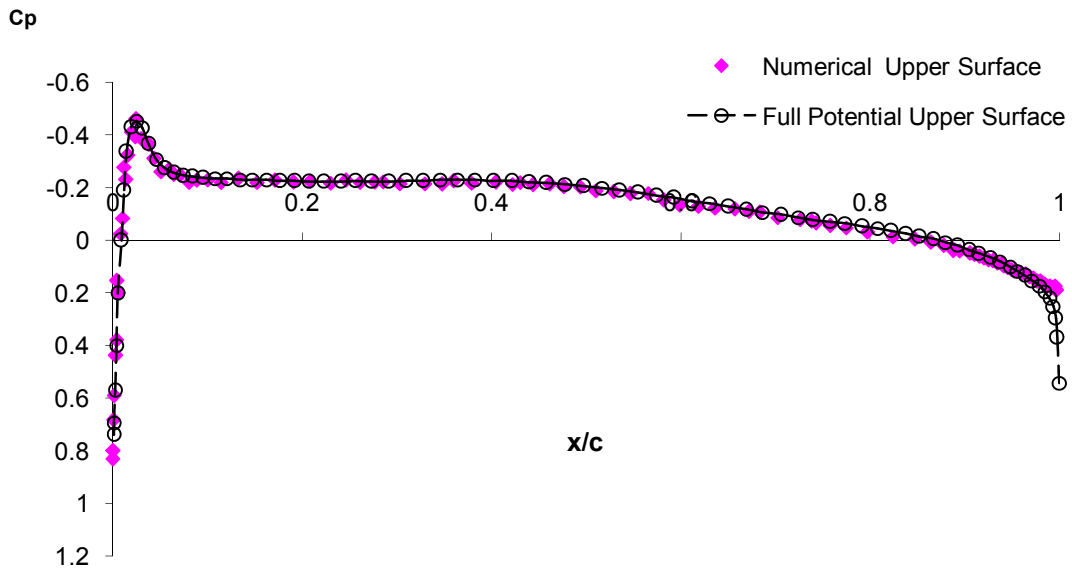


Figure 4-13. Numerical (STARCCM+ N-S  $k-\omega$  SST) and Full-Potential Pressure Distribution over upper-surface Onera M6 wing at  $Re = 2.3 \times 10^6$ ,  $M = 0.2$ ,  $\eta = 0.483$  and  $\alpha = 0^\circ$ .

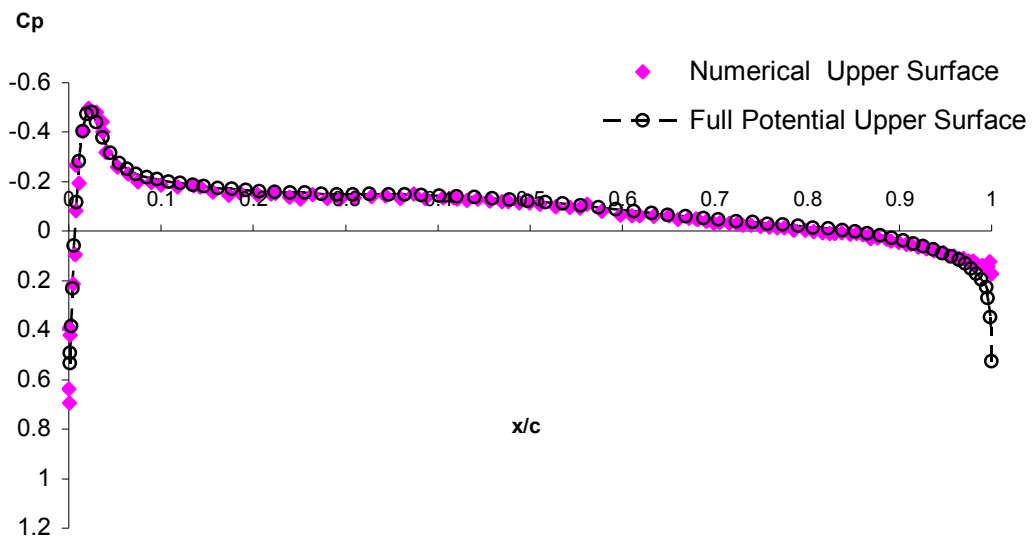


Figure 4-14. Numerical (STARCCM+ N-S  $k-\omega$  SST) and Full-Potential Pressure Distribution over upper-surface Onera M6 wing at  $Re = 2.3 \times 10^6$ ,  $M = 0.84$ ,  $\eta = 0.987$  and  $\alpha = 0^\circ$ .

This validation exercise was found to be generally in good agreement with the previous studies at the same flight conditions. Shock capturing capabilities of the

current numerical method were found to be somewhat better or similar in comparison with others, the lower pressure coefficient were in the other hand under-predicted by the current study when compared to experimental and previous research data. A divergence from the experimental data near the trailing edge at  $\eta = 0.99$  was observed in the previous studies as well (Chalasani et al 2005).

The conclusion of this validation exercise and the referred wok on both STARCCM+ and FP codes is that both studies should be sufficiently accurate to predict the flow-fields and trends of interest in the present study.

## 5. Experimental Arrangements

In order to validate the computational fluid dynamics design process for the Jetpod wing configuration, a wing model was designed to obtain experimental data at various low speed Reynolds Numbers. An advantage of wind tunnel testing is that conditions can be held constant and varied incrementally in order to isolate different effects, which has been of great use for this investigation.

Initial tests were carried out on an isolated wing, to simulate low speed ( $M \sim 0.1$ ) cruise conditions. Preliminary investigations of the wing performance at zero yaw were carried out, which were then followed by a succession of tests under different yaw conditions. The second set of tests was a series of ground effect simulation investigations, carried out to examine the aerodynamic behaviour of the wing in ground effect. All the ground tests were carried out at zero yaw conditions and for various ground heights, details of which will follow later in this section. For all the tests carried out, force and moment measurements were taken, followed by near wake flow investigations and laser smoke flow visualisations, where appropriate.

The experimental programme was conducted at City University's Handley Page laboratory using the T2 and T3 wind tunnels. This was influenced by the limitations of the balance in T3 and simultaneously the ground instalment incapability in T2 wind tunnel. Hence, the use of two different tunnels necessitated the verification of tunnel-to-tunnel repeatability.

### 5.1 The T2 Wind Tunnel

The T2 tunnel is a closed-circuit return type wind tunnel, with a rectangular working section of maximum width 81cm; height 112cm and length 168cm with corner fillets (see *Figure 5-1*). The tunnel is fitted with a six-component balance system externally



## 5.2 The T3 Wind Tunnel

The T3 tunnel is also a low speed, closed-circuit return type wind tunnel, with a regular octagonal working section of maximum width of 115cm; height 150cm and length 150cm, (see *Figure 5-2*). The tunnel is fitted with only a three-component balance system externally positioned above the working section. The T3 wind tunnel employs an inverter that is capable of continuous variation of velocity in the range of approximately 3 m/s up to 45 m/s. As with T2, various velocities were tested, and a final choice on 30 m/s as the most convenient velocity has been made. This decision was due to unsteadiness in form of oscillations exhibited by the model. This was present at the higher angles-of-attack range for speed of 30 m/s and above. Therefore, to keep interference at minimum all ground effect tests were run at 30m/s. The unsteadiness might be described as a high-frequency, low-amplitude oscillation, T3 only has a pitch mechanism. Wind speed is measured by a Furness FCO16 digital water manometer, which indicates the difference between the tunnel working section and contraction pressures. After passing the contraction section the free-stream longitudinal turbulence intensity in the empty working section is known to be around 0.5%. Previous tests in T3 have shown the velocity distribution to be fairly uniform with the variation across the majority of the working section being confined to less than 1.5%

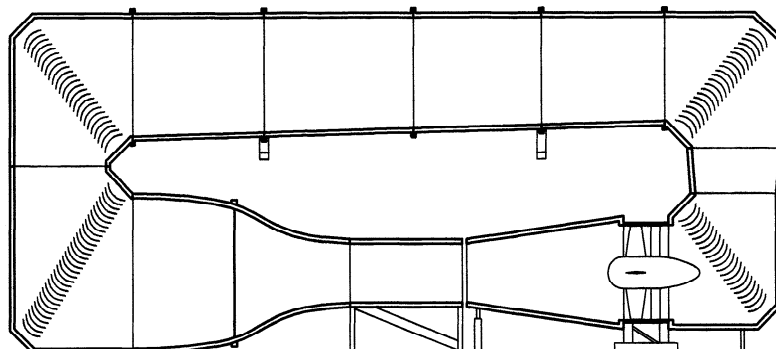


Figure 5-2:T3 Wind Tunnel

### 5.3 Wing Model

Due to the complexity of the geometry of the Jetpod, only the wing was tested experimentally. A full-wing model was built in the Centre for Aeronautics workshop, the size of which was chosen to be based on a maximum 60cm full span. This decision was influenced by the size of the tunnel working sections, and the desire to keep blockage low whilst providing the greatest Reynolds Number possible. The 0.05 scale model of the wing (shown in Figure 5-3) was constructed of wood, and was manufactured to match the specifications detailed in section 1.1.4 to within  $\pm 2\text{mm}$  for span and  $\pm 0.3\text{mm}$  for chord and thickness .



Figure 5-3: Wooden Wing Model Utilized in T2 and T3 Wind Tunnels

A downstream view of the model mounted in T2 is shown in *Figure 5-4*. Two fixed vertical struts, which support the major part of the model weight, positioned the model longitudinally in the test section, with the wing root chord consistent with the tunnel centreline. Consequently, the model was located approximately in the middle of the usable portion of the test section. Strut support of a wing model configuration in the wind tunnel becomes a challenging endeavour since

it is desirable to avoid attaching the struts through a major lifting surface portion of the model; hence the wing was mounted inversely from the pressure side of the wing. The positioning of the struts on the model was based on literature suggestion of where the least interference might take place, as well as the width positioning facility of the balance system and the thickness of the wing to support a pivot attachment point. As recommended by Barlow et al the struts were positioned at 40 % chord of the central section of the wing (Barlow et al. 1999).

Due to the limitations of the wind tunnel arrangement dual struts which would account for the interference drag were unable to be used. Hence, the interference drag was unable to be calculated and therefore subtracted from the total drag.

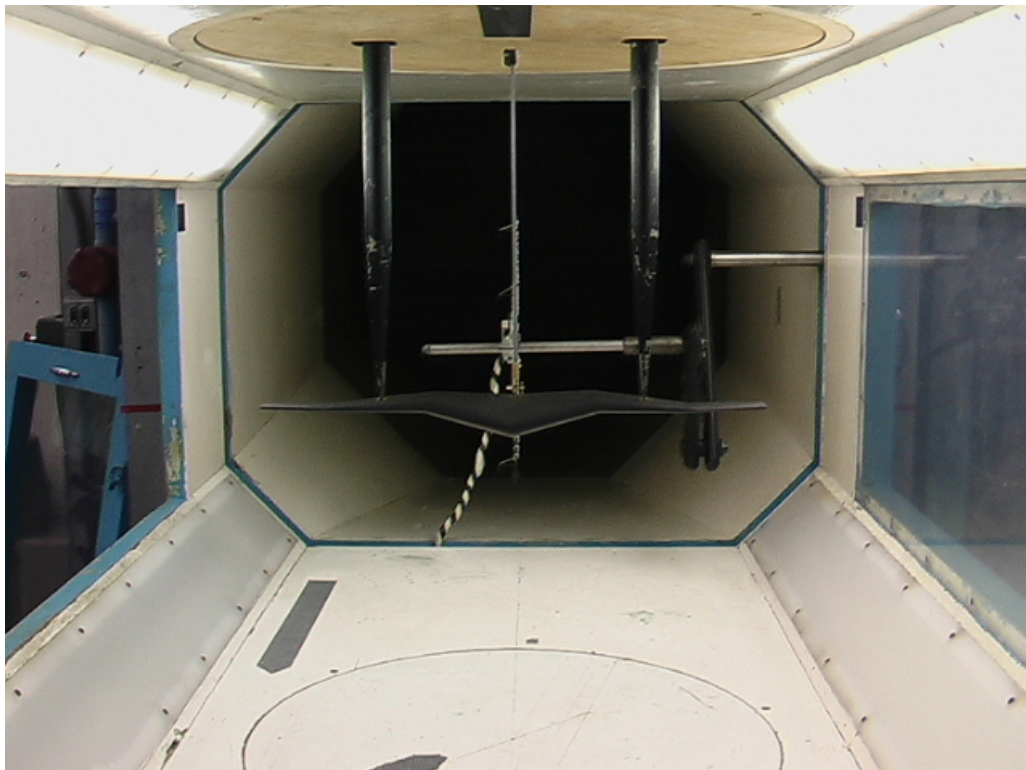


Figure 5-4: Downstream View of the Model Mounted in T2

To ensure that flow distortion from the struts was as small as possible, the T2 struts were fitted with streamlined shrouds depicted in *Figure 5-5*.

Variation in the model angle of attack was made possible by use of a tail arm and pitch rod, which connected to the pitch arm of the balance. This approach enabled varying the angle of attack during the run.



Figure 5-5: Shielded Strut in T2 Wind Tunnel

For the T3 tests a single-strut mounting system was employed. The strut was positioned at the centre of gravity on the root chord of the model and the model was inserted in the test section in the “right-way-up” position. The decision to employ a single-strut system was influenced by the need to change the elevation of the wing model relative to the ground board. No shielding methods were employed for the T3 tests, as the strut had been designed to have an aerofoil-like shape.

Due to the nature of the T3 tests the balance pitch mechanism could not be employed. Therefore, the angle of attack had to be varied manually during the run, as the wing was being fixed in position by a hinge and a locking bolt. A systematic approach to changing the angle of attack was adopted before each run, where the wing angle of attack was initially set at  $0^\circ$ , as measured by a FISCO Solatronic Inclinator (Model EN17) which has an accuracy of  $\pm 0.5^\circ$ .

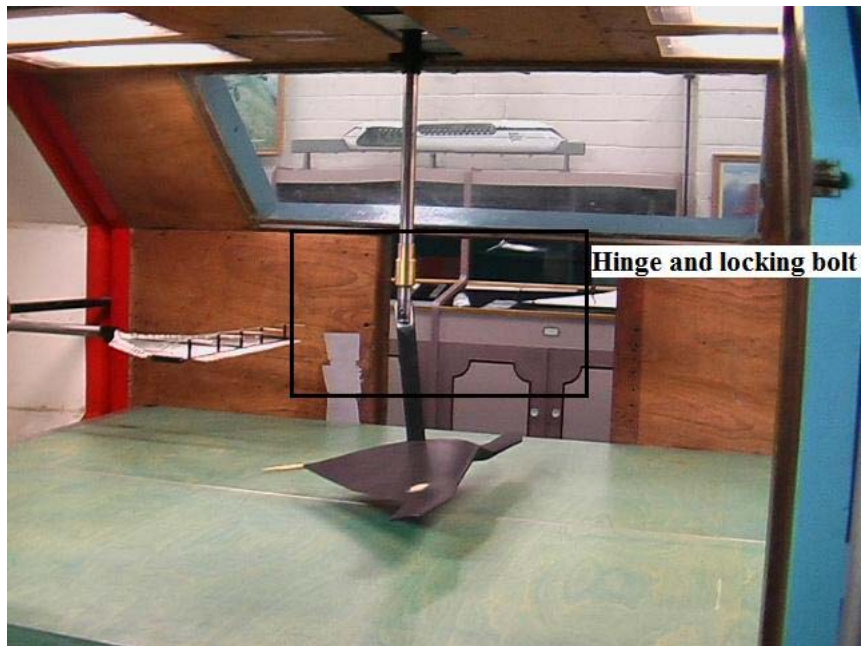


Figure 5-6: T3 Strut System (wing model at  $\alpha = 6^\circ$ )

#### 5.4 Ground Board

Reviewing the literature revealed that the use of a stationary ground board has proven to be satisfactory and considerably less complex than the use of the more physically rigorous moving-belt method; particularly for cases where low ground heights are avoided (Lockwood and Phillips 1968; Thomas et al 1979). Hence, in order to avoid introducing complex systems a decision to use a fixed ground board was made.

All the ground effect tests were carried out in T3. The selection for the boards was a straight-walled ground plane of constant thickness. The board was 1385 mm long, spanning the width of the tunnel at 1146 mm; with a thickness 225 mm (see Figure 5-7). The flat board has an elliptical leading edge with a ratio of 3:1. Previous measurements have shown that the T3 tunnel has a straight flow with little up or side flow angularity. The challenge was to fix the ground plane in a position which was insensitive to any flow angularity induced by the tunnel set up.

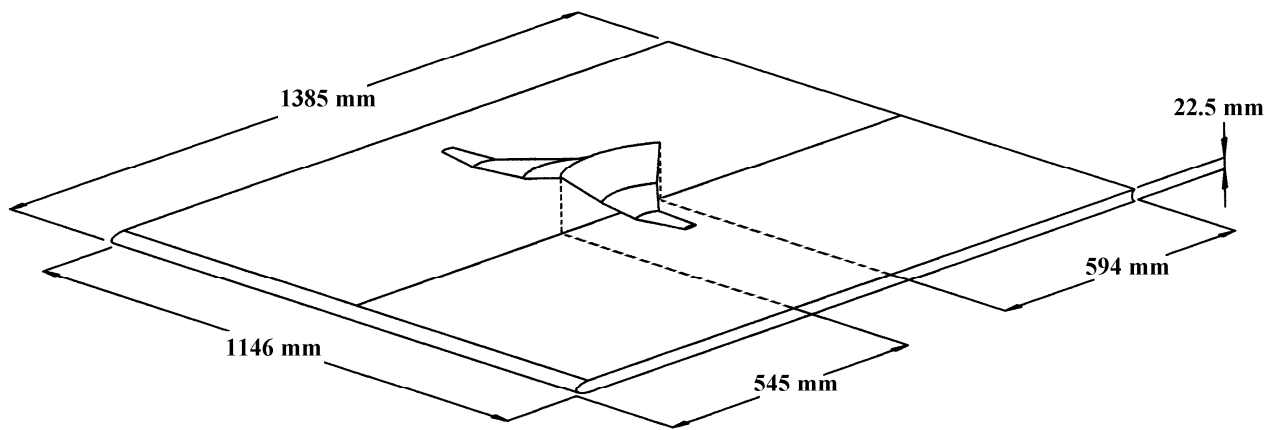


Figure 5-7: Schematic of the Wing Model Set-up with Respect to the Ground Board

The board was fixed and secured to the two side walls of the tunnel at a distance of 223 mm from the tunnel floor. A downstream view of the test section showing the test set-up with the ground plane installed is presented in Figure 5-8.

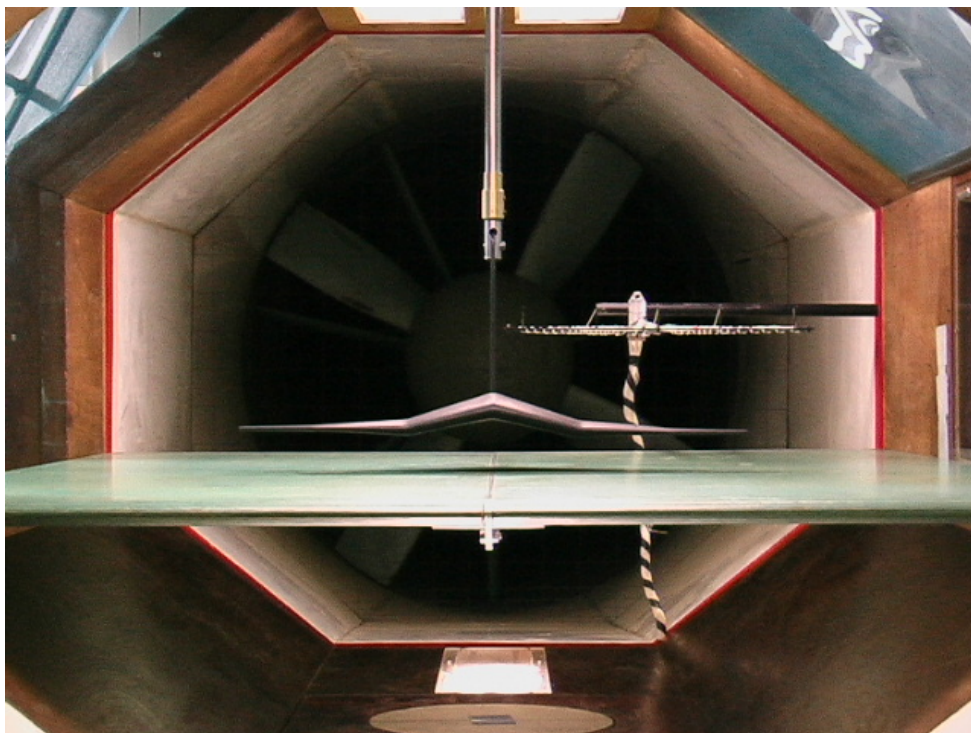


Figure 5-8: Downstream View of the Model and Ground Board Installed in T3

Prior to testing an effort was undertaken to characterise the flow in the empty tunnel environment. As part of this flow characterisation a rake system was employed to measure the boundary layer of the ground plate at both the location where the model was to be mounted (initially model mounting centre location was located approximately half way between the tunnel floor and the ceiling) and downstream of the model where near wake investigation would take place.

At this flow condition, the measured velocity profile indicated that the edge of the boundary layer i.e  $u/U \sim 0.99$  occurs at a height of approximately 15 mm from the ground board.

During the tests a pitot static tube was used to measure the free-stream flow velocity above the ground board to ensure that this matched the free-stream value indicated by the tunnel static pressure measurements. The free-stream tunnel static measurement facility is located further from the model and hence the ground board, therefore it was considered necessary to use a pitot static tube at the working section to measure the static pressure measurement should they be any different which would then give in accurate estimation of the tunnel velocity and aerodynamic forces. These values were then used for the aerodynamic force calculations, although in general very small difference between the two measurement facilities was observed.

## **5.5 Data Measurement and Analysis**

### **5.5.1 T2 Testing**

The experiments were conducted at different Reynolds Numbers, based on the mean chord and free-stream conditions. Initially tests in T2 were carried out at four different speeds to assess the Reynolds Number effects, if any, on the lift and drag performance of the wing. The chosen test speed at which evaluation experiments were carried out in the T2 tunnel was 35.8 m/s. The maximum achievable Re number was  $3.6 \times 10^5$ .

Testing was carried out at a range of angles of attack  $-10^\circ < \alpha < 30^\circ$ , with steps of approximately  $\Delta\alpha = 2^\circ$ , for zero yaw conditions. A similar range of the angles of

attack was retained for the yaw test, where the yaw angle was varied in the range -  $2^\circ < \Psi < 15^\circ$ .

The validity of the experimental findings is based upon the ability to minimize variances and errors associated with the method of data measurement and collection. To minimize the effects of hysteresis, each test case was started with the wing positioned at zero angle of attack and later, when the uniform speed was established, the wing was then set to the relevant angle of attack for the measurements to be taken. The angle of attack was set to increase and decrease in the same manner, and a set of readings were taken.

To avoid hysteresis in the pitch channel of the balance, each test was carried out using exactly the same method. Firstly, the wing was pitched to -10 degrees and then back up to zero, where the tunnel was started and the angles were then changed by increasing them to the maximum value, bringing them back to -10 and then back to zero again. This method was repeated for all tests. For the purposes of reliability, a 10 second time period was used for each test case, during which all the relevant readings would take place with data sampled at 10Hz. Average readings were then calculated and transferred to the data file. Lift, drag and moment measurements were taken from the output values of the balance system.

The presence of the struts meant that a few quantities had to be considered with regards to the balance output. The first is the direct aerodynamic force on the exposed strut; the second is the effect of the strut's presence on the airflow of the wing and similarly, vice versa. Accordingly, experimental testing of the strut drag effect was carried out for all relevant wind tunnel speeds used for the Reynolds Number effect analysis. The strut drag data can then be subtracted from the total drag values recorded by the balance during testing.

### 5.5.2 T3 Testing

Initially, tests in T3 were run to assess the tunnel-to-tunnel repeatability, no significant differences were noted in the lift coefficient between the two tunnels, small differences are noted in the drag coefficient data at the lower angles of attack (see Figures 5-8 and 5-9).

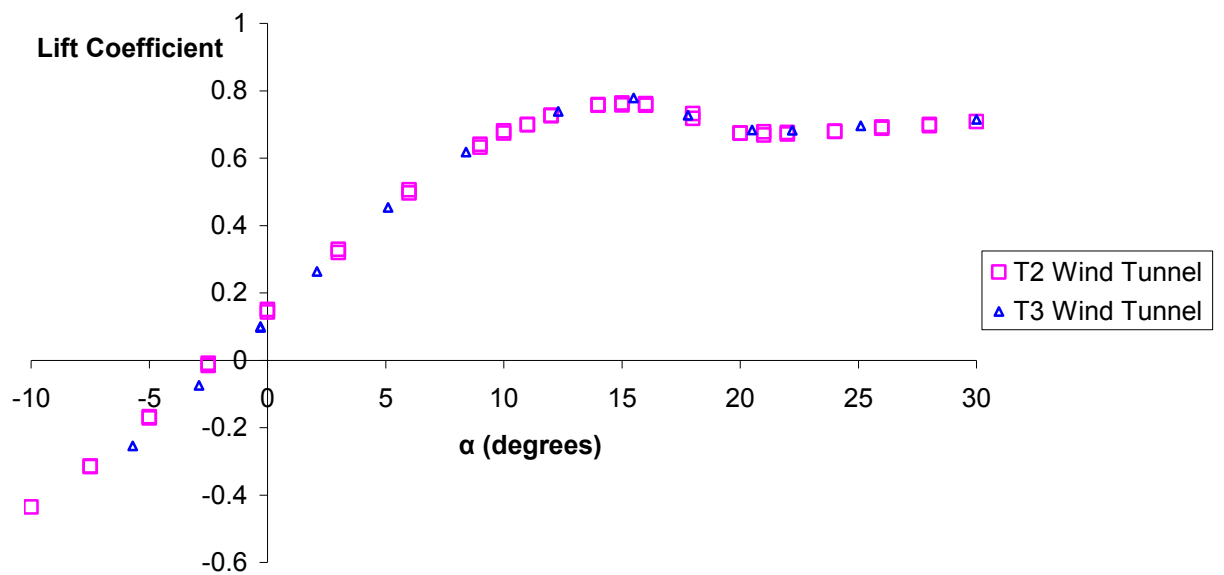


Figure 5-9. Tunnel-to-tunnel repeatability test at  $V=35\text{m/s}$  (Lift Coefficient)

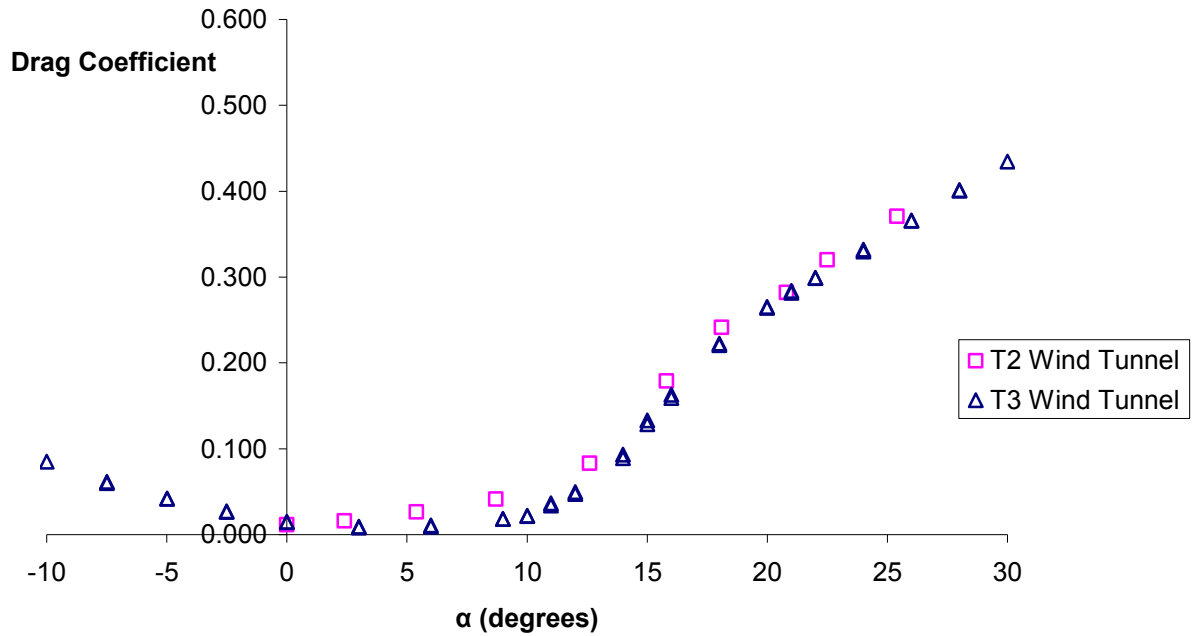


Figure 5-10. Tunnel-to-tunnel repeatability test at  $V=35\text{m/s}$  (Drag Coefficient)

Reference dynamic pressures in the T2 wind tunnel were measured in the pre-selected location in the test section with isolated transport model in place, but before the ground plane installation. These measurements dynamic pressures provided target values for setting tunnel conditions after the ground plane was installed. Similarly with T2 testing, Reynolds Number effects were investigated initially in testing stage. The chosen test speed at which experiments were carried out in the T3 tunnel was 30 m/s. The maximum achievable Re number was  $3.1 \times 10^5$ . The ground board was then installed for the second set of tests and heights above the ground of 35 to 270mm were tested, equivalent to  $0.035 < h/b < 0.55$ .

Angle of attack was set at  $0^\circ$  and then during the tests was manually changed, covering the range of  $0^\circ < \alpha < 30^\circ$ , with steps of approximately  $\Delta\alpha = 2^\circ$ . The procedure was repeated for all tests, a 15 second time period was used for each test case, during which all lift, drag and moment measurements were taken with data sampled at 10Hz. The time period chosen for these tests was chosen to provide a more accurate time average.

It is important to note that the greater ground heights in the wind tunnel were limited by the support system limitations and that higher angles of attack could not be entirely covered for the small ground heights as the pitch arm was touching the ground floor. To avoid discrepancies in the results, due to the nature of the angle of attack change assessments, additional run-to-run repeatability was examined for all heights. Strut drag was also assessed for each of the speeds used in the tests. In addition, as the angle of attack was changed, the drag of the isolated struts and support structure attached to the model (angle of which changed with angle of attack see Figure 5-6) was measured for all the angles employed in the testing procedure. Similarly, as with the previous tests, the strut drag data was then be used to subtract from the total drag values obtained, the lift force increment being found to be negligible.

### 5.5.3 Wake Measurement

In order to validate some of the near wake phenomena noticed in the numerical analysis, a set of tests were carried out to examine the near wake of the model in both wind tunnel tests.

Pressures were measured with a 40 tube pitot-static rake depicted in Figure 5-11. The rake consists of forty pitot tubes and five static tubes. Static tubes are positioned parallel to the pitot rake except offset by 25 mm, to avoid interference effects on the static pressures. A schematic view of the rake is shown in Figure 5-12.

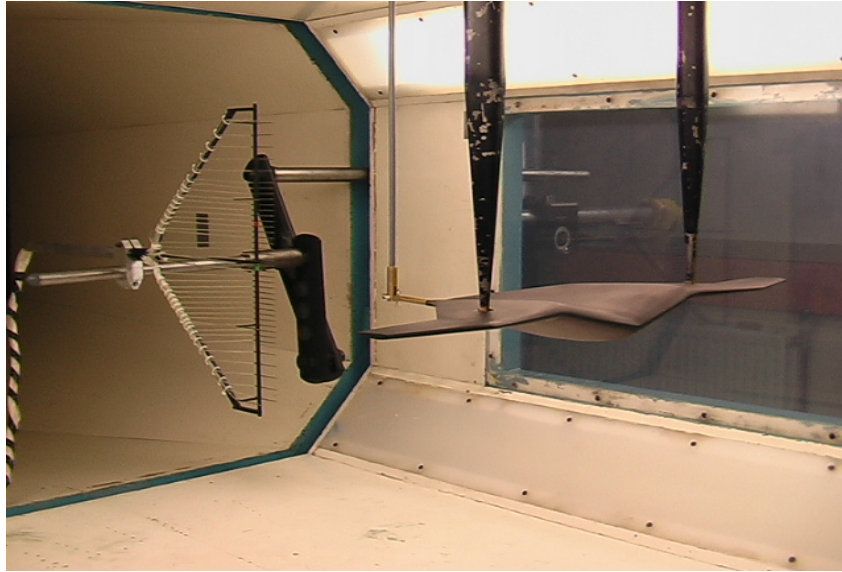


Figure 5-11: Wake Rake

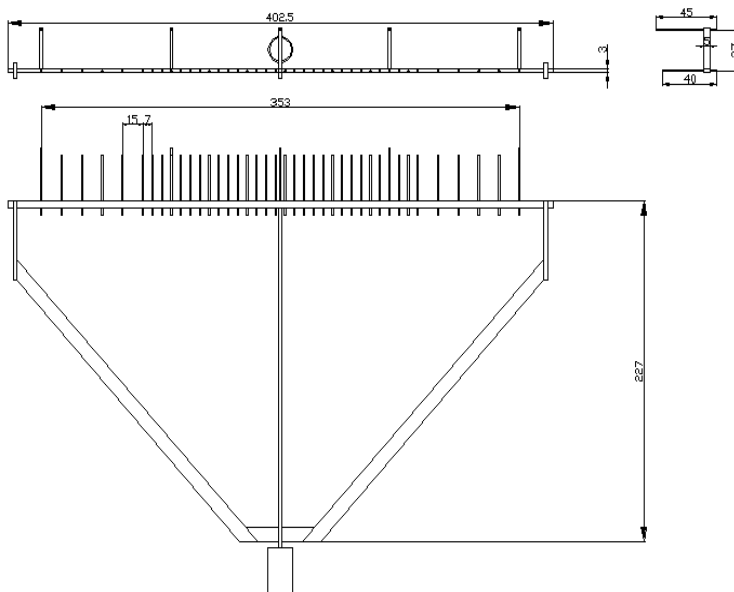


Figure 5-12: Schematic View of the Wake Rake Utilized in T2 and T3 Tests

Measurements of the wake pressures were taken via an ESP pressure scanner rated at  $\pm 2.5$  psig connected to a Chell CANdaq data acquisition system. The scanner employs a one port per transducer system and together with the pressure system provides an accuracy of  $\pm 0.06\%$  full-scale deflection.

Each tube on the rake was connected to one of the scanner's 64 ports, the output of which was then transmitted via Ethernet to a computer running the data acquisition software that controlled how the data was logged. These data were taken for each of the pitot and static tubes, to obtain the total and static pressures, respectively. This method was used for both T2 and T3 testing.

For the T2 testing the pitot-static rake was positioned vertically as seen in Figure 5-13. Measurements were taken with the rake initially positioned in the plane of  $z/b = 0.5$ . The rake was then moved to different spanwise positions using the T2 manual traverse system. Increments of  $0.015 z/0.5 b$  were used to cover positions for the port side of the wing model.

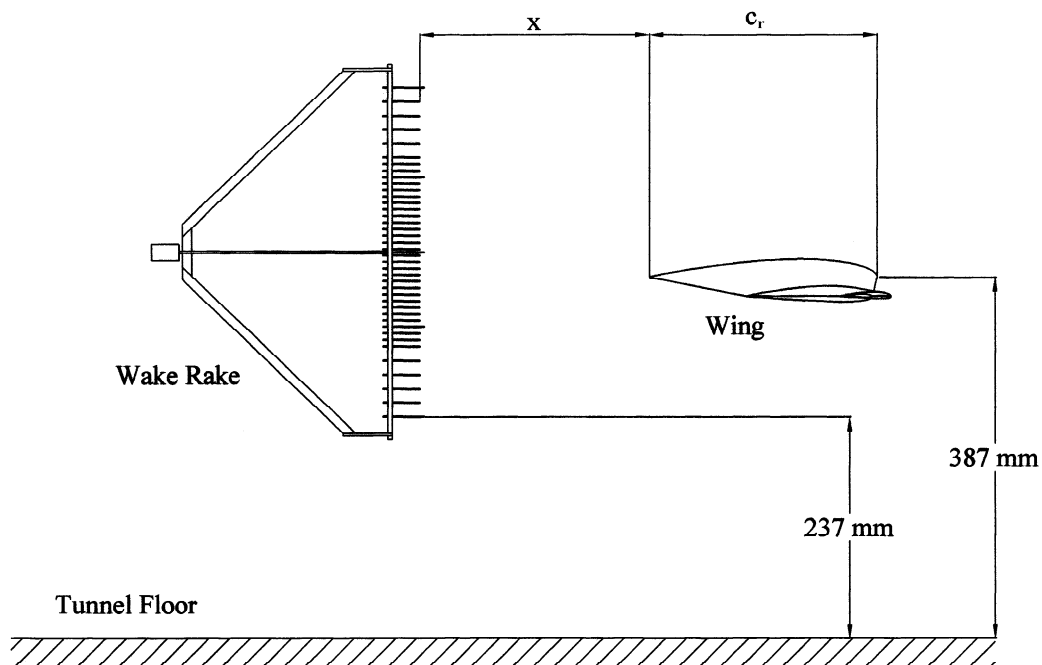


Figure 5-13: Wake Rake Positioning for the T2 tests

For the T3 testing the rake was positioned horizontally as illustrated in Figure 5-14. This was done in order to capture the smallest scale changes in the boundary layer region of the ground board. Only port side measurements were considered, with the rake initially being positioned 5mm from the ground board. The rake was then moved different lateral ( $y$ ) positions, for all the tests considered.

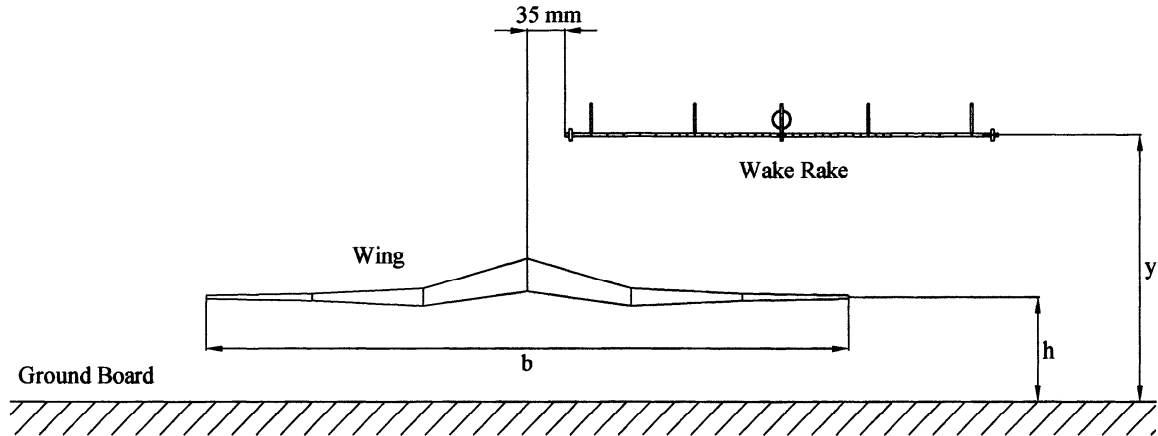


Figure 5-14: Wake Rake Positioning for the T3 Tests

Increments of  $y/0.5b = 0.015$  distances were employed for all other regions together with  $y/0.5b = 0.025$  for the immediate ground board region.

Rake pressure data were sampled at a rate of 100 Hz over a 10 second period. As the shape of the wing changes significantly in the span-wise direction, the momentum deficit in the wake was taken at three different downstream percentage maximum chord lengths ( $x/c = 1, 1.5,$  and  $2$ ) as measured from the root trailing edge ( $x$  values from Figure 5-13), for both sets of testing.

#### 5.5.4 Force and Moment Processing

The lift, drag and pitching moment measurements taken for each test were converted into appropriate non-dimensional coefficients to enable comparison between numerical and experimental results. Lift, drag and moment coefficients were computed from the following formulae

$$C_L = \frac{L}{\frac{1}{2} \rho V^2 S} \quad (5.1)$$

$$C_M = \frac{M_{w-on} - M_{w-off}}{\frac{1}{2} \rho V^2 S \bar{c}} \quad (5.2)$$

And

$$C_D = \frac{D}{\frac{1}{2}\rho V^2 S} \quad (5.3)$$

The drag obtained from the test denotes the total drag of the wing, struts and any interference drag.

$$C_{Dtotal} = C_{Dwing} + C_{Dsting} + C_{Dws} + C_{Dsw} \quad (5.4)$$

Where  $C_{Dws}$  is the interference drag of the wing on the strut is flow field and  $C_{Dsw}$  is the strut interference on the wing flow field.

The clean drag coefficient was then obtained by subtracting the strut drag reading for the appropriate test configuration. These were taken only with the struts in the tunnel. The interference drag was not included in these computations as the suggested procedure to obtain this information was unable to be employed. The interference drag was unable to be obtained due to the wing tunnel arrangement. Limitations on the arrangement of dual struts restricted the interference drag calculations. Nevertheless, interference drag is considered to be very small with regards to the total drag obtained in the test (Barlow et al. 1999).

### 5.5.5 Wake Analysis

For comparison of the results, total pressure coefficients in the near wake were calculated. As each tube provides a reading of the pressure difference

$H_1 - p_{atmospheric}$ , the total pressure coefficient can then be calculated by using the following formula:

$$\frac{H_1 - p_\infty}{H_\infty - p_\infty} = Cp_{total} \quad (5.5)$$

where  $H_l$  is the local total pressure,  $H_\infty$  is the free-stream total pressure and  $p_\infty$  the free-stream static pressure. The coefficients are then computed in the same manner for every span wise and downstream position.

## **5.6 Visualization**

Flow visualization is an important tool in fluid dynamics research, as it aids the understanding of the on or off-surface flow activities of the models tested. There are various visualizations techniques available, and for these tests two methods of flow visualisation were carried out. All the visualisation tests were conducted in T2 wind tunnel.

### **5.6.1 Laser Smoke visualisation**

Smoke can be used to show and track strong features such as tip or leading-edge vortices. The most widely used method for producing smoke at larger wind tunnels today is the wand system with polyethylene glycol. An Aerotech ATE Limited smoke generator was used to create smoke to use in conjunction with a laser sheet to visualise flow. The fluid pumped by the generator, a mix of 9-1 water and glycol, is vaporised at the tip of the probe by an electrical heating component. The smoke probe was located at various span- positions and at approximately  $\frac{1}{4} c$  distances upstream of the wing model leading edge.

## **5.7 Wind Tunnel Boundary Corrections**

The results taken in the wind tunnel are expected to differ from free air, due to the presence of the boundaries. The presence of wind tunnel walls and their boundary layer will affect the streamline pattern of the model tested. Hence, these effects have to be included in the results so as to attain accurate results free air force and moment data.

The interference on the measured forces and moments in wind tunnel testing can be said to arise from ‘solid blockage’ and ‘wake blockage’. Usually it is assumed that these two blockage components are independent from each other. Another important modification that is applied to the measurements obtained for wing model testing is the correction for the angle of attack, which is discussed below.

### 5.7.1 Solid Blockage

In a closed wind tunnel solid blockage refers to a decrease of the effective working section area due to the presence of the model, hence leading to an increase in the dynamic pressure and the force and moments at a given angle of attack. Further details on the matter can be found in Pope and Barlow et al (Pope 1952; Barlow et al. 1999).

Solid blockage can be determined by representing the wing model with an infinite array of double images extending above and below the model in the tunnel. The specific correction factor as given by Pope is:

$$\varepsilon_s = \frac{\Delta V_s}{V} = \frac{K_1 \tau_1 (\text{wing volume})}{C^{3/2}} \quad (5.6)$$

where  $\tau_1$  is a factor that depends on the tunnel working section shape and model span to the tunnel ratio,  $K$  is a body shape factor, wing model in this case and  $C$  is the frontal cross-sectional area of the tunnel.

As the angle of attack of the model increase, it should be incorporated in the correction for the solid blockage. Batchelor notes that the increase in the solid blockage is proportional to  $\alpha^2$  and is defined by the following equation (Batchelor 1964):

$$\varepsilon_{s\alpha} = \varepsilon_s \left( 1 + 1.1 \frac{c}{h} \alpha^2 \right) \quad (5.7)$$

Where  $c$  is the chord of and  $h$  is the tunnel height.

### 5.7.2 Wake Blockage

As any wing model tested will have a trailing wake, according to continuity the velocity in the wake will be lower than the velocity in the closed tunnel. This will then induce a velocity increment at the model giving rise to wake blockage.

The effect of wake blockage can be calculated by using Prandtl's approach to represent the wake by an equivalent source which is matched by a sink further downstream in the tunnel. This image system for the three-dimensional case, consists of a double infinite source-sink system spaced a tunnel height and a tunnel width apart.

Given the speeds of the test the effect of the compressibility in the wake blockage can be ignored. The correction factor for wake blockage may then be computed from:

$$\varepsilon_w = \frac{V_w}{V} = \frac{1}{4} \frac{S}{hB} C_D \quad (5.8)$$

where  $h$  has its predefined meaning,  $B$  is the width of the working section, and  $S$  is the reference area, wing model in this case.

The increase in drag then due to the wake blockage effects is defined as:

$$\Delta C_{wb} = \frac{K_1 \tau_1 (\text{wing volume})}{C^{3/2}} C_{D0} \quad (5.9)$$

where  $\tau_1$ ,  $K_1$  and  $C$  have their predefined meanings and  $C_{D0}$  is the uncorrected zero-lift drag measurement.

The total correction factor  $\varepsilon$ , is now given as the sum of the wake and solid blockage effects:

$$\varepsilon = \varepsilon_s + \varepsilon_w \quad (5.10)$$

The corrected velocity is obtained from:

$$V_\infty = V(1 + \varepsilon) \quad (5.11)$$

Where  $V_\infty$  is the actual free-stream velocity and  $V$  is the measured velocity from the tests.

The correction factors then need to be applied to the measured data obtained from the balance system for the T2 and T2 tests.

The corrected lift, drag and moment coefficients are then obtained from

$$C_{L\infty} = \frac{C_L}{(1 + \varepsilon)^2} \quad (5.12)$$

$$C_{D\infty} = \frac{C_D}{(1 + \varepsilon)^2} \quad (5.13)$$

And

$$C_{M\infty} = \frac{C_M}{(1 + \varepsilon)^2} \quad (5.14)$$

where  $C_L$ ,  $C_D$  and  $C_M$  are the measured lift drag and pitching moment coefficients whilst  $C_{L\infty}$ ,  $C_{D\infty}$  and  $C_{M\infty}$  are the corrected values.

Corrections also need to be applied to the Reynolds Number as follows:

$$Re_\infty = Re(1 + \varepsilon) \quad (5.15)$$

Pressure coefficient corrections were also applied by using the following equation:

$$C_{p\infty} = \frac{C_p - 1 + (1 + \varepsilon)^2}{(1 + \varepsilon)^2} \quad (5.16)$$

### 5.7.3 Corrections for the Angle of Attack

The presence of the wind tunnel walls is also expected to influence the effective angle of attack during testing. Tunnel walls induce an up-wash which explains that corrections need to be applied to the measured angle of attack. To obtain the

correction values for the angle of attack, the wing model as Pope suggests, is assumed to be represented by a single vortex at its  $\frac{1}{4}$  chord point, and Pope suggests that the boundary induced up-wash angle varies almost linearly along the chord. For a three-dimensional body (i.e. the model tested) the variations of the boundary induced up-wash are found to be linear in the increase of the angle of attack, hence the effect may be treated as the loading on a circular arc aerofoil.

If the effect of camber is neglected the amount of correction needed for the angle of attack, is given by:

$$\Delta\alpha_{total} = \frac{1}{8\pi} \frac{c^2}{h^2 + (\frac{c}{4})^2} c_l \quad (5.17)$$

Where  $c_l$  is the sectional lift coefficient and c and h have their predefined meanings

Or by using Goldstein's formula as (Pope 1952):

$$\Delta\alpha = C_L \left[ \frac{\pi}{96} \left(\frac{c}{h}\right)^2 - \frac{41\pi^3}{92160} \left(\frac{c}{h}\right)^2 \right] \quad (5.18)$$

where  $C_L$  is the measured lift coefficient.

All the measured data from both wind tunnel tests were subsequently corrected for blockage effects.

Blockage factors obtained for the current model in T2 were  $\epsilon_s=0.0044$  and  $\epsilon_w=0.0007$  giving a total  $\epsilon = 0.0051$ . and for T3 were  $\epsilon_s=0.0048$  and  $\epsilon_w=0.0008$  giving a total  $\epsilon = 0.0056$

## 6. Low-Speed Experimental and Numerical Wind Tunnel Test Results

The following section outlines the experimental results obtained on the scale model of the isolated wing, tested at various low speed Reynolds Numbers. In addition, numerical analyses of the scale model are carried out at the same flow conditions as the experimental tests. The core purpose of this study was to obtain numerical algorithm validity, such as the adequate selection of the turbulence model and grid, as well as solver set-up and off-surface radius of interest. Of equal interest was to obtain an initial evaluation of the aerodynamic phenomena involved with W-shaped-leading-edge reversed delta planform wing ahead of the full-scale investigations, in order to assemble the main areas of investigation. This has been done to reduce the number of simulations ahead of time, so giving better turn-around time by investigating only the significant areas, as the subsequent high Reynolds Number cruise simulations are a lot more demanding with respect to computer memory and consequently, time to converge.

A comparison and discussion of the low speed results acquired from both the experimental tests and numerical wind tunnel simulations will be presented in this section. This will be accomplished with the aid of plots and images of the flow-field associated with the tests.

Detailed information on the experimental set-up and apparatus has been given in Section 4, and so no further elaboration on the matter will follow, except to briefly reiterate the experimental conditions: the tests were carried out on a 5% scale model tested at four Reynolds Numbers and at a range of angles of attack ( $-10^\circ < \alpha < 30^\circ$ ), with steps of approximately  $\Delta\alpha = 2^\circ$

Similarly, from a numerical point of view, the primary objective of the tunnel simulation was to achieve a flow solution in the test section similar to the tunnel

operating conditions. Improper velocity or pressure conditions at the tunnel contraction exit can, for instance, affect the velocity in the test section and lead to errors. Consequently, analogous conditions as for the above experiments were necessary for the numerical set-up. Thus, initially the experimental tests were run, followed by the numerical simulations where the boundary conditions for the flow initialization were taken from the experimental data. The numerical tests were run at a Reynolds Number of  $Re = 3.6 \times 10^5$  and at a range of angles of attack between  $0^\circ < \alpha < 18^\circ$ .

Finally, in the absence of surface pressure data from the experimental model, numerical and experimental near-wake analyses were carried out to examine the flow behavior in the near-wake of the model. Yet again, for comprehensive information on the experimental arrangements for the near-wake tests see Section 5 of this dissertation.

## **6.1 Experimental Reynolds Number Effect Study**

To begin with, a series of tests were carried out in the T2 wind tunnel to assess the Reynolds Number effects, if any, on the lift, drag and pitching moment behavior of the wing. The tunnel was run at four different speeds, to obtain four different Reynolds Numbers of  $1.5 \times 10^5$ ,  $2.1 \times 10^5$ ,  $3.6 \times 10^5$  and  $4.1 \times 10^5$ . Experimental evaluation of the strut drag was carried out for all relevant wind tunnel speeds used for the Reynolds Number effect analysis. The resulting drag values were subtracted from the balance output to eliminate the strut contribution. Wind-off pitching moment contributions at each angle were also assessed and subtracted from the data. The corrected results obtained for each speed were then plotted to check for possible variations. Figures 6-1 to 6-4 illustrate the force and moment coefficients obtained.

No major difference in results was observed as Reynolds Number was varied, this being particularly true for the lift coefficient plots. There appears to be a clear trend with  $Re$ -lift curve slope at low incidences in particular. Only a minor decrease of the drag coefficient was noted with the increase of the Reynolds Number, which was

slightly more noticeable at  $11^\circ < \alpha < 15^\circ$ . The behavior of the lift-to-drag ratio shown in the subsequent plots is then directly linked to the drag coefficient, resulting in lower lift-to-drag ratios at lower Reynolds Numbers i.e.  $Re = 1.5 \times 10^5$  and  $Re = 2.1 \times 10^5$ .

Pitching moment coefficients gave the most variation with respect to Reynolds Numbers, mostly at the two lower Reynolds Number tested. The differences may be due to a combination of hysteresis and the sensitivity of the pitching moments on data acquirement. Even so, repeatability of the test set-up was maintained for the higher velocities ( $U = 30, 35\text{m/s}$ ) and the differences were considered small enough that no further investigations were carried out. Overall, the results for all Reynolds Numbers are believed to agree well. Since no substantial difference was noticed between any of the plots, even at the lowest Reynolds Numbers, the chosen Reynolds Number at which evaluation experiments were carried out in the T2 tunnel was  $3.6 \times 10^5$ . Henceforth, all the comparisons for the rest of this section will, unless stated otherwise, refer to the experimental data obtained at this Reynolds Number only.

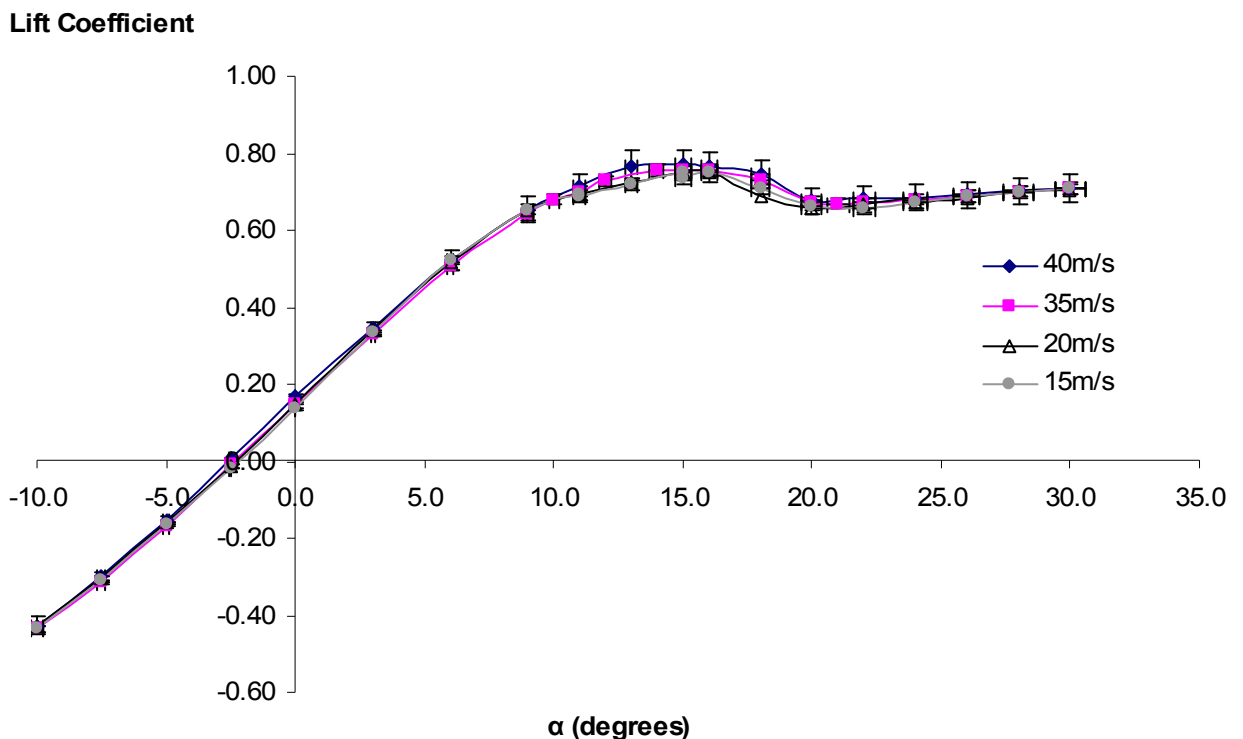


Figure 6-1. Experimentally lift drag coefficient at  $M = 0.1$  and  $Re = 4.1 \times 10^5$  ( $v = 40\text{m/s}$ ),  $Re = 3.6 \times 10^5$  ( $v = 35\text{m/s}$ ),  $Re = 2.1 \times 10^5$  ( $v = 20\text{m/s}$ ), and  $Re = 1.5 \times 10^5$  ( $v = 15\text{m/s}$ )

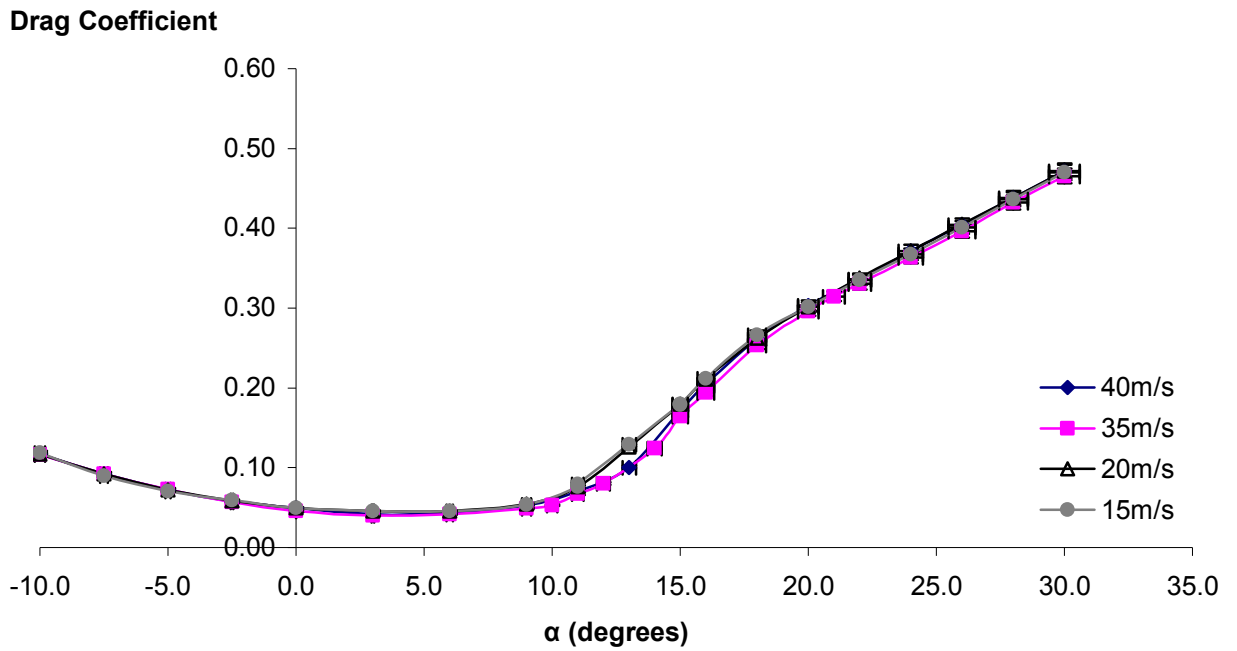


Figure 6-2. Experimentally measured drag coefficient at  $M = 0.1$  and  $Re = 4.1 \times 10^5$  ( $v = 40\text{m/s}$ ),  $Re = 3.6 \times 10^5$  ( $v = 35\text{m/s}$ ),  $Re = 2.1 \times 10^5$  ( $v = 20\text{m/s}$ ), and  $Re = 1.5 \times 10^5$  ( $v = 15\text{m/s}$ )

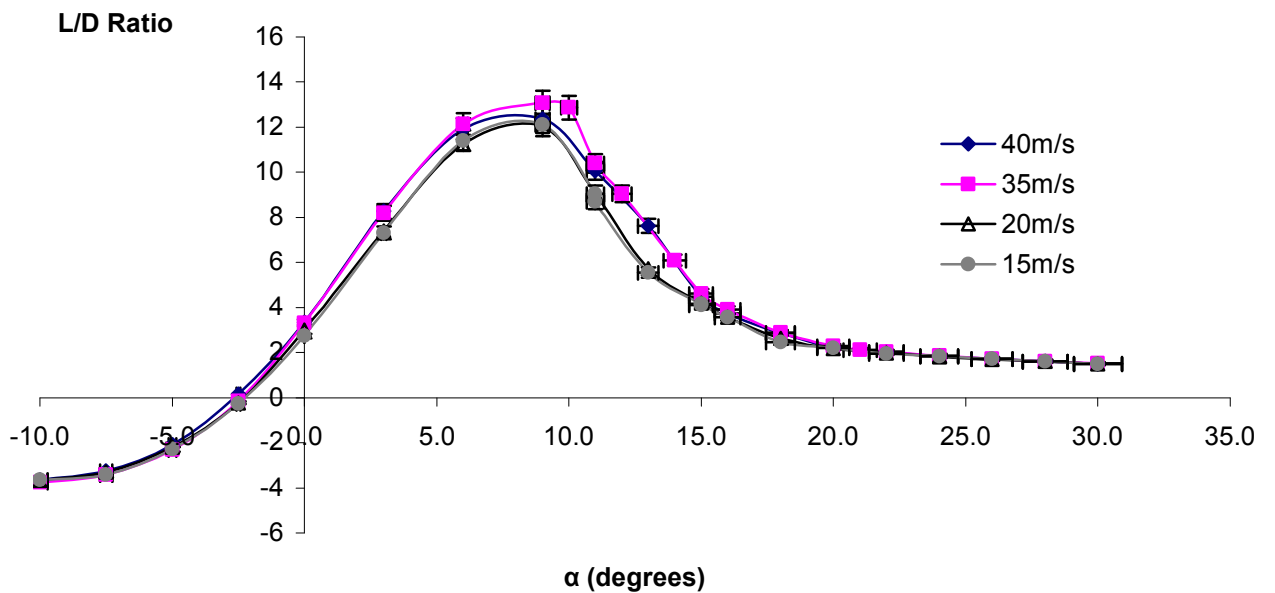


Figure 6-3. Experimentally measured lift-to-drag ratio at  $M = 0.1$  and  $Re = 4.1 \times 10^5$  ( $v = 40\text{m/s}$ ),  $Re = 3.6 \times 10^5$  ( $v = 35\text{m/s}$ ),  $Re = 2.1 \times 10^5$  ( $v = 20\text{m/s}$ ), and  $Re = 1.5 \times 10^5$  ( $v = 15\text{m/s}$ ).

## Moment Coefficient

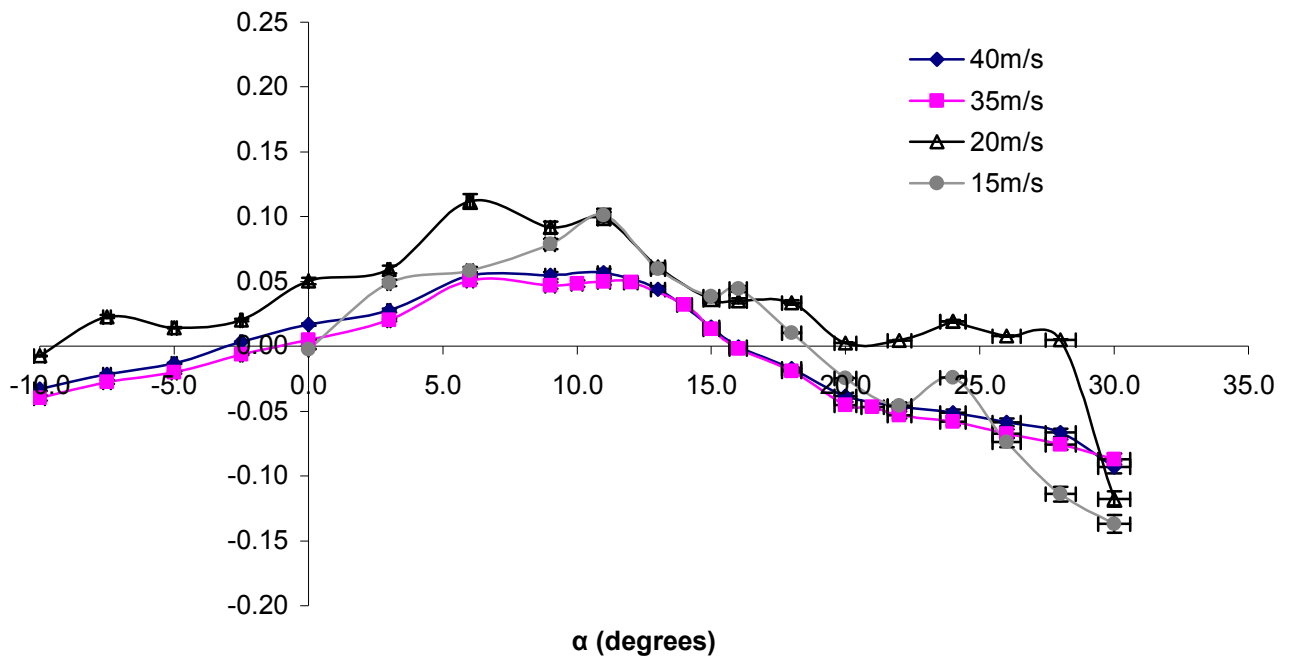


Figure 6-4. Experimentally measured moment coefficient at  $M = 0.1$  and  $Re = 4.1 \times 10^5$  ( $v = 40\text{m/s}$ ),  $Re = 3.6 \times 10^5$  ( $v = 35\text{m/s}$ ),  $Re = 2.1 \times 10^5$  ( $v = 20\text{m/s}$ ), and  $Re = 1.5 \times 10^5$  ( $v = 15\text{m/s}$ ).

## 6.2 Wind-tunnel Numerical Simulations

Following the conclusion of the Reynolds Number effects tests, numerical simulations were consequently run at the chosen Reynolds Number of  $Re = 3.6 \times 10^5$ , with equivalent Mach number of  $M = 0.1$ . As stated previously, boundary conditions that were similar to the experimental tests were initiated to ensure no discrepancies between the studies.

In order to save time and computer memory only half of the wing was modelled, with symmetry boundary conditions being used to simulate the full configuration. The far-field boundaries were extended to about ten root-chord lengths from the wing surface geometry in the upstream, radial, and downstream directions. The computational model for the wind tunnel simulations did not include any mounting hardware or wind tunnel structure. Due to the computational and time constraints as well as the large

number of cases needed to be modeled a choice on not modeling the wind tunnel hardware was made. Additionally the experimental data were corrected for both wall interference and tare effects; as such it was considered that the time and computer limitations would be greatly assisted if the mounting hardware was excluded from the computational model.

ICEM CFD commercial meshing software was used to generate a fixed unstructured viscous computational grid that was used to discretize the domain. For every computation a grid was established and then refined, smoothed and updated as the research progressed. As a result of this procedure, three different unstructured grids were obtained for the wind tunnel simulations.

For all grids triangular cells were generated for the surfaces, with hybrid tetrahedral, prism and pyramid grids used to occupy the volume inside the flow domain. Initially the triangular surface mesh was generated, followed by the fully tetrahedral baseline mesh which was subsequently converted to a mixed element mesh by merging the semi-structured tetrahedral layers in the boundary layer region into prismatic elements. To capture complex flow regions, wing surface volume grids were clustered near the leading edge, trailing edge and tip (Figure 6-5). The prism cells, having a total of twenty-two layers (Figure 6-6), were mostly used to model the boundary layer region, whereas tetrahedral cells were used to model the inviscid region. The justification of the use of prismatic elements was thoroughly explained in section 2 of this thesis: this was mainly to provide a distinct decoupling in the discretisation between the normal and tangential directions in the boundary layer region. Pyramid cells are required in cases where quadrilateral prismatic faces are exposed. Small size cells were employed in the wing vicinity area to ensure accurate investigation of the near-surface and near-wake phenomena, with larger cells in the far-field and on the boundaries to impose the boundary conditions.

The initial (coarse) grid used for the wind-tunnel computations consisted of approximately 1.8 million cells. However, during calculations it was noticed that the grid was not fine enough to capture the near-wake correctly, therefore this grid was afterwards locally refined (see Figure 6-7) to achieve a finer resolution, especially in the near-wake region (by employing a density box around the wing), hence obtaining

a 2.2 million cell (medium) grid. The last grid (fine grid) obtained for these simulations consisted of approximately 2.8 million cells. This grid consisted of fine boundary cells, which were created to provide an average  $Y^+ = 0.2$  in the near surface region, as depicted in Figure 6-8, thus facilitating the integration of the turbulence model up to the wall. Hence, no wall functions were employed for the wind tunnel simulations. To initialize the simulation on the computational domain, pressure and temperature boundary conditions as obtained from the wind-tunnel tests were set at the far-field boundaries.

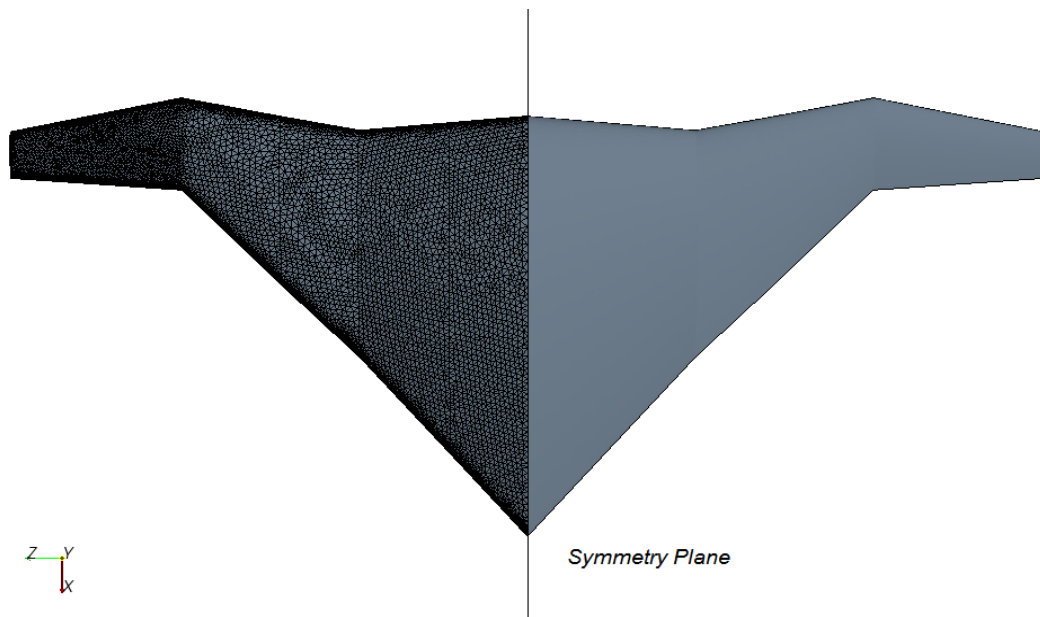


Figure 6-5. W-leading-edge-wing unstructured computational grid-planform view.

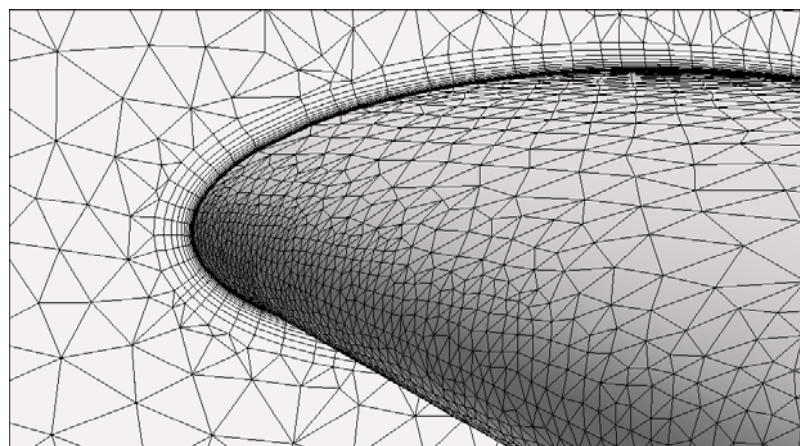


Figure 6-6. Computational grid in the near-surface region.

Along with the momentum residuals, force and moment coefficients were observed as a convergence criterion for the numerical tests. The solutions were considered to have converged when no variations greater than  $\pm 0.001$  in either the force ( $C_L$  and  $C_D$ ) or moment coefficients were observed over 100 iterations and momentum residuals were seen to be reduced by at least three orders in all cases.

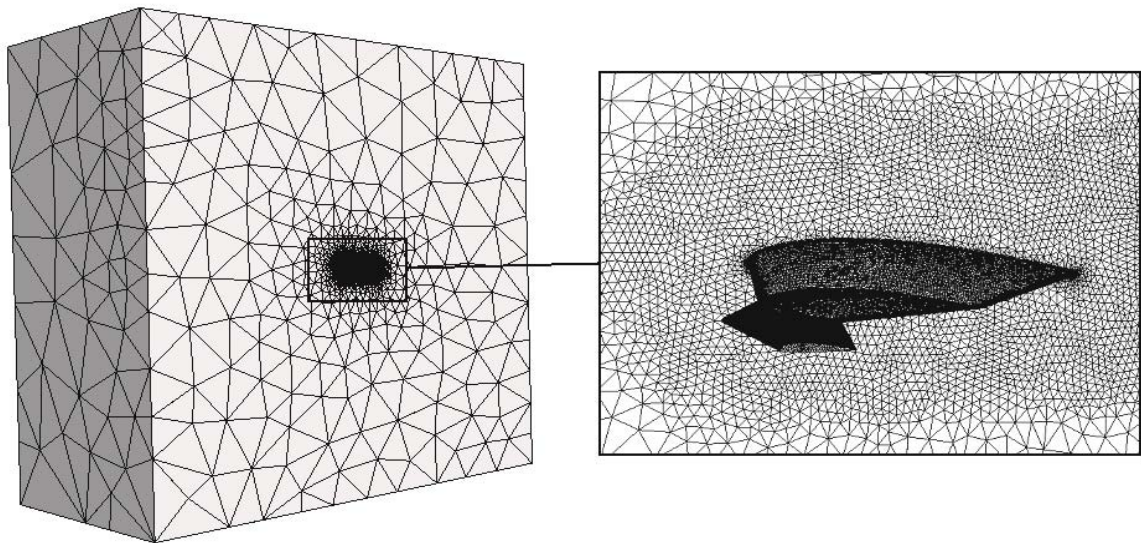


Figure 6-7. Complete computational unstructured grid domain and fine grid density box around the wing (inset).

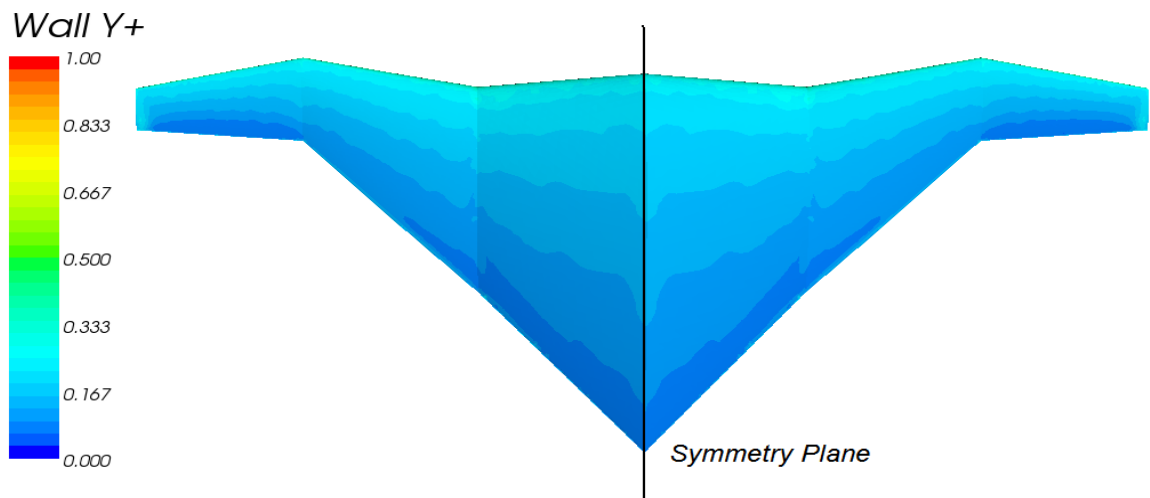


Figure 6-8. Predicted  $Y^+$  distribution on the wing at  $M = 0.1$  and  $Re = 3.5 \times 10^5$  and  $\alpha = 12^\circ$

### 6.3 Results-Forces and Moments

Figures 6-9 to 6-12 represent the lift coefficients, drag coefficients, moment coefficients and lift-to-drag ratios obtained by both numerical (fine and medium grids) and experimental methods. Standard methods for the propagation of errors were used to estimate the uncertainty in the experimental data, which is illustrated on each graph by means of error bars. In general, errors were found to be quite low with an average error of  $\pm 1.4\%$  in the lift,  $\pm 1.4\%$  in the drag and  $\pm 2\%$  in the pitching moment. Errors in the lateral forces and moments were somewhat larger, with an average value of  $\pm 2\%$ .

Figure 6-9 illustrates the variation of lift coefficient with angle of attack. The findings show agreement between the experimental results and the fine grid computations. Numerical results only very slightly over-predict the lift coefficient. The difference is greater between the experimental results and the numerical predictions obtained with a medium grid.

For all grids employed in this study, the numerical lift coefficient at zero angle of attack is, to some extent, lower than the experimental one. Also, a minor off-setting of the curve is observed up to  $\alpha = 9^\circ$ . This may be due to various factors, such as numerical as well as experimental errors. It is important to note that, after the experimental test was completed, investigation into the pitch and yaw mechanisms detected a small (approximately  $1^\circ$ ) systematic error in the setting of both the angle of attack and yaw angle. In addition, the setting of the zero angle of attack of the model was found to be a little intricate due to the geometry of the wing. This might have had an effect on the minor off-setting of the lift curve. From the numerical studies point of view, the discretisation scheme, grid or the turbulence model choice may have had an effect on the results. It needs to be mentioned, however, that the other turbulence model employed (k- $\epsilon$  Realizable), over predicted the lift coefficient even more and failed to correctly predict the stall. A comprehensive discussion of the turbulence model choice is included in section 7.

The discrepancies with numerical findings may also be associated with the setting of the external boundaries for the CFD simulation, which, to avoid outflow problems, were placed a lot further away than they are in the tunnel. Other experimental imperfections, such as test section turbulence levels, flow angularity and flow non-uniformity, will also affect the accuracy of the results.

Drag coefficient results also reveal agreements between experimental values and the fine grid data. Slight differences are noticed at higher angles of attack. With the increase of the angle of attack the numerical drag coefficient is noticed to further deviate from the experimental data. This is also noticed in the lift-to-drag ratio plots, with somewhat higher ratios being predicted by the numerical investigations. Similar factors as for the lift coefficient discussion above may also be responsible for these differences. However, the dissimilarity may not be wholly attributable to numerical errors: the interference drag between the mounting system and the model was unable to be calculated and hence was not removed from the total drag. Discrepancies in the comparison may be associated with this interference effect.

As all numerical moment coefficient data are computed from the wing leading edge, for the purpose of direct comparison moment coefficient data from the experimental results have been converted to having the wing leading edge as the moment reference point. The moment coefficient data do not display such a good agreement as the other three plots. In general, the pitching moment is under predicted, with larger discrepancies observed for the medium grids. It is well known that moment coefficients data are the most sensitive when comparing numerical and experimental predictions (Pao et al 2005). The discrepancies were also noticed between experimental tests alone as the data are sensitive to the way the pitching of the model is performed. These discrepancies then further increase between the experimental and numerical studies. As with lift and drag, factors such as grid resolution and turbulence modeling might also have contributed to the dissimilarity.

Although further refinement might bridge the gap in findings between the two studies, it was deemed unnecessary. It is important to note that the trends in  $\alpha$  and  $Re$  are more important in this study than absolute magnitudes. In general, therefore, a close agreement in the lift, drag and moment coefficient results was attained, which further

validates the computational algorithm employed for the numerical analysis. Also, the above results indicate that the final, fine mesh achieved a reasonably good predictive ability over the majority of the flow conditions considered.

From an aerodynamic characteristics viewpoint the wing is observed to have very good lift-to-drag ratio, soft stall characteristics and favorable longitudinal stability up to stall. The maximum lift-to-drag ratio is attained at the range of  $6^\circ < \alpha < 9^\circ$ , whereas the maximum lift capabilities of the wing are reached around  $14^\circ < \alpha < 16^\circ$ , this range understandably being the region where rapid increase of drag starts to occur. Further observations if the above results are related for full-scale flight will be given in the following section.

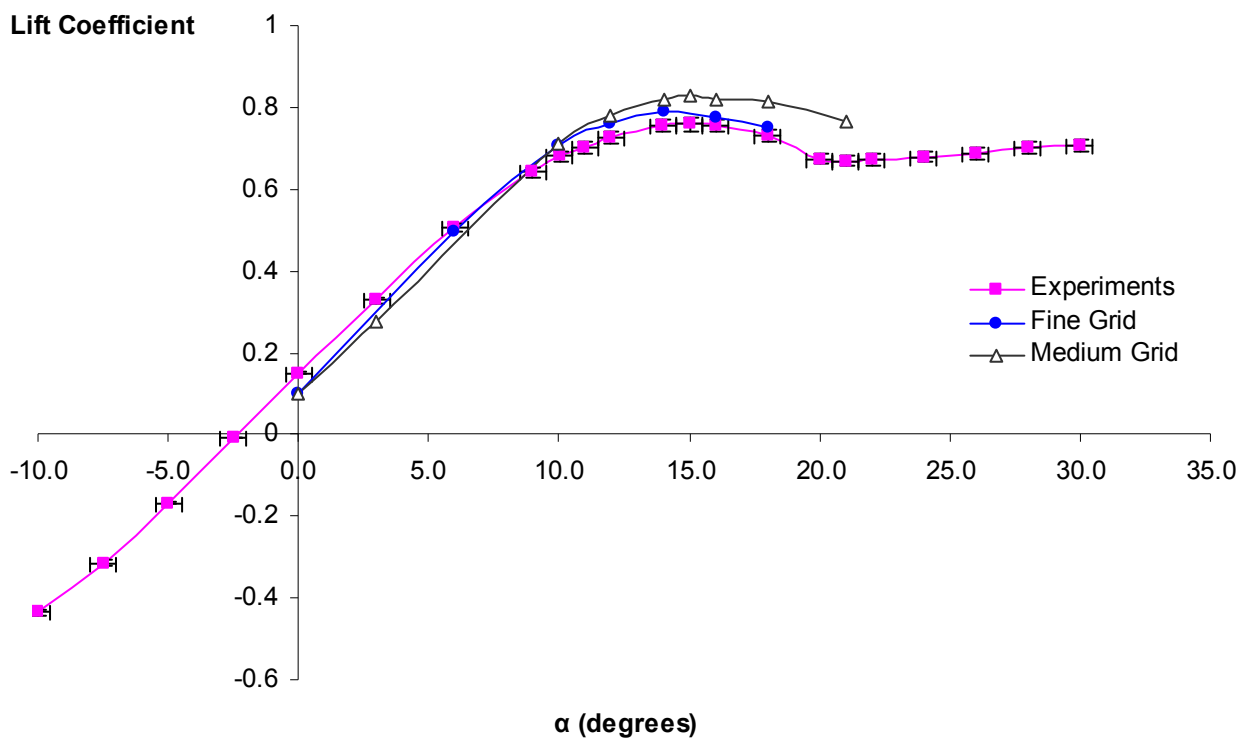


Figure 6-9. Comparison of numerically predicted (fine and medium grid) and experimentally measured lift coefficient at  $M = 0.1$  and  $Re = 3.6 \times 10^5$

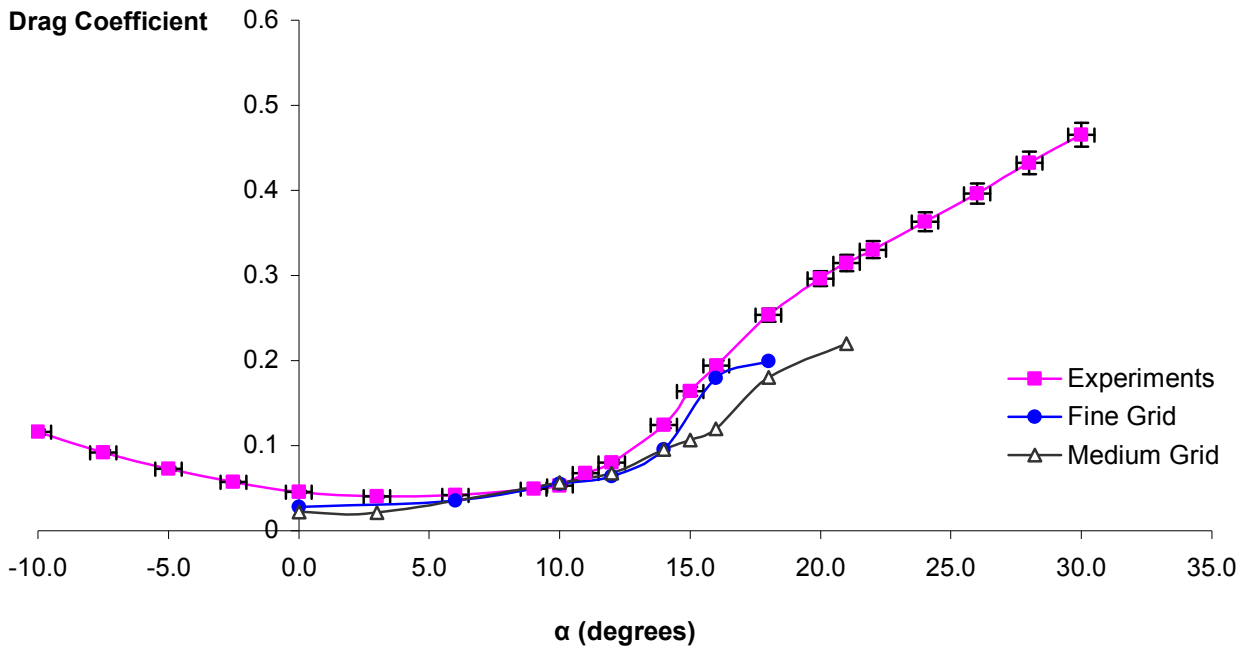


Figure 6-10. Comparison of numerically predicted (fine and medium grid) and experimentally measured drag coefficient at  $M = 0.1$  and  $Re = 3.6 \times 10^5$

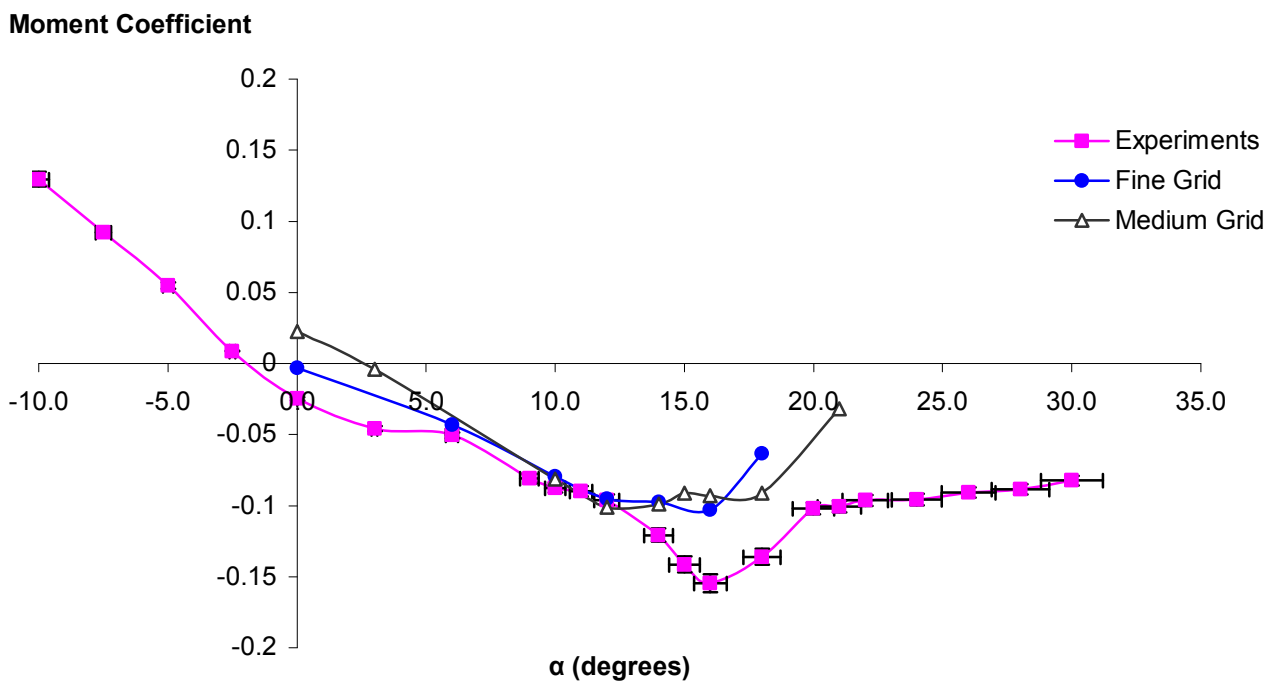


Figure 6-11. Comparison of numerically predicted (fine and medium grid) and experimentally measured moment coefficient at  $M = 0.1$  and  $Re = 3.6 \times 10^5$

## Lift-to-Drag Ratio

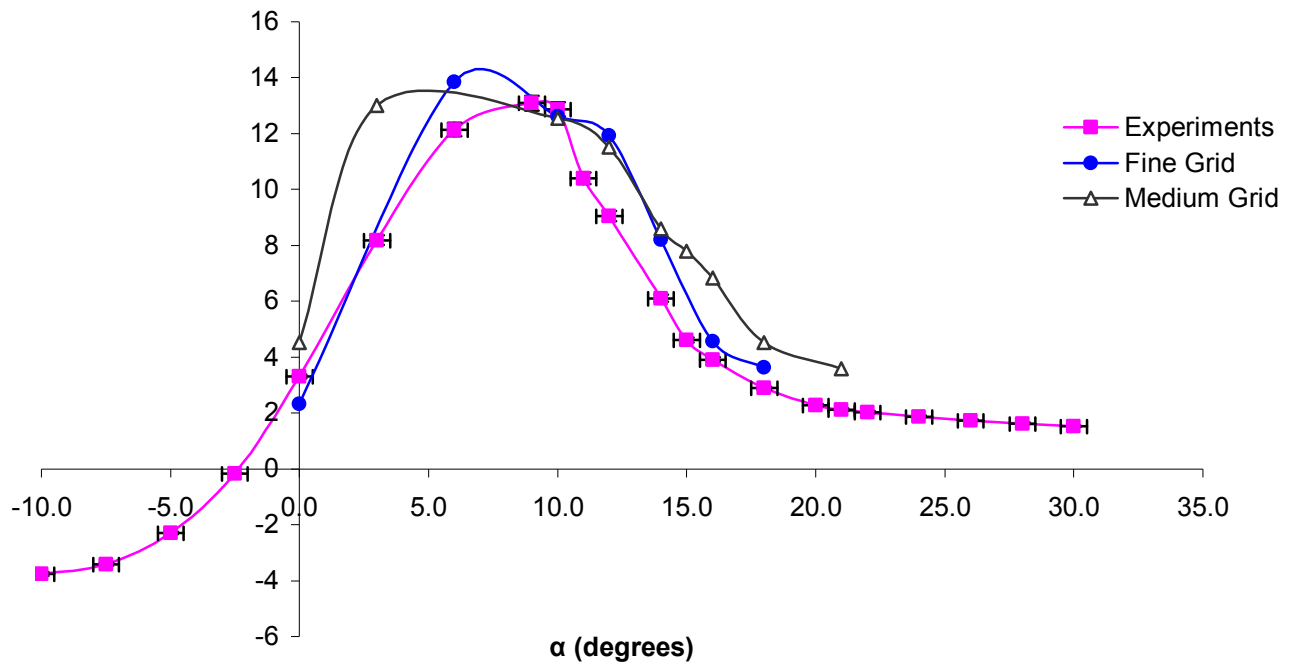


Figure 6-12. Comparison of numerically predicted (fine and medium grid) and experimentally measured lift-to-drag ratio at  $M = 0.1$  and  $Re = 3.6 \times 10^5$

### 6.4 Results Near-Wake Analysis

In order to verify the numerical results, off-surface investigations of some other form of comparison were necessary. This has been done with experimental and numerical near-wake momentum deficit examinations to further ensure reliability of the computational results. On the other hand it is also important to investigate the near-wing flow from an aerodynamics viewpoint, as some features survive in the near-wake.

A vertically positioned pitot-static rake was used in the experimental tests to analyse the near-wake flow. As discussed in section 4, the shape of the W-leading-edge wing changes significantly in the span-wise direction, hence the rake positioning from the trailing edge was significantly further for the near-tip regions. Therefore to ensure invariable distances with respect to the local chord the momentum deficit in the wake was taken at three different downstream root chord lengths ( $x/c_r = 2, 1.5,$  and  $1$ ).

For each angle of attack, experimental near-wake pressure data were obtained at a total of 44 spanwise positions. For further information on the experimental test set-up and equipment arrangements please refer to section 5 of this thesis.

The same three downstream rake locations as for the experimental tests were also employed in the numerical examinations. Numerical grid sensitivity studies revealed that further refinement of the medium grid (as discussed in sub-section 6.2) gave better agreement with the initial experimental results. Despite adequate refinement of the near-wake numerical grid, it was observed that, for the  $x/c_r = 2$  location, the tip vortex at higher angles of attack was still not captured correctly. Further refinement on the numerical grid wake region would improve the tip and wake capturing, however this imposed a significant restraint on the processing computational time required to reach a converged solution. As such additional computational recourses were required. The effects were considered greater than the purpose of the study therefore a decision was made that for comparison studies only the data obtained at  $x/c_r = 1.5$  will be addressed.

Figure 6-13 shows the final numerical and experimental near-wake lattices. Since no exhaustive investigation on the strength or accurate positioning of wake phenomena were to be carried out, both experimental and numerical grids were considered adequate in capturing the flow behaviour in the near-wake for comparison purposes only.

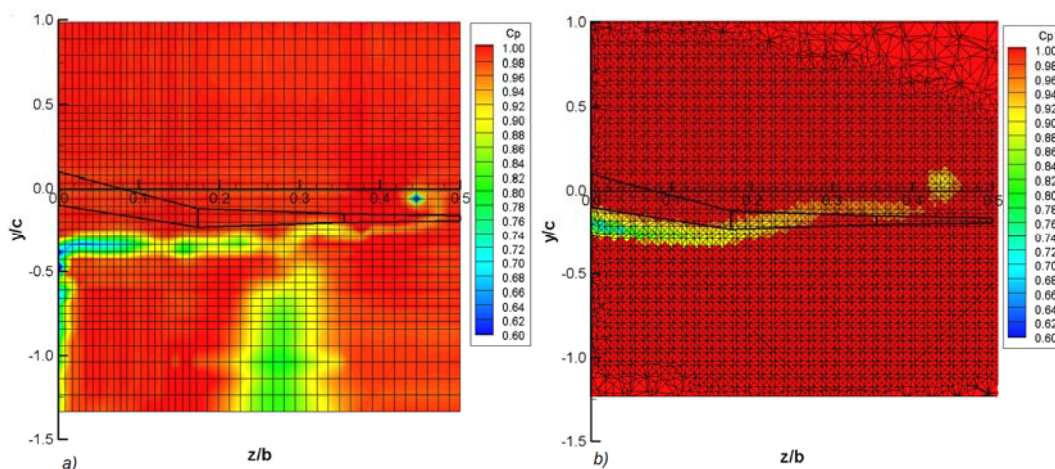


Figure 6-13. Near-Wake grid example at  $M = 0.1$  and  $Re = 3.6 \times 10^5$  and  $\alpha = 10^\circ$  for a) experimental results from the T2 tunnel and b) numerical tests.

Preliminary experimental tests revealed that a significant wake was generated by the struts (see Figures 6-14 a) and 6-15 a)). In order to reduce the wake from the struts, aerofoil-shaped fairings were employed, which were not attached to the balance. Such streamlined fairings aimed to reduce the strut wake to a minimum (since such features do not exist for the full-scale vehicle) without affecting the aerodynamic forces and moments. In this way, it was believed that the tare drag of the struts would also be decreased.

On the contrary, it was found that, although the strut wake was reduced, the near-wake results obtained with the fairings showed even more discrepancies with numerical results (see figures 6-14 b) and 6-15 b)). Severe interference effects were noticed, which could be a result of various factors. Positioning the fairings at absolute zero degrees was quite delicate, and may not have been completely accurate. Also, the length of the fairings was greater than suggested by the literature. Finally, a small cavity between the fairing and the struts may have been the main cause of the large vortical features appearing in the wake. Owing to these discrepancies, the rest of the tests were run without the fairings, as the wake of the unshielded struts was considered to have far less of an impact on results, compared with errors obtained with the fairings.

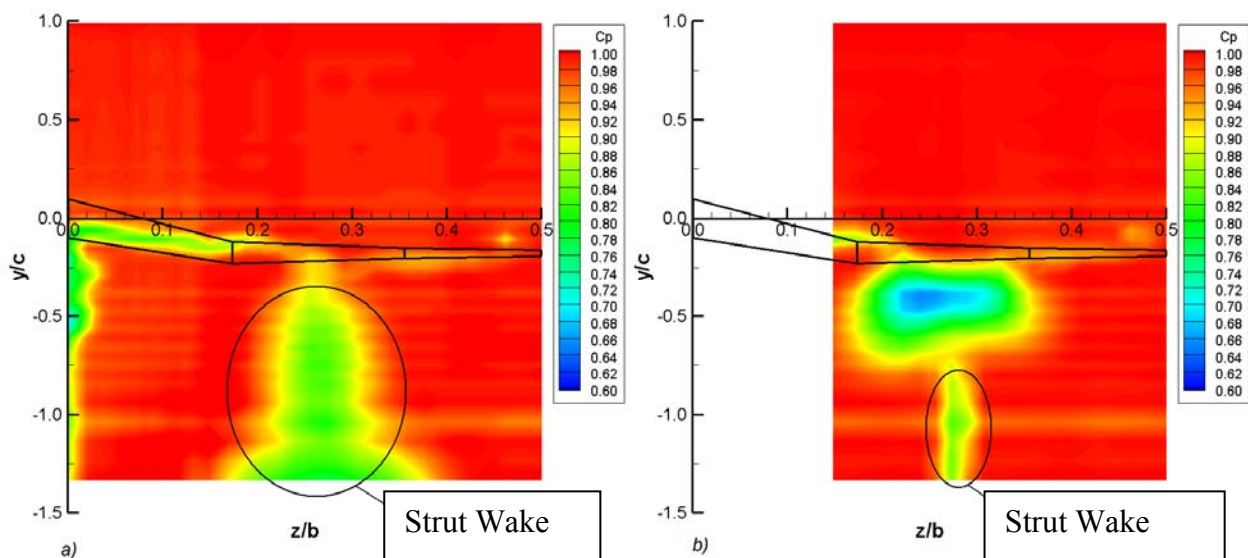


Figure 6-14. Experimental strut wake effects comparison at  $M = 0.1$  and  $Re = 3.6 \times 10^5$  and  $\alpha = 0^\circ$  for a) struts without fairings and b) struts with fairings

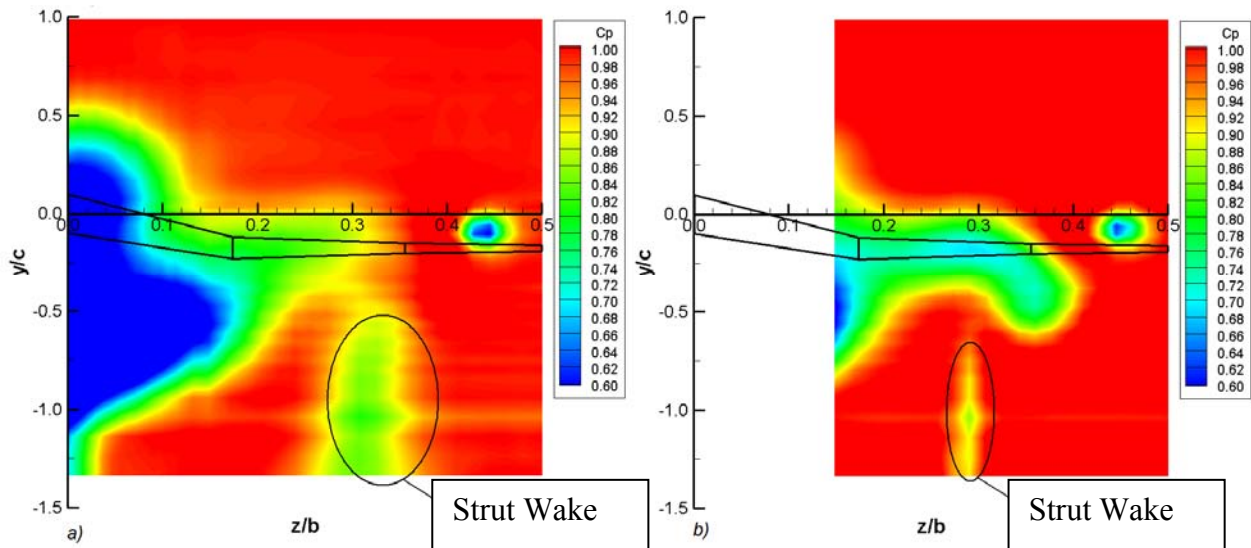


Figure 6-15. Experimental strut wake effects comparison at  $M = 0.1$  and  $Re = 3.6 \times 10^5$  and  $\alpha = 24^\circ$  for a) struts without fairings and b) struts with fairings

Figures 6-16 to 6-11 depict the total pressure coefficient plots obtained (at  $x/cr = 1.5$ ) by both numerical and experimental tests. It can be seen that the effect of the strut wake has been removed from the experimental representations. This was done due to the fact that effect of the T2 struts on the wing wake was small enough to justifiably be removed from the plots, even if primarily for aesthetic reasons. Also, later tests in T3, using a single, centrally mounted strut, conclusively proved that the strut wake does not strongly interfere with the wing wake even at the highest angles of attack. The effects of the strut wake were removed by applying the free-stream values for pressure as far from the model, by taking care in the regions near the wing wake. This was done in order to make a like with like comparison with the numerical results.

Generally, qualitative agreement exists between predicted and measured total pressure coefficients. For angles of up to  $\alpha = 12^\circ$ , near-wake plots reveal ‘common-trend’ wake manifestations, comparable to conventional wings. The tip vortex is seen to increase in strength with angle of attack and the wake of the wing is generally thin, with a relatively constant total pressure coefficient of 0.8. At  $\alpha = 14^\circ$ , which is approximately the maximum lift angle, the wake behavior somewhat differs from familiar expectations. At this stage an inboard vortex seems to appear in the near-wake results, at approximately  $z/b = 0.25$ . It can be seen that this vortex is different from the tip vortex. Interestingly, it was found that this rotational flow manifested

from the mid-part of the wing, as can be observed in both experimental and numerical plots. The strength of the secondary vortex is more prominent in the numerical results, whereas the tip vortex was more distinct in the experimental plots. However, the general shape of wake is very similar for both studies.

It can be seen that the strength of the inboard vortex was increased with further increase in angle of attack. At  $\alpha = 16^\circ$ , it was observed that, the flow over most of the mid-part and tip sections of the wing had separated (this was also noticed from pressure coefficient plots shown in Figure 6-20). Again, good agreement is found between the predicted and experimental results. The numerical results once more do not capture the strength of the tip vortex correctly, yet the formation and strength of the inboard vortex is in agreement with the experimental results.

At  $\alpha = 18^\circ$  the wing undergoes stall on the inboard section, as most parts of the flow on the upper surface have now separated. The appearance of the inboard vortex at the mid-part of the wing is more prominent in the numerical results, whereas both studies reveal agreement on the deep stall characteristics of the inner section. A third vortical structure may be associated with this phenomenon (see Figure 6-21). Further details on this matter are given in section 7.

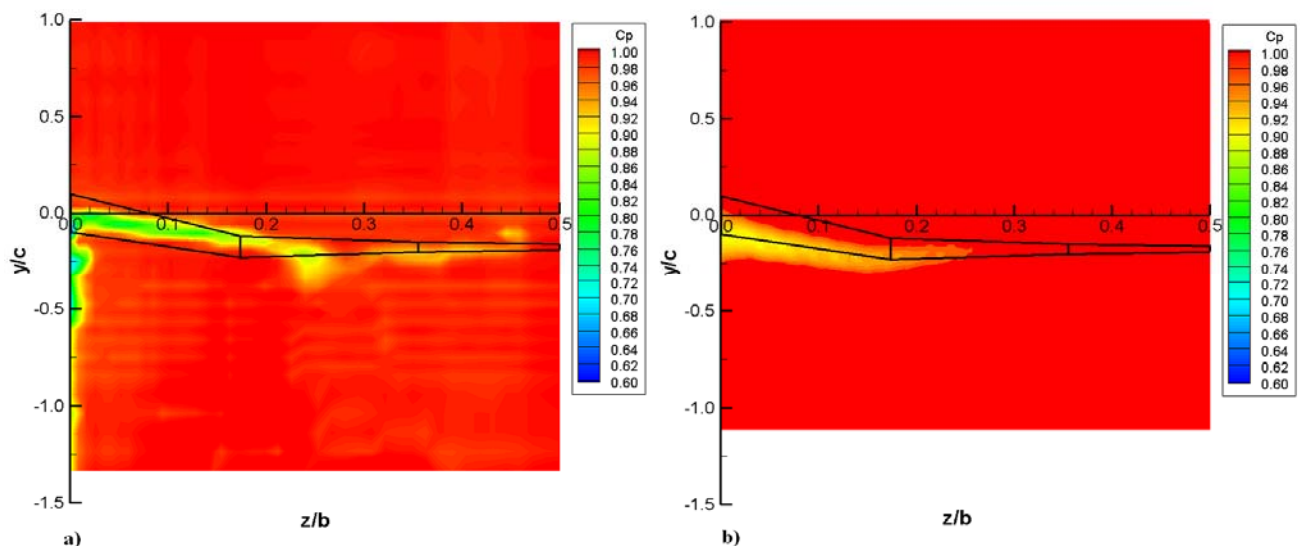


Figure 6-16. Near-wake total pressure coefficients at  $\alpha = 0^\circ$  a) experimental and b) numerical

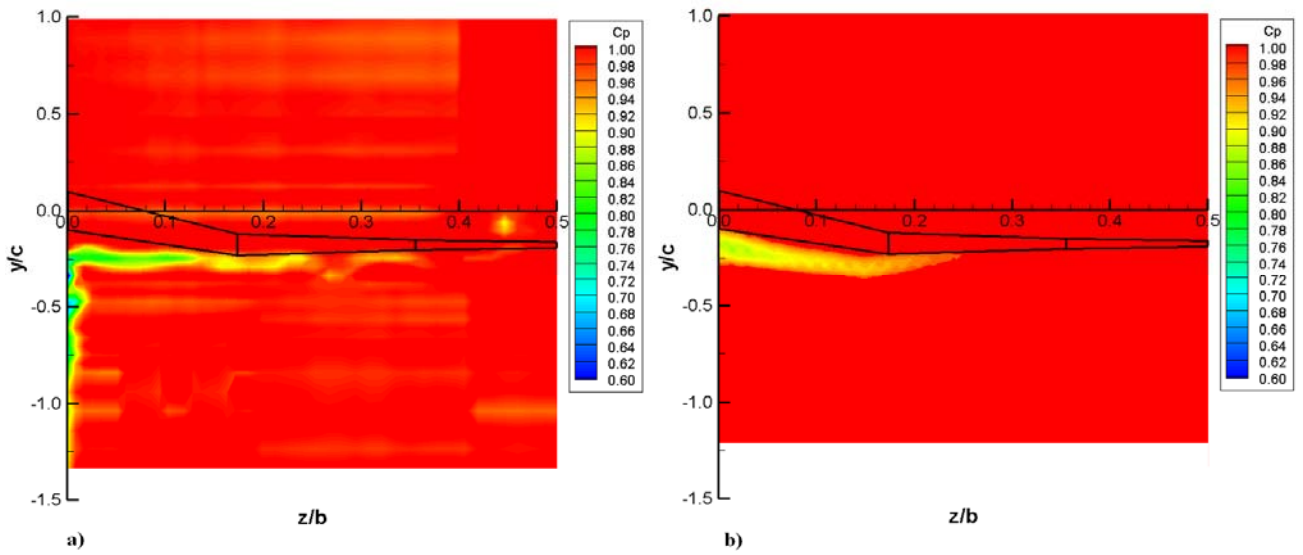


Figure 6-17. Near-wake total pressure coefficients at  $\alpha = 6^\circ$  a) experimental and b) numerical

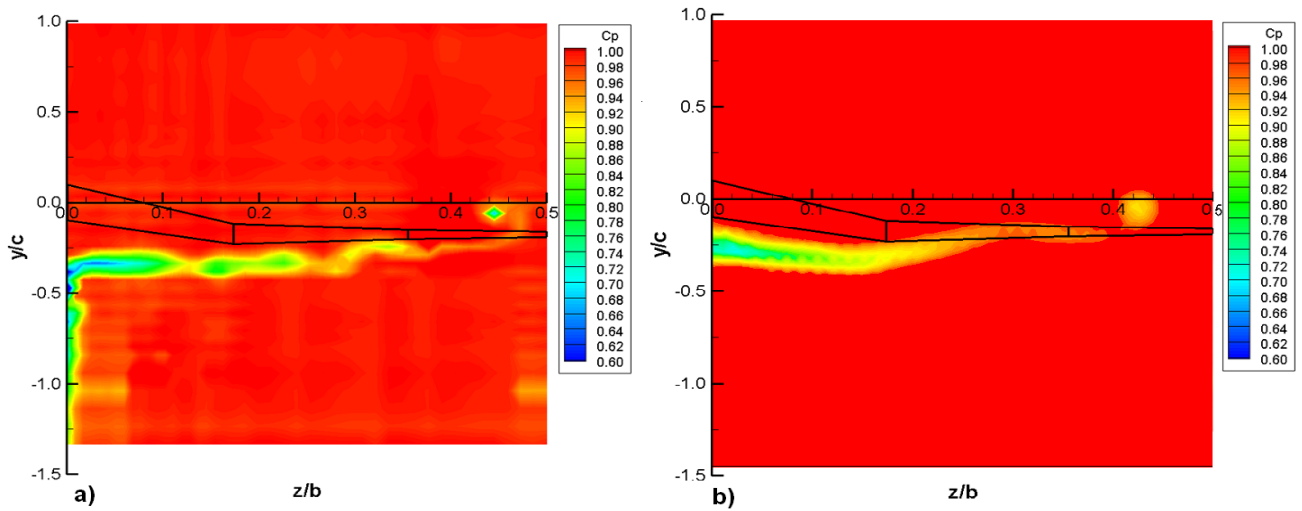


Figure 6-18. Near-wake total pressure coefficients at  $\alpha = 10^\circ$  a) experimental and b) numerical

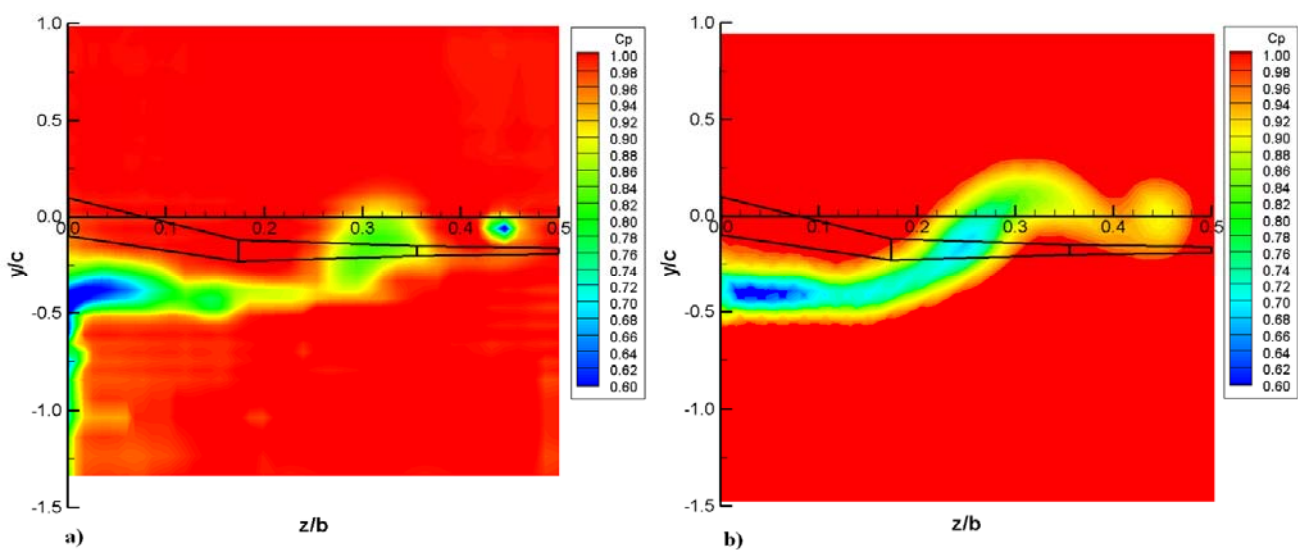


Figure 6-19. Near-wake total pressure coefficients at  $\alpha = 14^\circ$  a) experimental and b) numerical

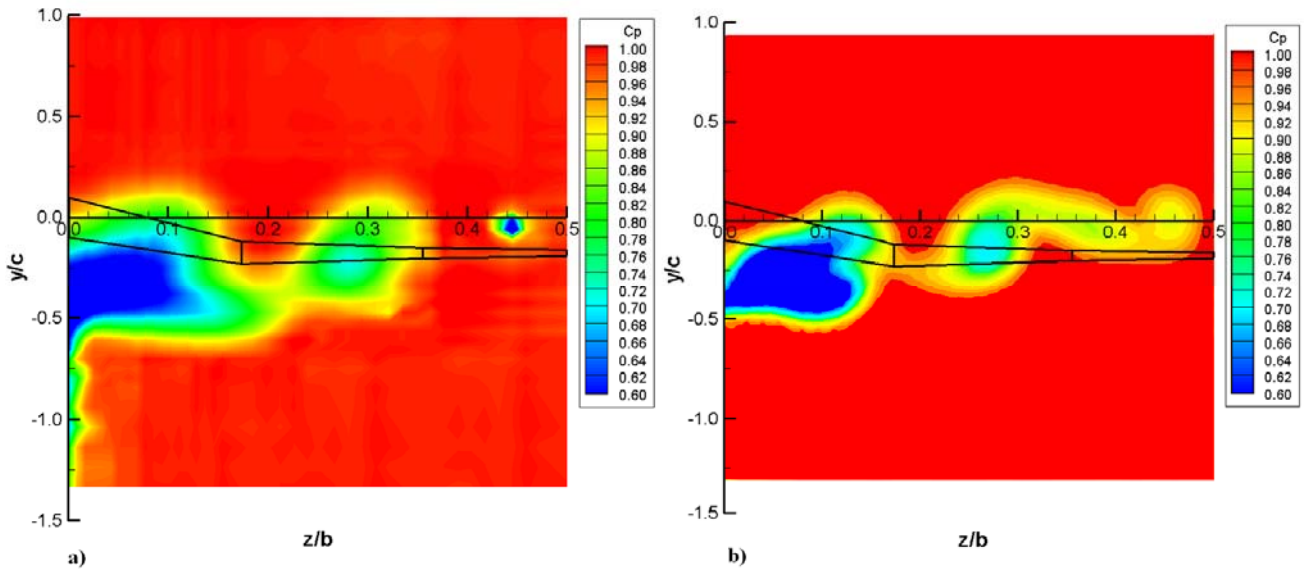


Figure 6-20. Near-wake total pressure coefficients at  $\alpha = 16^\circ$  a) experimental and b) numerical

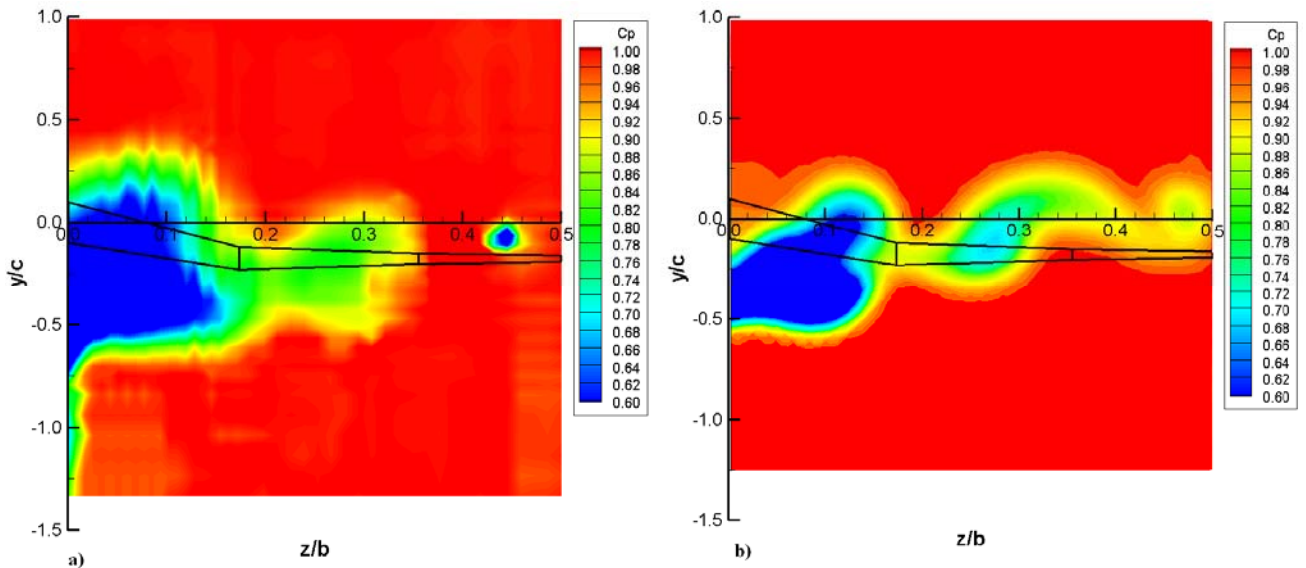


Figure 6-21. Near-wake total pressure coefficients at  $\alpha = 18^\circ$  a) experimental and b) numerical

In general very good agreement is noted between experimental and numerical near-wake analyses. The zigzag nature of the experimental wake flow results at  $\alpha = 18^\circ$  may be associated with vibrations of the support structure in the wind tunnel. The small differences in the shapes may also be due to various factors such as freestream turbulence, local surface roughness, local geometric imperfections in the model shape in comparison with the computational one or local surface imperfections (protuberances, holes, dents, etc).

To verify the above near wake behavior, preliminary predicted upper surface pressure distributions plots revealed that, for the particular Reynolds Number assessed, the

wing's suction side was subjected to a large adverse pressure gradient. Figures 6-22 and 6-23 depict the upper surface pressure and shear-stress distributions, which may be associated with the rotational features observed on the near-wake. Shear-stress distribution results show regions of near zero shear-stress indicative of flow separations regions on the upper surface, with separated flow over the most part of the tip region at  $\alpha = 14^\circ$ . Accordingly, further details of this assessment are included as part of the discussion of the full-scale tests in the subsequent section.

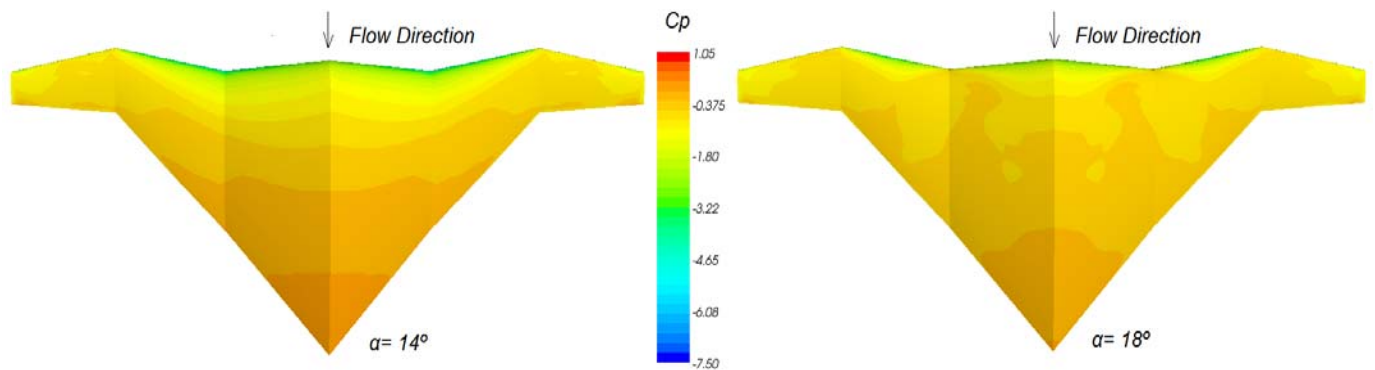


Figure 6-22. Numerically predicted upper-surface pressure distribution at  $M = 0.1$  and  $Re = 3.6 \times 10^5$  for a)  $\alpha = 14^\circ$  and b)  $\alpha = 18^\circ$

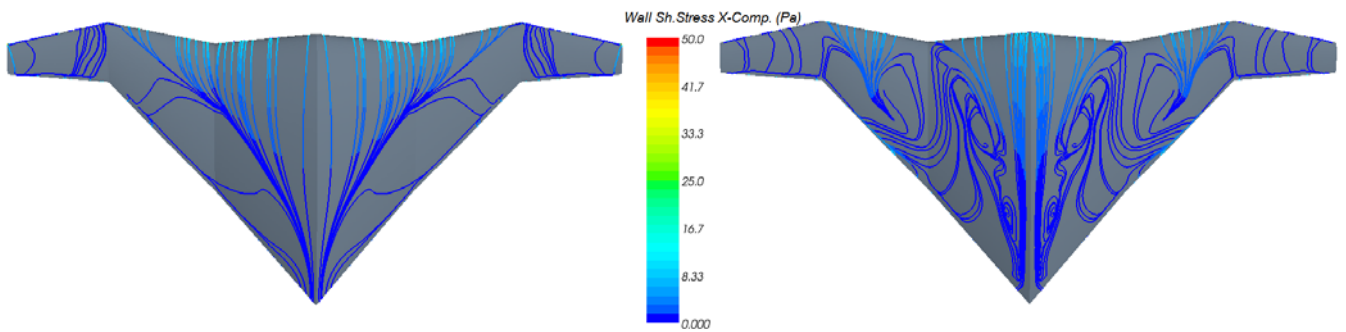


Figure 6-23. Numerically predicted upper-surface wall shear-stress streamlines at  $M = 0.1$  and  $Re = 3.6 \times 10^5$  for a)  $\alpha = 14^\circ$  and b)  $\alpha = 18^\circ$

## Summary

The key observations from these results were: in terms of preliminary aerodynamic analyses a strong inboard vortex was noticed to appear on the near-wake at higher angles of attack, which were present at all three downstream locations assessed. This flow was not noticed at lower angles of attack and was certainly very different from the tip vortex in direction, shape and strength. Thus, an assessment of the origin and direction of the vortex was deemed necessary. The cause of this rotational flow feature was not investigated at this stage, but it gave a starting point for further research during the full-scale simulations and, especially, ground effect analyses, where the wake structure and effects are of principal significance.

The general success of the numerical/experimental investigation was effectively achieved, and explicit regions of interest were identified, which were further investigated on the full-scale high-Reynolds Number numerical studies in detail in the next section. In brief limited plots for preliminary aerodynamic investigations have been given with no elaboration on aerodynamics being carried out at this stage. Also, although the Reynolds Number utilized for the above tests does not match that of the full-scale wing, these tests have initiated further investigations.

It needs to be mentioned that previous studies on the appearance of vortices on highly swept and sharp delta wings have concluded that initial vortex formation, and subsequent vortex interactions, are not qualitatively influenced, to first order, by Reynolds Number (Bushnell 1993). This is not necessarily the case for rounded leading edge wings as Reynolds Number might have a stronger effect, which must be taken into consideration for the present study.

Despite minor differences in general, the obtained results showed a strong agreement between the two studies employed. Overall this leads to a conclusion that the agreement of the two methods gave some confidence for the employment of the numerical Navier-Stokes/ hybrid grid method for further calculations on the W-leading edge wing for the full-scale simulations.

## 7. Full-scale High-speed Numerical Analyses of W-shaped-leading-edge wing Aerodynamics in Cruise Flight

This section presents the detailed analyses of the full-scale W-shaped-leading-edge reversed delta planform wing in cruise configuration. Two numerical approaches were employed to predict the flow-field characteristics. The first was a coupled Navier-Stokes finite-volume compressible viscous unstructured method. The second was a finite-difference, compressible, inviscid semi-structured full-potential flow solver.

The explicit coupled, quasi-steady Navier-Stokes equations were solved at a Reynolds Number of  $3 \times 10^7$ ,  $M = 0.45$  (cruise conditions for the Jetpod aircraft) and a range of angles of attack ( $0^\circ < \alpha < 18^\circ$ ). At full scale it is assumed that boundary layer transition occurs relatively close to the leading-edge and therefore a fully turbulent boundary layer is computed over the whole configuration (see Figure 7-1). All computations were obtained with the ideal gas assumption supplemented by Sutherland's viscosity law, together with invoking static pressure boundary conditions on the far-field perimeter, and no-slip conditions on the wing surface. The Reynolds stresses in the momentum equations were computed using the  $k-\omega$  SST two-equation model, the choice of which was influenced by a comparative study, as discussed below. Turbulence properties were assigned as discussed in section 3 of this thesis. Nonlinear, inviscid, velocity-potential equations were solved at the same flight conditions as detailed above and a range of angles of attack ( $\alpha < 10^\circ$ ). As with the Navier-Stokes computations, the same boundary conditions were applied for the full-potential calculations, where applicable.

It is known that all numerical solutions of fluid flows contain errors that must be minimised, where possible, if the solutions are to be useful in the design process. These errors can be categorised into errors due to discretisation, iteration or convergence and turbulence modelling errors. Accordingly, the study addressed all of the above separately to maintain a methodical approach to obtaining added accuracy in the results.

A discussion on the sensitivity of the full-scale computations to the above-mentioned errors follows in this section.

In order to understand the differences in overall wing performance, such as local pressure gradients, and areas of separated flow over the wing, detailed plots of the pressure and wall shear stress streamline distributions are also produced. The “sensitive” regions of interest were established in the previous section, thus, further assessment, such as both on- and off-surface flow visualization and investigation, will be performed in more detail.

Finally, a thorough discussion of the general performance of the W-shaped leading-edge wing at the assessed flight conditions will follow, with further information on the additional areas of investigation, as required.

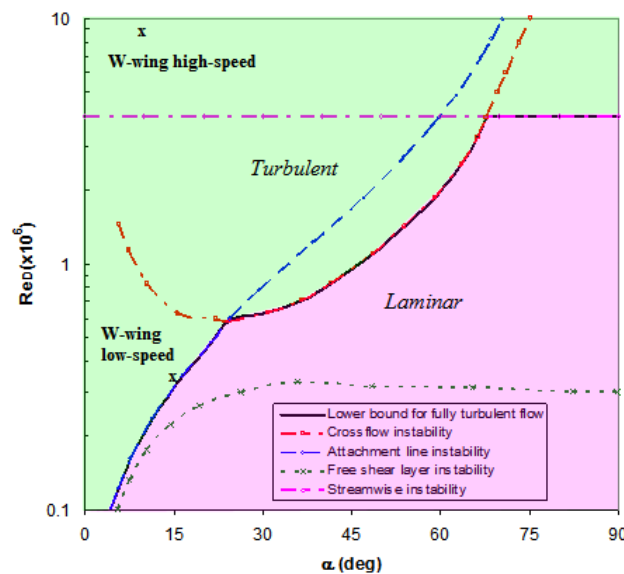


Figure 7-1. Boundary layer state at separation, together with dominant transition mechanism as a function of incidence and Reynolds Number (Poll 1985)

## 7.1 Grid Dependency Analyses

As with the low-speed, scaled isolated wing tests, the grid generation process involved an initial comparative study to obtain grid-independent results. Grids of similar structure as for the wind tunnel simulation tests were generated; also, the half-wing modelling approach and use of symmetry boundary conditions to reflect the complete wing were maintained. Wing geometries were modelled from their original surface definitions and volume geometries were modelled based on the surface grid. The hybrid tetra/prism/pyramid approach outlined in the previous section proved to be of an adequate nature; consequently, the approach was adopted in these studies as well. A reasonable image of the flow around a body is necessary for a useful understanding of the aerodynamics of the problem, hence, the far-field boundaries were extended to about 10 maximum chord length from the wing surface geometry in the upstream, radial, and downstream directions.

Multiple grids were obtained and then refined so as to improve the grid in an evolving process until the appropriate best quality was achieved. The initial coarse grid consisted of 0.9 million cells. A refinement ratio of 2 was applied to this baseline grid, which provided the second so-named medium grid of 1.7 million cells in total. The finest grid obtained, with a refinement ratio of 3, consisted of 3.2 million cells. The initial grid was generated to obtain a  $Y^+$  of less than 30 in the near-surface region. The final near-surface grid (fine) was generated with 24 prism layers, resulting in an average  $Y^+$  of less than 10 (see Figure 7-2a). Hence, for the full-scale simulations, wall functions were necessary to simulate the near-wall region. The solver's built-in automatic wall treatment (that automatically shifts from low to high-Reynolds Number model, based on grid spacing) was used to model the boundary layer.

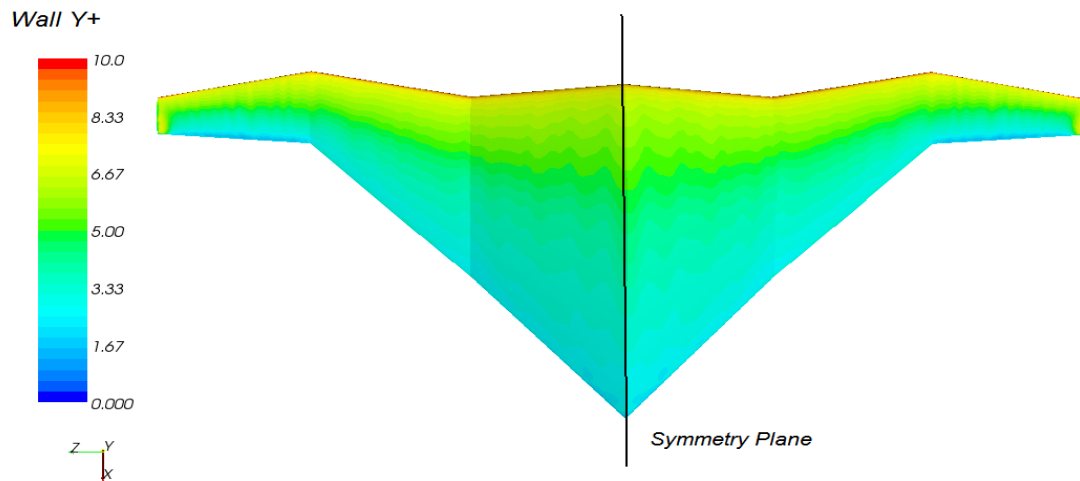


Figure 7-2a. Predicted  $Y^+$  distribution on the wing at  $M = 0.45$  and  $Re = 3 \times 10^7$  and  $\alpha = 10^\circ$  (fine grid).

The practice of leading and trailing edge cell clustering as well as defining smaller cells placed around the wing as employed for the low-speed tests was also applied on these tests. The cell size around the entire wing was created with a width of twice the root chord in the radial direction (see Figure 7-2b).

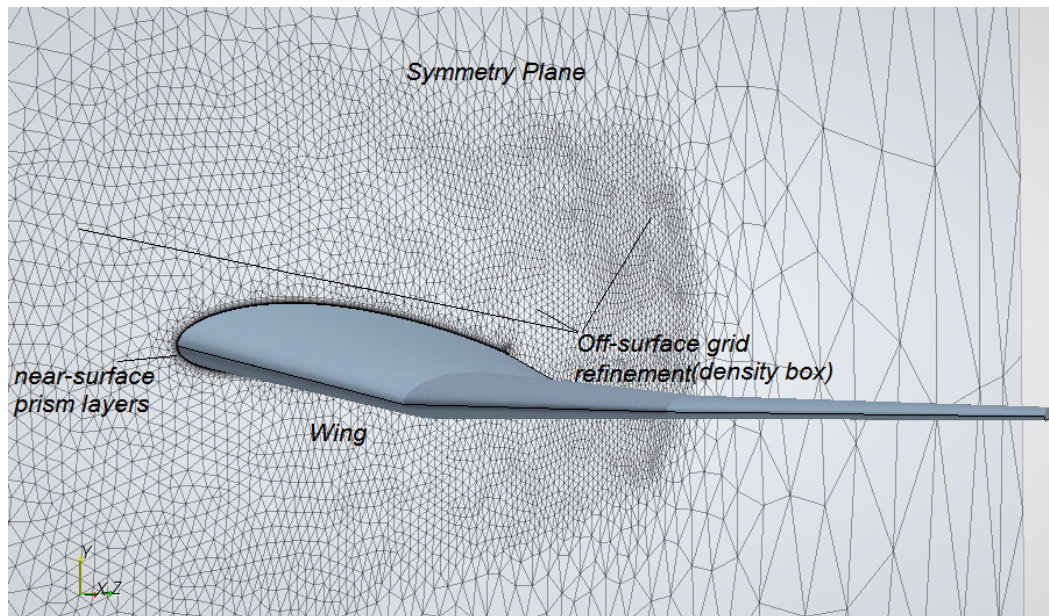


Figure 7-2b. Medium near-surface full-scale grid cell refinement

Lift and drag coefficients for the three different grids are shown in Figures 7-4 and 7-5. From these plots it can be seen that the medium and fine grid results showed a general

trend in behaviour, this is particularly true at lower angles of attack. The coarse grid was insufficient in matching predicting drag coefficients at pre-stall conditions. An entire grid independent solution was still not achieved; further additional refinement would have levelled out the gap between the results for different grids. Such refinement was however limited by the computational resources available seeing as a single run for one angle of attack would take several weeks to converge. These limitations prompted the use of the fine and medium grids throughout the study as the difference in the results in the regions of  $L/D_{max}$  was considered to be small enough for the results to be considered acceptable.

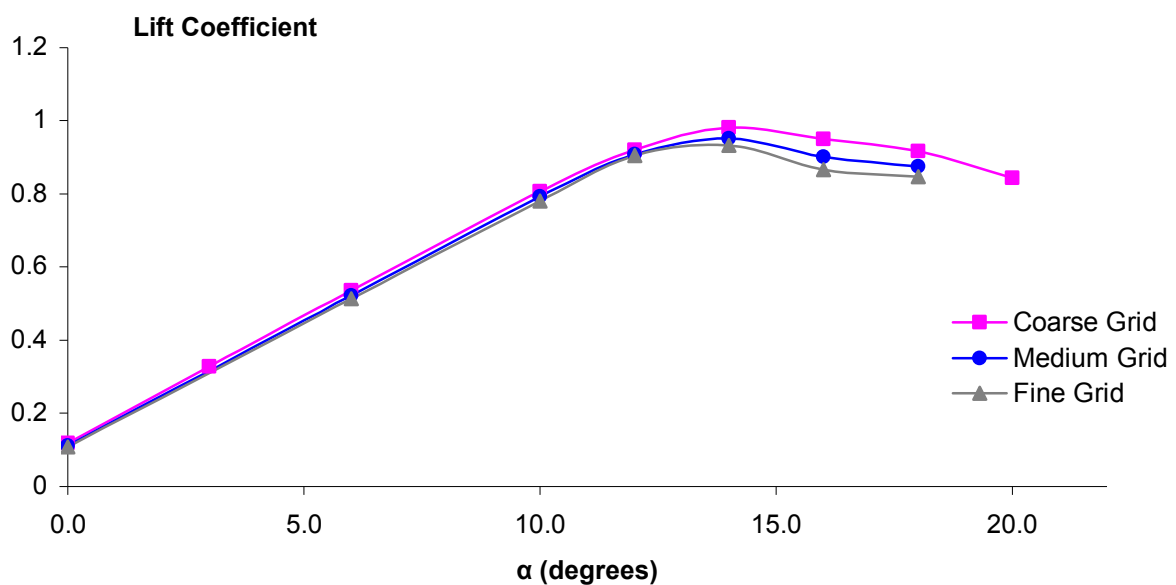


Figure 7-3. Numerically predicted lift coefficients, with three different grids at  $M = 0.45$  and  $Re = 3 \times 10^7$

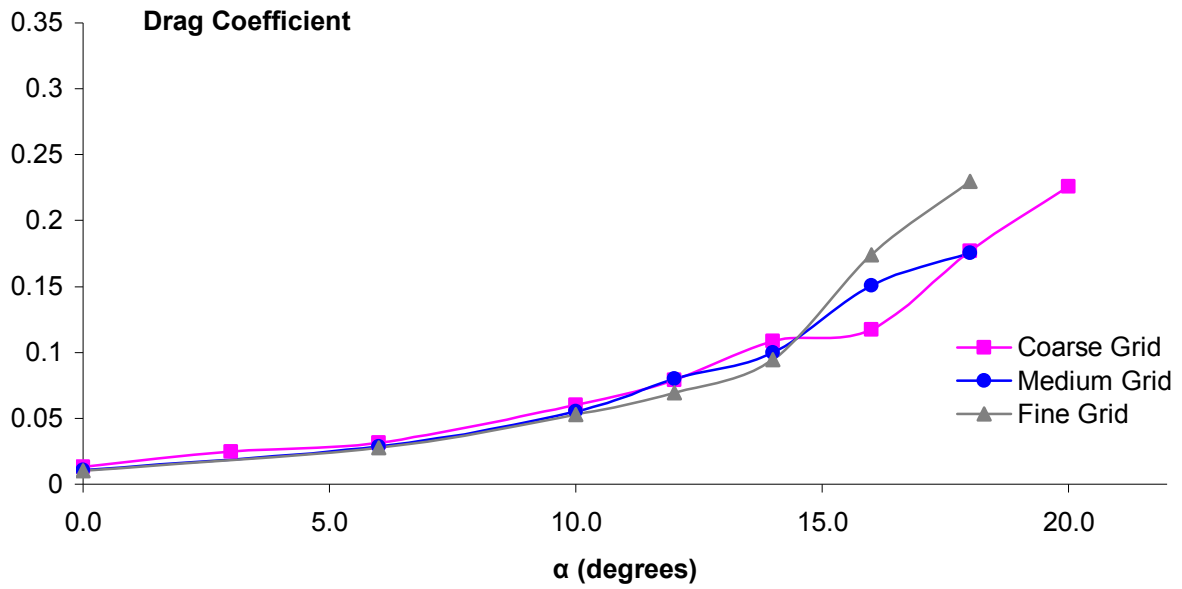


Figure 7-4. Numerically predicted drag coefficients, with three different grids at  $M = 0.45$  and  $Re = 3 \times 10^7$

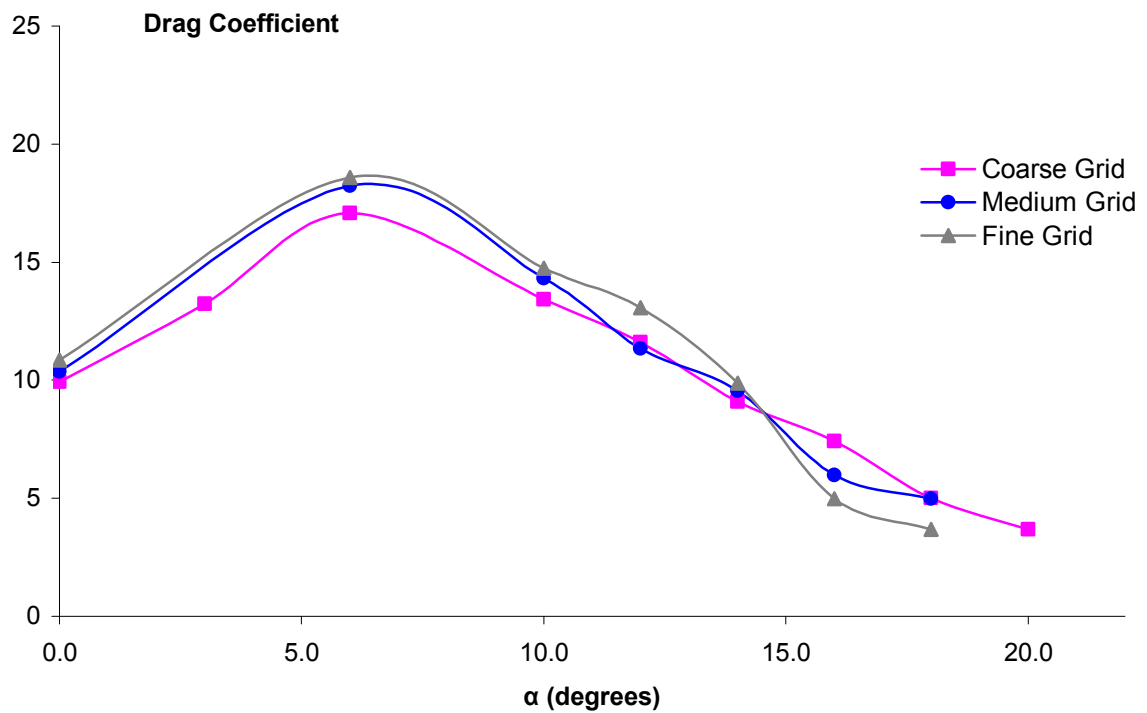


Figure 7-6. Numerically predicted L/D ratio, with three different grids at  $M = 0.45$  and  $Re = 3 \times 10^7$

## 7.2 Convergence Monitoring

Upon discretisation of the governing flow equations, the resulting linearized algebraic equations so formed are usually solved by an iterative method. Consequently, a suitable convergence criterion, identifying an adequate point to stop the solution, has to be defined. Thus, residuals of continuity, momentum, energy and turbulence were monitored for every solution. As in most engineering applications, where possible, a three or more orders of magnitude reduction in the chosen flow parameters was selected as an initial indication to stop the solution.

Residuals are a good indication of solution convergence; however, they are not sufficient unless coupled with the monitoring of the lift, drag and moment coefficients. For this reason, to determine if a steady state had been attained, the coefficients were monitored as well as the residuals. A steady state was defined as no perceptible variation in pitching moment, lift or drag coefficient over several hundred iterations when plotted on a scale with ranges  $\pm 0.001$  about the nominal value.

To accelerate convergence for the full-scale cases the numerical tests were initiated at a lower  $\alpha$  with a segregated solver; predicted results were then employed as initial boundary conditions for the coupled simulations. It was noticed from the study that as angle of attack was increased, the required number of iterations for convergence was increasing as well. This was also accompanied with a reduction in the convergence level, attributable to grid, choice of turbulence or initial boundary condition definition. For higher angles of attack, iterations of the order of 10,000 or more had to be carried out to obtain a steady state.

Figure 7-6 a) is an illustrative example of the residuals for cruise conditions at a Reynolds Number of  $3 \times 10^7$ ,  $M = 0.45$  and an angle of attack of  $6^\circ$  (after 1800 iterations the simulations were switched from segregated to coupled explicit). Figure 7-6 b) is an example of the normal force residuals for cruise conditions at an angle of attack of  $6^\circ$ .

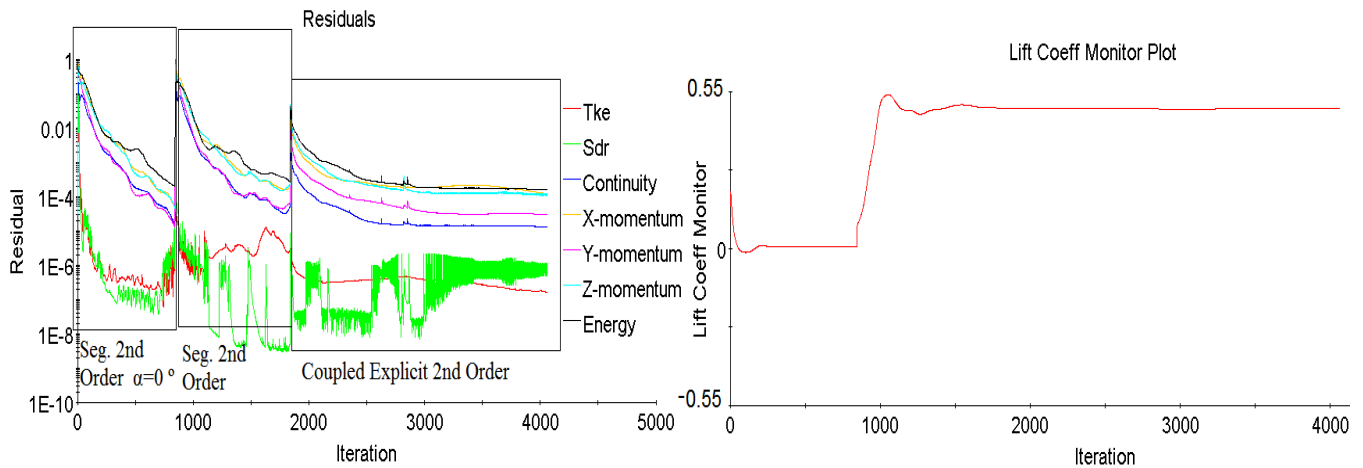


Figure 7-7. Convergence residuals and normal force coefficient monitors for numerical predictions, at  $M = 0.45$  and  $Re = 3 \times 10^7$  and  $\alpha = 10^\circ$ .

### 7.3 Turbulence models

Seeing as a review of literature on the choice of turbulence model only did not reveal a single “best” model for transonic wing type applications, the right choice of turbulence model to be used in the analysis was found to be of paramount importance. For this initial assessment study, a turbulence model dependence analysis was carried out, wherein the effects of the two most popular two-equation eddy-viscosity turbulence models (the  $k-\omega$  SST and the Realizable  $k-\epsilon$  of Shih et al) were investigated and assessed. To ensure that all discrepancies between the two studies were only turbulence model associated, the same grid, boundary conditions, discretisation scheme and turbulence initial conditions were used for both cases. If the flow solutions did not differ significantly it could then be assumed that the resulting flow predictions should be reasonably accurate.

Figure 7-8 depicts a comparison of the lift and drag coefficient results obtained from the two methods employed. Up to  $\alpha = 10^\circ$  virtually no difference in the results was noticed. Inconsistency between the two models began to appear at higher angles of attack, where the  $k-\epsilon$  model under-predicted the stall angle, and consequently the drag coefficients at those angles. Furthermore, the lift at high angles was also higher for the Realizable model, indicating flow attachment even after stall. This is consistent with many earlier observations (Johnson 1994; Lien and Leschziner 1995), where inadequacies of the  $k-\epsilon$  model have been reported (see section 2 for broad review on

turbulence model choice criteria). The above results, coupled with the literature that advocated the use of the k- $\omega$  SST model throughout the rest of the study.

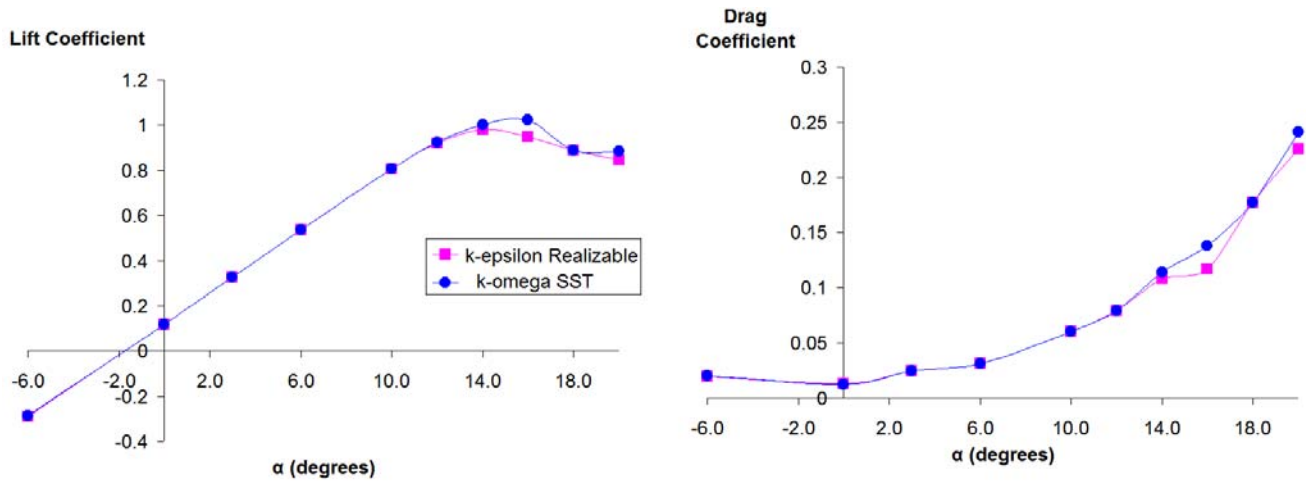


Figure 7-5. Turbulence model sensitivity analyses; numerically predicted a) lift coefficient and b) drag coefficient at  $M = 0.45$  and  $Re = 3 \times 10^7$

#### 7.4 Results of Full-Scale High-Speed Numerical Analyses

In the following, the longitudinal aerodynamic characteristics (lift, drag, pitching moment coefficients and wing pressure distributions) of the W-shaped leading-edge wing, as obtained by both Navier-Stokes and full-potential methods, are presented. Different types of pressure distribution (i.e static and total), for both on- and off-surface cases, are utilized to predict the downstream flow evolution. These are plotted for each angle of attack investigated, and then correlated with the force and moment coefficients for the investigation of the flow behavior.

Figures 7-8 to 7-11 present the lift, drag and moment coefficient data for the full-scale simulation, obtained at  $M = 0.45$ ,  $Re = 3 \times 10^7$  and a range of angles of attack. Lift and drag coefficients are also compared between the two methods, whereas pitching moment coefficient examinations were not possible with full-potential code. As the full-potential method allows for calculations of induced drag only, a general analytical method (Shevell, 1989) was employed to estimate the parasite drag, and so obtain

comparable data (see Appendix for details of the process used to estimate the parasite drag).

**Lift Coefficient**

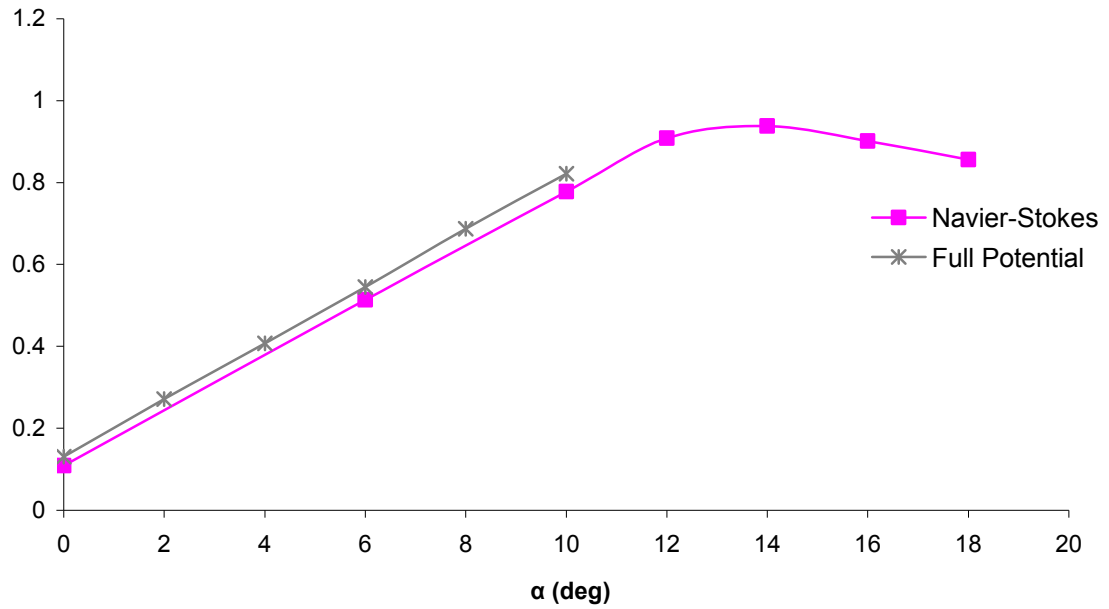


Figure 7-6. Numerically predicted lift coefficients, with two numerical methods at  $M = 0.45$  and  $Re = 3 \times 10^7$

**Drag Coefficient**

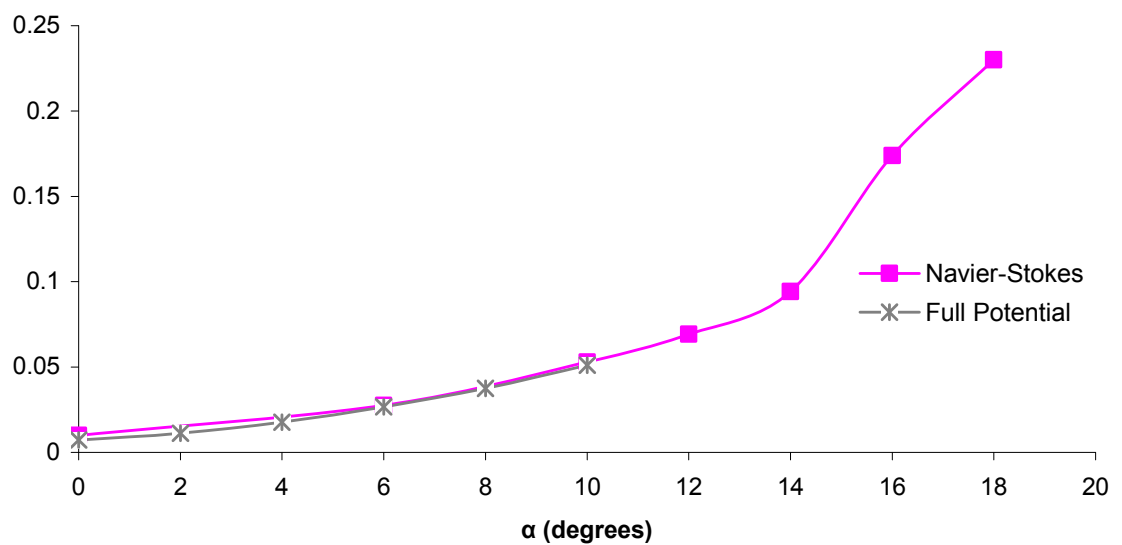


Figure 7-7. Numerically predicted drag coefficient, with two numerical methods at  $M = 0.45$  and  $Re = 3 \times 10^7$

### Drag Coefficient

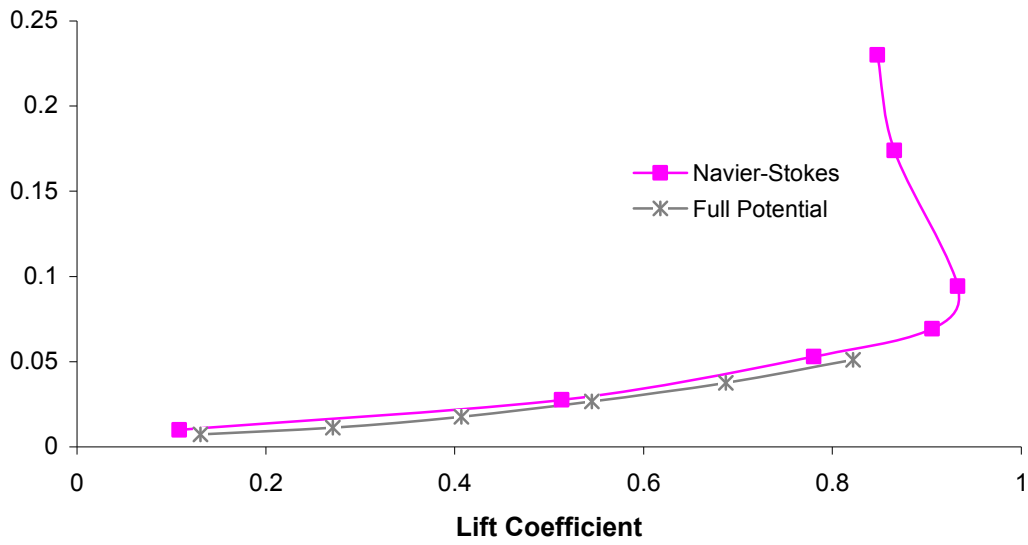


Figure 7-8. Numerically predicted drag vs lift coefficients, with two numerical methods at  $M = 0.45$  and  $Re = 3 \times 10^7$

### Moment Coefficient

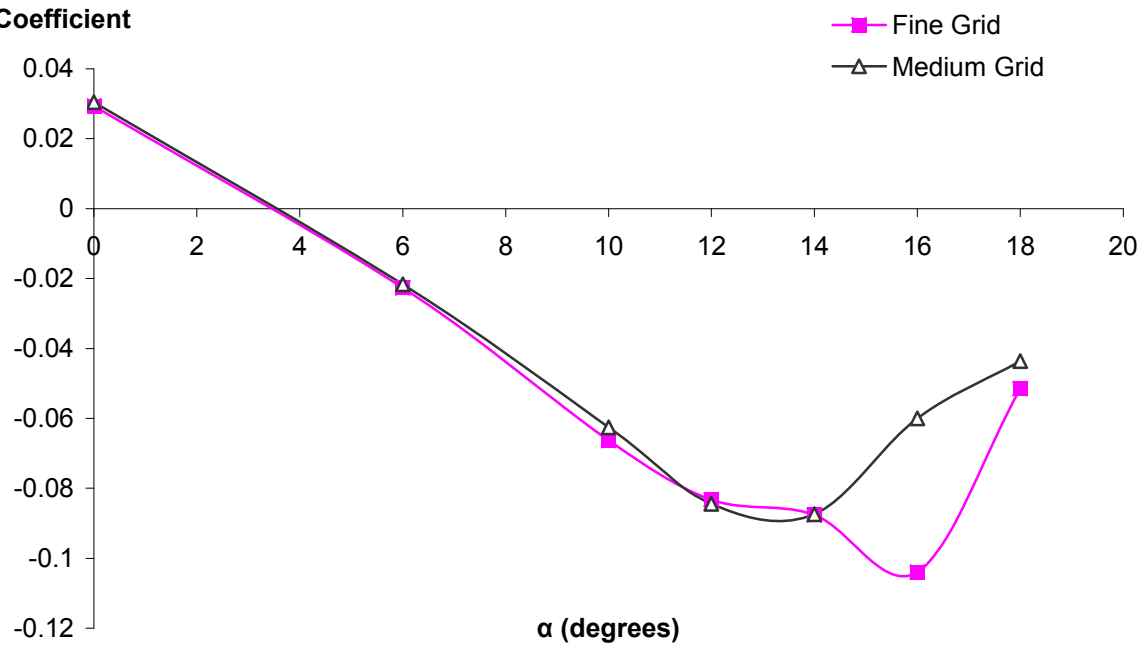


Figure 7-9. Numerically predicted pitching moment coefficients, with two grids at  $M = 0.45$  and  $Re = 3 \times 10^7$

From the above plots (Figure 7-8 to 7-11) it can be seen that there is general agreement between the results obtained by both numerical methods. An offset is identified between the lift curves obtained from the two methods; however, the offset is systematic between the two curves, resulting in the same lift-curve slope. The maximum lift capabilities of the wing are reached around  $14^\circ < \alpha < 16^\circ$ . This is in agreement with the low speed results. At higher angles the lift coefficient decreases; however, due to the computational requirements of carrying out such calculations, no angles of attack further than  $\alpha = 18^\circ$  were tested. It is unlikely that the Jetpod aircraft will experience any flows at  $\alpha > 15^\circ$ .

Drag plots reveal a good agreement between the two methods, even at high angles of attack. Up to  $\alpha = 10^\circ$ , the drag curves are relatively linear with respect to the angle of attack as the drag increases very slowly. At higher angles (above stall) a rapid increase in the drag curves is seen.

The drag vs lift coefficients are plotted in Figure 7-10, these plots shows disagreement between the two methods. This may be mainly attributable to the lift coefficient offset, and the effect is clearly more sensitive at lower angles of attack, where the values of the lift and drag coefficients are small. The full-potential method only predicts the drag due to lift and the additional parasite drag is calculated analytically which may cause the difference between the results. The Navier-Stokes method in the other hand accounts for both pressure and shear drag which vary with angle of attack and are therefore considered more accurate in comparison.

Generally, the wing possesses very good lift-to-drag ratio characteristics. The maximum lift-to-drag ratio of 18.5 is attained in the range of  $5^\circ < \alpha < 8^\circ$ . This is also in agreement with the low-speed tests.

Pitching moment coefficient plots obtained by Navier-Stokes computations on both fine and medium grids are presented in figure 7-11. The only significant variation between the two grids occurred at the stall conditions. Favorable pitching moment

characteristics (i.e.  $\frac{dC_m}{d\alpha} < 0$ ) are observed up to approximately  $\alpha = 16^\circ$ . This shows that the wing is statically stable up to maximum lift conditions. This behavior is consistent

with other observations on combined-sweep wings. Lemme's (1946) study of M-wings concluded that, with the increase of the angle of attack, the wing becomes nose heavy instead of tail heavy. Similar observations have been reported by Purser and Spearman (Purser and Spearman, 1951), whereby the pitching-moment curve for a W-wing was reported to become nearly linear when compared with a regular aft-swept wing. The W-wing was also found to display longitudinal stability near the stall.

To further understand the nature of the aerodynamic characteristics of the W-shaped leading-edge wing, pressure distributions for  $0^\circ < \alpha < 18^\circ$  are presented in the following figures.

Figures 7-12 to 7-17 present the upper and lower pressure distributions at cruise conditions and  $\alpha = 0^\circ, 10^\circ, 12^\circ, 14^\circ, 16^\circ$  and  $18^\circ$  respectively. First thing to note is also, the fact that there is a lack of any strong shockwave features. Up to  $\alpha = 12^\circ$ , a familiar trend in the pressure distributions is noticed on both upper and lower surfaces of the wing. As expected, the cruise wing results indicated the typical localized peak pressure coefficient to be near the leading edge, with gradual pressure recovery farther along the upper surface. With increasing angle of attack, peak suction increases near the wing leading edge and relatively high loading along the inboard portion of the wing can be seen; this is typical of common airfoil behavior due to high velocity flow and thin boundary layers. At  $\alpha = 14^\circ$ , upper-surface pressure distributions show almost constant pressure on the outboard portion of the wing, as well as an adverse pressure gradient on the trailing edge region. It is known that the response of the suction side boundary layer to the adverse pressure gradients, associated with the increasing incidence, dictates the lift and drag behavior. Thus, at this stage, it is considered that the footprints of static stall start to appear. This is also confirmed by the force coefficient plots (see Figure.7-8 and 7-9). At  $\alpha = 14^\circ$  the tip of the wing starts to stall, therefore the lift starts to decrease and the drag to increase. The results suggested that the maximum lift appears to be limited by the design of the wing tip section. Other parts of the wing at  $\alpha = 14^\circ$  show a mostly attached flow.

At  $\alpha = 16^\circ$ , it was observed that, the flow over most of the mid-part and tip sections of the wing had separated. At this stage common signs of stall are now evident, with rapid

pressure change near the leading edge, a relatively constant pressure distribution maintained throughout the rest of the wing's upper surface and adverse pressure gradients detected in the trailing edge region. The effect of stall is apparent in the force coefficient plots, with rapid increase of drag being noted (see Figure 7-9).

Figure 7-10. Predicted pressure distributions on the upper (on the left) and lower (on the right) surfaces at  $\alpha = 0^\circ$ ,  $M = 0.45$  and  $Re = 3 \times 10^7$

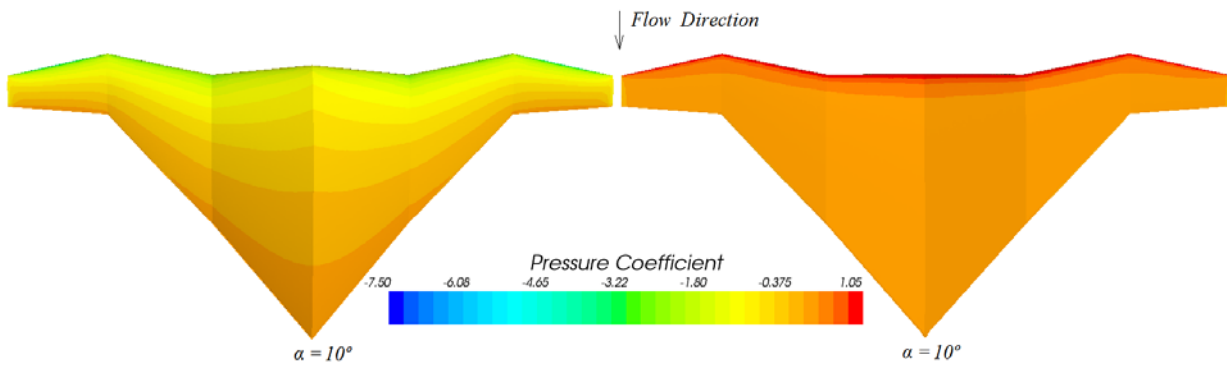


Figure 7-11. Predicted pressure distributions on the upper (on the left) and lower (on the right) surfaces at  $\alpha = 10^\circ$ ,  $M = 0.45$  and  $Re = 3 \times 10^7$

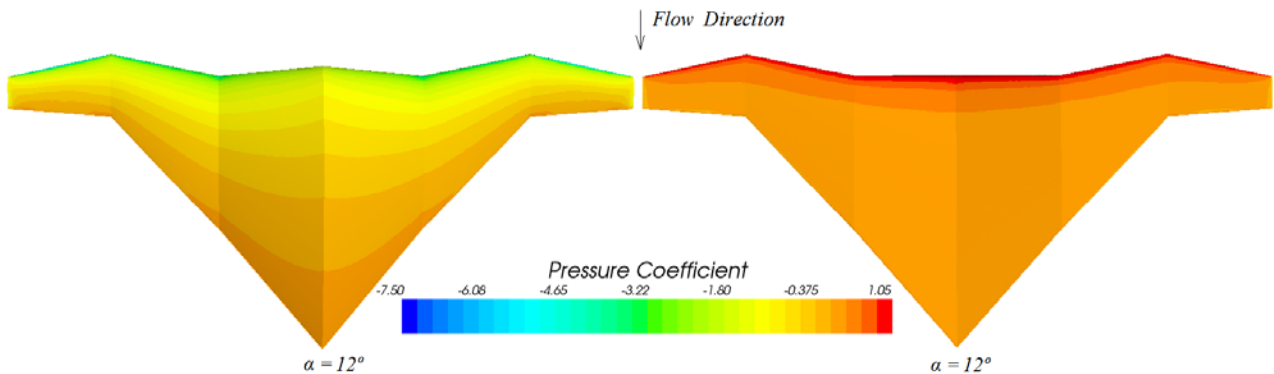


Figure 7-12. Predicted pressure distributions on the upper (on the left) and lower (on the right) surfaces at  $\alpha = 12^\circ$ ,  $M = 0.45$  and  $Re = 3 \times 10^7$

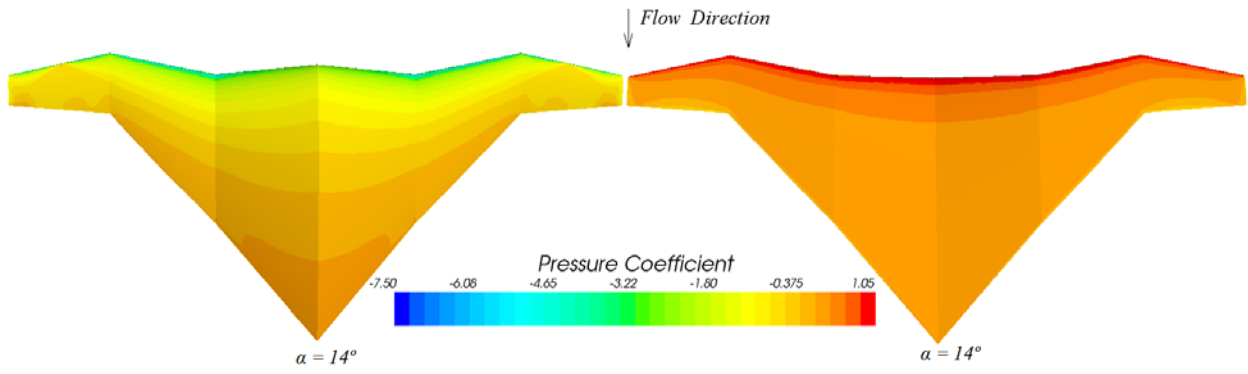


Figure 7-13. Predicted pressure distributions on the upper (on the left) and lower (on the right) surfaces at  $\alpha = 14^\circ$ ,  $M = 0.45$  and  $Re = 3 \times 10^7$

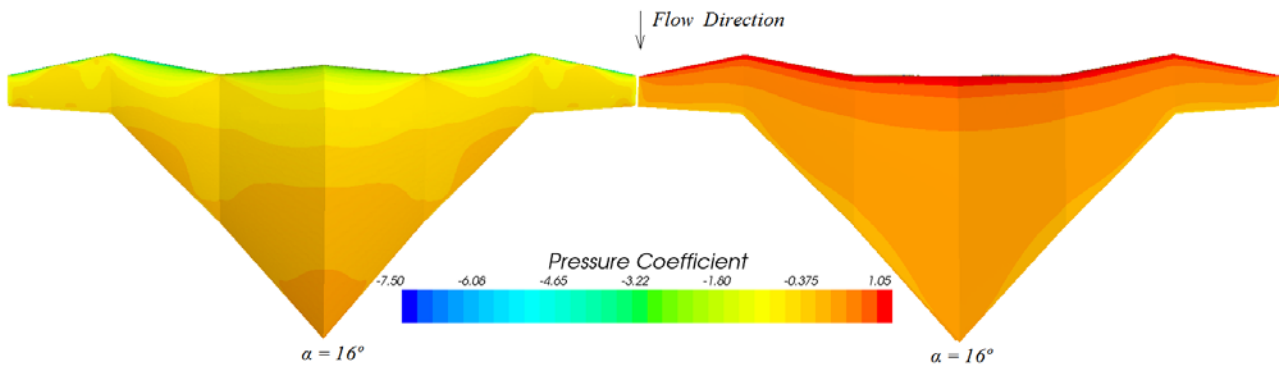


Figure 7-14. Predicted pressure distributions on the upper (on the left) and lower (on the right) surfaces at  $\alpha = 16^\circ$ ,  $M = 0.45$  and  $Re = 3 \times 10^7$

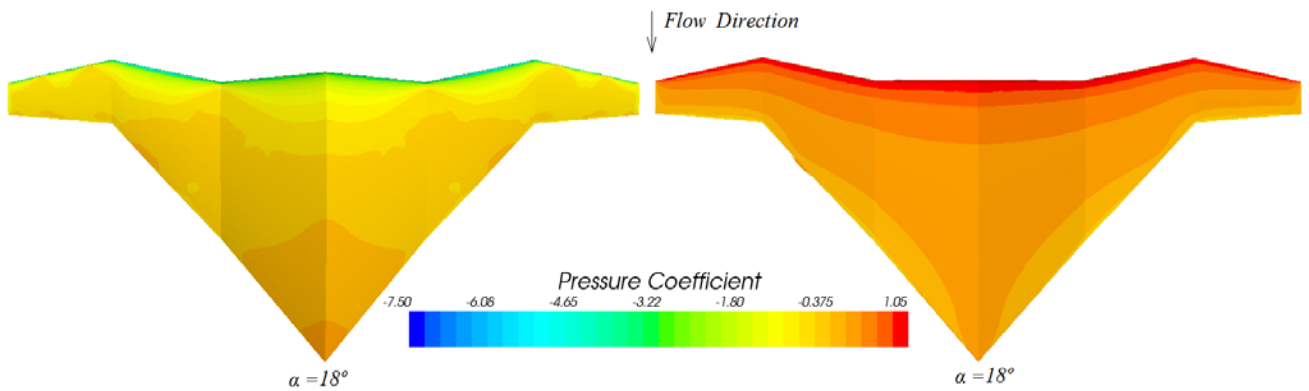


Figure 7-15. Predicted pressure distributions on the upper (on the left) and lower (on the right) surfaces at  $\alpha = 18^\circ$ ,  $M = 0.45$  and  $Re = 3 \times 10^7$

Generally, the pressure coefficients near the leading edge became increasingly more negative with increasing angle. Simultaneously, on the lower surface of the wing, pressure distributions reveal a pressure increase with angle of attack.

In the main, as expected, wing loading decreased at angles of attack higher than the stall angle. For both post-stall angles investigated ( $\alpha = 16^\circ$  and  $\alpha = 18^\circ$ ), the pressure distribution at the crank section between the inboard and central wing showed no severe pressure gradients. This might be an indication of separated flow at the crank; however, additional investigations with off-surface flow visualization are necessary.

In order to verify the flow performance, comparisons of the shear-stress profile were made, the results of which are plotted, side-by-side, in the subsequent figures.

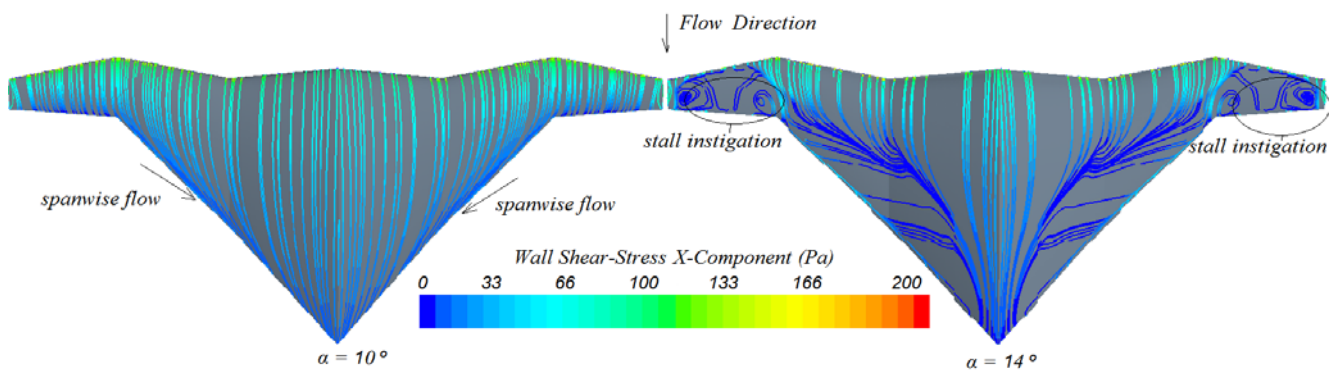


Figure 7-16. Predicted wall shear stress streamlines at  $\alpha = 10^\circ$  and  $\alpha = 14^\circ$ , at  $M = 0.45$  and  $Re = 3 \times 10^7$

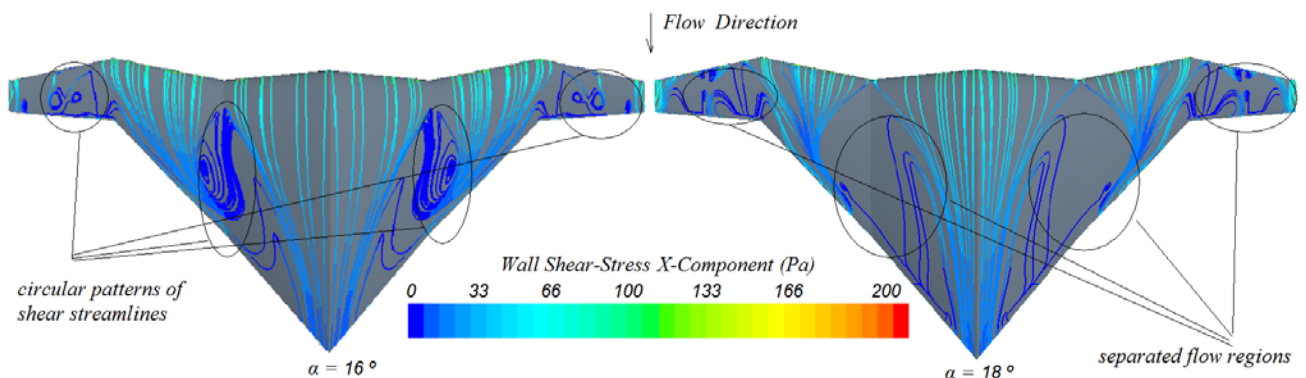


Figure 7-17. Predicted wall shear-stress streamlines at  $\alpha = 16^\circ$  and  $\alpha = 18^\circ$ , at  $M = 0.45$  and  $Re = 3 \times 10^7$

The wall shear-stress streamline plots reveal the flow activities with increasing angle of attack; the direction of the flow is of importance in this case as comparison of the wing with regular sweep wings is to be made. Shear streamlines show a relatively straight flow for angles of  $\alpha < 10^\circ$ . Features indicative of attached flow were visible in the streamlines for  $\alpha < 12^\circ$ . However, at  $\alpha = 10^\circ$  and above the flow starts to move inboard as the angle of attack is increased. The strength and significance of this action is increased with angle of attack, as depicted in Figure 7-18 for  $\alpha = 14^\circ$ .

These features are in a different manner to a regular aft-swept design, as the spanwise flow is not only directed towards the outboard section (see Figures 2-4 and 2-3 for aft sweep behavior). Most of the inboard flow shifting is noticed at the central wing, with slight inboard spanwise movement noted at the inboard section of the wing. This performance is in accordance with forward-sweep wing behavior, which associates well with the forward-sweep (central) section of the wing. Nevertheless, the inboard aft-swept section was also affected by this characteristic of the central part.

The uncommon spanwise motion of the inboard section may be affected by the higher degree of aft-sweep of the central wing dictating the flow behavior. The process of inboard motion has been previously explained as a tip stall delay characteristic (see section 2 for a review on forward and aft sweep wing aerodynamic characteristics). The outboard section of the wing still maintained the aft-sweep trait where the tip is the stall start-up region.

When separation occurred the wall streamlines run very close together and approach a tangent or a separation line. The appearance of circular streamlines indicates separated flow regions, as well. These can be initially observed near the tip region for  $\alpha = 14^\circ$ . These regions show high spanwise flow which is highly three-dimensional. At  $\alpha = 16^\circ$  and  $\alpha = 18^\circ$  most part of the wing now exhibits irregular streamlines (Figure 7-19). Trailing edge separation streamlines can also be seen for most part of the wing above stall angles. The constrained separation lines at mid-wing for  $\alpha = 16^\circ$  have a circulatory behavior. The constrained streamlines present the so-called foci and saddle points from topological analysis (Tobak and Peake, 1982). Such behavior was detrimental to the wing performance as a drop in lift and increase in drag was noticed. The extent and

effect of such a pattern will be discussed later with reference to off-surface visualization of the particle traces.

It can also be observed that for all angles investigated, tip section shear stress was never zero, which is indicative of a tip vortex. Closer examination of the off-surface flow is necessary in the locality of stall start-up. It is believed that the combination of sweep on a single design is deterring the flow from the outboard direction, which suggests a weaker tip vortex. This is a highly desirable feature for an air-taxi type aircraft, as the separation distance between individual aircraft could be reduced.

In order to find the associated separation lines and possibly identify the cause of separation, contours of wall shear-stress have also been investigated. The manner of such contours on the wing's upper surface (Figure 7-20) was typical of a regular wing at similar conditions, it being characterized by large values near the leading edge which decrease downstream due to slowing flow and thicker boundary layers. Close investigations of the wall shear-stress contours revealed regions of near-zero shear stress at various small parts near the leading edge (see Figure 7-20). This conduct is of a similar nature as the separation bubbles noted for subsonic blunt leading-edge wings. Separations of such kind may be associated with regions of local supersonic flow.

The above results initiated another investigation, those of Mach contour lines, to observe whether any detrimental effect on the wing performance is associated with this phenomenon.

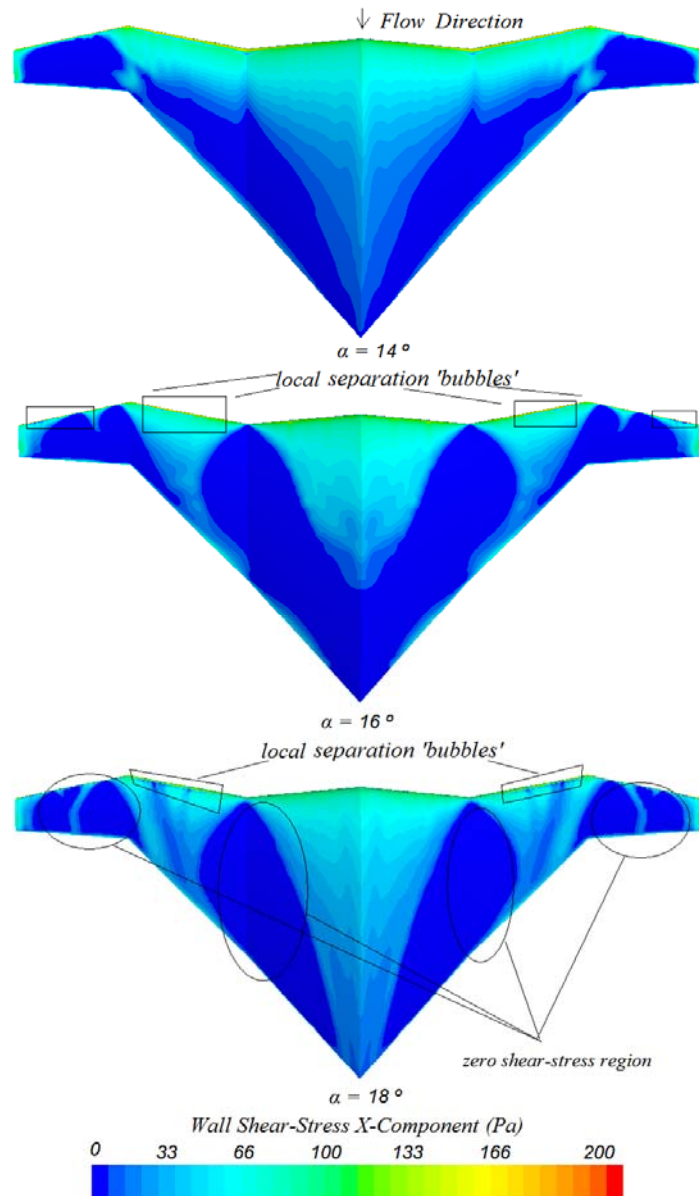


Figure 7-18. Predicted wall shear stress contours at  $\alpha = 16^\circ$  and  $\alpha = 18^\circ$ , at  $M = 0.45$  and  $Re = 3 \times 10^7$

Figure 7-21 depicts the various spanwise Mach number contours on the upper surface of the W-wing at  $\alpha = 12^\circ$ ,  $\alpha = 14^\circ$  and  $\alpha = 18^\circ$ . These investigations were carried out in order to determine whether the results from figure 7-20 were associated with regions of high local Mach number.

The investigation revealed that regions of local supersonic flow appeared as early as  $\alpha = 10^\circ$ , although they are not visible on the shear-stress distributions. The supersonic pockets have shown no particular effects on the aerodynamics, as no irregularities have

been noticed at and above  $\alpha = 10^\circ$ . Local supersonic areas have been observed for all angles above  $\alpha = 10^\circ$ , with the highest strength noticed at max lift conditions. This is particularly true at the intersection of the inboard and central sections of the wing, where the highest Mach numbers have been observed. (See figure 7-21 at  $\alpha = 14^\circ$ ). However, it is believed that the static stall appearance at this angle is associated with the tip stall, rather than any unfavorable effects associated with local shock regions. Nonetheless, the strength of the shock may influence the wing behavior at subsequent angles of attack, and may induce early separations on the leading edge of the wing above stall angles. At this stage, such phenomena are not of great interest as the wing incidence would not normally be increased beyond stall incidence at cruise conditions.

It needs to be mentioned that the above indications of local shock regions prompted another grid resolution study, concentrating on the shock locations. Further local refinements, especially for the high  $\alpha$  cases, were carried out to smooth the uncertainties of the shear and pressure results. A representation of the refined grid is given below (Figure 7-22). Fortunately, the results obtained for pressure and shear monitoring showed no difference from the results obtained with the original grid. A very small difference was detected in the lift and drag coefficients between the two grids. However, as no major disagreement between the two grids was noted, the results obtained with the original grid are considered reasonable.

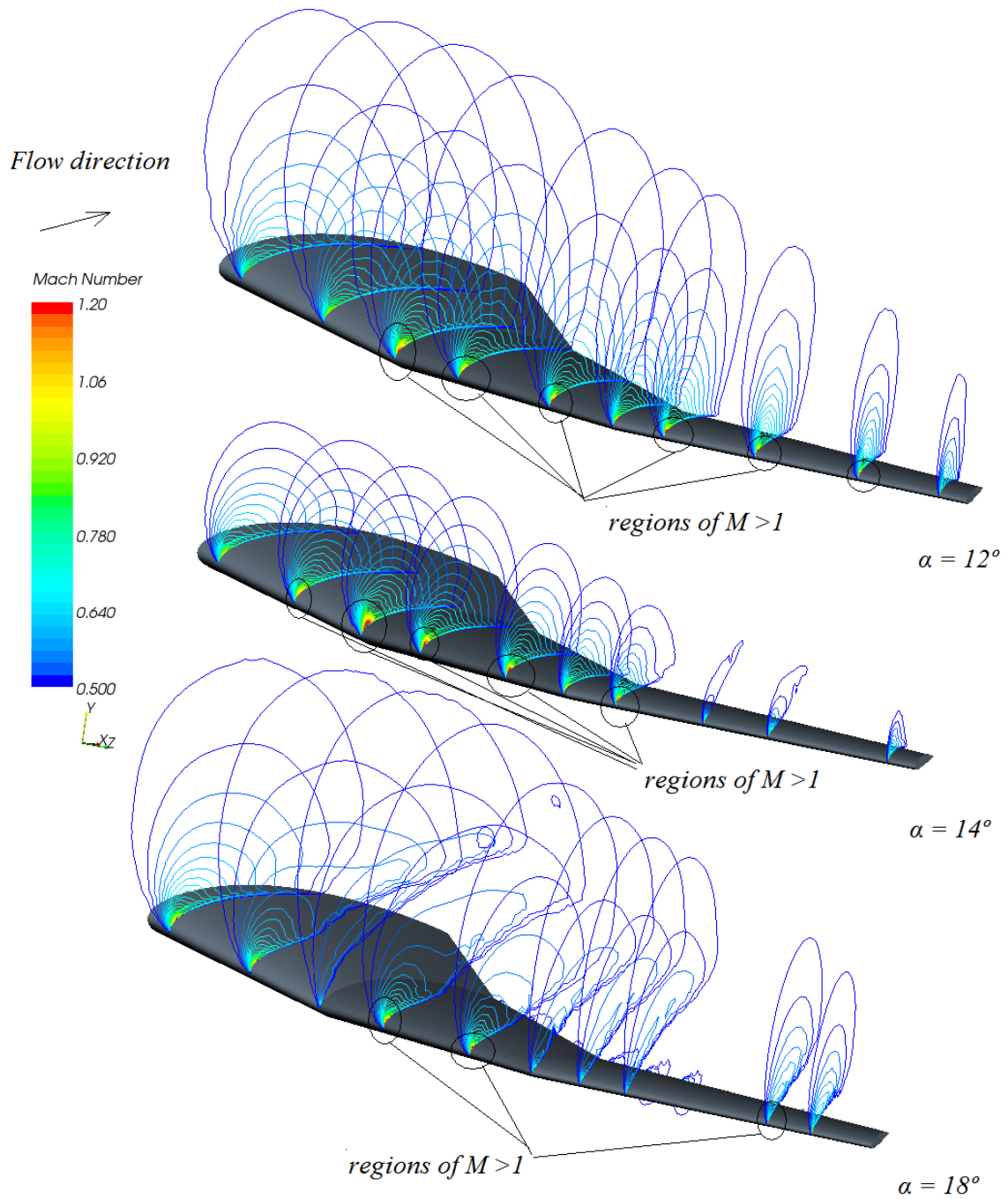


Figure 7-19. Predicted Mach number distributions at  $\alpha = 12^\circ$ ,  $\alpha = 14^\circ$  and  $\alpha = 18^\circ$ , at  $M = 0.45$  and  $Re = 3 \times 10^7$

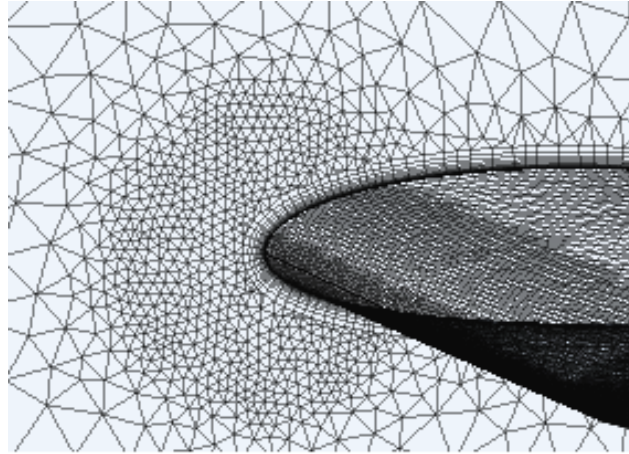


Figure 7-20. Leading-edge refined grid.

To complement all of the above results, such as adverse pressure gradients associated with pressure contours, local shock regions and shear-stress contours, off-surface total pressure coefficient plots have been presented.

Figure 7-23 and 7-24 illustrate the total pressure coefficients at  $\alpha = 6^\circ$ ,  $\alpha = 10^\circ$ ,  $\alpha = 14^\circ$  and  $\alpha = 16^\circ$  for numerous chordwise locations between  $0 < x/c < 1$ . A comparison of total pressure distributions for various alpha conditions of the wing were employed to potentially verify the reasons for stall appearance; in particular, whether it is related to the geometry, flow physics or both.

Generally for all plots one can see the roll-up of the vortex around the tip of the wing from the lower surface to the upper surface which corresponds to the low total pressure distributions at the wing-tip region, which is present for all the plots shown.

It was observed that the flow over most of the wing remains attached up to  $\alpha = 12^\circ$ , at which point the trailing edge total pressure distributions reveal very low values, indicative of the onset of trailing edge separation. At  $\alpha = 14^\circ$ , the separation region described previously for the outboard section has been confirmed. Nevertheless, separation does not seem to be associated with the junction between the various sweeps as the leading edge flow remains attached even at higher angles of attack. The onset of the static stall at  $\alpha = 14^\circ$  is caused by the adverse pressure gradient and consequently

trailing edge separation initiated at approximately  $\alpha = 12^\circ$ . At this stage the rest of the wing seems to maintain an attached flow.

At  $\alpha = 16^\circ$ , the inboard wing shows mostly separated flow with a small region of low total pressure. This region might be an onset of separation at this section. It is unclear whether the separation is due to the geometry of the inboard leading edge crank or a product of regions of local supersonic shocks noticed to have the highest Mach numbers at the exact location at  $\alpha = 14^\circ$  (depicted in Figure 7-21). Interestingly, at  $\alpha = 16^\circ$ , most of the central wing seems to exhibit attached flow, as, unlike the other areas, no regions of low total pressure are noticed on this section. These results show that the combined sweep actually appears to be aiding in maintaining flow attachment, since the forward swept part of the wing terminates the propagation along the entire/rest part of the wing. It also needs to be mentioned that the high-chord at the centerline gives lower lift coefficient values and helps to delay stall.

Although, not demonstrated here at  $\alpha = 18^\circ$ , the small separation pocket, described above, increased, giving separated flow at the leading edge of the inboard crank. However, even at  $\alpha = 18^\circ$  there is residual leading-edge suction. This is indicative that the big inboard separation is still trailing edge separation that rapidly moves up. It is believed that slight optimization of the outboard section of the wing might improve further the aerodynamics of the W-wing; both in terms of stall delay as well as increasing the maximum lift conditions. By contrast, the inboard and central parts of the wing still show good characteristics, such as less outboard spanwise flow as well as maintaining flow attachment even after the stall angle of attack.

As an additional feature of the current wing Figure 7-25 illustrates spanwise lift coefficient distribution at  $\alpha = 6^\circ$  where  $L/D_{max}$  is reached. It can be observed that the lift coefficient distribution varies from the elliptical loading in conventional concepts. Lift coefficients in the order of 0.8 are reached at 20% span. A steep decline is then noted reaching lift coefficients of 0.34 at the tip of the wing.

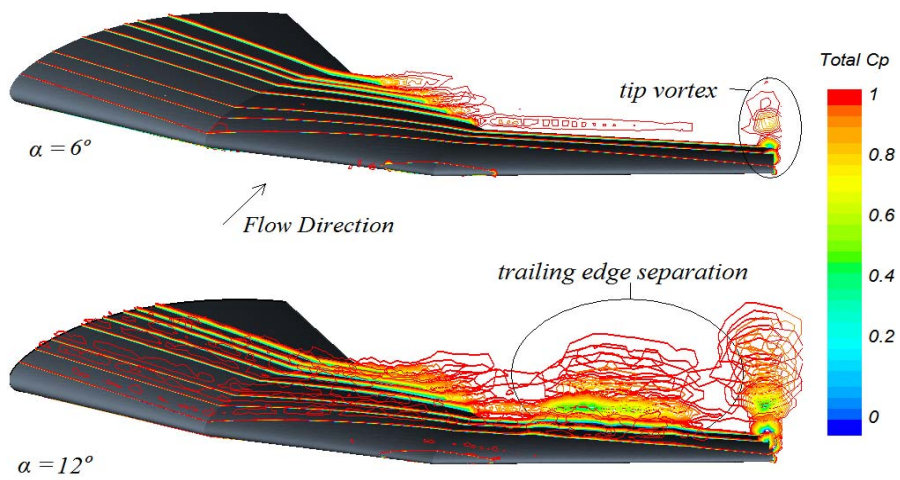


Figure 7-21. Predicted total pressure distributions at  $\alpha = 6^\circ$ ,  $\alpha = 12^\circ$ , at  $M = 0.45$  and  $Re = 3 \times 10^7$

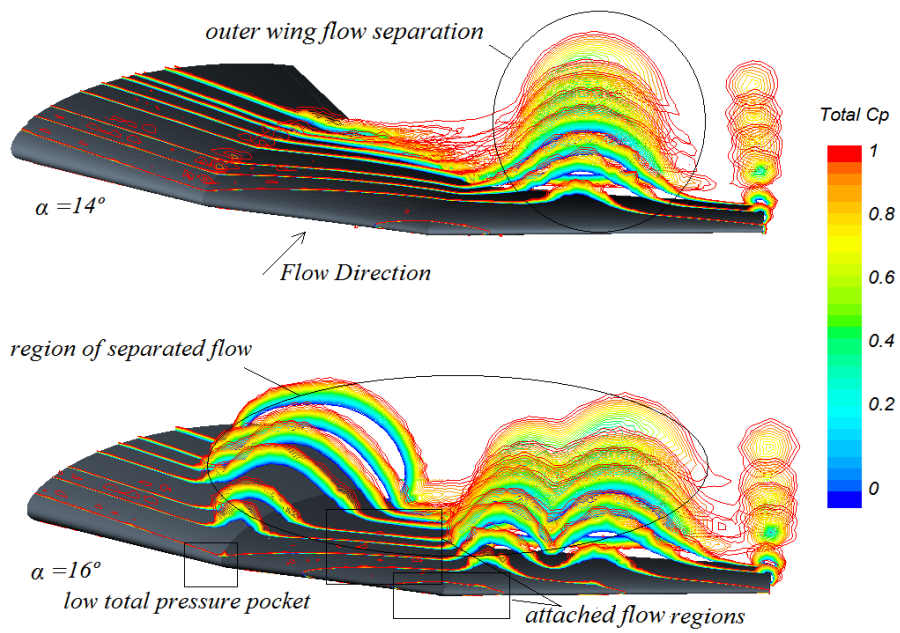


Figure 7-22. Predicted total pressure distributions at  $\alpha = 6^\circ$ ,  $\alpha = 12^\circ$ ,  $\alpha = 14^\circ$  and  $\alpha = 16^\circ$ , at  $M = 0.45$  and  $Re = 3 \times 10^7$

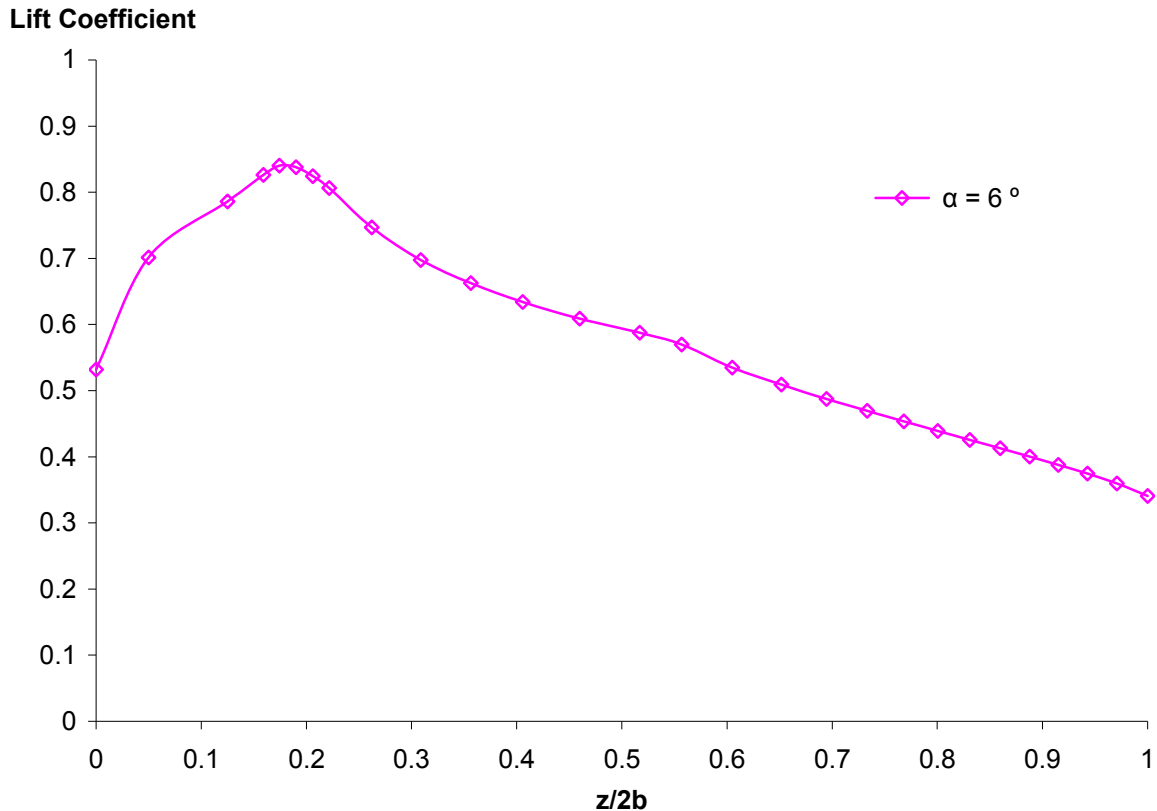


Figure 7-23 Wing spanwise lift distribution at  $L/D_{max}$  at  $M=0.45$  and  $Re = 3 \times 10^7$

### 7.5 Results Near-Wake Analysis

This part is a follow-up investigation on the regions of interest that were identified in the low-speed study described in section 6 of this thesis. In brief, to recap from this study, the near-wake analyses at angles of  $\alpha = 14^\circ$  and above showed that the wing exhibited some form of vortical or rotational flow. For that reason, in order to explain and verify the reappearance of such structure at high Reynolds Number, near-wake momentum deficit analyses were carried for the W-wing at high-speed conditions. These features are of particular interest because it is known that the influence of the pressure gradient from the wing on wake development and structure are very significant (Liu 1999).

The following Figures (7-26 to 7-28) represent the associated wake total pressure coefficients obtained at  $x/c_r = 1.5$  and angles of attack of  $\alpha = 10^\circ$ ,  $\alpha = 14^\circ$ ,  $\alpha = 16^\circ$  and  $\alpha$

= 18°. In accordance with the low speed results, the near-wake plots at  $\alpha = 10^\circ$  indicate typical wake features, comparable to conventional wings, where the wake of the wing is relatively constant with a total pressure coefficient of 0.8-0.9. As expected, the tip vortex increases in strength with increasing angle of attack. At  $\alpha = 14^\circ$ , illustrated in Figure 7-26, the inboard vortex seems to appear in the near-wake at approximately  $z/b = 0.3$ . This is also in accordance with the low-speed tests. As noted previously this vortex is different from the tip vortex; also the strength and rotational shape are more prominent in the cruise results than in the low speed results (see Figure 6-17 for comparison). The scale of the secondary inboard vortex is observed to be of wider diameter than the tip vortex, and of greater strength. However, a comparison between the secondary and tip vortices may not be entirely viable, as scatter in correct strength formation (which was also noted in the low-speed analyses) may be due to the grid size at the tip region. Nevertheless, the profile and general behaviour have been proved to be of accurate representation, as the results from section 6 of this thesis had initially shown.

Such rotational behaviour has in the past been described as a characteristic of the boundary layer separation at that region. This phenomenon, as illustrated by Gad-el Hak and Bushnell, is a consequence of separation where the rotational flow region next to a wall abruptly thickens and the normal velocity component increases (Gad-el-hak and Bushnell 1991).

The point of boundary layer separation, as described by Gad-el-hak and Bushnell does not necessarily coincide with the point of vanishing wall shear. This was found to be true in this study too. As illustrated in the above plots (Figure 7-18 and 7-19), the separated region and the inboard vortex next to the wall, particularly for  $\alpha = 16^\circ$ , have been associated with the rotational features observed in the near-wake.

The effect of the secondary flow may also be noticed in the drag plots; it appears that the vortical structure may be responsible for the increase in drag at angles of  $\alpha = 14^\circ$ , and above.

Figure 7-28 also shows the near-wake behavior for the higher angles of attack ( $\alpha = 16^\circ$  and  $\alpha = 18^\circ$ ). In these conditions, the appearance of the structure was more pronounced,

and the vortex was seen to grow in diameter. At  $\alpha = 16^\circ$ , most of the inboard stall described in previous plots can now also be associated with large stall regions, with the lowest total pressures noticed at  $z/b = 0.1$ . The above practice is repeated for  $\alpha = 18^\circ$ , with growing stall area and particularly altered secondary vortical structure. The secondary vortex is also noted to shift inboard with increasing angle of attack: the greatest rotation noticed at  $\alpha = 18^\circ$  is now at  $z/b = 0.25$ .

Spalart has reported that multiple vortices can merge, particularly if co-rotating, and if the distance between them is smaller than the diameter of the core (Spalart 1998). Such an occurrence is particularly associated with sharp leading-edge wings or double delta wings and this seems to be true in this case as the vortices seem to co-rotate and, as previously stated, the distance between them increases with angle of attack. The resulting wake instability and roll-up is very similar to what is seen on double delta wing and gives the impression that the occurrence of such behavior is associated with the wing crank.

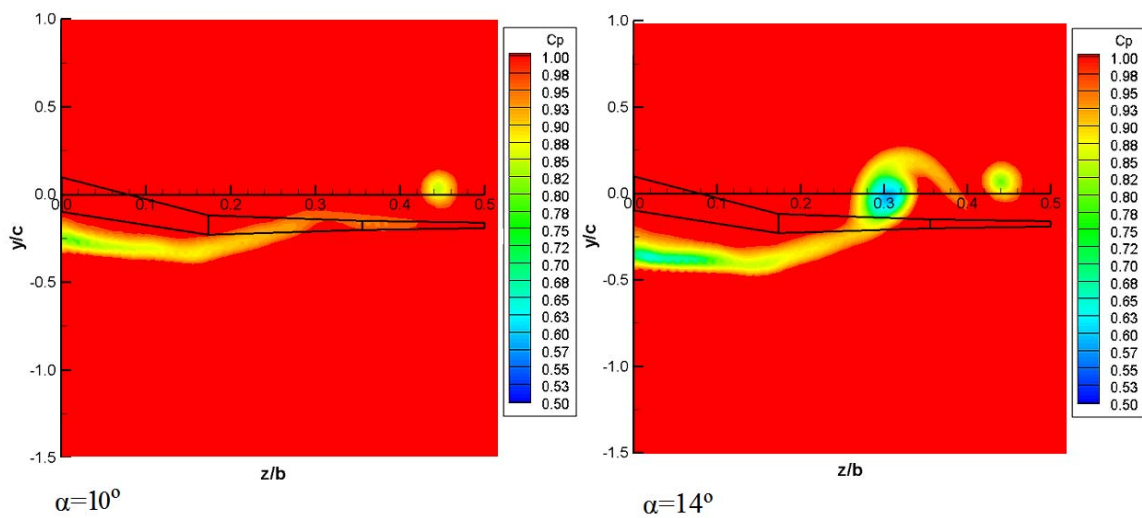


Figure 7-24. Near-wake total pressure coefficient plots at  $x/c_r = 1.5$ ,  $\alpha = 10^\circ$  and  $\alpha = 14^\circ$ , at  $M = 0.45$  and  $Re = 3 \times 10^7$

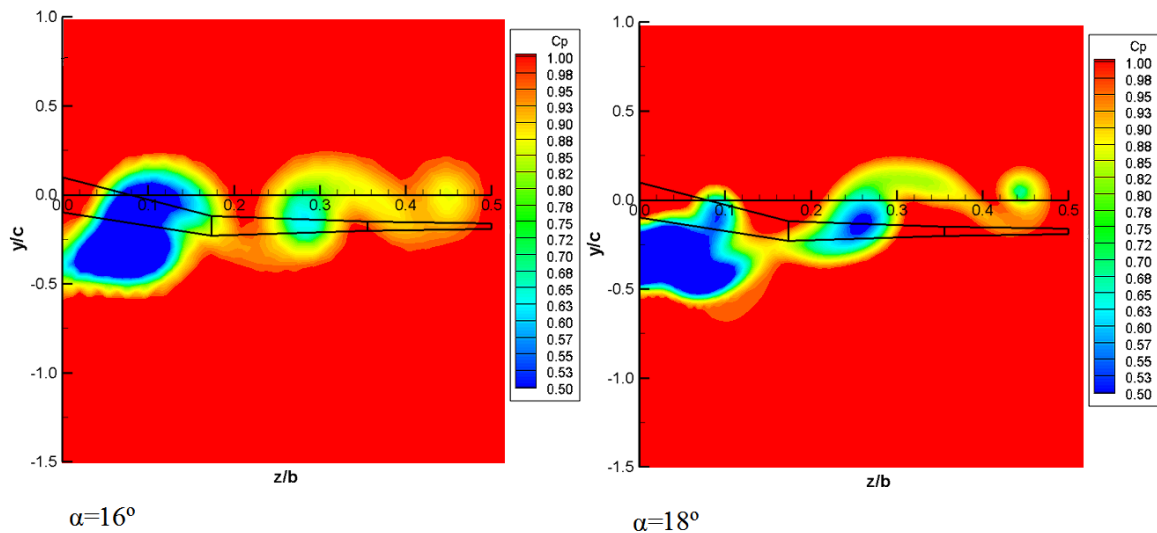


Figure 7-25. Near-wake total pressure coefficient plots at  $x/c_r = 1.5$ ,  $\alpha = 16^\circ$  and  $\alpha = 18^\circ$ , at  $M = 0.45$  and  $Re = 3 \times 10^7$

To precisely determine the point where the inboard vortex began, off-surface streamlines in conjunction with the near-wake total pressures are presented below to capture flow activities near the wing surface.

Flow streamlines over the W-wing, at  $\alpha = 14^\circ$ ,  $\alpha = 16^\circ$  and  $\alpha = 18^\circ$  can be seen in the plots below (Figures 7-29 to 7-31). Inward spanwise flow movement was noted for  $\alpha = 14^\circ$ , together with the launch of the secondary flow at approximately  $z/b = 0.4$ . This is the region noted previously as the onset of the static stall, and consequently as it can be seen, the onset of the secondary flow. A close-up investigation of the streamlines at the spanwise separation position reveals that the vortical feature, similar to stall cells in conventional wings, is then driven downstream by the free-stream flow. The rotated flow is due to boundary layer separation accompanied then by a thickening of the inboard vortex region and instigation of vorticity. Interestingly, it was found that this inboard vortex manifested from the mid-part of the wing, and not the junction between sweeps. Therefore, leading to the conclusion that the inboard vortex may not arise from a local geometry feature (i.e. junction between sweeps) but from the global wing geometry and its associated flow physics.

A closer examination of the off-surface streamlines in the region of rotation onset was carried out at  $\alpha = 16^\circ$  (see Figure 7-30). These plots clarify the earlier observed on-

surface recirculation region discussed with shear-stress behavior (Figures 7-20). It can now be made clear that the circulated flow observed in Figure 7-20, rolls-up, which is usually associated with vortical onset of the so-called stall cells. This type of rotational feature is also referred to as a “tornado-vortex” (Leary, 2001). The ever-increasing stall cell region, may also be seen in Figure 7-31 for  $\alpha = 18^\circ$ .

It is known that downstream of the separation point the shear layer either passes over a range the region of recirculation fluid and reattaches to the body surface or forms a wake and never reattaches to the body (Gad-el-hak and Bushnell 1991). The latter is the case here.

The occurrence of the deep stall on the inboard section of the wing will have possible implications on the tail-plane position. High tailplane positions may be necessary to avoid interference and unfavourable effects of deep stall. Although no extensive studies have been carried out to investigate these effects it is believed that low tail efficiencies and incidence would be affected by the stall of the W-wing at higher angles of attack. However, should a decision on employment of leading edge devices be made, the extent of deep stall can be delayed.

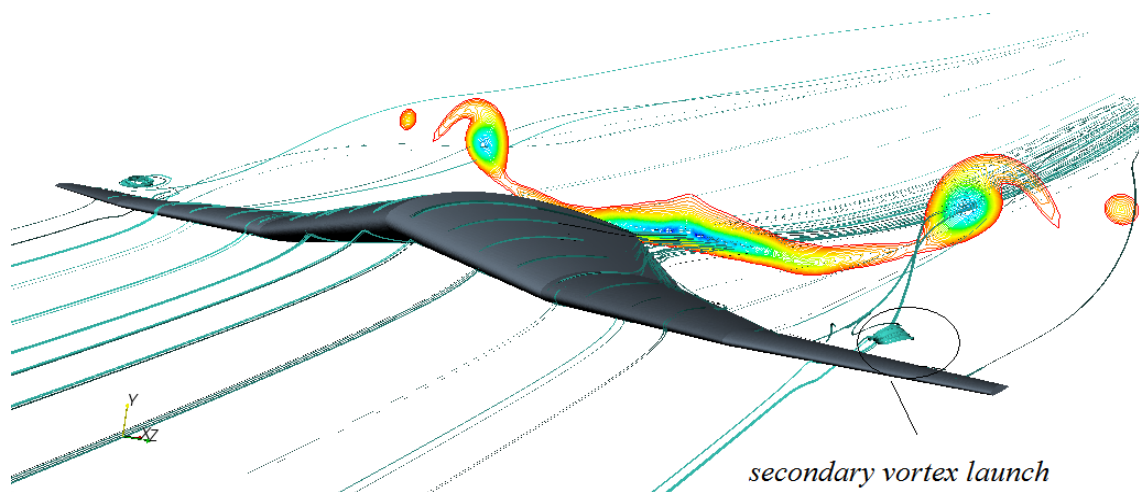


Figure 7-26. Off-surface particle traces at  $\alpha = 14^\circ$ , at  $M = 0.45$  and  $Re = 3 \times 10^7$

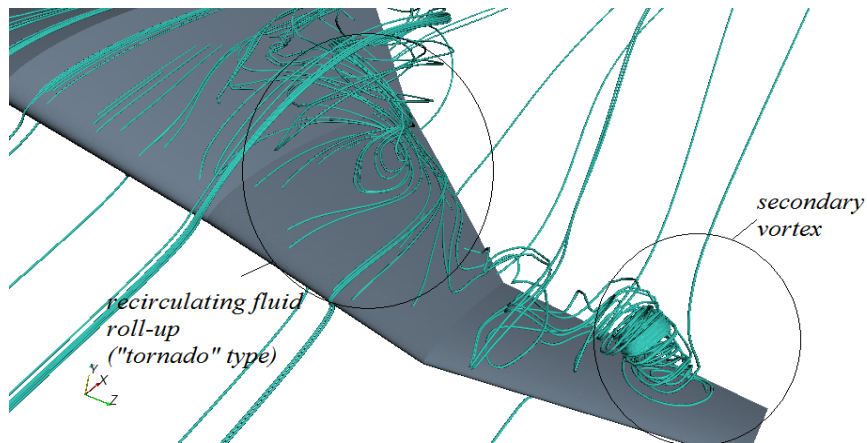


Figure 7-27. Off-surface investigations of the source of the vortical structure at  $\alpha = 16^\circ$ , at  $M = 0.45$  and  $Re = 3 \times 10^7$

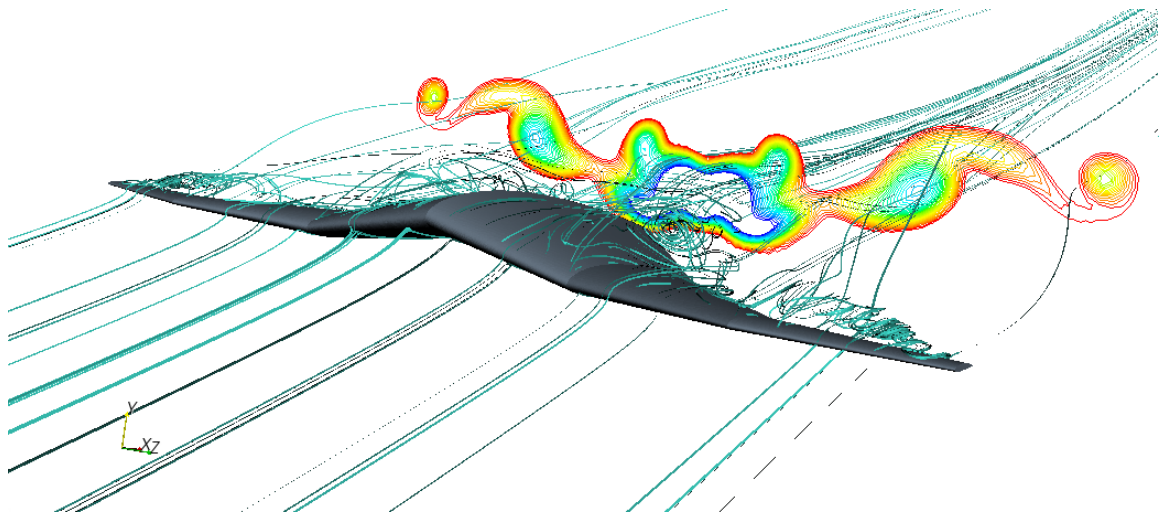


Figure 7-28. Off-surface particle traces at  $\alpha = 18^\circ$ , at  $M = 0.45$  and  $Re = 3 \times 10^7$

## Summary

The general aim of this section was to establish the aerodynamic behavior of the wing at cruise conditions, by numerical analyses only. The above discussion details the predicted results of the flow field characteristics as a continuation of the low-speed tests described in the previous section. A comprehensive investigation on the longitudinal characteristics has been carried out, with the aid of on and off-surface visualization as well as force and moment coefficient for a range of angles of attack.

Initially, errors minimizing analyses were undertaken, such as grid and turbulence models as well as general convergence criteria were discussed. A very good agreement was achieved between the two numerical methods employed, with minor differences in lift coefficients, which may be improved with grid refinement.

The key finding from the predictions were: in terms of aerodynamic analyses the wing exhibits soft stall and good lift-to-drag ratio, as well as statically stable pitching moment response up to stall conditions. Maximum lift was reached at  $14^\circ < \alpha < 16^\circ$ . Generally, for all angles investigated, common trend pressure distribution characteristics were noted, with static stall onset at the outboard section of the wing at  $\alpha = 14^\circ$ . This was also verified by the drag coefficient plots as well as off-surface investigations discussed latter in the section.

As mentioned in section 1 of this thesis general specification of the wing suggest that cruise  $C_L$  of should be approximately 0.2 this is obtainable with the above wing with the current conditions studied (i.e Mach 0.455). In general the computed  $C_L$  with the numerical methods in cruise conditions fall within the top level requirements for the current design.

From on-surface streamline observations it was noted that the wing's inboard and central sections behaved in a similar manner to the forward swept wings, with inboard spanwise flow characteristics. This characteristic is believed to divert the flow from the outboard vortex, which is a desirable condition for air-taxi type aircraft.

Furthermore, regions of local supersonic flow were observed to appear at  $\alpha = 10^\circ$  and above, which showed no detrimental effect on the performance of the wing, moreover the angles where these pockets appear are less likely to be employed at cruise conditions.

Off-surface investigations showed the wing's abilities to maintain attached flow at the central section well after stall was reached; it also confirmed that the causes of separation were an implication of the flow physics rather than the geometry. However, a closer investigation of the off-surface total pressure at the inboard crank region at  $\alpha = 16^\circ$  showed that the crank design may induce separation at the leading edge, with the

flow never re-attaching again. This suggests that careful considerations have to be made when the intersection regions are developed to avoid geometry-induced shortcomings.

In accordance with the low-speed results, some form of inboard vortex was noticed to appear in the near-wake at higher angles of attack. The rotational nature of this phenomenon seems to be associated with the wing crank or discontinuity and the corresponding local change in span wise lift distribution. The resulting wake roll-up is very similar to that seen in delta wings. However, due to computational constraints the exact extent of this observable fact was not investigated.

An assessment of the origin and direction of the vortex was deemed necessary and it was noted that the secondary inboard vortex was not instigated by the outboard crank, as initially assumed, but was in fact a typical stall onset with recirculated flow observed from on-surface streamlines, which was later driven downstream by the free-stream flow. The recirculated flow then maintains the rotation, which is then observed in the near-wake analyses. Similar observations have also been noticed at  $\alpha = 16^\circ$  and above with deep stall features emanating from most of the inboard and central part of the wing. The only concern raised with respect to this is the tailplane positing, as the settings may be dictated by the stall behavior.

Generally, the the above results presented an indication of the capabilities of the W-wing in cruise, and offer directions for the next step in evaluating wing's performance and, ultimately, in improving the model to postpone separation so that drag is reduced, stall is delayed, lift is enhanced and pressure recovery improved. A general conception on the crank effects was that the cranks gave varied characteristics. On one hand, the combined sweep is deterring the flow from outboard movement, and producing above average aerodynamic characteristics such as high lift-to-drag ratio and statically stable wing. Further investigation on the tip design is recommended as well as additional investigations of the crank design in order to avoid geometrically induced separation.

## **8. Experimental and Numerical Test**

### **Results for the W-wing in Ground Effect**

It is well acknowledged that take-off and landing are one of the most crucial stages of aircraft flight, as the speeds are low and high angles of attack are required. For that and other reasons explained below, an assessment of the W-wing's performance under ground effect is of principal importance at the initial stages of wing design.

As enhanced short take-off and landing potential is required for a Jetpod-type aircraft, for which the W-wing is designed, exceptional performance in ground vicinity is desired. Previous studies (see section 2) have shown that there is a reduction of drag, particularly induced drag, and thus an increase of lift-to-drag ratio in ground vicinity. Consequently, it is important to examine the extent of the increased aerodynamic capabilities, if any, in the influence of the ground. These enhanced features would aid further the take-off and landing capabilities, which would assist in reducing the required runway length and aircraft clearance, two very important effects for a Jetpod type aircraft.

This section outlines the experimental and numerical results obtained on the scale model of the isolated wing in ground-effect. Additionally, numerical analyses of the full-scale wing are also included. The initial assessments were performed in order to confirm the well-documented facts of the wing behavior in the proximity of the ground. Further analyses were then carried out to assess the behavior of some of the previously noted vortical flow features in ground effect.

Both the experimental and computational analyses were carried out for various ground-height-to-span ratios ( $h/b$ ) in the range of  $0.06 \leq h/b \leq 0.45$  as well as the ground free case ( $h/b > 1$ ). Note that all heights reported for the experimental tests are from the edge of the ground boundary layer to the leading edge of the wing.

The experimental tests were run in a subsonic wind tunnel at a Reynolds Number of  $Re = 3 \times 10^5$ , Mach number of  $M = 0.09$  and at a range of angles of attack ( $-10^\circ < \alpha < 30^\circ$ , with steps of approximately  $\Delta\alpha = 2^\circ$ ). A static ground board, with elliptic leading edge, was installed in the wind tunnel to simulate the ground. Although experimental methods to assess ground effect generally require complex systems to ensure accurate ground simulation, a simplified approach that uses a fixed board, typically adopted to reduce time and cost (as is the case here), may be employed with reasonable results. A more detailed assessment of the consequences of such a choice has been addressed in section 2 of this thesis.

Segregated quasi-steady incompressible Navier-Stokes equations, complemented by Menter's  $k-\omega$  SST turbulence model, were solved for both full-scale configurations and wind tunnel simulations. Wind tunnel simulation tests were carried out at the same conditions as the experimental tests ( $Re = 3 \times 10^5$  and  $M = 0.09$ ). Full-scale numerical simulations were run at Reynolds Number of  $6.9 \times 10^6$  and Mach number of  $M = 0.11$ . The image (symmetry) method was used to account for the presence of the ground for the numerical computations. Also, for comparison purposes, simulations with a fixed ground, where no-slip wall conditions were applied to the ground boundary, were carried out.

It is known that the near-wake behavior of wings in ground effect differs from that in free-flight conditions; hence, an investigation of the near-wake was deemed necessary. For the purpose of describing the wing's performance in ground effect, and in accordance with previous procedures, detailed plots of the pressure and wall shear stress streamline distributions were also produced.

## 8.1 Grid Dependency Analyses

Because of the “symmetry plane” ground simulation strategy employed in this study, separate grids had to be generated for each combination of angle of attack and  $h/b$  ratio considered. This procedure involved numerous grids and therefore a thorough grid sensitivity study was limited. However, from previous studies a general idea of appropriate grid size had already been established. This was then employed for each grid generated for the ground effect analyses, with further refinement near the tip of the wing and the surrounding areas, especially at the lowest  $h/b$  ratios. In order to compare the predicted results with the wind tunnel tests, a fixed ground was also simulated for various angles of attack. Accordingly, to account for the ground boundary layer development, appropriate grids were also generated for this case.

Due to the unstructured nature of the grid, no grid was of the exact same number of cells as any other; however, a range of approximately 2.6 to 2.8 million cells was maintained. Grids of similar structure as for the wind tunnel free-flight simulation tests were generated. The half-wing modelling approach, use of symmetry boundary conditions to reflect the complete wing, and the hybrid tetra/prism/pyramid approach were implemented in these studies as well.

Grids generated for the full-scale simulations were also generated separately for each angle of attack and  $h/b$  ratio; in addition, a greater number of prism layers were employed to ensure compatibility with the Reynolds Number involved in these studies.

A total of 20 prism layers were implemented for the wind-tunnel simulations (i.e. at a Reynolds Number of  $Re = 3 \times 10^5$ ), whereas a 22 layer approach was maintained for the full-scale simulations at  $Re = 6.9 \times 10^6$ . Figure 8-1 is an illustrative example of the computational grid generated for  $h/b = 0.09$ .

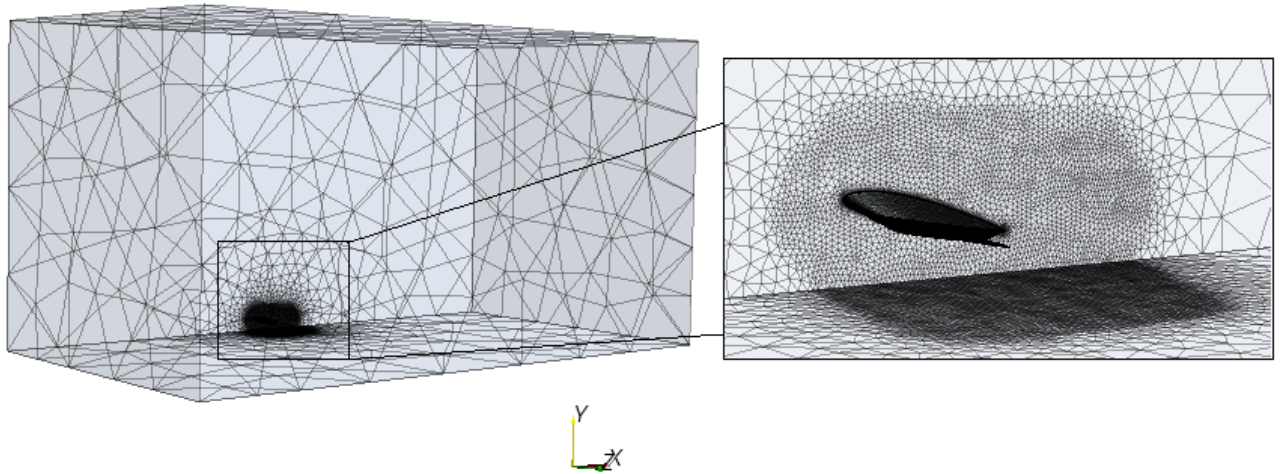


Figure 8-1. Ground effect- domain grid layout with a close-up view of the near wing grid clustering (inset).

## 8.2 Convergence Monitoring

The same convergence criteria outlined in sections 6 and 7 were also adopted throughout the ground effect analysis. A variation on the time and criteria to convergence was noted for various  $h/b$  ratios and between the two ground-simulation methods employed in the study.

An illustrative example of the residuals for wind tunnel conditions at a Reynolds Number of  $Re = 3 \times 10^5$ ,  $M = 0.09$ ,  $h/b = 0.145$  and  $\alpha = 10^\circ$  is given in Figure 8-2. Part a) describes the behavior of the residuals when the image method was employed to model the ground, whereas part b) depicts the residual behavior when a fixed board was utilized. As can be seen, no major difference between the two methods can be noticed in terms of behavior and order of convergence, as both cases took approximately the same number of iterations to reach a steady state (where residuals of about  $10^{-4}$  were obtained).

Figure 8-3 depicts the behavior of the residuals for the full-scale simulations at  $Re = 6.9 \times 10^6$ ,  $M = 0.11$  and  $\alpha = 0^\circ$  when a)  $h/b = 0.145$  and b)  $h/b = 0.27$ . It was observed that for higher  $h/b$  ratios residual steady state was delayed in comparison with the lower  $h/b$ ; nevertheless, the end convergence results and order of magnitude were distinctly enhanced when the wing was further from the ground.

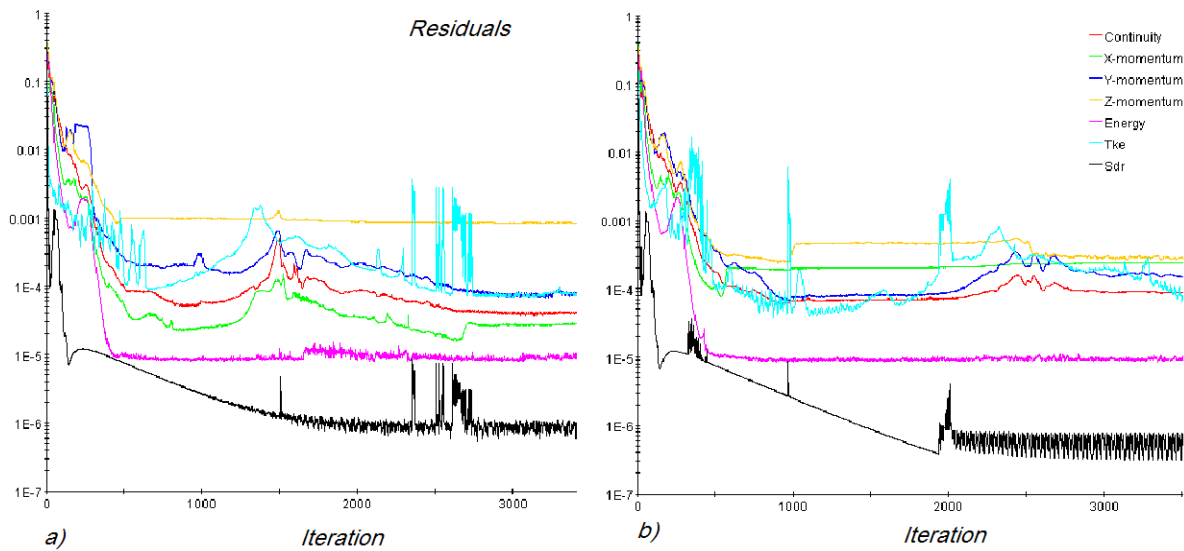


Figure 8-2. Convergence residuals for ground effect numerical predictions, at  $h/b = 0.145$ ,  $M = 0.09$ ,  $Re = 3 \times 10^5$  and  $\alpha = 10^\circ$  with a) image and b) fixed ground method.

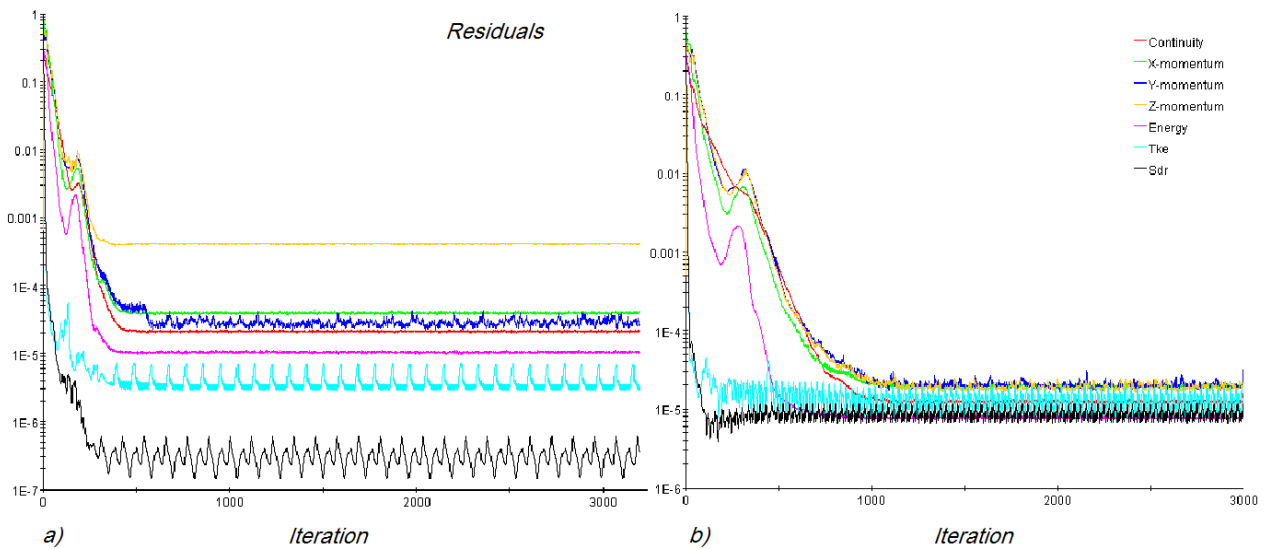


Figure 8-3. Convergence residuals for ground effect numerical predictions, at  $M = 0.11$ ,  $Re = 6.9 \times 10^6$  and  $\alpha = 0^\circ$  for a)  $h/b = 0.145$  and b)  $h/b = 0.27$ .

### 8.3 Results of Low-Speed Experimental and Numerical Analyses

Primarily for accuracy purposes, a series of tests were carried out in the T3 wind tunnel to assess the tunnel-to-tunnel difference (in comparison with T2), if any, on the lift and drag coefficients (see Section 5 for comparison). As with the T2 wind tunnel

tests, the T3 experiments were run at ground-free conditions at four different speeds, equivalent to Reynolds Numbers of  $1.5 \times 10^5$ ,  $2.1 \times 10^5$ ,  $3.6 \times 10^5$  and  $4.1 \times 10^5$ .

Due to the structure of the sting system employed for the T3 tests, sting drag had to be calculated at each ground height and angle of attack tested, and for all relevant wind tunnel speeds. During the investigation some unsteadiness exhibited by the model over the higher angles-of-attack range was reflected in the quality of the data for Reynolds Numbers of  $3.6 \times 10^5$  and above. The unsteadiness might be described as a high-frequency, low-amplitude oscillation, which damped out at times, but was generally present while data were being recorded. An attempt to reduce the scatter from the effects of the oscillations was made. This was done by averaging several data points taken for each angle of attack; hence all the plotted experimental results represent the average value of several data points.

In general, a good agreement was achieved between the results obtained from the two tunnels in both lift and drag coefficients. No substantial difference was noticed between any of the plots, despite the fact that a manual inclinometer was employed to change the angle of attack. However, the effect of the vibrations/unsteadiness was noticed to have a consequence on the near-wake measurements, therefore a decision was made to run the T3 tests at a lower Reynolds Number ( $Re = 3 \times 10^5$ ), where the above effects were less noticeable.

Due to the manual change of the pitching angle, the pitching moment zero contributions obtained at each angle were found to have some erroneous output. However, no other alternative support system to carry out ground effect tests was possible; this was an experimental shortcoming that had to be accepted. Thus, no pitching moment comparison between the two tunnels was carried out.

In order to verify the well documented general trend of the wing behavior in ground effect, the longitudinal aerodynamic characteristics (lift, drag and lift-to-drag ratio) of the W-shaped wing, as obtained by experimental and Navier-Stokes computations are depicted below. The general trends of the wing in ground vicinity have already been

established in section 2.4 of this thesis, and diverse opinions on the matter have been reported.

Figures 8-4 to 8-6 represent the lift and drag coefficients obtained from the experimental results. Standard methods for the propagation of errors were used to estimate the uncertainty in the experimental data. In general, average errors were found to be  $\pm 1\%$  in the lift,  $\pm 1\%$  in the drag and  $\pm 2\%$  in the pitching moment. From Figures 8-4 to 8-6 it can be seen that for the lowest ground heights the maximum achievable angles of attack were limited to less than the stall angle, due to the very close location of the ground. These ground heights ( $h/b < 0.07$ ) were assessed for comparison purposes only, as in the full-scale flight case they would be unrealistic:  $h/b = 0.09$  is the lowest possible ground height achievable with the current wing positioning settings for the Jetpod aircraft.

From the lift and drag coefficient results the usual trends of wing near-ground behavior were noticed. As expected, lift coefficient and L/D ratio increase with decreasing ground clearance, which is in agreement with the existing reports on the wing-in-ground-effect discussed in section 2 (e.g. Wu and Rozhdestvensky, 2005). As an example from the W-wing results, a 30% increase in the lift coefficient at  $\alpha = 12^\circ$  and  $h/b = 0.09$  is observed when compared to the ground free case. However, the effect of the ground is observed to start at  $\alpha = 0^\circ$ , which is contrary to the general trend described in section 2. Unlike other reports (Tuck 1983; Suh and Ostowari 1988; Morishita and Tezuka 1994; Hsiun and Chen 1996), no major difference was noted from the drag coefficient plots for all  $h/b$  ratios investigated, especially at lower angles of attack. The findings from this study are, however, in agreement with Hooker's study (Hooker 1995). From the drag coefficient plots it was also observed that for angles higher than  $\alpha = 12^\circ$  and  $h/b$  below 0.27, an increase in drag is apparent.

From both lift and drag coefficient plots it can be seen that the effect of the ground starts to deteriorate at  $h/b = 0.45$ , where after the coefficients are almost identical to those from the ground free case. Note that, in the experimental investigations, ground height ratios of  $h/b > 0.45$  were not achievable due to the wind tunnel working section geometry and support system limitations.

Figures 8-6 and 8-7 depict the variation of lift and drag coefficients with  $h/b$  at constant  $\alpha$ . Drag coefficients plots reveal no particular change with changing ground height only a slight reduction at  $h/b < 0.15$  is noticed. The lift coefficients in the other hand do increase with the decreasing ground height and this is clearly noticed from plots in figure 8-6.

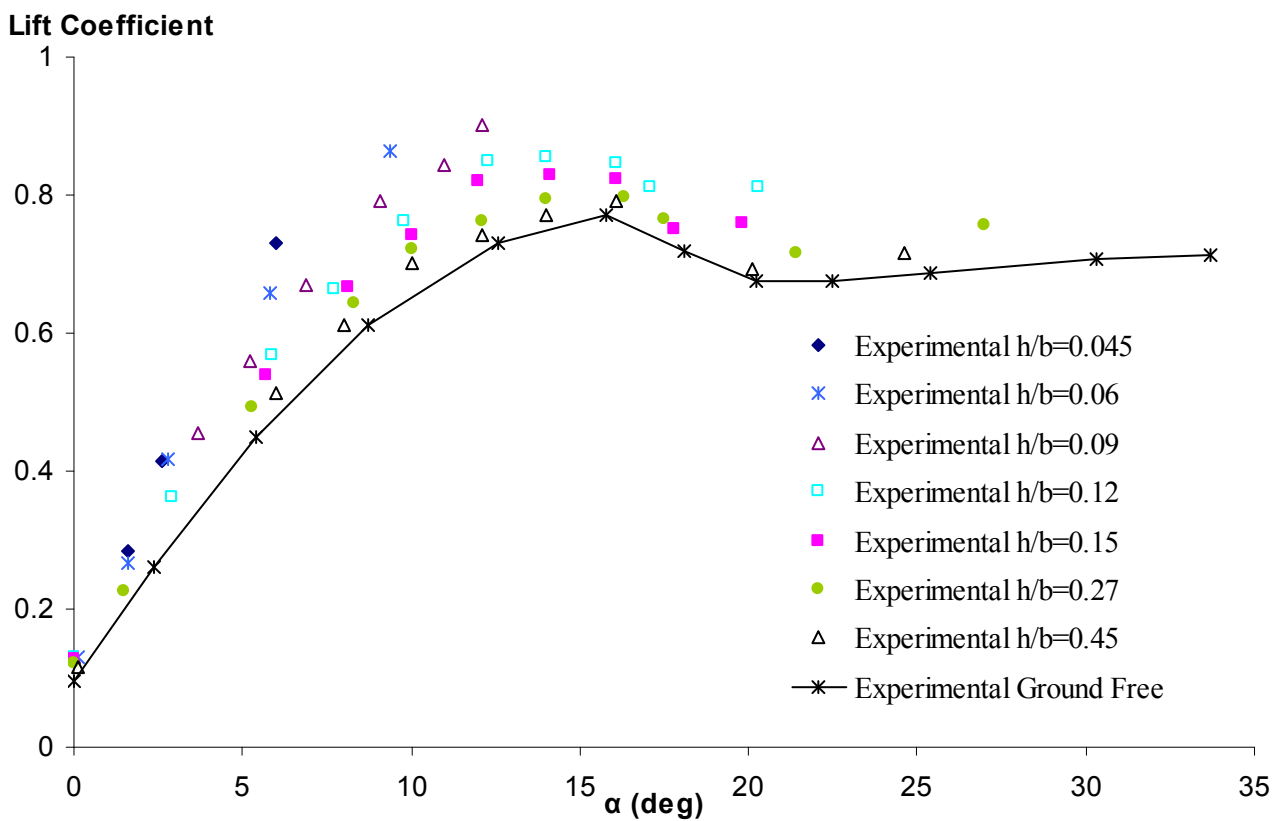


Figure 8-4: Experimental variation of lift coefficient with changing angle of attack at different ground clearances,  $Re = 3 \times 10^5$  and  $M = 0.09$

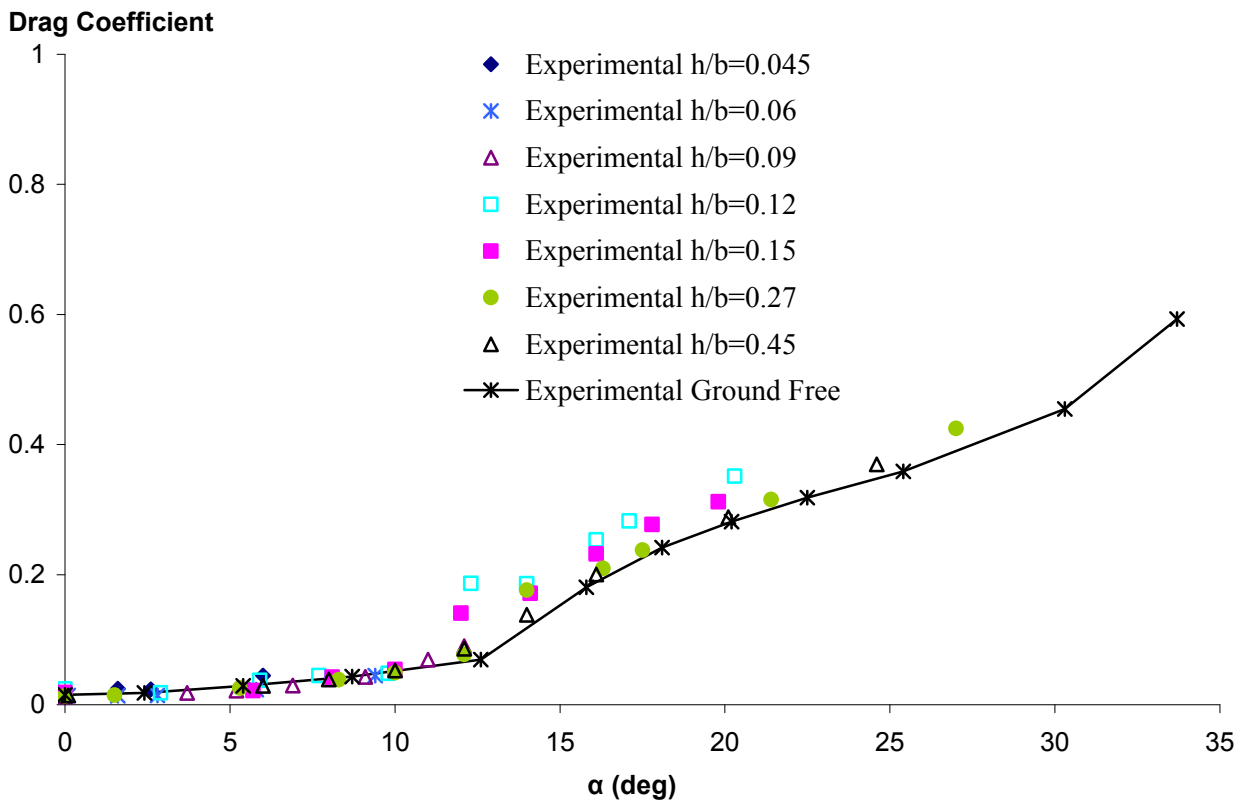


Figure 8-5. Experimental variation of drag coefficient with changing angle of attack at different ground clearances,  $Re = 3 \times 10^5$  and  $M = 0.09$ .

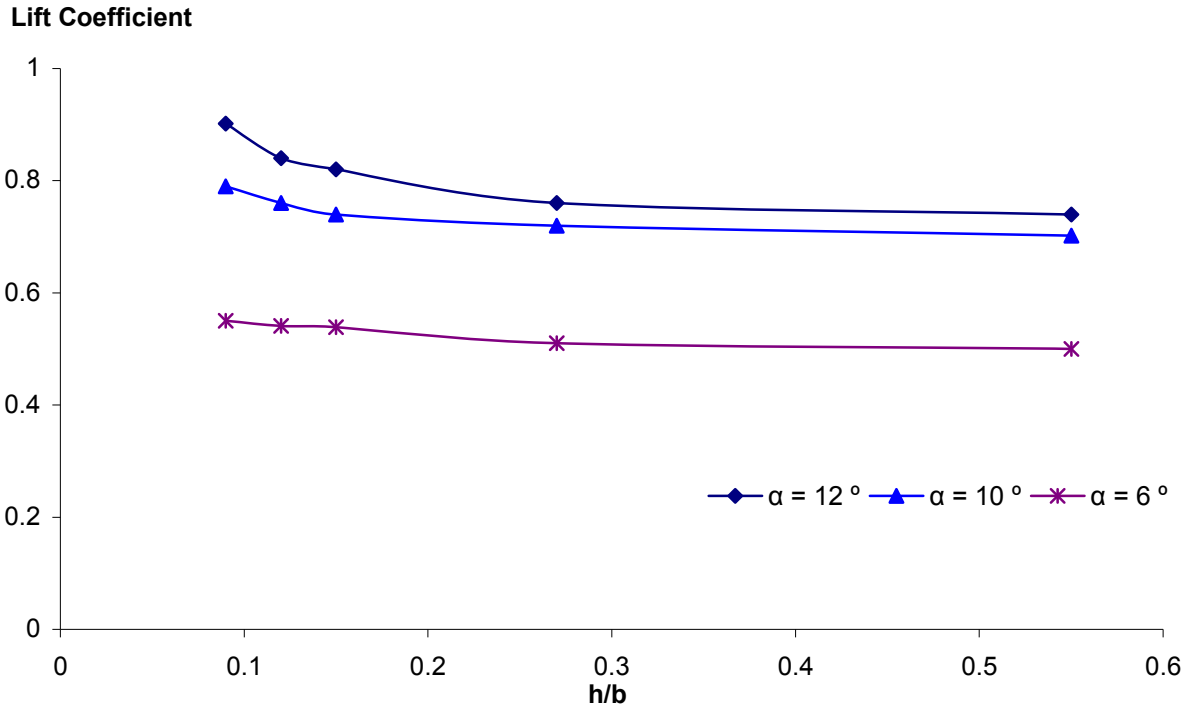


Figure 8-6. Experimental variation of lift coefficient with changing  $h/b$  at various  $\alpha$ ,  $Re = 3 \times 10^5$  and  $M = 0.09$ .

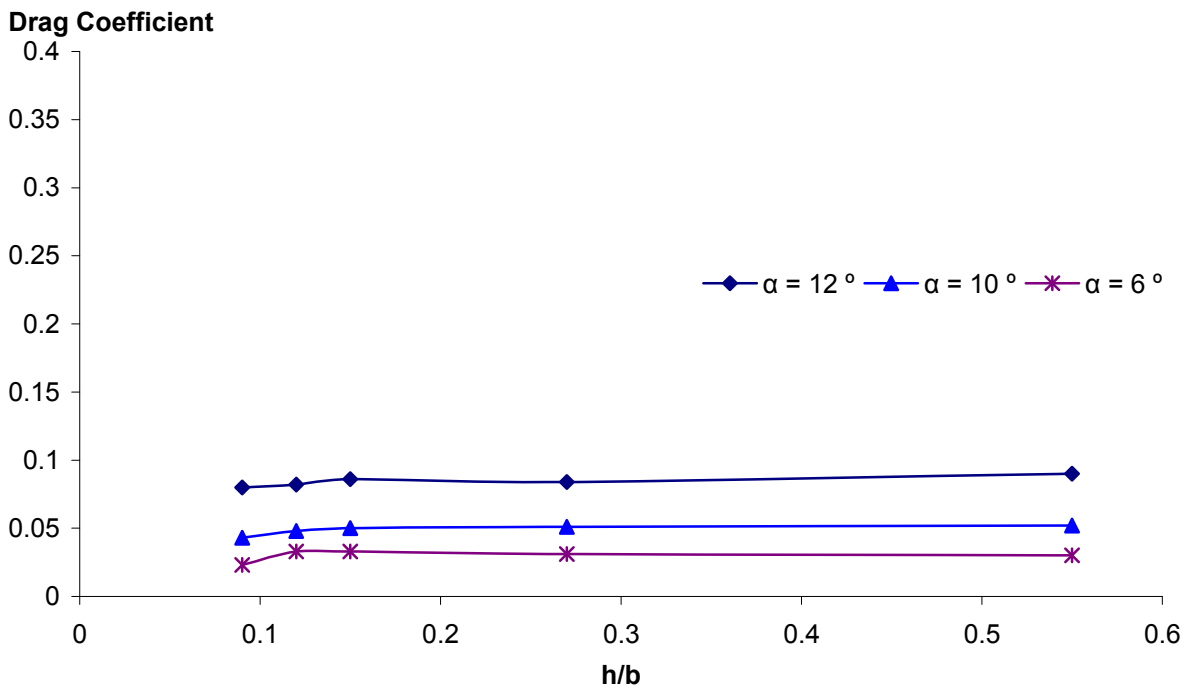


Figure 8-7. Experimental variation of drag coefficient with changing angle of attack at different ground clearances,  $Re = 3 \times 10^5$  and  $M = 0.09$ .

Figures 8-8 and 8-9 illustrate the variation of lift and drag coefficient with angle of attack, as obtained by the numerical investigations. The findings show a similar trend as the above experimental plots with a disagreement between the lift coefficient results, which increases with increasing angle of attack. It can be observed that the greatest difference between the numerical results obtained by the image method and the experimental data is present at maximum lift conditions. The difference between the two investigations is also noticed to increase with increasing ground height. The best agreement between the two methods was observed at  $h/b = 0.09$ , although the image method still gave slightly higher lift coefficient values at the highest angle investigated ( $\alpha = 12^\circ$ ). At this angle, a numerical simulation with the ground board present gave a better agreement with the experimental results. This development was noted for all the cases investigated i.e. as expected, the fixed ground board numerical simulations always gave a better agreement with the experimental results. Nonetheless, both methods matched the behavior of the experimental findings regarding lift coefficient increasing with decreasing ground height.

Figures 8-10 and 8-11 show the variation of lift and drag coefficients with  $h/b$  at constant  $\alpha$ . Drag coefficients plots similar to the experimental data reveal no particular change with changing ground height with a discrepancy at  $\alpha = 10^\circ$  image method calculations which may be associated with a numerical error. The lift coefficients in again as in the experimental data do increase with the decreasing ground height, with less increase noted from the fixed ground board modeling approach results.

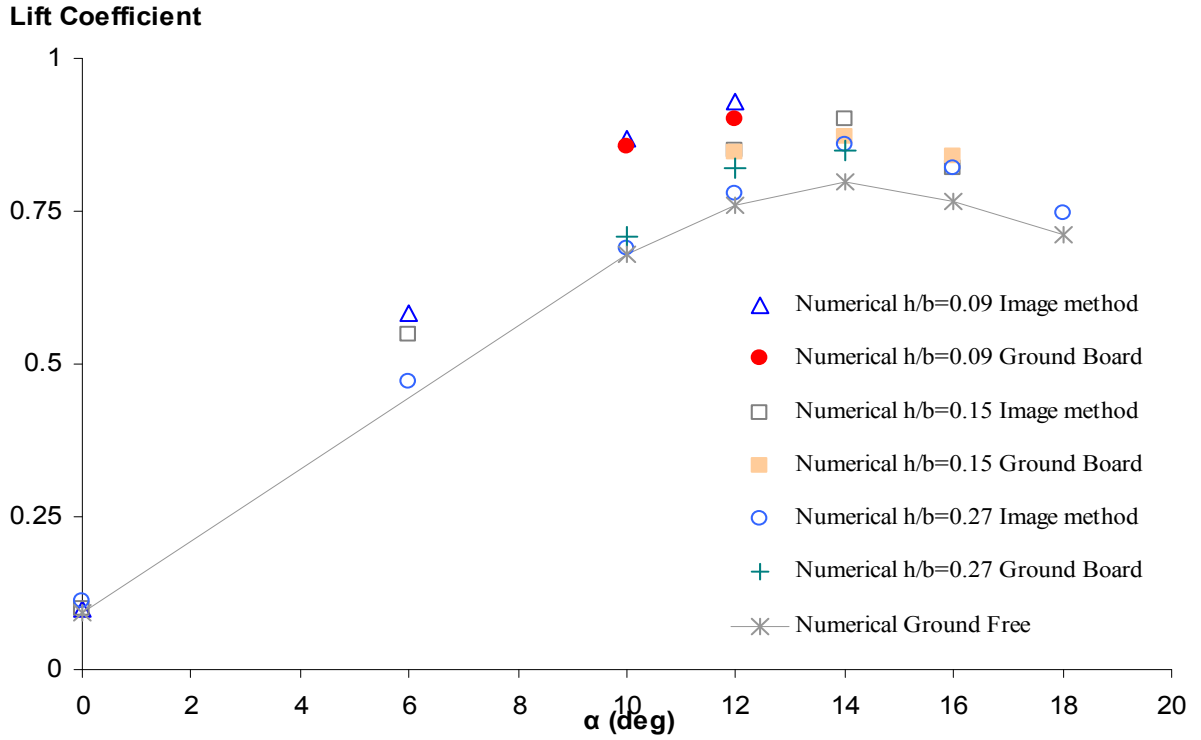


Figure 8-8. Numerical lift coefficient with changing angle of attack at different ground clearances,  $Re = 3 \times 10^5$  and  $M = 0.09$ .

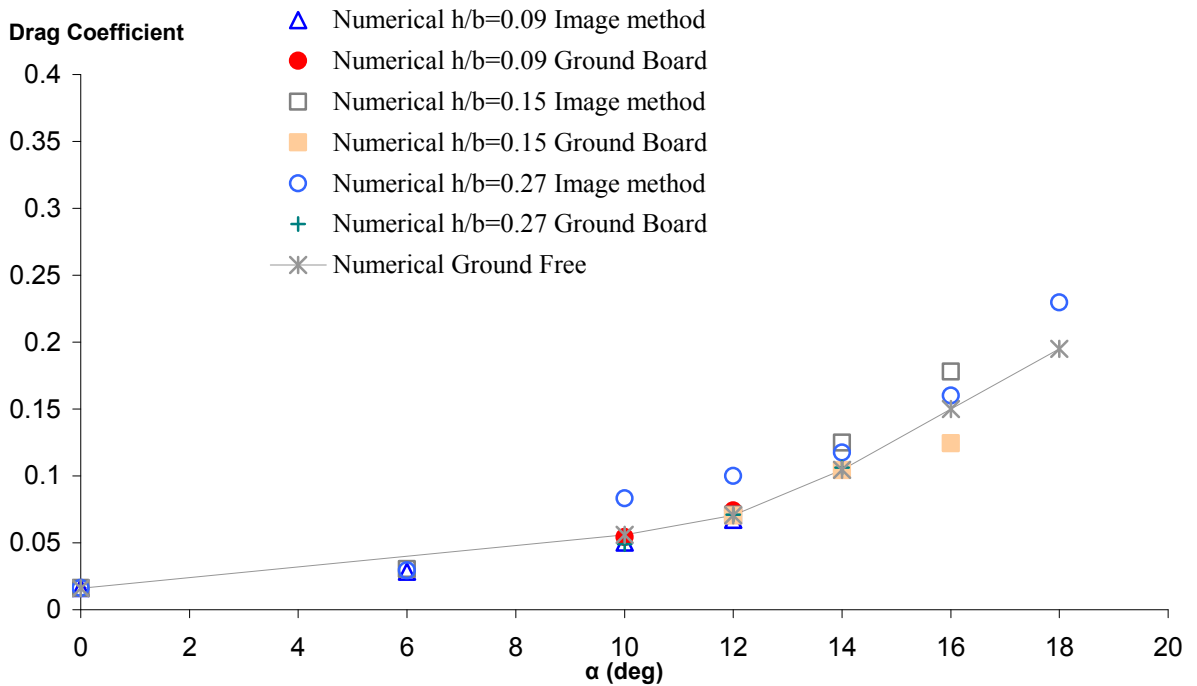


Figure 8-9. Numerical drag coefficient with changing angle of attack at different ground clearances,  $Re = 3 \times 10^5$  and  $M = 0.09$ .

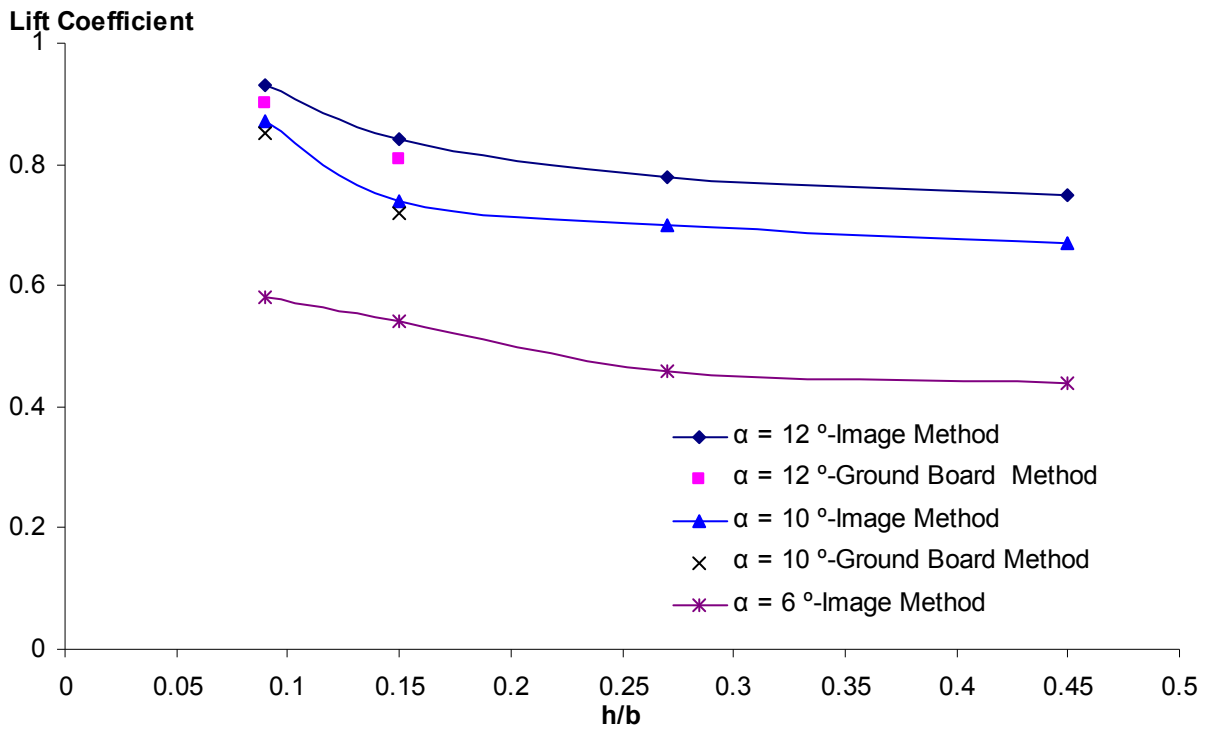


Figure 8-10. Numerical variation of lift coefficient with changing angle of attack at different ground clearances,  $Re = 3 \times 10^5$  and  $M = 0.09$ .

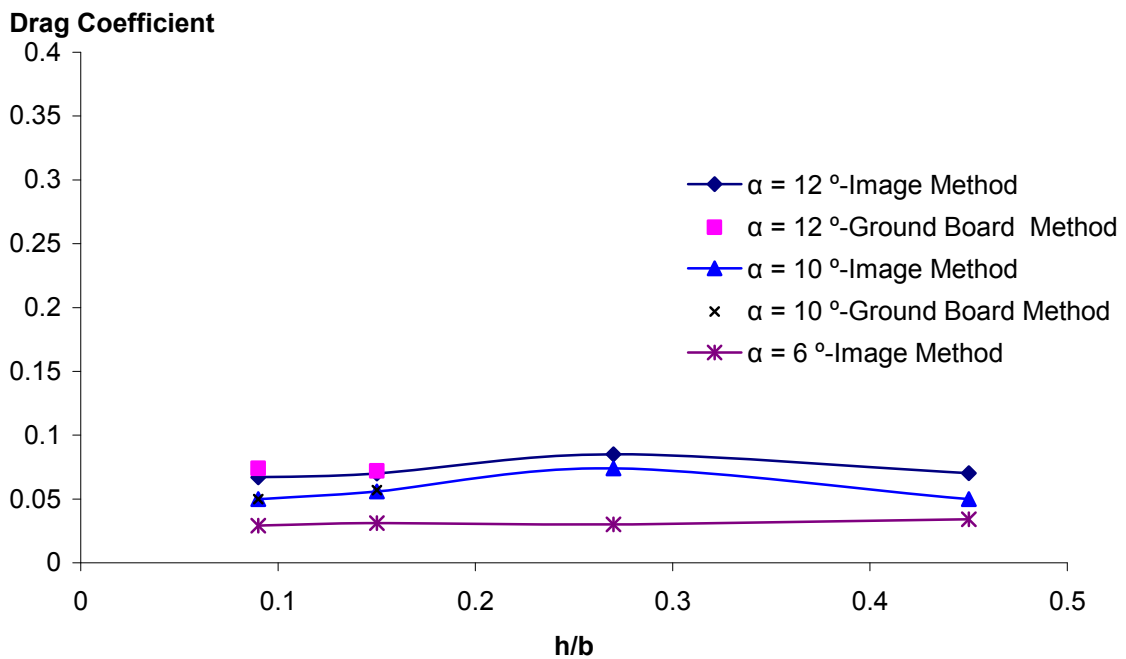


Figure 8-11. Numerical variation of drag coefficient with changing angle of attack at different ground clearances,  $Re = 3 \times 10^5$  and  $M = 0.09$ .

The above findings are also in agreement with previous studies, where the difficulty with the fixed ground in wind tunnel testing was raised (George 1981). George reported that the image method was found to give higher lift coefficients when compared to the static wind tunnel testing. Also, as elaborated in more detail in section 2, the effect of the fixed-ground boundary layer is more prominent as  $\alpha$  increases, which is also noticed here. Nonetheless, the above findings are a known fact that have been stated in the past, The disagreement, therefore, is attributable to the shortcomings of the experimental method employed as well as the limited number of sensitivity analyses, which was influenced by the amount of grids required for this study.

On the other hand, surprisingly good agreement is achieved between the experimentally and numerically derived drag results, especially at the lower angles of attack. Both the image and the fixed ground numerical simulations give very similar results, which are almost identical to the experimental data. Minor disagreements are mostly noticeable at the higher angles of attack, where the drag coefficients for  $h/b = 0.15$  were smaller when obtained by numerical simulation.

### 8.3.1 Near-Wake Analysis

Previously during this study it was reported that a vortical feature was noticed to emanate from mid-wing at stall conditions. This was observed from near-wake analyses of both low-speed wind tunnel tests on the scaled wing and full-scale numerical simulations. This part is a follow-up investigation on the wing near-wake when in ground proximity. Experimental tests were conducted by employing a horizontally positioned pitot-static rake, located at  $x/c_r = 1.5$ . The use of a horizontal rake allowed data measurement at regions very close to the ground, with the flexibility of choosing rake movement at the smallest scales.

Initially, wind tunnel tests were carried out for the ground alone case, where the rake was used to obtain an average effective ground height, which would later be used to obtain the relevant  $h/b$  ratio, in order to compare with numerical results. Figure 8-12

gives the total pressure plots at the downstream location of the impending wing positioning, which would correspond to  $x/c_r = 1.5$ . Similarly with the force coefficient plots, near-wake experimental investigations were carried out for two ground heights ( $h/b = 0.045$  and  $h/b = 0.06$ ), which although not realistic for this case, are still useful when considering the extent of the ground boundary layer effect on the wing aerodynamics, and thus the accuracy of the results obtained at those small heights with a fixed board.

Figures 8-13 and 8-14 illustrate the near-wake behavior for  $h/b = 0.045$  and  $h/b = 0.06$ , at  $\alpha = 0^\circ$  and  $\alpha = 6^\circ$ , respectively. From these plots it can be seen that at  $\alpha = 0^\circ$  and  $h/b = 0.045$ , the wake of the wing is completely merged with the ground boundary layer, with a noticeably larger wake at the mid-wing when compared with the ground-free case (see Figures 6-14 to 6-19). Similarly, at  $\alpha = 0^\circ$  and  $h/b = 0.045$ , the wing's mid- and outer-section wake is not present in the plots, which suggests mix-up with the ground boundary layer. A “sea-wave type” flow roll-up at the tip is noticed at both these very low ground heights. This action is fortified with increasing  $\alpha$ , as can be seen from the  $\alpha = 6^\circ$  plots (Figure 8-14). The “sea-wave” seems to be created by the interference of the tip vortex with the ground boundary layer, causing a possible detachment of the boundary layer and the creation of secondary vortex or rotational flow emerging from the ground. Generally, the near-wake performance at these ground heights is not comparable with the ground free case due to the severe interference from the ground boundary layer, which is otherwise not present in real flight. Hence, the results for  $h/b < 0.09$  may be considered as not accurate.

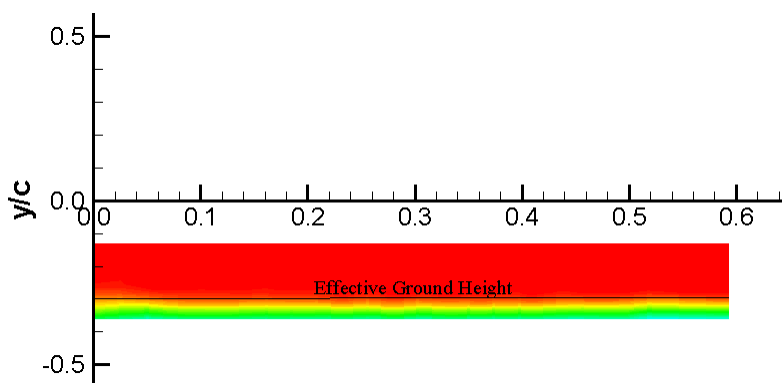


Figure 8-12. Experimental near-wake total pressure distribution for the ground-alone case at  $Re = 3 \times 10^5$  and  $M = 0.09$ .

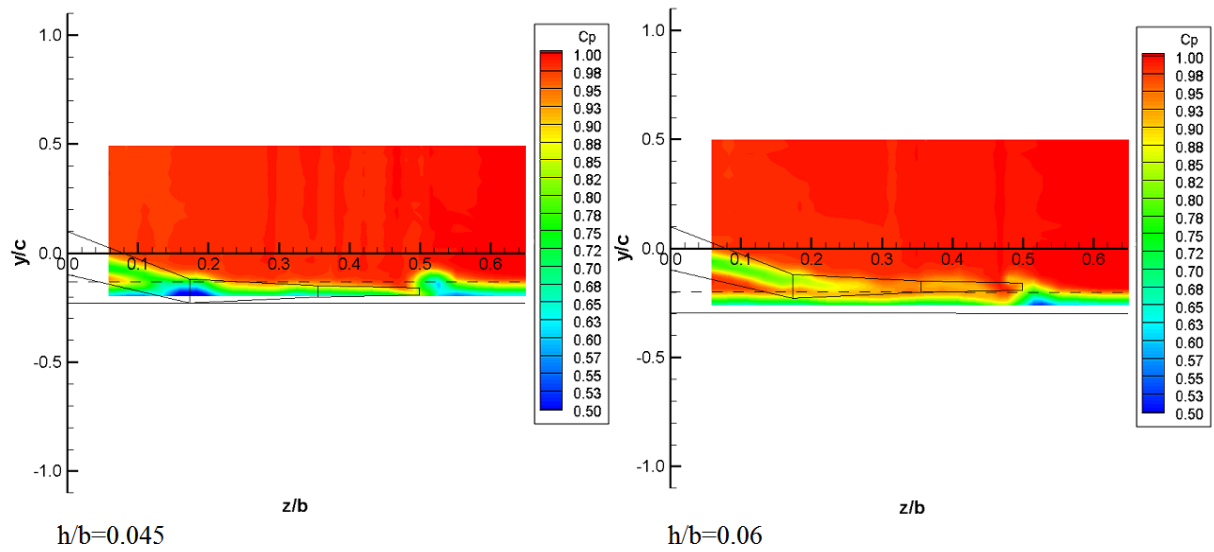


Figure 8-13. Experimental near-wake total pressure distribution at  $\alpha = 0^\circ$ ,  $Re = 3 \times 10^5$  and  $M = 0.09$ .

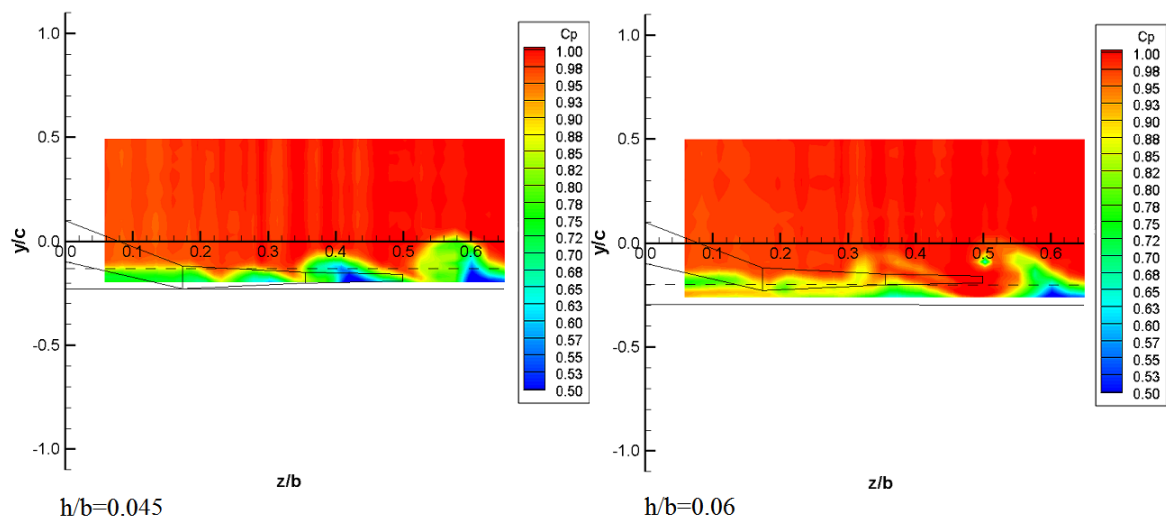


Figure 8-14. Experimental near-wake total pressure distribution at  $\alpha = 6^\circ$ ,  $Re = 3 \times 10^5$  and  $M = 0.09$ .

Figure 8-15 depicts the near-wake total pressure distribution at  $h/b = 0.09$  and at  $\alpha = 6^\circ$  as obtained by a) experimental and b) numerical investigations. There is a good agreement between the two methods. The ground boundary layer is affected by the wing, as it can be seen to reduce at the wing tip with a thickening near the wind tunnel

walls at  $z/b = 0.6$ . At the same conditions and  $\alpha = 10^\circ$  (see Figure 8-16), the results between the two studies begin to differ: the experimental plots show a weaker wake at mid-wing with stronger tip vortex and the flow possibly even starting to rotate at the mid-wing, and almost no ground boundary layer being present at that location. The image method, on the other hand, gives a weaker tip vortex. Figure 8-17, illustrates the near-wake plots as obtained by simulating the ground in the numerical computations, which agree better with the experimental ones; however, the rotational flow at mid-wing is still not present.

At greater ground heights, say  $h/b = 0.145$ , similarities between the experimental and numerical plots are observed for the lower angles of attack (see Figure. 8-18), where experimental results show an effect on the ground boundary layer still being present. At  $h/b = 0.145$  and  $\alpha = 10^\circ$ , the numerical image method (as shown in Figure 8-19) correctly predicts the secondary vortex emanating from mid-wing as observed from the out-of-ground study; however, the strength of the vortex is far greater. Figure 8-20 illustrates the behavior of the wake at the same conditions as above, only with ground board present in the numerical simulations. The results give a better agreement in terms of the strength of the vortex, but the positioning is not the same as the experimental plots. A difference is also noticed in the predicted size of the inboard wake, which was much smaller than in the experiments. This may be due to the grid capabilities of the numerical model to correctly predict the stall region, as the shape is mirrored even when the ground was included in the simulations.

An interesting feature which can be observed from all the above discussed near-wake plots is the outward tip vortex movement, which increases with decreasing ground height. It has been reported previously that this movement will increase the effective aspect ratio of the wing and therefore the lift and  $L/D$  ratio. However, the outward movement in this case is rather small which would not have a significant effect on lift and  $L/D$  ratio. A plan-view of the tip vortex movement from the numerical simulations of three ground heights ( $h/b = 0.09$ ,  $h/b = 0.145$  and  $h/b = 0.45$ ) is shown in Figures 8-22 and 8-23. It can be seen that in ground effect (i.e.  $h/b = 0.09$ ), at a given downstream location, the tip vortex moves outboard by almost the same distance as the inboard tip vortex shift when out of ground (i.e.  $h/b = 0.45$ ).

This result is also present in the experimental near-wake total pressure plot findings, which clearly indicate that the tip vortex moves outwards along the  $z/b$  axes as the ground is approached. This outboard movement of the vortex core suggests that their influence on the wing would be reduced (Barber 2002).

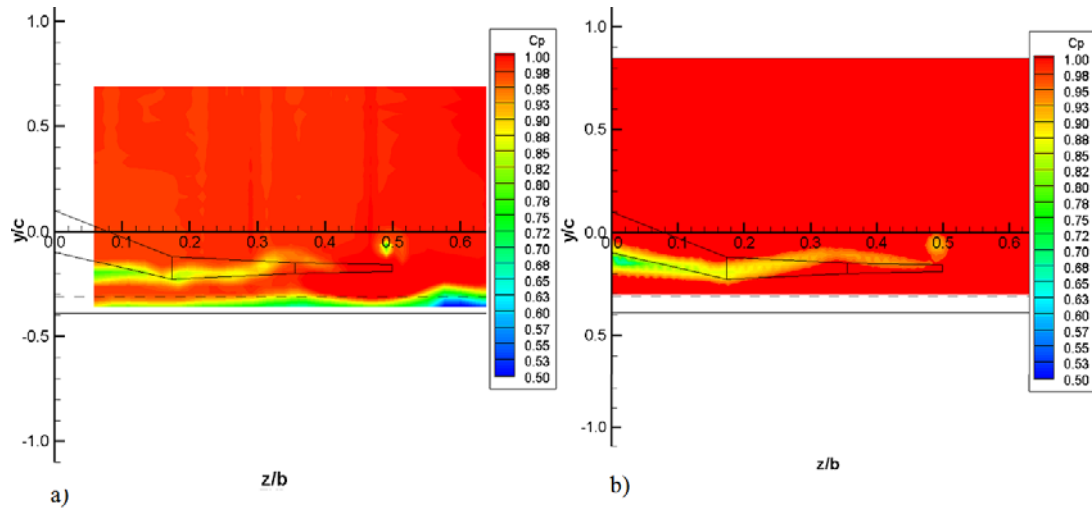


Figure 8-15. Near-wake total pressure distribution at  $\alpha = 6^\circ$ ,  $h/b = 0.09$ ,  $Re = 3 \times 10^5$  and  $M = 0.09$  a) experimental and b) numerical results.

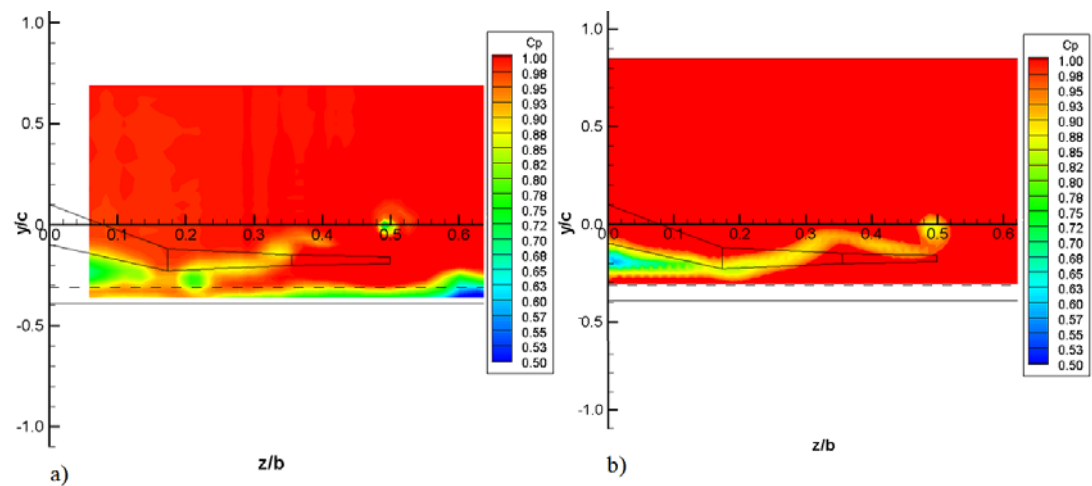


Figure 8-16. Near-wake total pressure distribution at  $\alpha = 10^\circ$ ,  $h/b = 0.09$ ,  $Re = 3 \times 10^5$  and  $M = 0.09$  a) experimental and b) numerical results.

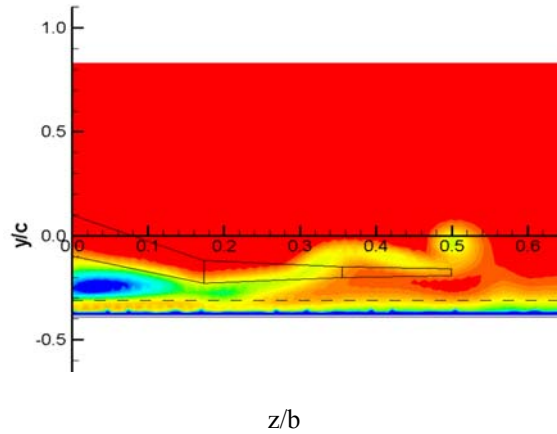


Figure 8-17. Numerical fixed-ground results of the near-wake total pressure distribution at  $\alpha = 10^\circ$ ,  $h/b = 0.09$ ,  $Re = 3 \times 10^5$  and  $M = 0.09$ .

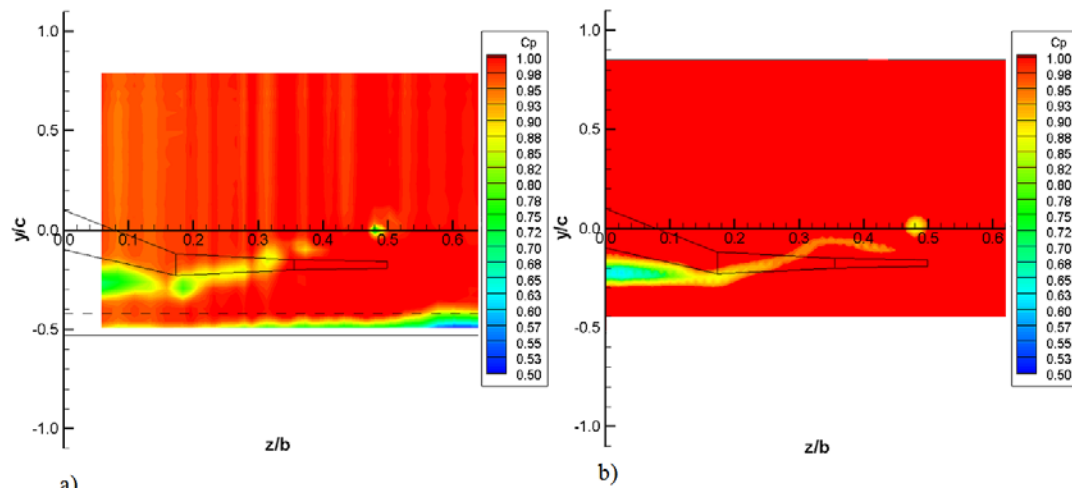


Figure 8-18. Near-wake total pressure distribution at  $\alpha = 10^\circ$ ,  $h/b = 0.145$ ,  $Re = 3 \times 10^5$  and  $M = 0.09$  a) experimental and b) numerical results.

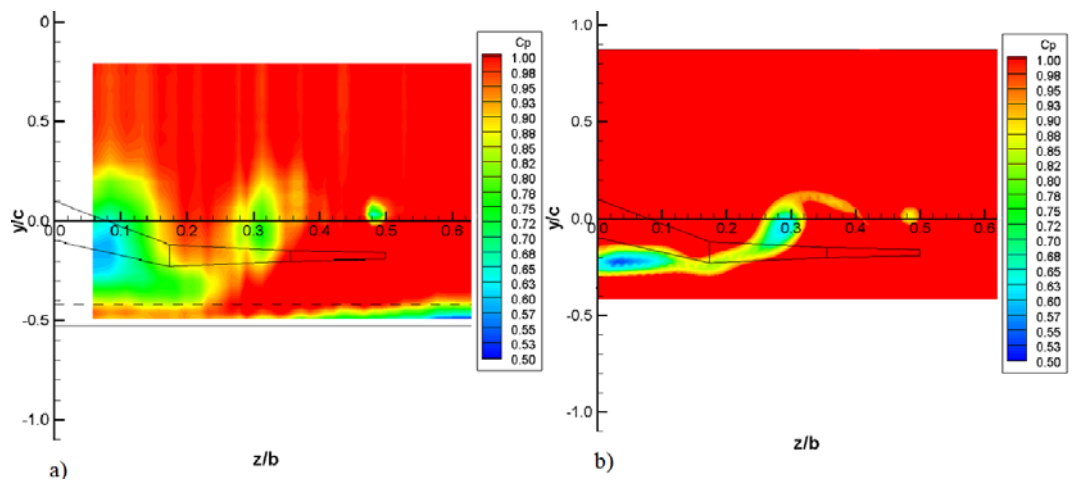


Figure 8-19. Near-wake total pressure distribution at  $\alpha = 16^\circ$ ,  $h/b = 0.145$ ,  $Re = 3 \times 10^5$  and  $M = 0.09$  a) experimental and b) numerical results.

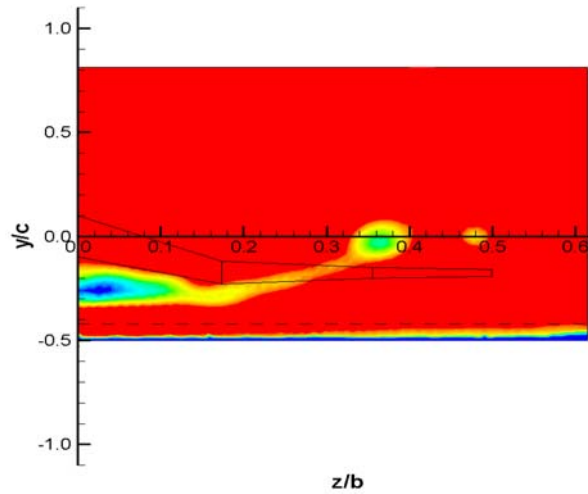


Figure 8-20. Numerical fixed-ground results of the near-wake total pressure distribution at  $\alpha = 16^\circ$ ,  $h/b = 0.145$ ,  $Re = 3 \times 10^5$  and  $M = 0.09$ .

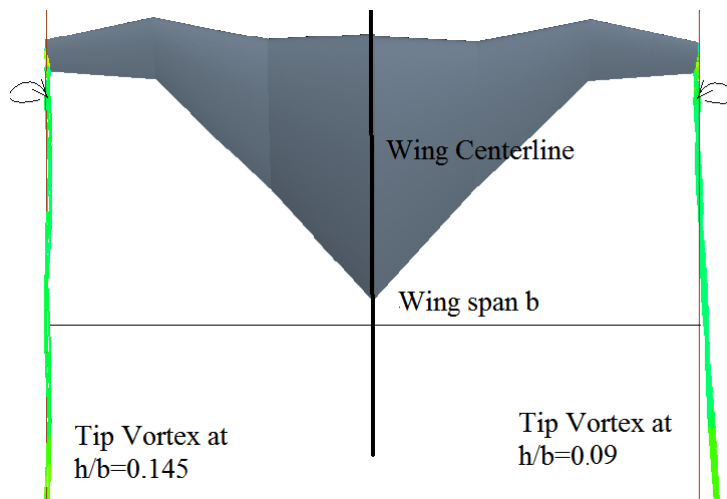


Figure 8-21. Plan-view of the tip vortex performance when the wing is in ground effect at  $h/b = 0.145$  and  $h/b = 0.09$ .

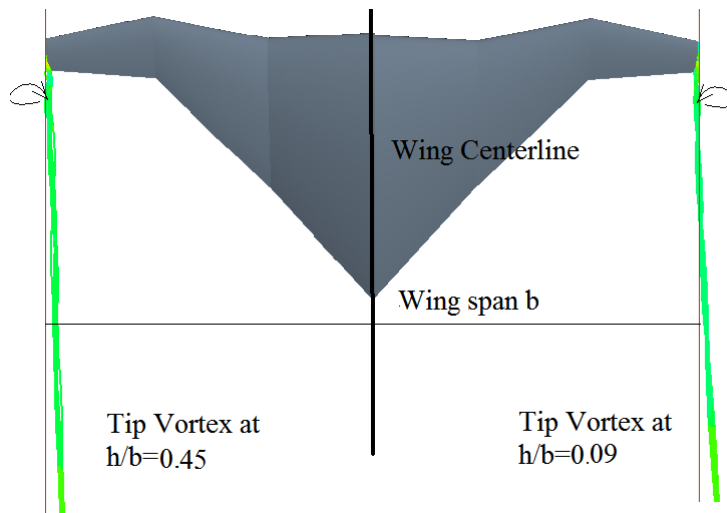


Figure 8-22. Plan-view of the tip vortex performance when the wing is in ground effect at  $h/b = 0.45$  and  $h/b = 0.09$ .

Generally, agreement exists between predicted and measured data on the ground-effect study of the scaled wing, though lift coefficients agreed poorly in comparison with the drag coefficient. Application of a fixed ground board gave lower lift coefficients than the image method, therefore resulting in lower L/D ratios, particularly at the higher angles of attack.

Results obtained for drag coefficients agreed very well between the numerical and experimental data. The near-wake plots reveal better agreement when the ground board was simulated as well on the numerical predictions. Due to experimental limitations, ratios of  $h/b > 0.27$  were unable to be tested. However, the results show only a very slight variation in this region ( $h/b \approx 0.27$ ), suggesting that the effect of the ground on the wing aerodynamics has decreased significantly.

From an aerodynamics standpoint, the low-speed results indicate that the wing is possessed of very good ground effect capabilities, with high lift coefficients and no drag increase as the ground approaches. Near-wake phenomena reveal a very strong effect of the ground boundary layer on the wing wake, therefore making the results obtained at  $h/b < 0.09$  questionable. For  $h/b = 0.09$ , results showed that ground presence does have an effect on the inboard secondary vortex developing from the

wing at stall conditions: Ground proximity increases the strength of the vortex, and its onset is apparent at lower angles of attack.

#### 8.4 Results of Full-Scale Numerical Analyses

Full-scale numerical analyses were carried out at a Reynolds Number of  $6.9 \times 10^6$  and Mach number of  $M = 0.11$ . The image (symmetry) method was used to account for the presence of the ground for the numerical computations, where symmetry boundary conditions were applied to the ground plane in the computational domain. The rest of the geometry was modelled in the same manner as described previously in sections 6 and 7. Generally, the numerical results for the full-scale wing follow the trend and behaviour that was noted in the experimental and low speed numerical results.

Figures 8-23 to 8-24 depict the lift and drag coefficients as well as the lift-to-drag ratio for five various ground height tests ( $h/b = 0.09$ ,  $h/b = 0.145$ ,  $h/b = 27$ ,  $h/b = 0.45$  and  $h/b = 0.55$ ). As can be seen from the plots, the lift coefficient increases with decreasing ground height, reaching a  $C_L$  of 1.2 at  $h/b = 0.09$  and  $\alpha = 12^\circ$ , an increase of approximately 33% in comparison with out-of-ground data. This gives an L/D ratio of 30, which is almost double that of the ground-free case ( $L/D = 16$ ). The large increase in the L/D ratio shows very good aerodynamic capabilities of the wing in ground effect, as also noted in the scale model tests. As the wing moves further away from the ground the lift coefficient decreases, and starts to approach that of the ground-free data. For example, it can be observed that at  $h/b = 0.55$  the wing seems to be out of the influence of the ground at the lower angles of attack; however, ground influence is still apparent at higher angles of attack.

From the drag coefficient plot, barely any change of the drag can be seen with varying ground height. Only a minor decrease is noticed at the higher angles of attack, whereas at the lower angles the data mirror completely the out of ground effect results. These findings are in disagreement with some of the previous studies discussed in section 2, where it was noted that the literature suggests there is a greater decrease in induced drag. To investigate induced drag behavior and carry out a

comparison, plots of  $C_D - C_{D0}$  (where  $C_{D0}$  is the drag at zero angle of attack) were generated and are shown in Figure 8-26. From these plots it can be seen that a minor decrease in the induced drag is indeed present, as the value of  $C_D - C_{D0}$  increases as the wing moves away from the ground. Also, to verify Hsiun and Chen's suggestion that there is only a decrease in pressure drag as the wing approaches the ground (Hsiun and Chen 1996), Figure 8-27 depicts the pressure and shear drag variation for three ground heights ( $h/b = 0.09$ ,  $h/b = 0.145$  and  $h/b = 45$ ). This showed that for all ground heights the shear drag remains the same, whereas the pressure drag decreases with ground proximity.

Pitching moment results show little variation between in and out-of-ground effect, for the ground heights obtained. As with the ground free results, favorable pitching moment characteristics (i.e.  $\frac{dC_m}{d\alpha} < 0$ ) are observed up to  $\alpha = 14^\circ$ . A small increase in the nose-up pitching moment is noticed for  $h/b < 0.27$ . Whereas, at stall conditions lower values of  $\frac{dC_m}{d\alpha}$  are observed for the wing when in ground effect.

Figures 8-29 and 8-30 show the variation of lift and drag coefficients with  $h/b$  at constant  $\alpha$ . Drag coefficients plots data reveal no particular change with changing ground height. The lift coefficients do increase with the decreasing ground height, with the highest increase noted for the high angles of attack

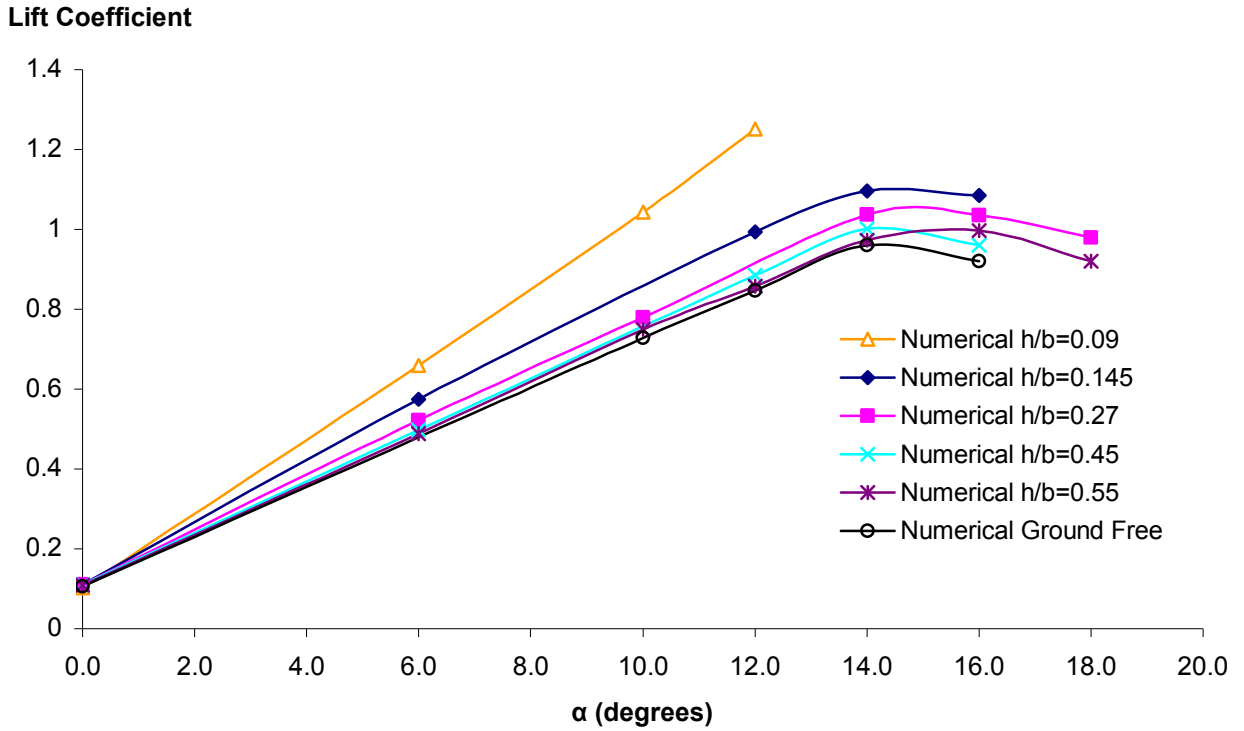


Figure 8-23. Full-scale numerical variation of lift coefficient with angle of attack at various  $h/b$ ,  $Re = 6.9 \times 10^6$  and  $M = 0.11$ .

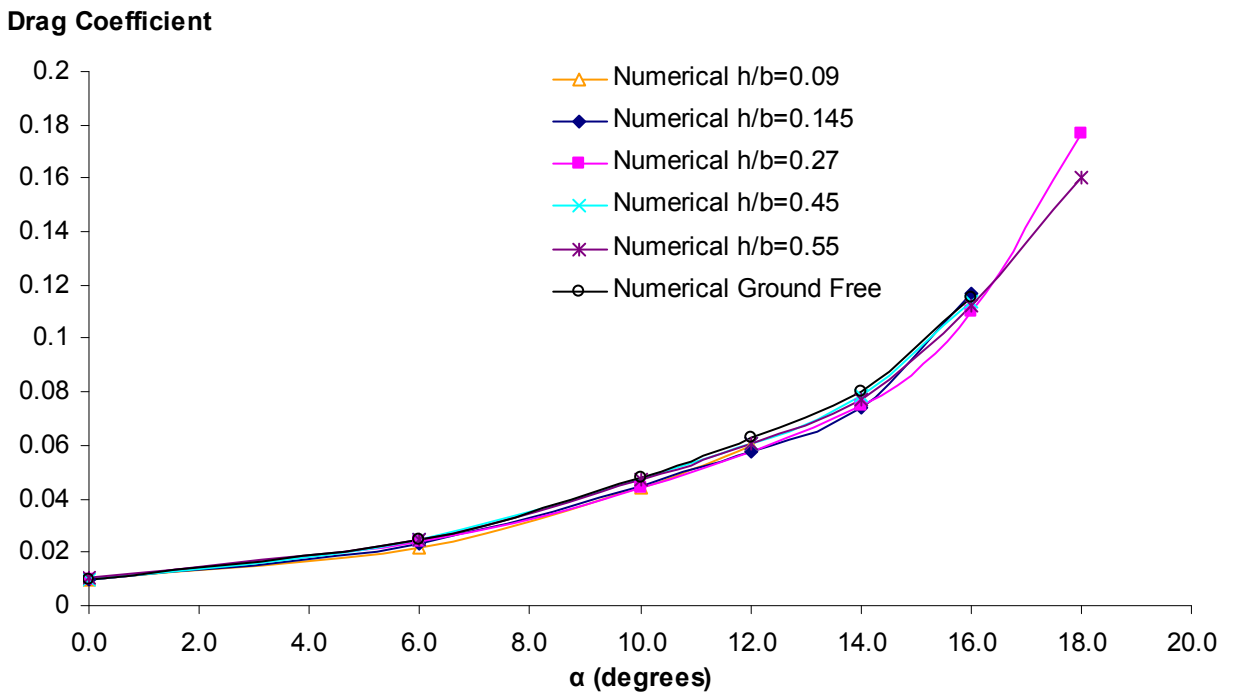


Figure 8-24. Full-scale numerical variation of drag coefficient with angle of attack at various  $h/b$ ,  $Re = 6.9 \times 10^6$  and  $M = 0.11$ .

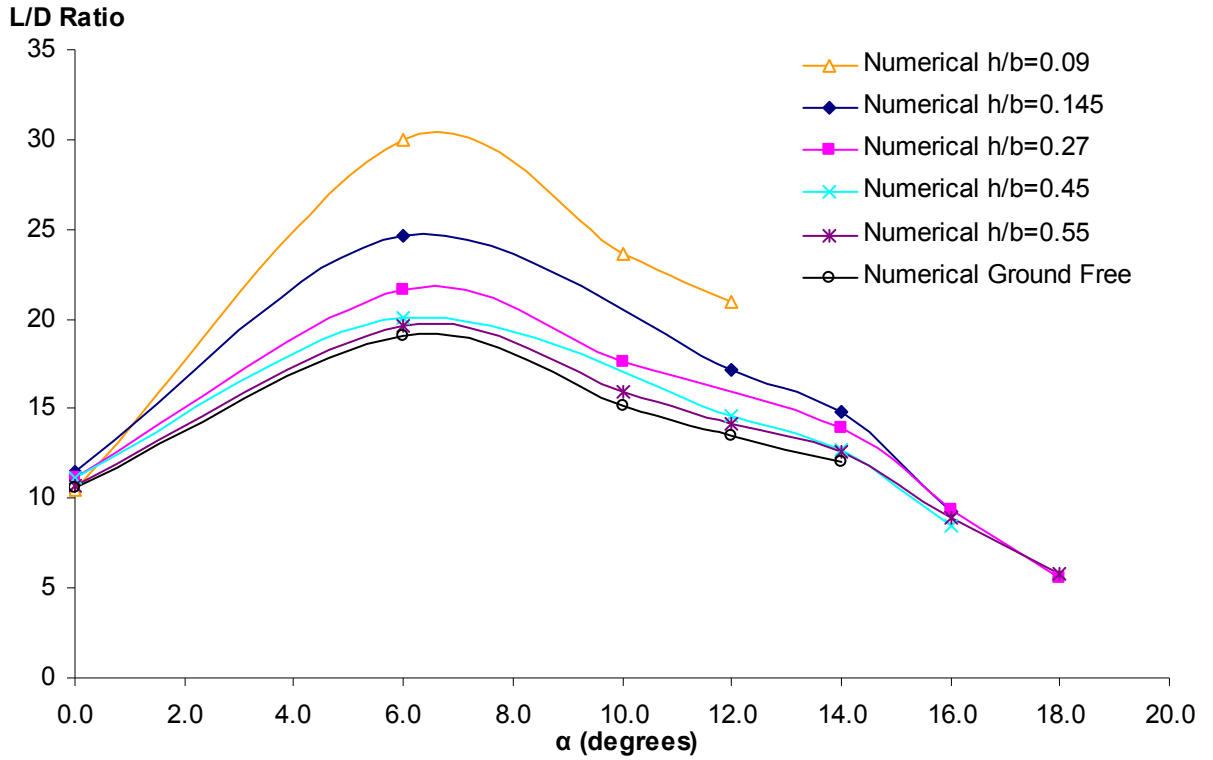


Figure 8-25. Full-scale numerical variation of lift-to-drag ratio with angle of attack at various  $h/b$ ,  $Re = 6.9 \times 10^6$  and  $M = 0.11$ .

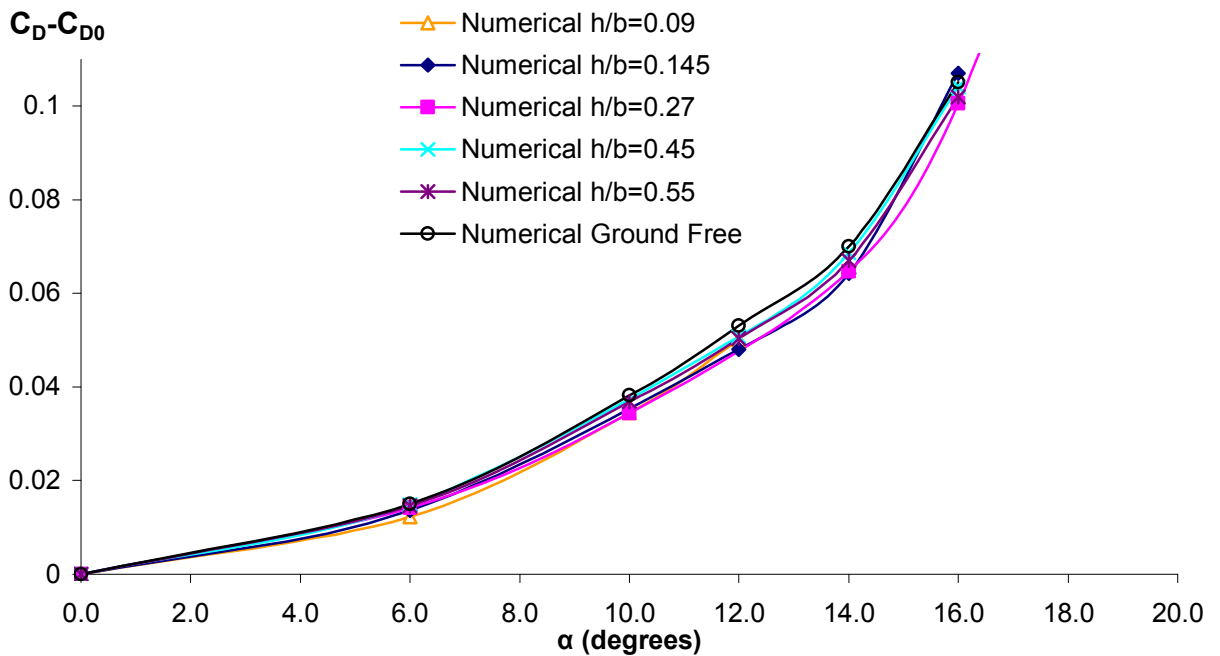


Figure 8-26. Full-scale numerical variation of  $C_D - C_{D0}$  with angle of attack at various  $h/b$ ,  $Re = 6.9 \times 10^6$  and  $M = 0.11$ .

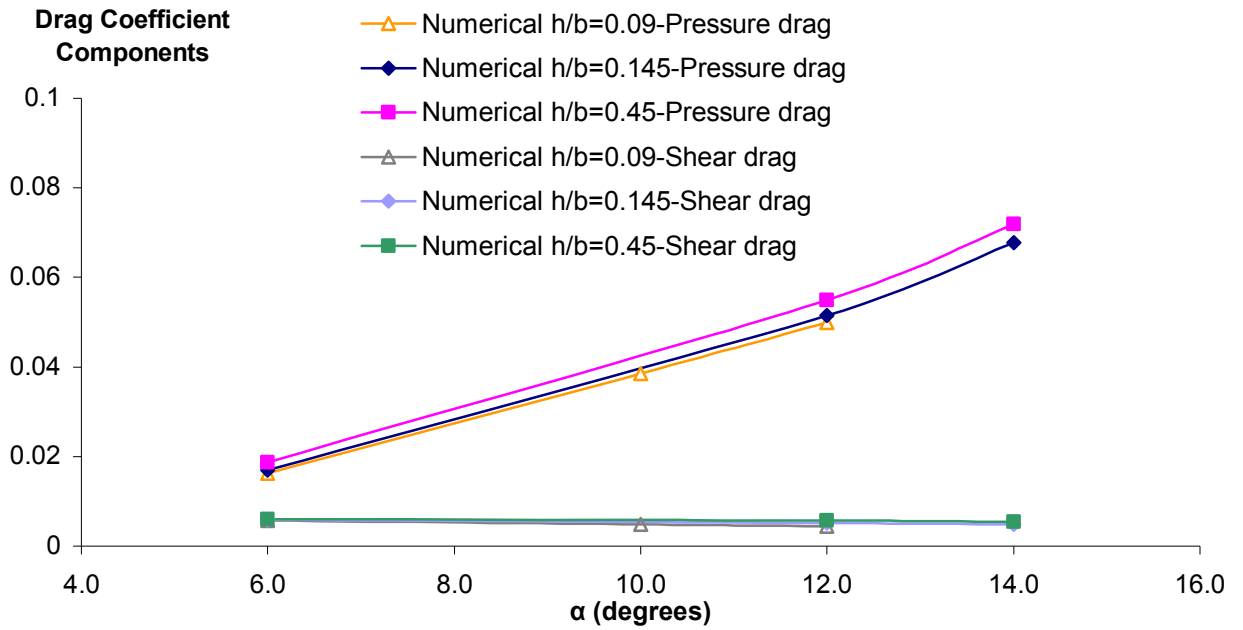


Figure 8-27. Full-scale numerical variation of pressure and shear drag coefficient with angle of attack at various  $h/b$ ,  $Re = 6.9 \times 10^6$  and  $M = 0.11$ .

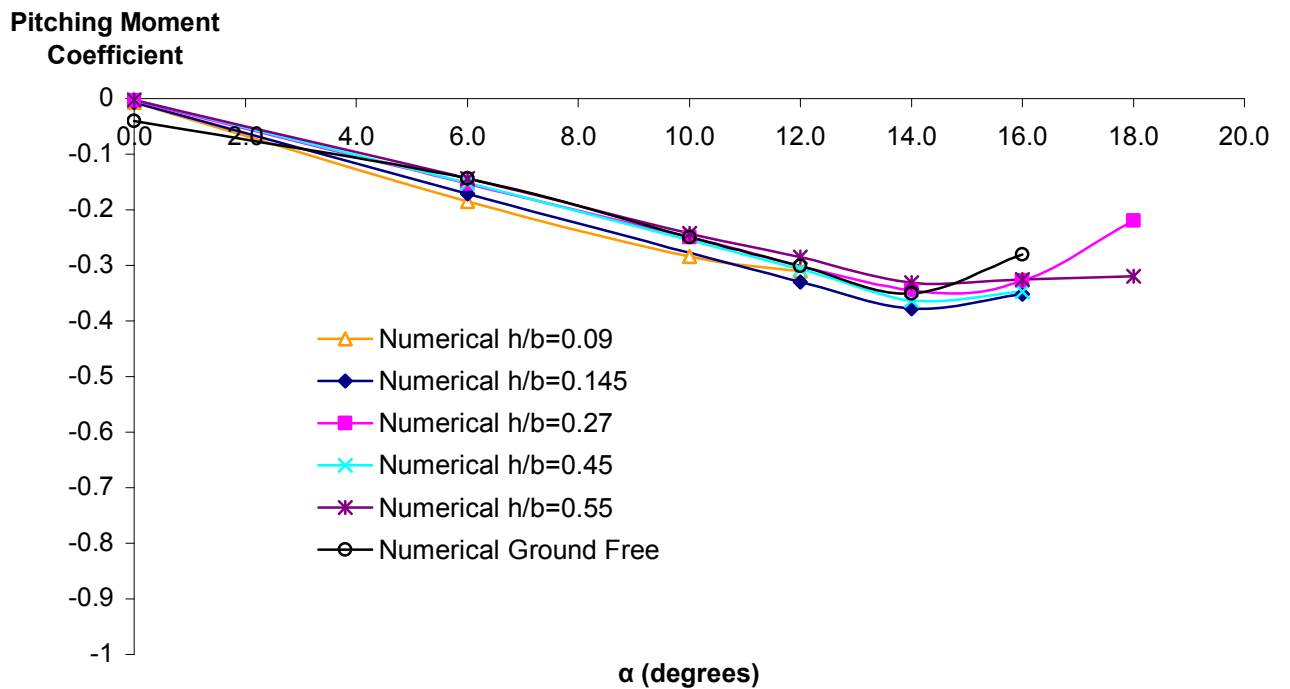


Figure 8-28. Full-scale numerical variation of pitching moment coefficient with angle of attack at various  $h/b$ ,  $Re = 6.9 \times 10^6$  and  $M = 0.11$ .

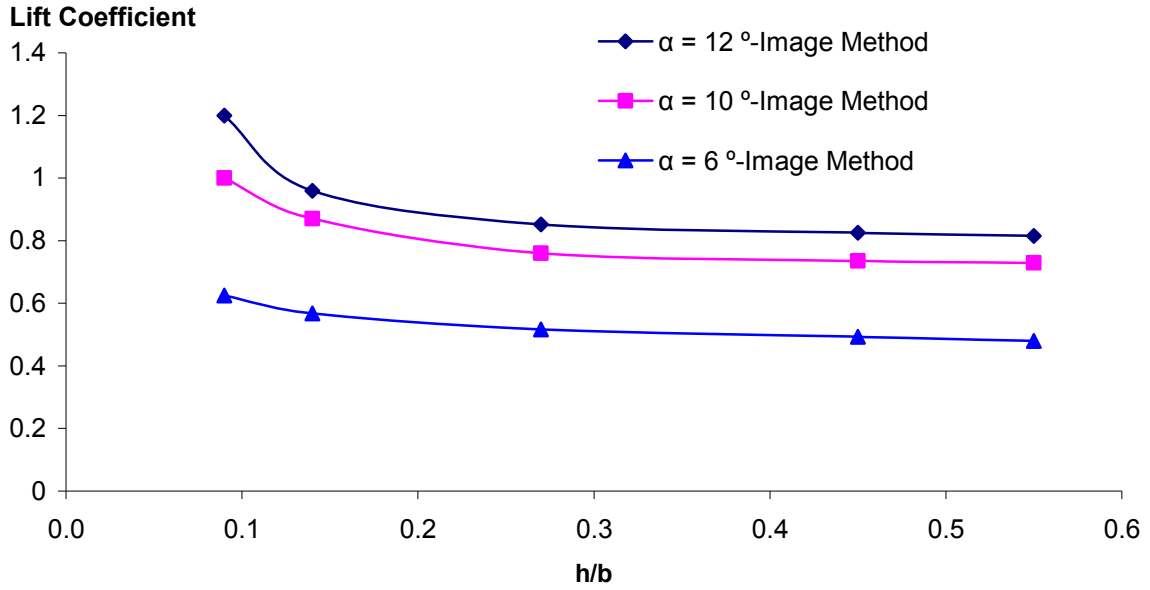


Figure 8-29. Full-scale numerical variation of lift coefficient with  $h/b$ , at various  $\alpha$   $Re = 6.9 \times 10^6$  and  $M = 0.11$ .

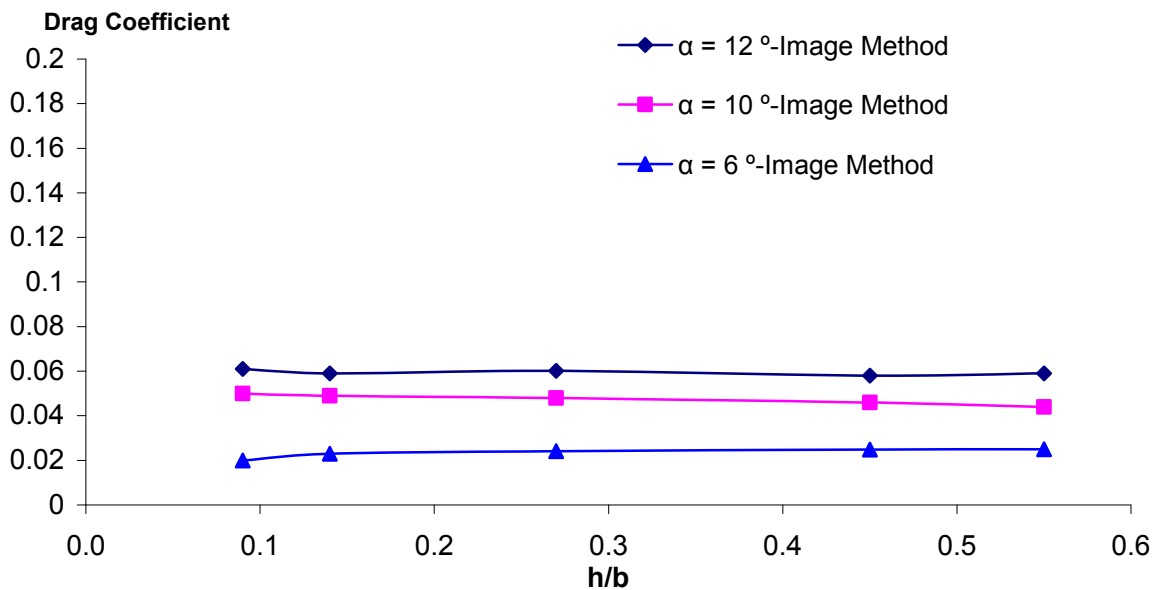


Figure 8-30. Full-scale numerical variation of drag coefficient with  $h/b$ , at various  $\alpha$   $Re = 6.9 \times 10^6$  and  $M = 0.11$ .

In order to further understand and investigate the nature of the aerodynamic characteristics of the W-wing in ground proximity, and substantiate the above obtained lift and drag performance, pressure and shear distributions were also

examined. Figures 8-31 to 8-33 represent the upper and lower surface pressure distribution for the ground-free case at a Reynolds Number of  $6.9 \times 10^6$  and Mach number of  $M = 0.11$ . Figures 8-34 and 8-35 illustrate the pressure distribution at the same flow conditions as above and  $h/b = 0.09$ . As expected, from the lower-surface plots, when compared to the ground-free case, it was observed that the pressure increases with decreasing ground height, particularly near the wing leading edge. Similarly, an increase is noticed with increasing angle of attack, with regions of high pressure covering a large part of the lower wing (as for example at  $h/b = 0.09$  and  $\alpha = 12^\circ$ ). This was furthermore apparent at  $h/b = 0.145$  (Figs. 8-36 to 8-37), where the wing is clearly still under ground influence. Results also showed that ground effect increases slightly the magnitude of the low pressure region on the upper surface of the wing.

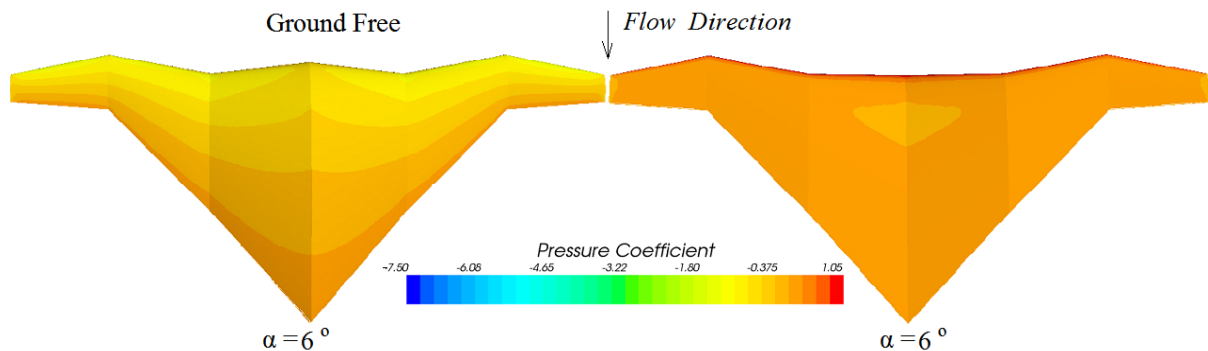


Figure 8-31. Predicted pressure distributions on the upper and lower surfaces at ground free,  $\alpha = 6^\circ$ ,  $Re = 6.9 \times 10^6$  and  $M = 0.11$ .

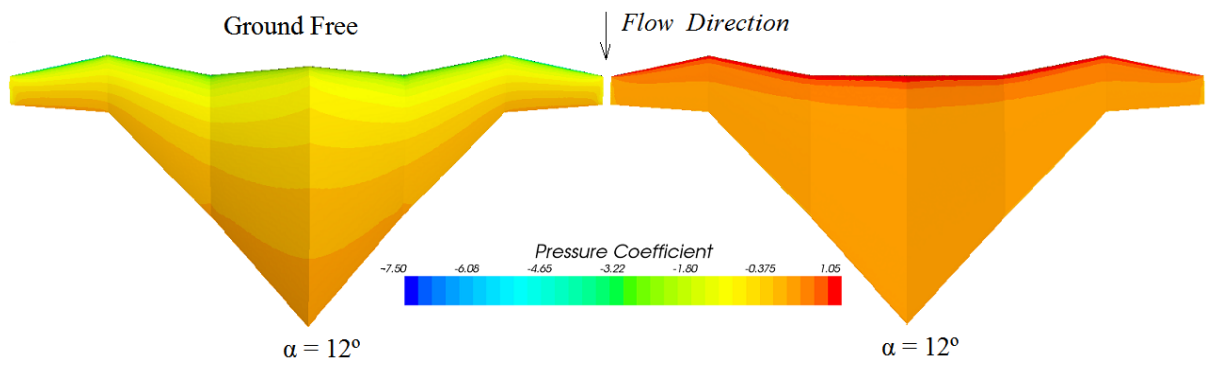


Figure 8-32. Predicted pressure distributions on the upper and lower surfaces at ground free,  $\alpha = 12^\circ$ ,  $Re = 6.9 \times 10^6$  and  $M = 0.11$ .

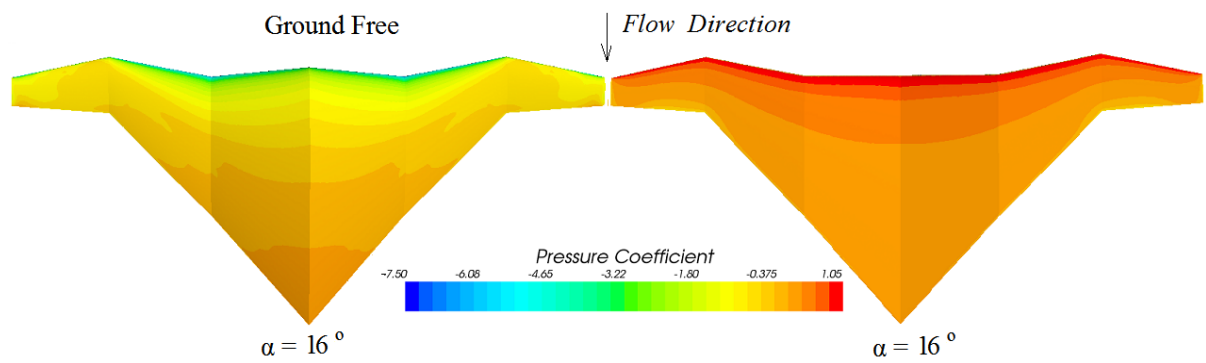


Figure 8-33. Predicted pressure distributions on the upper and lower surfaces at ground free,  $\alpha = 16^\circ$ ,  $Re = 6.9 \times 10^6$  and  $M = 0.11$ .

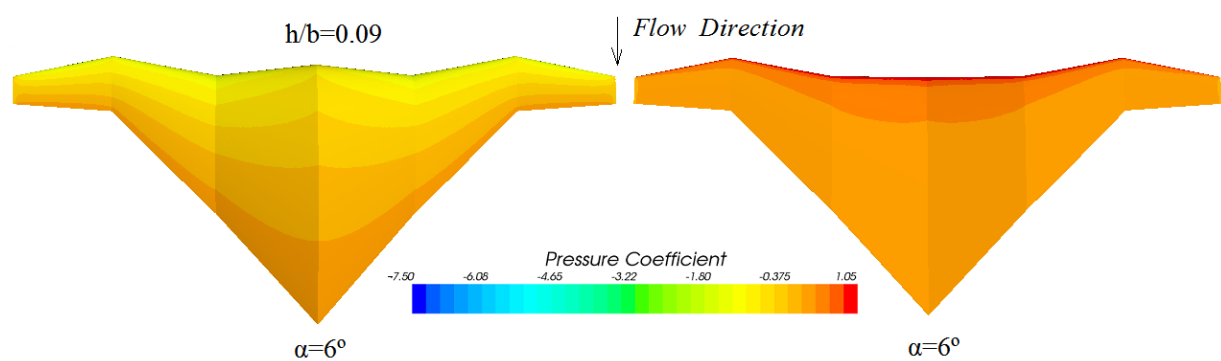


Figure 8-34. Predicted pressure distributions on the upper and lower surfaces at  $h/b = 0.09$ ,  $\alpha = 6^\circ$ ,  $Re = 6.9 \times 10^6$  and  $M = 0.11$ .

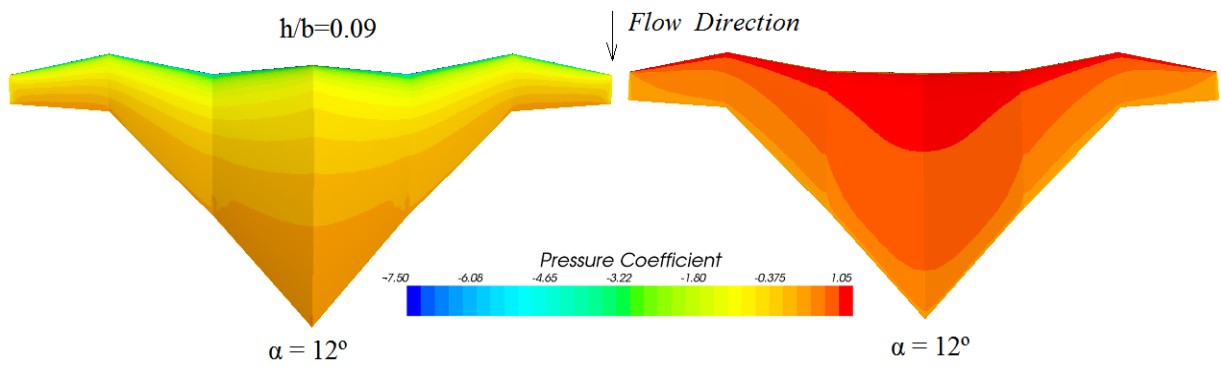


Figure 8-35. Predicted pressure distributions on the upper and lower surfaces at  $h/b = 0.09$ ,  $\alpha = 12^\circ$ ,  $Re = 6.9 \times 10^6$  and  $M = 0.11$ .

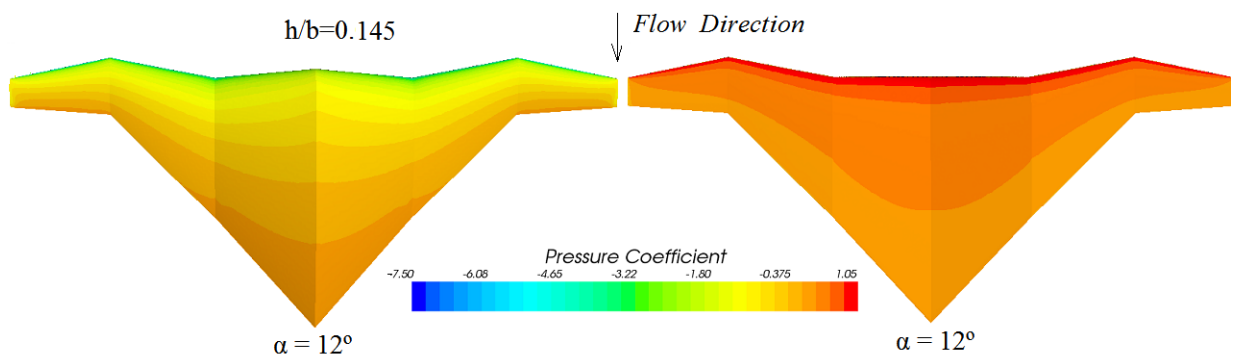


Figure 8-36. Predicted pressure distributions on the upper and lower surfaces at  $h/b = 0.145$ ,  $\alpha = 12^\circ$ ,  $Re = 6.9 \times 10^6$  and  $M = 0.11$ .

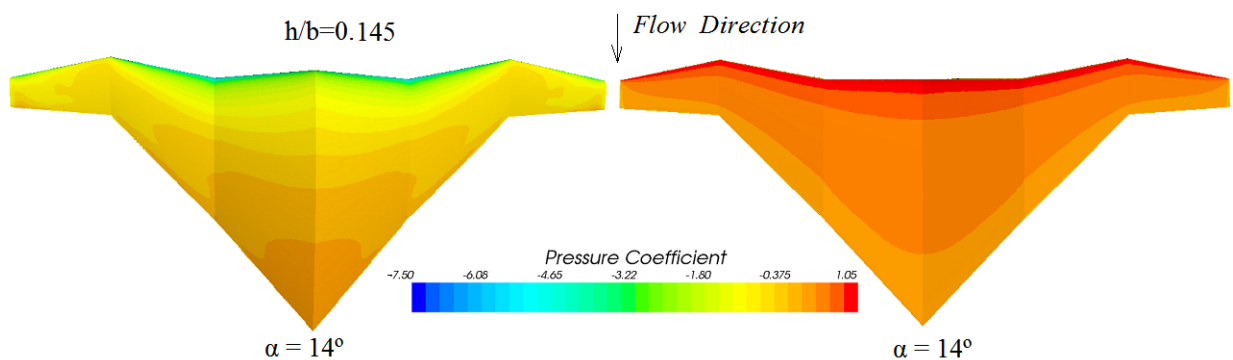


Figure 8-37. Predicted pressure distributions on the upper and lower surfaces at  $h/b = 0.145$ ,  $\alpha = 14^\circ$ ,  $Re = 6.9 \times 10^6$  and  $M = 0.11$ .

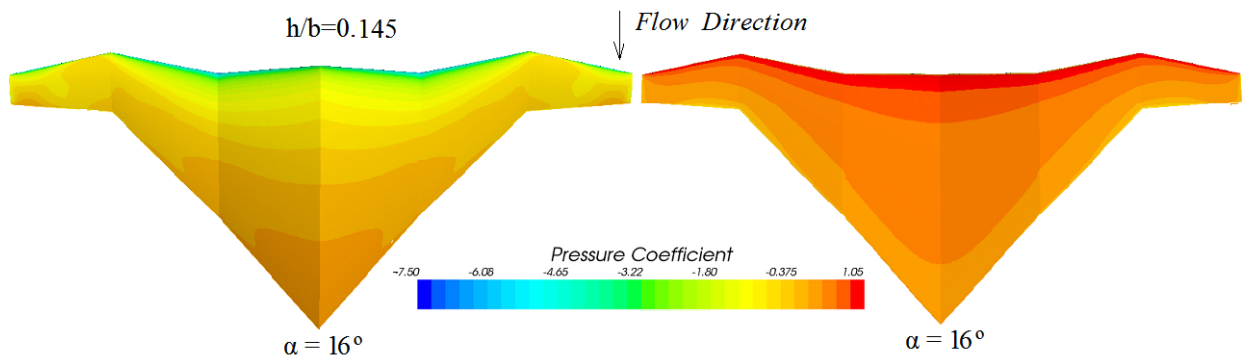


Figure 8-38. Predicted pressure distributions on the upper and lower surfaces at  $h/b = 0.145$ ,  $\alpha = 16^\circ$ ,  $Re = 6.9 \times 10^6$  and  $M = 0.11$ .

Figures 8-39 to 8-41 below illustrate the Mach contour distributions on the ground (symmetry plane) as the wing approaches. The figures show a front view of the wing and ground, with the wing set at an appropriate angle of attack ( $\alpha = 12^\circ$ ) at each  $h/b$  ratio. These ground Mach contour distributions are utilised to clarify the “ram-effect” that is produced when, for small clearances, the air tends to stagnate under the wing; hence, giving the highest possible pressures (Staufenbiel and Schlichting 1988).

At  $h/b = 0.09$ , regions of very slow moving flow are observed underneath the wing, and the ground at these settings is subjected to very strong pressure variations associated with the high pressure regions on the wing lower surface, as noted above. It can also be seen that at the ground section underneath the mid part of the wing, regions of very high velocity are noticed. This effect is only observed in the  $h/b = 0.09$  ratio plots. As the wing moves further from the ground, (Figures 8-40 and 8-41) so its influence on the ground is reduced and therefore the ram-effect is noticed to diminish, with only fairly small ground pressure variations observed at  $h/b = 0.45$

These plots in general do explain the ram-effect or the air-cushion effect reported previously, and it can be observed that the W-wing at low ground clearances creates a rather strong such effect, which is advantageous when short-take-off requirements are to be met.

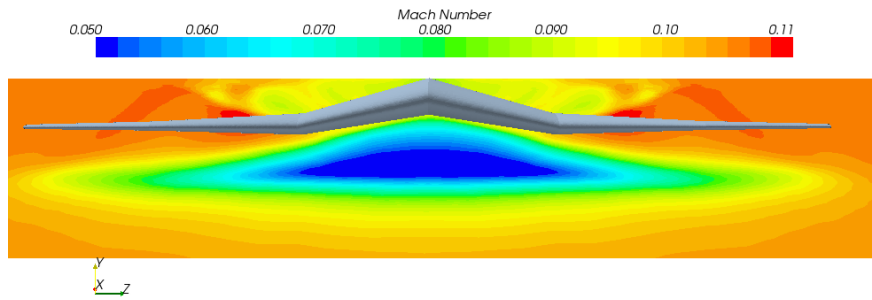


Figure 8-39. Ground Mach distribution contours at  $\alpha = 12^\circ$ ,  $h/b = 0.09$ ,  $Re = 6.9 \times 10^6$  and  $M = 0.11$ .

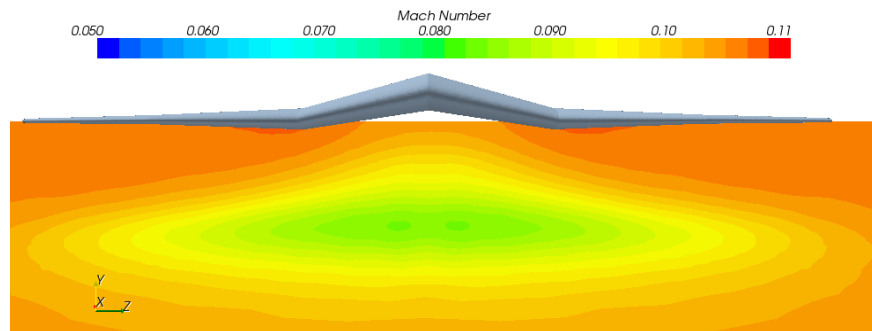


Figure 8-40. Ground Mach distribution contours at  $\alpha = 12^\circ$ ,  $h/b = 0.145$ ,  $Re = 6.9 \times 10^6$  and  $M = 0.11$ .

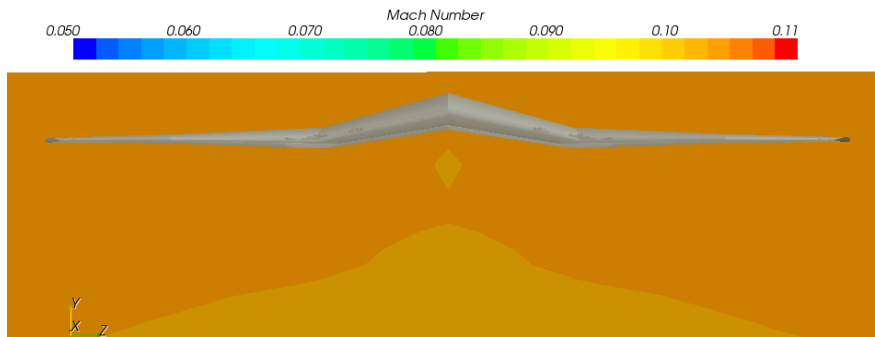


Figure 8-41. Ground Mach distribution contours at  $\alpha = 12^\circ$ ,  $h/b = 0.45$ ,  $Re = 6.9 \times 10^6$  and  $M = 0.11$ .

Shear stress distributions were employed to investigate the effect of the ground on flow separation at the sensitive near-stall angles. Figures 8-42 and 8-43 show the wall shear-stress magnitude streamlines at four different ground heights. A slight variation is observed from shear-stress streamlines for  $h/b = 0.09$ , at  $\alpha = 12^\circ$ , in comparison with  $h/b = 0.145$  at the same angle of attack. From Figure 8-42 it can be seen that in the presence of the ground the spanwise flow is more pronounced, as the streamlines show a more severe mid-wing spanwise movement. The streamlines are closer to each

other and this causes shear-stress to reduce. Therefore, greater regions of almost zero shear-stress magnitude are observed for this case, suggesting an increased tendency for the onset of trailing separation when compared to  $h/b = 0.45$ , where the wing is further away from the influence of the ground. At stall, (i.e.  $\alpha = 16^\circ$ ) the flow has separated from the tip of the wing, and it can also be seen that the separated region is greater as the ground approaches (as noted in Figure 8-43). These figures show that the ground does in fact affect the spanwise movement and separation onset, with increasing severity as  $h/b$  decreases. It also needs to be mentioned that, at the current flow conditions, the leading-edge inboard crank does not participate in the flow separation, as the flow in the area surrounding the crank is fully attached.

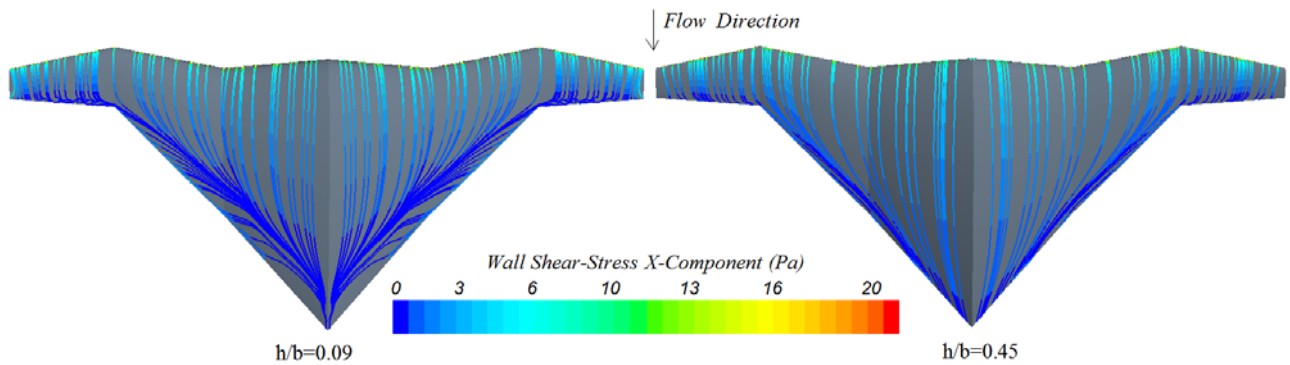


Figure 8-42. Wall shear-stress streamline distribution for  $h/b = 0.09$  (left) and  $h/b = 0.145$  (right) at  $\alpha = 12^\circ$ ,  $Re = 6.9 \times 10^6$  and  $M = 0.11$ .

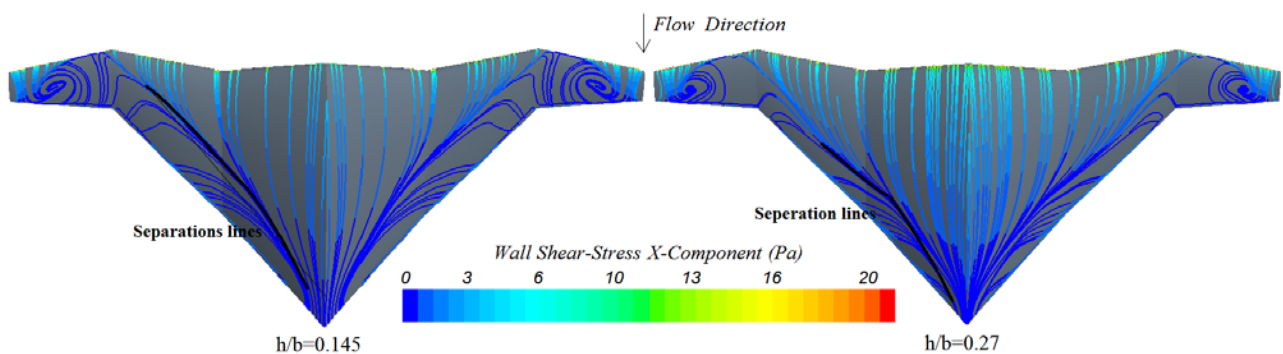


Figure 8-43. Wall shear-stress streamline distribution for  $h/b = 0.145$  (left) and  $h/b = 0.27$  (right) at  $\alpha = 16^\circ$ ,  $Re = 6.9 \times 10^6$  and  $M = 0.11$ .

To verify the above spanwise flow movement findings, off-surface streamlines plots are also given. Interestingly the off-surface streamlines, complemented by the near-wake behaviour, provide an explanation of the previously noticed high-velocity flow on the ground Mach contours. By comparing the images for  $h/b = 0.09$  and  $h/b = 0.145$ , both at  $\alpha = 12^\circ$ , the results (see Figures 8-44 and 8-45) show clearly that the reason behind the high velocity flow is the interaction of the wake with the ground. Although the image method is employed for this study, the plots reveal a strong interference of the ground with the wing wake suggesting not fully developed rotational flow emanating from the ground. This does not seem to have any effect on the longitudinal aerodynamic plots as no irregularities are noted at these conditions. Also, due to the fact that the wing will be at this ground height for a very short amount of time, the effect of this is considered not to be of significance.

Similarly with the results from section 7, the plots from Figures 8-46 and 8-47 reveal the secondary vortex emerging from the near wing tip region at  $\alpha = 16^\circ$ . A comparison of the behaviour of the inboard vortex in and out ground effect shows a slight difference. The strength of the secondary vortex is more pronounced near the ground (as depicted in Figure 8-46). This signifies an increase in their circulation and the suction they induce. A strong vortex core suggests delayed vortex breakdown, which could be an undesirable effect for the type of aircraft this wing is envisaged for. Furthermore, the effect of the ground is shown to move the secondary vortex inboard.

Full-scale numerical investigations of the near-wake total pressures reveal similar trends as noticed from the experiments and numerical analyses for the low-speed study. The outboard tip vortex movement, as well as the increasing appearance of the secondary vortex, have been observed. Previous studies (Steinbach 1997) have suggested that the tip vortex strength reduces with ground proximity, an effect which is linked with the induced drag reduction. However, the results from this study show no significant difference and no tip vortex strength reduction is noticed. This can also be observed from the near-wake total pressure plots illustrated in Figures 8-48. Also, from the same plots (at  $\alpha = 16^\circ$ ), it can be noticed that the strength of the inboard vortex increases with decreasing ground height, and the inboard wake is slightly greater when  $h/b$  is reduced. An interesting phenomenon is also the fact that the wake

is thinner in the inboard region when the full-scale results are considered, which implies that larger lift will be generated at that region.

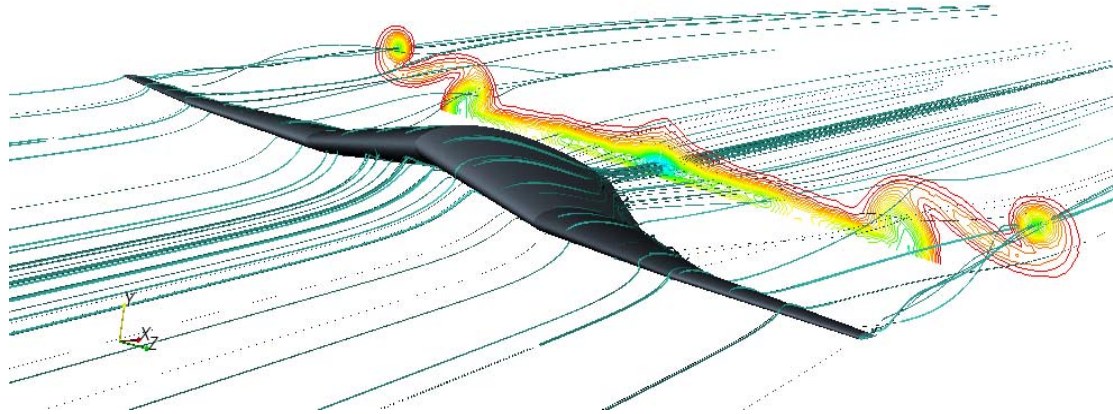


Figure 8-44. Off-surface streamlines and near-wake at  $h/b = 0.09$ ,  $\alpha = 12^\circ$ ,  $Re = 6.9 \times 10^6$  and  $M = 0.11$ .

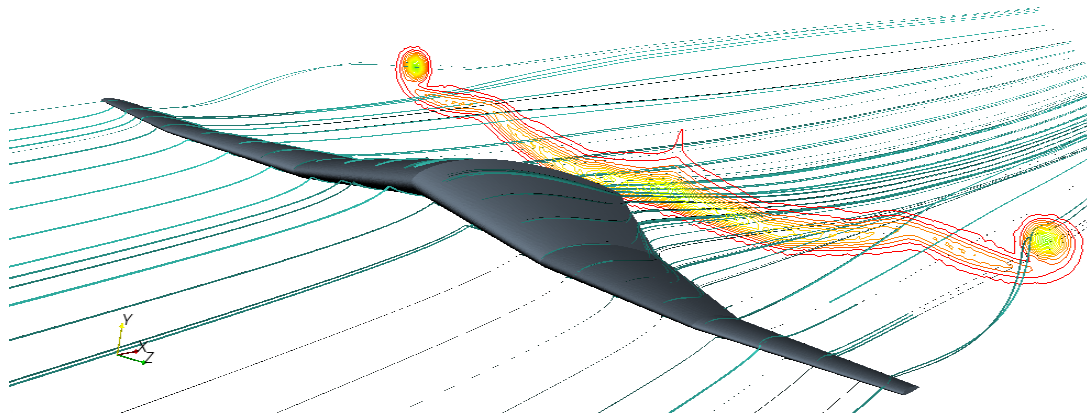


Figure 8-45. Off-surface streamlines and near-wake at  $h/b = 0.145$ ,  $\alpha = 12^\circ$ ,  $Re = 6.9 \times 10^6$  and  $M = 0.11$ .

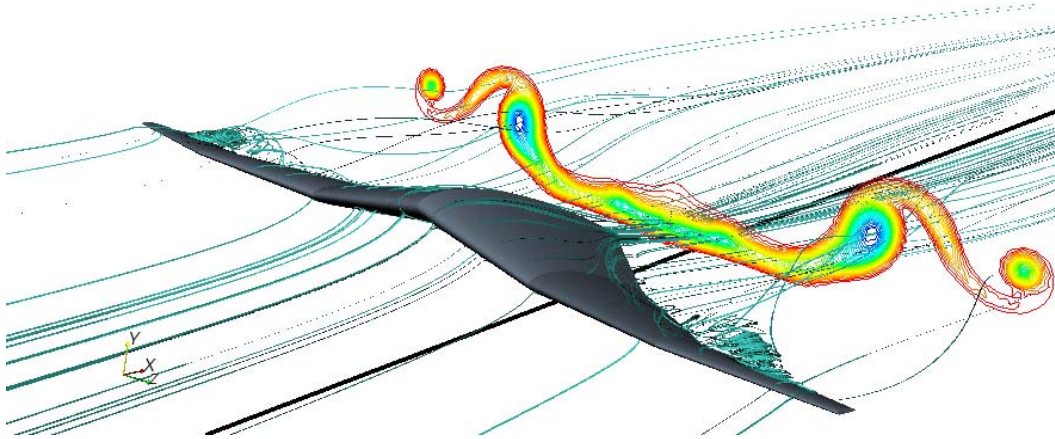


Figure 8-46. Off-surface streamlines and near-wake at  $h/b = 0.09$ ,  $\alpha = 16^\circ$ ,  $Re = 6.9 \times 10^6$  and  $M = 0.11$ .

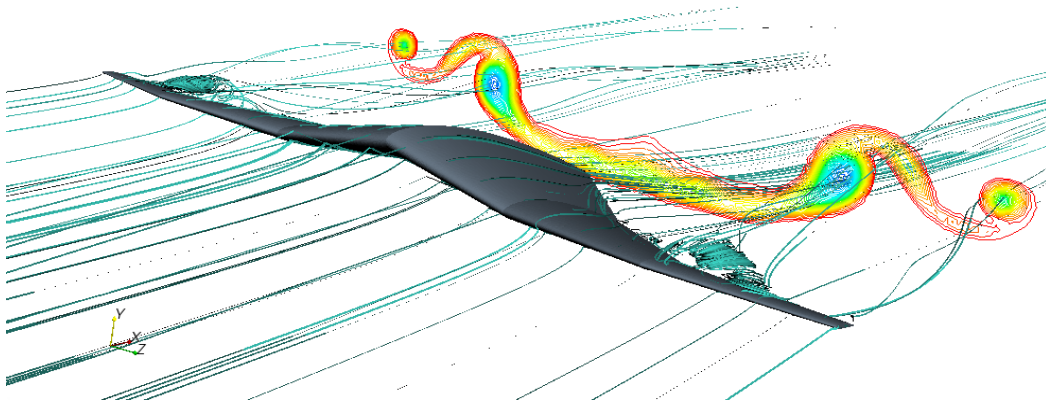


Figure 8-47. Off-surface streamlines and near-wake at  $h/b = 0.09$ ,  $\alpha = 18^\circ$ ,  $Re = 6.9 \times 10^6$  and  $M = 0.11$ .

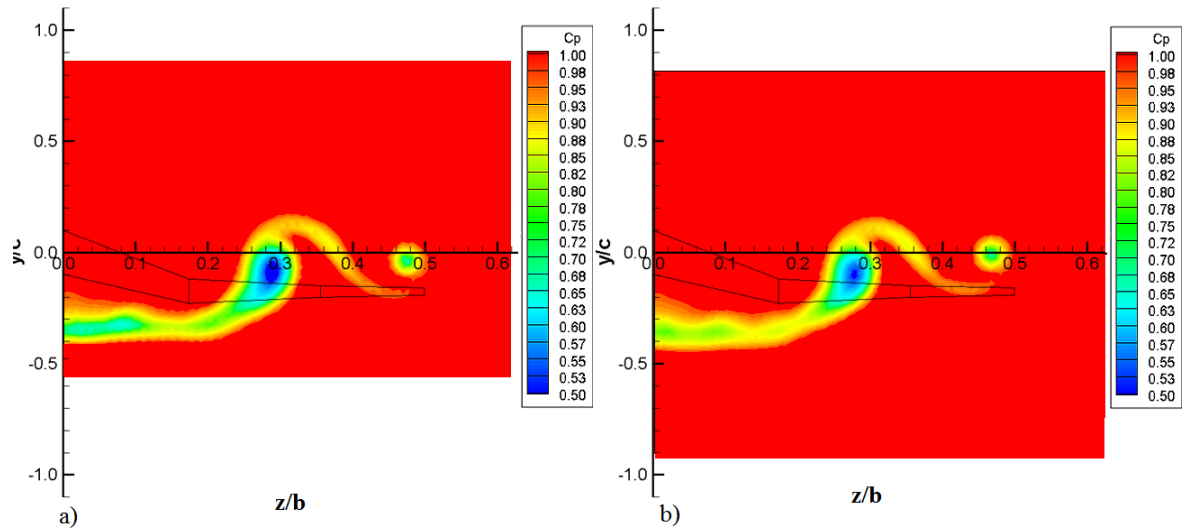


Figure 8-48. Numerical results of the near-wake total pressure distribution at  $\alpha = 16^\circ$ ,  $Re = 6.9 \times 10^6$  and  $M = 0.11$  at a)  $h/b = 0.145$  and b)  $h/b = 0.45$ .

## Summary

The general aim of this section was to establish the aerodynamic behavior of the W-wing in ground effect, by coupled experimental and numerical investigations. A good agreement was achieved between the two methods employed, with greater differences in lift coefficients for higher angles of attack, which were affected due to the employment of the fixed ground board to account for the ground in the experimental tests. The significant departure between the two solutions for the lift results improved when the fixed ground board was included in the numerical set-up. The differences between the lift coefficient results, although still present, were noticeably less than when the image method was employed. Drag coefficient results, on the other hand showed very agreement between the experimental and numerical results, both when image and fixed ground board methods were utilized.

Similarly, results from the near-wake momentum deficit, revealed agreement between the two methods. From the experimental results, a separation of vortex induced ground surface boundary layer during vortex-ground encounter was noticed, which affected the experimental results for  $h/b < 0.09$ . This suggests that careful considerations have to be made when the experimental results were to be considered, because of the fixed ground-board induced shortcomings.

In terms of aerodynamic analyses, the key finding from the predictions were: The results show a great increase of the lift coefficient and lift-to-drag ratio for the W-wing in ground effect. Values of  $L/D = 30$  are achieved for  $h/b = 0.09$ , which doubles the  $L/D$  in free-flight. As this is the current planned wing setting for the Jetpod, the results at this ground height are of particular significance.

As mentioned in section 1 of this thesis general specification of the wing suggest that a  $C_{LTOclimb}$  should be in the order of 0.73 which is in agreement with the above findings as maximum lift coefficient obtained with clean wing reached at  $14^\circ < \alpha < 16^\circ$  are approximately 0.9. In general the computed  $C_L$  for take-off and landing conditions fall within the top level requirements for the current wing design.

The current results also show regions of very low velocity and high pressure underneath the wing, suggesting a very strong “air cushion” effect being induced by the wing. The high  $L/D$  ratios for the W-wing planform were found to be particularly high when compared with similar data for other wings. Such high  $L/D$  ratios are very desirable for the performance of the STOL type aircraft for which the wing is intended. The wing also exhibits statically stable pitching moment response up to stall conditions. However, the spanwise flow velocities over the upper surface are increased with decreasing ground height and the associated stall vortex features are strengthened for cases of the higher angles of attack.

The off-surface streamline observations confirmed that the spanwise motion of streamlines is more apparent in ground effect. The stall-initiated inboard vortex onset was observed to increase in strength with decreasing ground height, as well as an outboard movement of the tip vortices, suggesting an increase of the effective aspect ratio of the wing. No effect of the inboard crank was noted at the speed employed for these tests.

On the whole, the the above results presented an indication of the capabilities of the W-wing in ground effect. A general conception was that the wing shows very good near-ground performance capabilities with high  $L/D$  ratios and a very strong “air-cushion” effect being affected by the wing’s design.

## **9. Assessment of the Aerodynamic Performance Improvement of the W-Shaped Leading-Edge Wing**

This section outlines results of a design study investigating variations on the original W-wing to identify possible modifications that would improve performance. The design study was performed in two parts. In the first part, further investigation of the wing-tip design and the design of the crank, by replacing the tip of the original wing with a forward-swept tip was carried out. Also, to compare the effect of the inboard crank, an un-swept mid-wing (i.e no crank) design was investigated, at the higher angles of attack only. In the second part, an investigation on variations of the sweeps on the combined-sweep wing were carried out, whilst employing the same aspect ratio and/or wing span as the original W-shaped leading-edge wing.

For the above-mentioned investigations, only high-speed numerical simulations were obtained. This was done by both Navier-Stokes and Full-Potential investigations for the free-flight configurations only. The attained results, such as lift, drag, and where applicable on- and off-surface flow investigations, were then compared with the original wing data available in the previous sections.

To reiterate on some of the findings in the previous chapters: classic static stall onset from the W-shaped leading-edge wing high-speed study was noted to appear at  $\alpha=14^\circ$ . The stall was initiated from the tip of the wing, by the effects of the trailing edge separation, which is a typical behavior of aft-swept wings. Later, with increasing angle of attack, the trailing edge separation moved inboard, with most of the region of

the wing being separated at  $\alpha=18^\circ$ . Additionally, an inboard vortex was noticed to appear in the near-wake at higher angles of attack, and regions of local supersonic flow were observed at  $\alpha=10^\circ$  and above. The results of the investigation from section 7 revealed that, at stall conditions, the crank could have an effect on the separation characteristics.

### **9.1 Numerical examination of un-swept mid-wing and forward-swept tip of the W-shaped leading-edge wing**

In the following paragraphs, high-speed numerical results of an un-swept mid-wing version (see

Figure 9-1) of the original W-shaped leading-edge wing studied in this research are presented. Additionally, high-speed numerical results of a forward-swept tip (see Figure 9-2) design of the original wing are presented. The wing-span of the original wing as well as the flow conditions were maintained for both studies (i.e. Reynolds Number of  $3 \times 10^7$  and Mach number of 0.45). The numerical methods utilised were identical to those described in section 7, with the same discretisation and turbulence closure model (k- $\omega$  SST). For simplicity purposes, the un-swept mid-wing version (see

Figure 9-1) of the original W-shaped leading-edge wing will hereafter be referred to as the W-wing Variant A and the forward-swept tip design of the original wing will be referred to as the W-wing Variant B. To carry out the comparison, the longitudinal characteristics as well as on surface distribution of shear stress and pressure are presented.

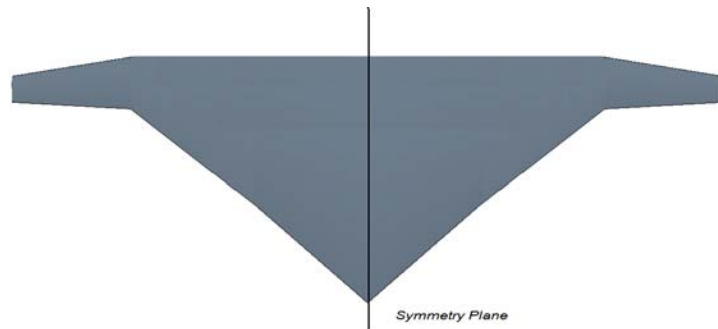


Figure 9-1. Un-swept mid-wing geometry.

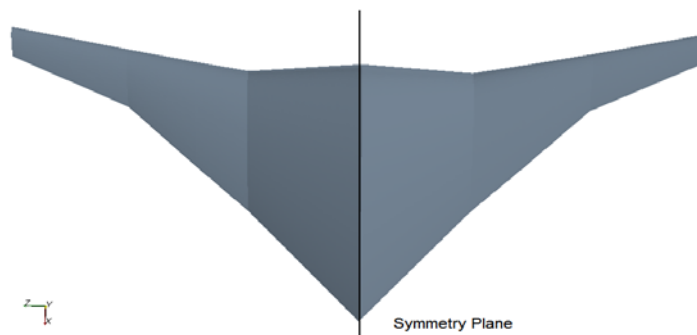


Figure 9-2. Forward-swept tip wing geometry.

Figures 9-3 to 9-6 present, the lift, drag, lift-to-drag ratio and pitching moment data comparison between the original wing, the W-wing Variant A and the W-wing Variant B. Only near-stall conditions were considered for the Variant A case; hence only data from  $\alpha = 14^\circ$ ,  $16^\circ$  and  $18^\circ$  are plotted. From Figure 9-3 it can be seen that the W-wing Variant B lift coefficient plots give similar values to those of the original wing up to  $C_{L_{max}}$ . At  $\alpha = 14^\circ$ , a slightly higher lift coefficient is obtained with both the Variant A and the Variant B wings. At  $\alpha = 16^\circ$ , the W-wing Variant B gives identical values to the original wing. The W-wing Variant A however, gives a higher lift coefficient at  $\alpha = 16^\circ$ , and a slightly lower one at  $\alpha = 18^\circ$ .

Drag plots (Figure 9-4), reveal slightly higher drag coefficients for the Variant A case at  $\alpha = 14^\circ$  and  $\alpha = 18^\circ$ , whereas the W-wing Variant B design data agree with the

original wing, as no major disagreement has been observed. These data, and the above mentioned lift results, then predict a very similar lift-to-drag ratio curve, plotted in Figure 9-5.

The only significant difference between the three designs, in terms of longitudinal characteristic, may be noticed from the pitching moment coefficient plots, shown in Figure 9-6. The obtained results for the three cases investigated show that the variant designs experience earlier longitudinal instability, beginning at  $\alpha = 14^\circ$ , while the original wing continues being statically stable up to stall ( $\alpha = 16^\circ$ ).

Thus, generally, no significant changes in the lift coefficient results are noticed between the three-designs. Similarly, no major drag difference is observed between the three cases studied herein. The greatest difference is noticed between the three designs near the stall conditions, where the original wing has been proven to possess better longitudinal stability in the near stall region. Therefore, in order to investigate other differences between the designs, if any, on and off-surface pressure and shear plots are presented.

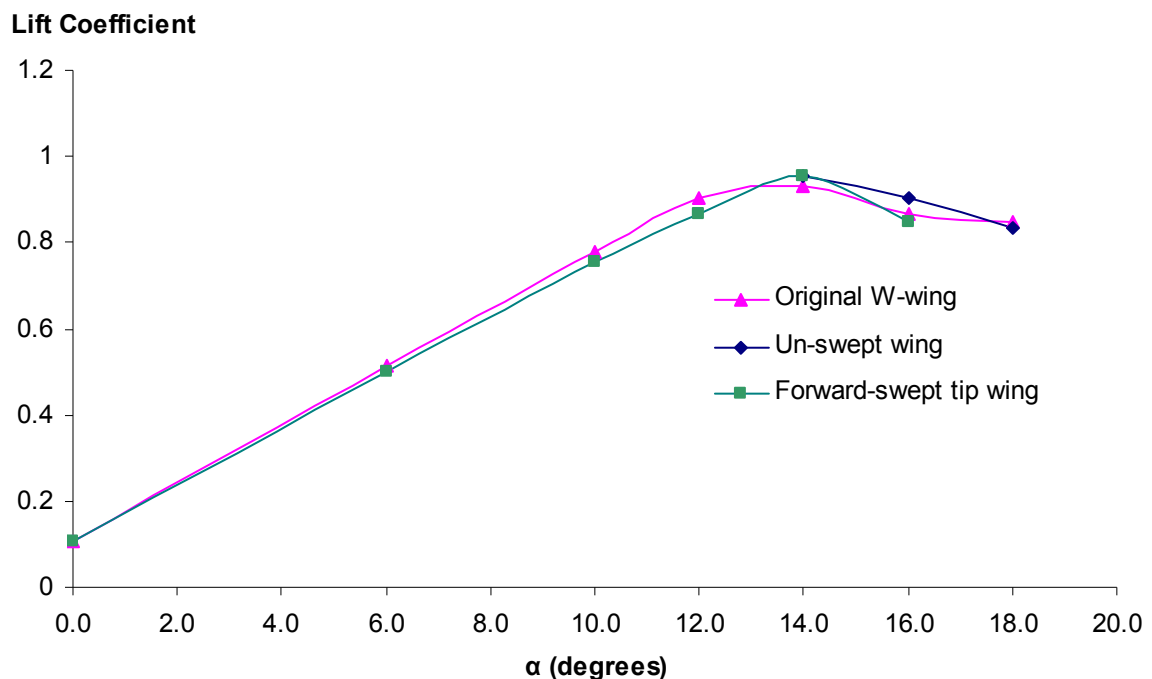


Figure 9-3. Numerically (Navier-Stokes) predicted lift coefficients for the three design variations at  $M = 0.45$  and  $Re = 3 \times 10^7$ .

### Drag Coefficient

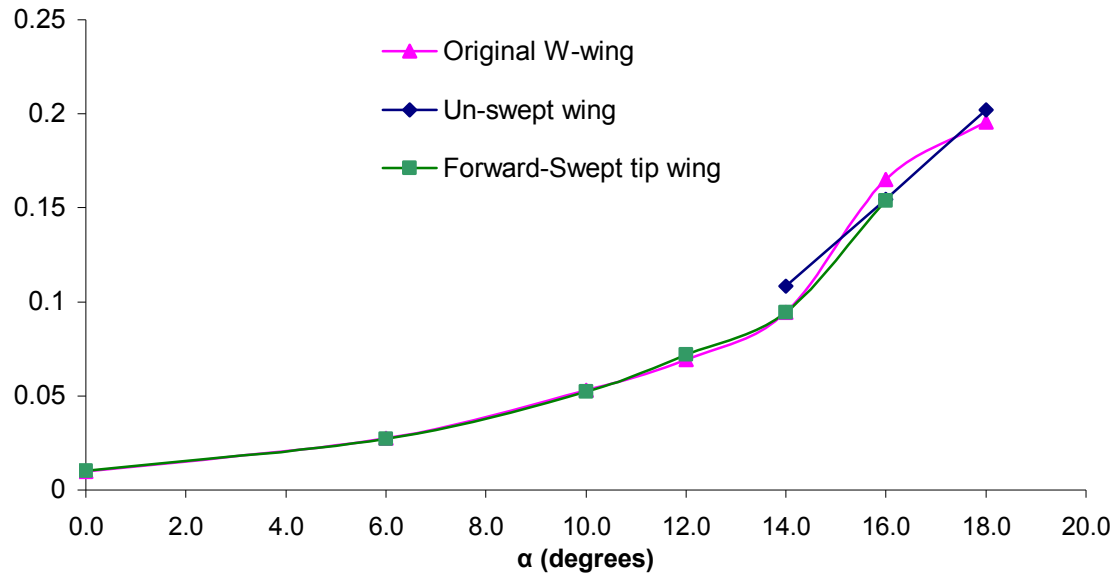


Figure 9-4. Numerically (Navier-Stokes) predicted drag coefficients for the three design variations at  $M = 0.45$  and  $Re = 3 \times 10^7$ .

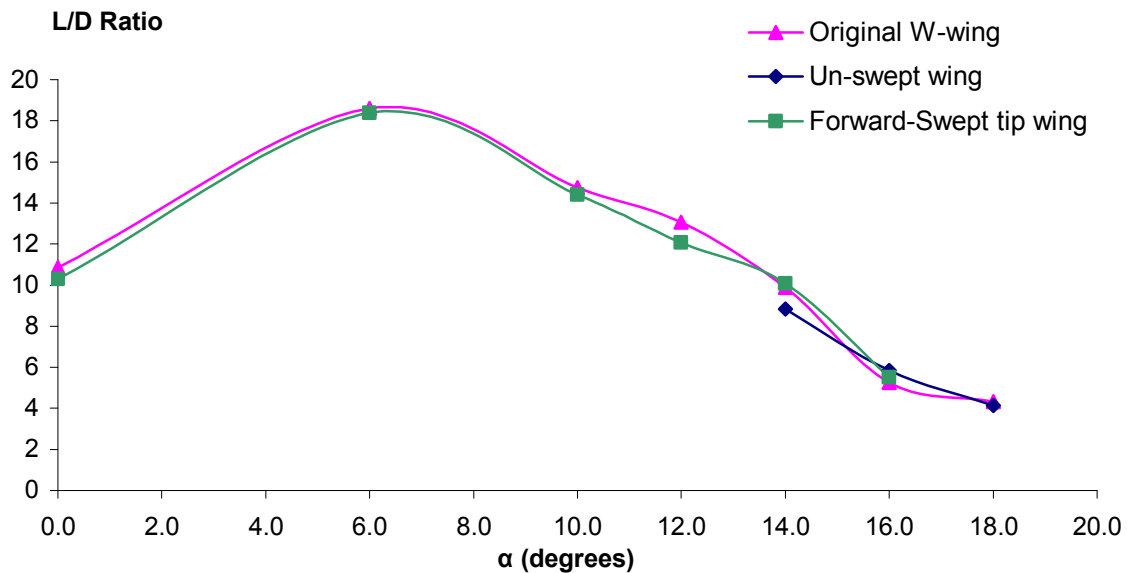


Figure 9-5. Numerically (Navier-Stokes) predicted lift-to-drag ratio for the three design variations at  $M = 0.45$  and  $Re = 3 \times 10^7$ .

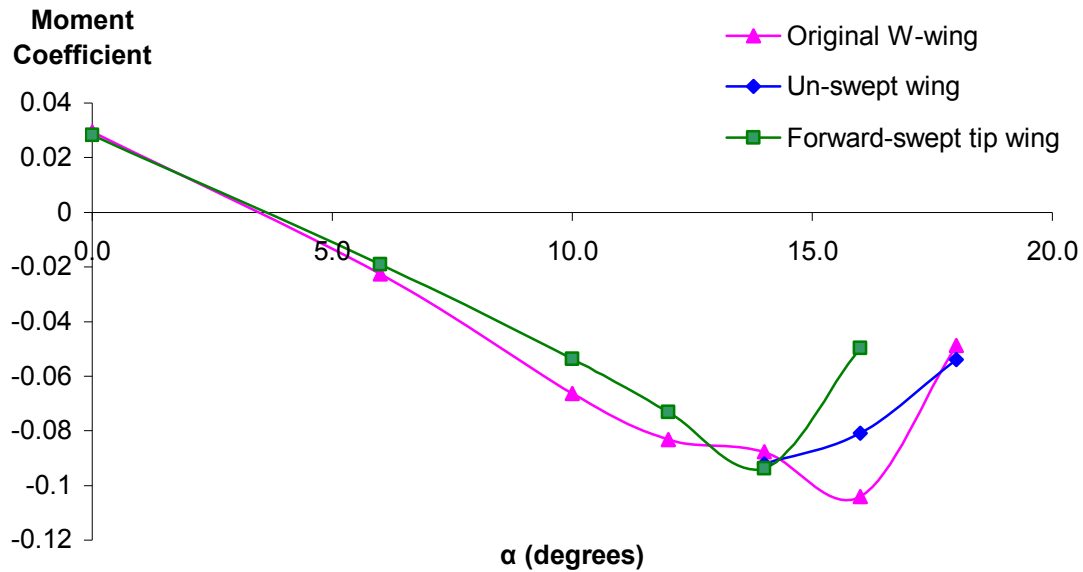


Figure 9-6. Numerically (Navier-Stokes) predicted lift-to-drag ratio for the three design variations at  $M = 0.45$  and  $Re = 3 \times 10^7$ .

Figures 9-7 and 9-8 present the upper and lower pressure distributions for the un-swept wing at  $\alpha = 16^\circ$  and  $\alpha = 18^\circ$ ,  $M = 0.45$  and  $Re = 3 \times 10^7$ . When compared with the results of the original wing (see Figures 7-16 and 7-17 from section 7), the Variant A results show more consistent leading edge suction pressures for the  $\alpha = 16^\circ$  case. However, higher adverse pressure gradients are also noticed at the same conditions, when compared to the original wing.

At  $\alpha = 18^\circ$ , similarity is noted between the upper pressure behaviours of the two designs (W-wing Variant A and original wing). Leading-edge suction discontinuities near the mid-wing region are also noted for the Variant A case, similarly to the original wing. The discontinuities are also present in the W-wing Variant B case, but at a slightly more outboard location, suggesting that the effect is indeed not entirely dependant on sweep.

The effect of the more severe adverse pressure gradients observed for the W-wing Variant A case may be observed from the shear-stress surface streamlines depicted in Figure 9-9, below. The streamlines show the separated (i.e. zero-shear) regions of the upper surfaces of the un-swept wing at  $\alpha = 16^\circ$  and  $\alpha = 18^\circ$ . These plots suggest greater separated regions when compared with the original wing (see Figure 7-19).

Additionally, from the shear stress streamlines, one can also prove that the absence of the forward-sweep in the mid-wing does have an effect on the spanwise motion of the flow. The separated flow region for the W-wing Variant A case now covers the mid-wing as well, and no tendencies to maintain attachment are observed. This can also be confirmed from the off-surface total pressure plots depicted in Figure 9-10. These plots, in contrast to the original wing's results (obtained at the same conditions), show separated regions at the mid-wing as well. This suggests that, in the absence of the forward-sweep, the un-swept wing struggles to maintain attached flow, or indeed prevent further separation on the rest of the wing.

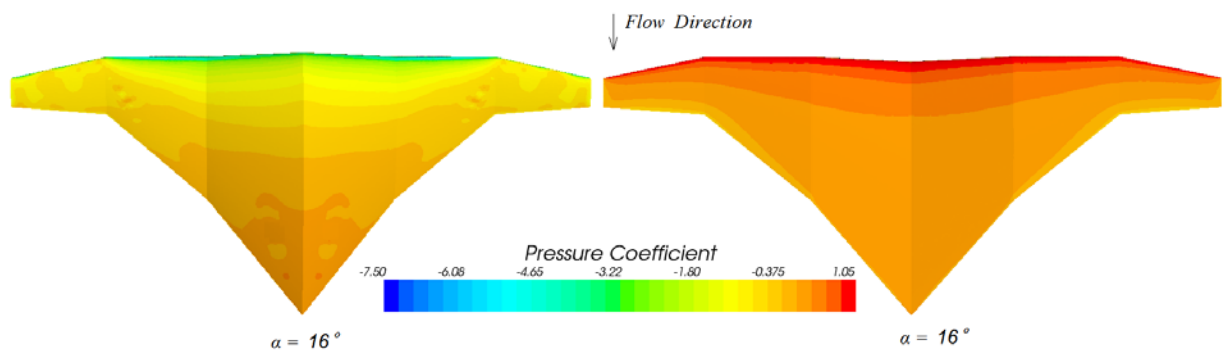


Figure 9-7. Predicted pressure distributions on the upper (on the left) and lower (on the right) surfaces of the W-wing Variant A at  $\alpha = 16^\circ$ ,  $M = 0.45$  and  $Re = 3 \times 10^7$ .

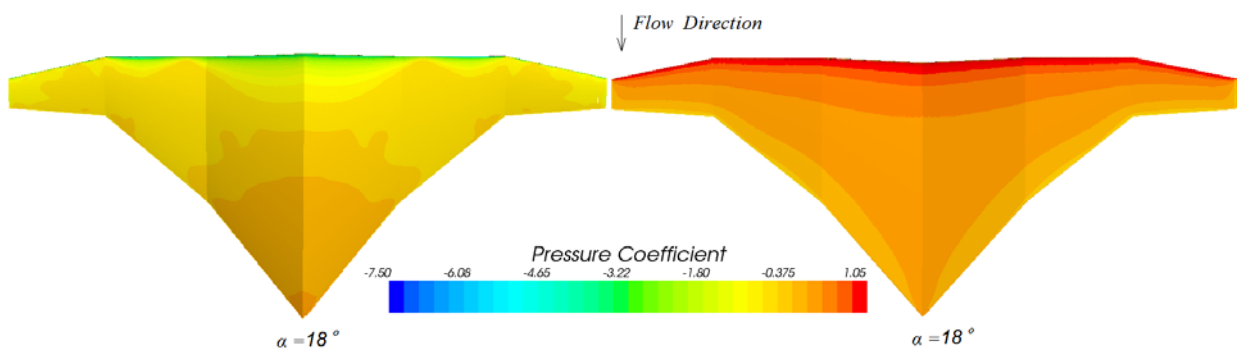


Figure 9-8. Predicted pressure distributions on the upper (on the left) and lower (on the right) surfaces of the W-wing Variant A at  $\alpha = 18^\circ$ ,  $M = 0.45$  and  $Re = 3 \times 10^7$ .

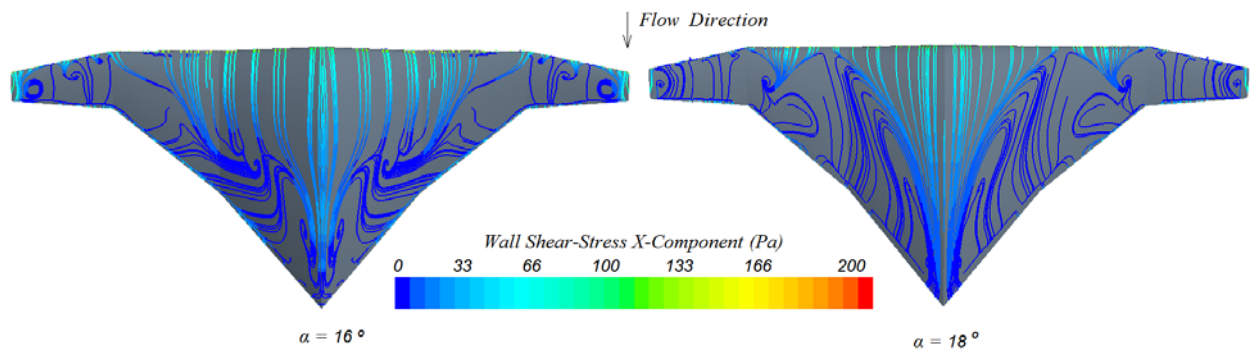


Figure 9-9. Predicted wall shear stress streamlines of the W-wing Variant A at  $\alpha = 16^\circ$  and  $\alpha = 18^\circ$ , at  $M = 0.45$  and  $Re = 3 \times 10^7$ .

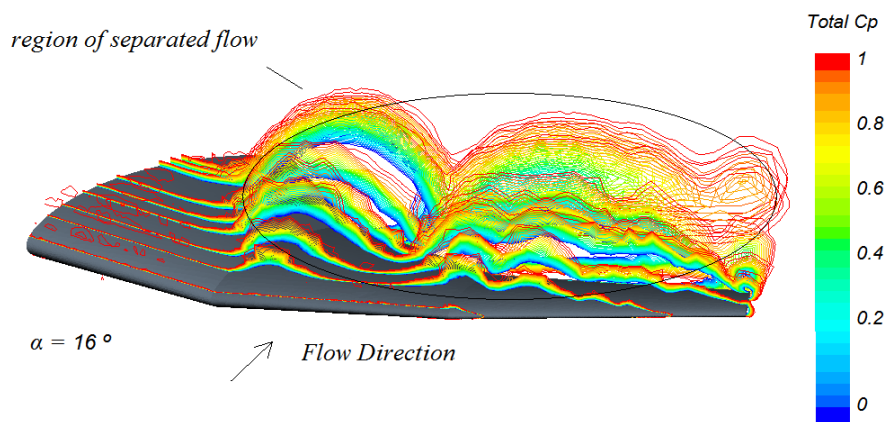


Figure 9-10. Predicted total pressure distributions of the W-wing Variant A at  $\alpha = 16^\circ$ ,  $\alpha = 18^\circ$ , at  $M = 0.45$  and  $Re = 3 \times 10^7$ .

In order to compare the separated regions and investigate the crank effect, if any, contours of shear-stress for the un-swept wing are plotted below (Figure 9-11). These plots show wall shear stress contours of the W-wing Variant A at  $\alpha = 16^\circ$  and  $\alpha = 18^\circ$ . In comparison with the original wing, these plots show similar trends (i.e. large separated regions), increasing with angle of attack. For the  $\alpha = 16^\circ$  case, there was no separation observed at the region where the crank would be located. The separation “bubbles” observed for the original W-shaped leading-edge wing, and which were associated with local supersonic shock regions, are also present in these plots. These separation regions are greater than on the original wing (see Figure 7-20), covering a larger part of the wing’s leading-edge. At  $\alpha = 18^\circ$ , most of the wing shows separated flow, and separated flow reaches the leading-edge for the mid-part of the wing.

As previously-mentioned in section 7 of this thesis, these angles of attack (i.e.  $\alpha = 16^\circ$  and  $\alpha = 18^\circ$ ) will not be employed during cruise-flight. These studies are, therefore, carried out mainly for comparison purposes only. Since, for the original wing, local separations near the crank regions were observed, the un-swept leading-edge wing would therefore assist in verifying these observations. However, from analysis of the shear-stress contours, although inconclusive, it can be said that the separation near the crank region may be associated with the local supersonics pockets, rather than the inboard crank. The effect may also be attributed to the anhedral starting at the crank region, which could have an effect as the angle is significant, or it may be due to the aerofoil choice. Further analyses with various aerofoils designed for the current flow conditions may show improvement to the near-crank aerodynamics.

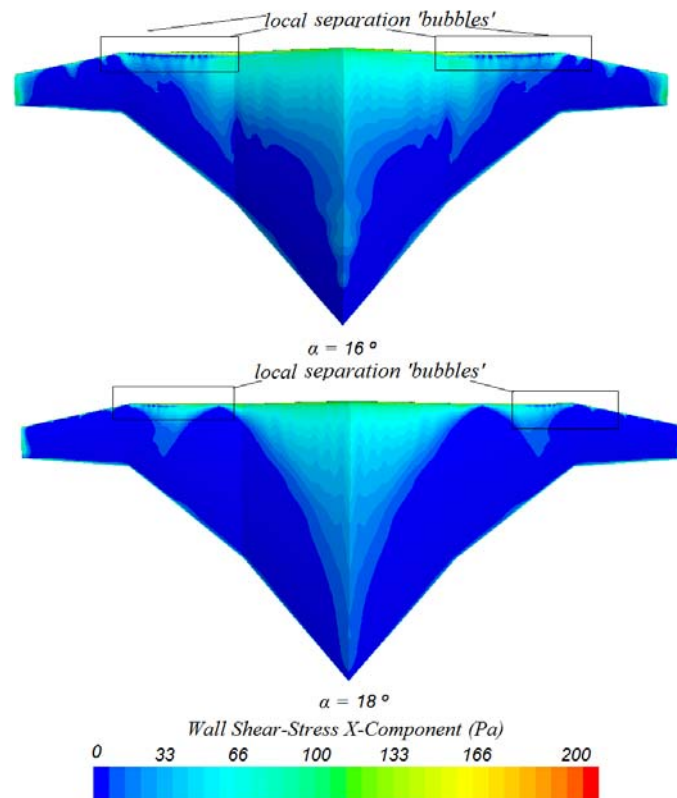


Figure 9-11. Predicted wall shear stress contours of the W-wing Variant A wing at  $\alpha = 16^\circ$  and  $\alpha = 18^\circ$ , at  $M = 0.45$  and  $Re = 3 \times 10^7$

In addition, near-wake distributions of the total pressures, compared with the original wing showed no general difference, Illustrated below are the near-wake plots at  $\alpha = 16^\circ$  for the un-swept mid-wing design. The results show similar behaviour to the

original wing, as an inboard vortex is also observed from the total-pressure plots given in Figure 9-12.

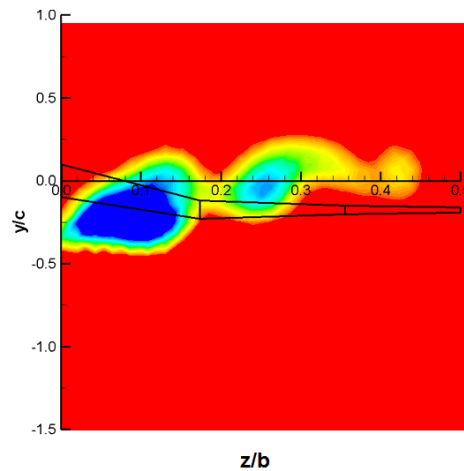


Figure 9-12. Near-wake total pressure coefficient plots for the W-wing Variant A at  $x/c_r = 1.5$ ,  $\alpha = 16^\circ$  at  $M = 0.45$  and  $Re = 3 \times 10^7$

The pressure distributions for the W-wing Variant B design are presented below. These plots show the upper and lower wing pressure performance, of the new design at  $\alpha = 14^\circ$  and  $\alpha = 16^\circ$ .

Upper and lower pressure distributions for the W-wing Variant B design  $\alpha = 14^\circ$  and  $\alpha = 16^\circ$  are presented below. The results near the tip region of the Variant B design at  $\alpha = 14^\circ$ , show a better performance when compared with the original wing (see Figure 7-15). The flow at the outer-part of the wing appears to be attached still, as the same leading-edge suction pressures are observed throughout the wing, up to the tip region. Also, gradual pressure recovery is noted for the tip region of the wing. The latter suggests that the forward design of the wing is still producing lift, as loading along the wing tip region is apparent. At  $\alpha = 16^\circ$  the upper surface pressure distributions resemble those of the original wing (see Figure 7-16), as almost constant pressures are observed over most parts of the wing, including the tip region. High adverse pressure gradients are also observed near the trailing edge of the entire wing. At this stage, classic signs of static stall are apparent, as can also be deduced from the drag coefficient plots (see Figure 9-4).

Thus, in terms of pressure distributions, the forward-swept design of the tip region generally shows a delay of stall of approximately  $\alpha = 2^\circ$ . This is an important feature as the W-wing design has high employability at near-ground conditions.

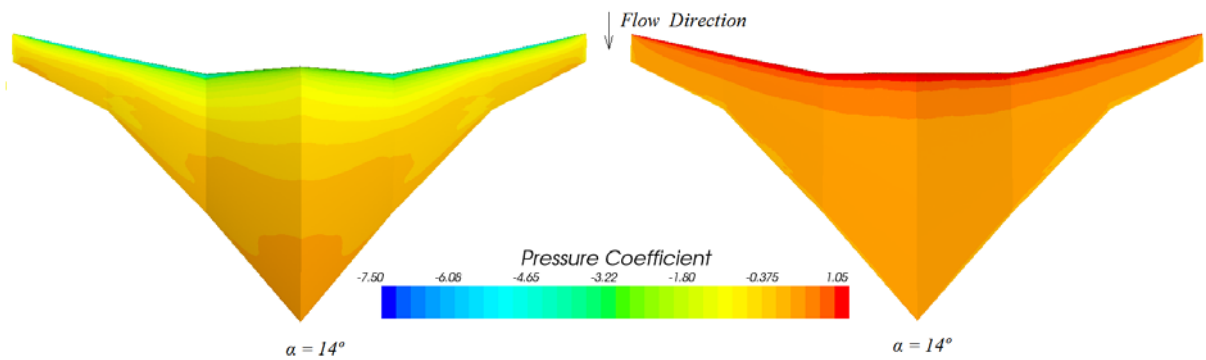


Figure 9-13. Predicted pressure distributions on the upper (on the left) and lower (on the right) surfaces of the W-wing Variant B at  $\alpha = 14^\circ$ ,  $M = 0.45$  and  $Re = 3 \times 10^7$ .

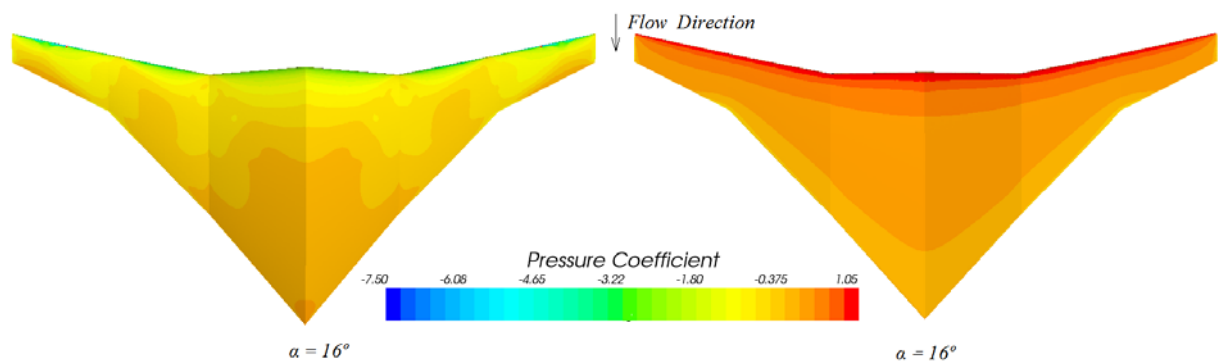


Figure 9-14. Predicted pressure distributions on the upper (on the left) and lower (on the right) surfaces of the W-wing Variant B at  $\alpha = 16^\circ$ ,  $M = 0.45$  and  $Re = 3 \times 10^7$ .

Figure 9-15 presents the upper surface shear-stress contours for the W-wing Variant B design at  $\alpha = 14^\circ$  and  $\alpha = 16^\circ$ . These are used to assess or verify the performance characteristics of the design. At  $\alpha = 14^\circ$ , wall shear stress contours suggest attached flow over the wing tip leading-edge region, which is contrary to the original wing behaviour, and shows that the entire wing is generating lift at this angle of attack. The

mostly zero shear-stress region observed for the original wing is not apparent in this case, as the mid and outer part of the wing show similar behaviour. However, one feature that was noticeably higher for this design is the leading edge local separation bubbles, similar to the ones observed for the original wing at the same conditions. These local separation regions, associated with zero shear-stress, continue along most parts of the central and outer wing.

At  $\alpha = 16^\circ$ , upper surface shear-stress contours reveal behaviour similar to the ones observed with the original wing, where zero shear-stress region cover a large portion of the wing, particularly at regions where local separation bubbles were noticed at  $\alpha = 14^\circ$ . At the inboard crank the separated region extends up to the wing's leading edge, which seems to be due to the supersonic pockets of flow at that section. The tip region of the wing still shows high shear-stress regions.

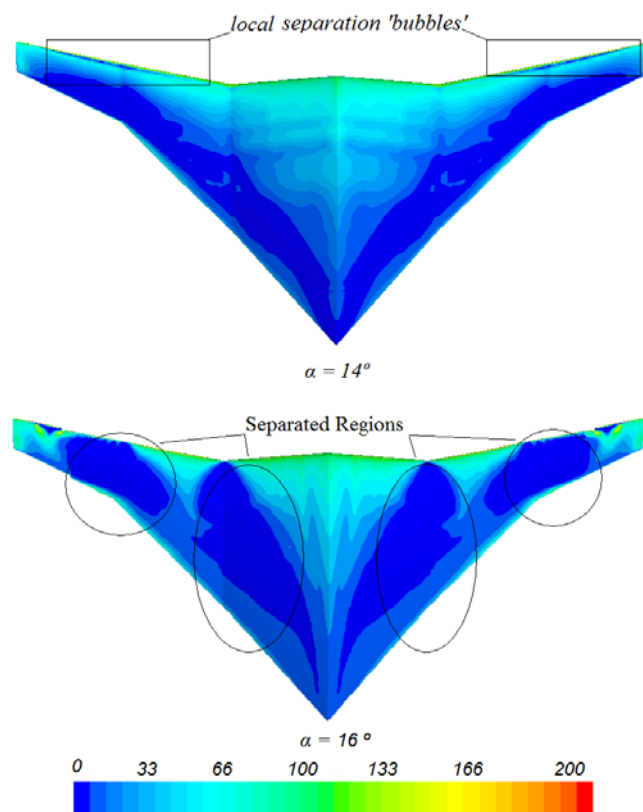


Figure 9-15. Predicted wall shear stress contours of the W-wing Variant B wing at  $\alpha = 14^\circ$  and  $\alpha = 16^\circ$ , at  $M = 0.45$  and  $Re = 3 \times 10^7$ .

The above separations pockets, or local supersonic regions, also appear in the Mach line contour plots given in Figure 9-16. For  $\alpha = 14^\circ$ , regions of high Mach numbers are observed at the leading edge region, with the highest ones observed at the crank. These pockets are slightly larger than the ones observed for the original wing. These local shock regions then effect the separation at subsequent angles of attack.

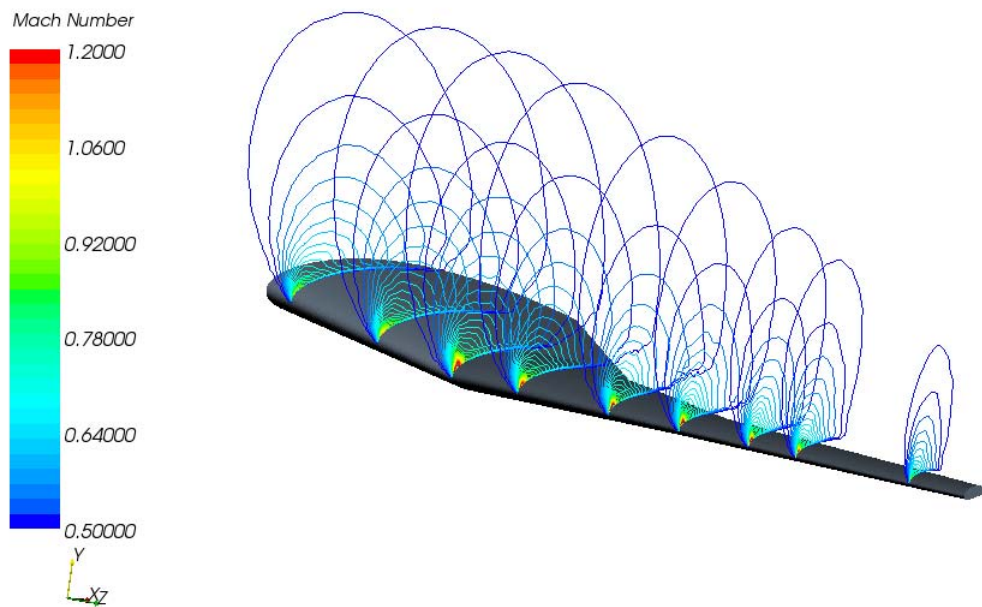


Figure 9-16. Predicted Mach number distributions of the W-wing Variant B at  $\alpha = 14^\circ$ ,  $M = 0.45$  and  $Re = 3 \times 10^7$ .

Off-surface total pressure distributions are also presented below for the W-wing Variant B design at  $\alpha = 14^\circ$  and  $\alpha = 16^\circ$ . From these plots (see Figure 9-17) at  $\alpha = 14^\circ$  one can now clearly see the effect of sweeping the tip forward, as the outer part of the wing shows attached flow (i.e. no region of the low total pressure coefficient) when compared to the original wing total pressure behaviours at the same conditions (as shown in Figure 7-24). Although, trailing edge separation has started to form at this stage, as can be observed from the plots, most of the upper surface of the W-wing Variant B design shows attached flow as the wing due to the tip modifications clearly holds high loading throughout.

Off-surface total pressure distributions (see Figure 9-17) for the W-wing Variant B at  $\alpha = 16^\circ$ , again show a similar pattern as the original wing results shown in Figure 7-24. Most of the separated region noted from the previous plots is also apparent in these plots, as the mid-wing shows less flow attachment preservation capabilities when compared to the original wing. The large region of the attached flow observed for the original wing, has narrowed for the W-wing Variant B. This is a rather interesting phenomenon: seeing as the mid-wing of the W-wing variant B has been kept the same for both the designs, one can only suggest that this effect may be associated with the stronger pockets of local shocks noted above, as the effect seems to be more severe as the mid-wing struggles to maintain its further separation prevention status.

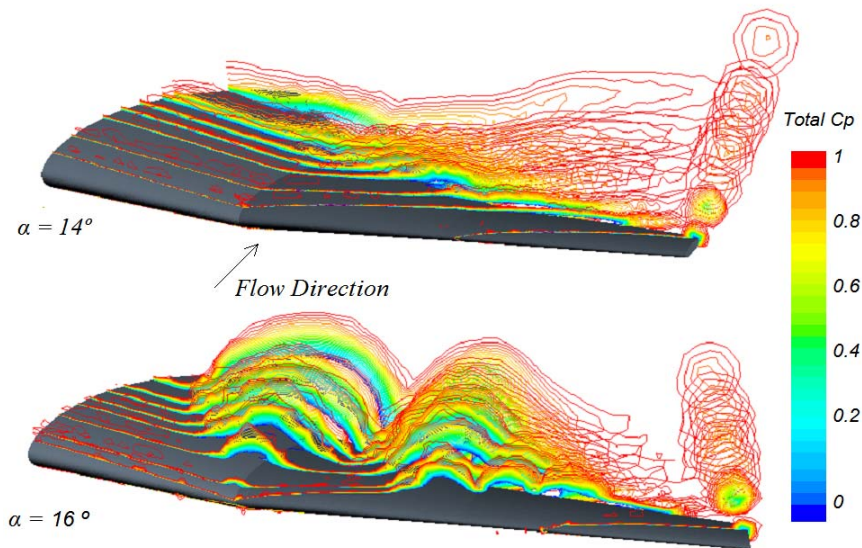


Figure 9-17. Predicted total pressure distributions of the W-wing Variant B at  $\alpha = 14^\circ$ ,  $\alpha = 16^\circ$ , at  $M = 0.45$  and  $Re = 3 \times 10^7$ .

Another investigation of interest to this study was to observe the near-wake behaviour of the W-wing Variant B near the stall. Figures 9-18 and 9-19 illustrate the near-wake total pressures for the W-wing Variant B case at  $\alpha = 14^\circ$  and  $\alpha = 16^\circ$ . The results for  $\alpha = 14^\circ$  show a larger wake being generated by the inboard portion of the wing, with no secondary vortex apparent from the results. The secondary vortex characteristic noted in the previous sections of this thesis, which was associated with the flow separation onset at the tip region, is not present in these plots as the tip is still maintaining lift

producing capabilities and no static stall is evident. At  $\alpha = 16^\circ$  ( see Figure 9-19) the near-wake plots show similarity with the original wing, as a large wake is being generated from the inboard wing, and the secondary vortex due to stall has formed, although in this case it is located further inboard.

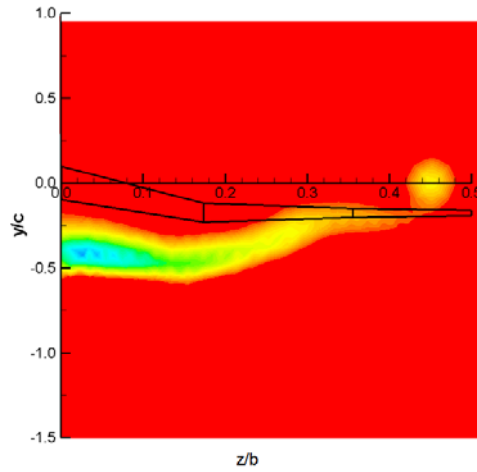


Figure 9-18. Near-wake total pressure coefficient plots for the W-wing Variant B at  $x/c_r = 1.5$ ,  $\alpha = 14^\circ$  at  $M = 0.45$  and  $Re = 3 \times 10^7$ .

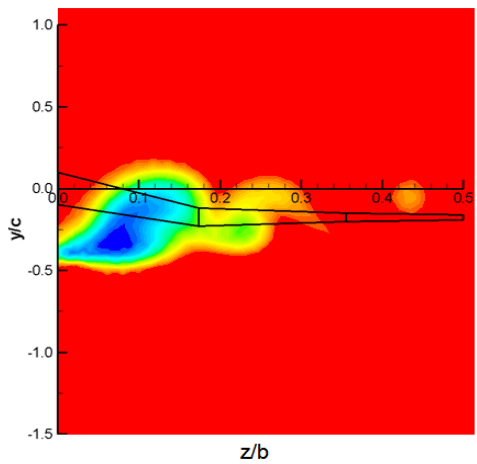


Figure 9-19. Near-wake total pressure coefficient plots for the W-wing Variant B at  $x/c_r = 1.5$ ,  $\alpha = 16^\circ$  at  $M = 0.45$  and  $Re = 3 \times 10^7$ .

## 9.2 Numerical Full-Potential investigation on variations of the sweeps on the original wing

This section describes further design investigations carried out by employing the full-potential numerical method. These investigations involved variation of the sweeps on the original W-shaped leading-edge wing, whilst maintaining the same aspect ratio and/or wing span. Several geometric options were examined for angles of attack up to  $\alpha = 10^\circ$ . Due to the limitations of the code, angles of attack higher than  $\alpha = 10^\circ$  were not possible. Figures 9-20 illustrates a top-view of the half-wing geometry of the designs investigated. Table 9-1 details the sweep and anhedral/dihedral angle details where applicable for each variant investigated.

The full-potential code only accounts for half of the wing geometry as the total coefficients are then calculated based on symmetry application, similar to the Navier-Stokes computations carried out in the previous sections. The full-potential method also calculated only the corresponding vortex drag. Therefore, to obtain the parasite drag coefficient, and hence the total drag coefficient, analytical methods (described in the appendix of this thesis) were employed.

### Variations

		AR	Span (m)	Anhedral (deg)	Sweep (deg)	
<b>Original Wing</b>	<b>Variant 1</b>	5.5	11.38	12	3/-11/12	(no modifications)
	<b>Variant 2</b>	5.5	11.38	6	3/-11/12	
	<b>Variant 3</b>	5.5	11.38	12	10/-11/12	
	<b>Variant 4</b>	5.5	11.38	12	10/-11/12	
<b>Aft-swept wing</b>	<b>Variant 1</b>	5.5		12	18	(constant AR)
	<b>Variant 2</b>		11.38	12	18	(constant span)
<b>Unswept leading edge</b>	<b>Variant 1</b>	5.5		12	0	(constant AR)
	<b>Variant 2</b>		11.38	12	0	(constant span)
<b>Forward-swept wing</b>	<b>Variant 1</b>	5.5		12	-.11/-11/12	(constant AR)
	<b>Variant 2</b>		11.38	12	-.11/-11/12	(constant span)

Table 9-1. Variations of the original wing investigated with FP method

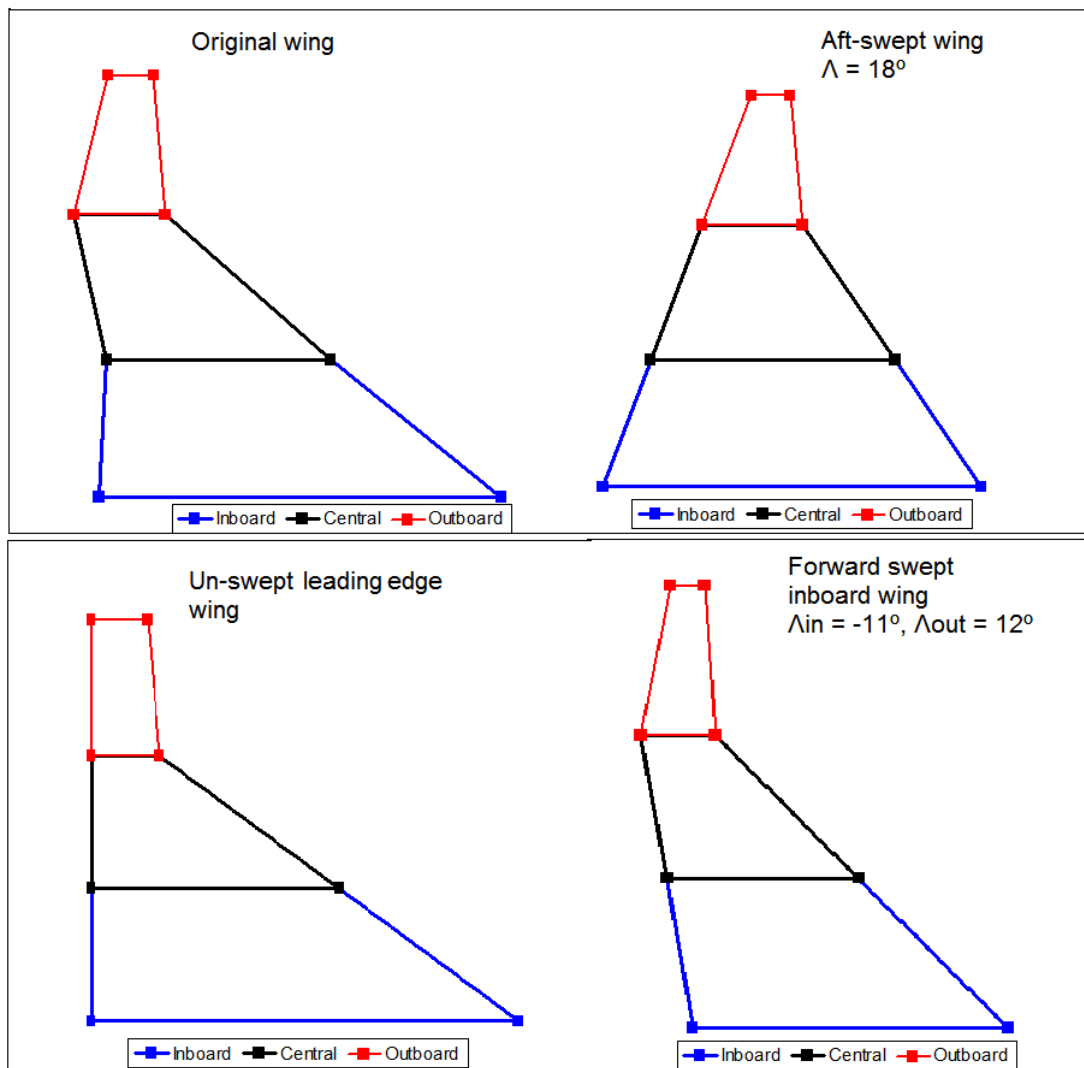


Figure 9-20. Geometry diagram for all wing variations

The lift curves for the different design variations are given in Figure 9-21. Results show that the conventional aft-sweep design, with the same AR as the original wing, gives the highest lift coefficients when compared to the other variations. Slightly less lift is produced by the same conventional wing, with the same wing span as the original wing; nonetheless, the values are still higher than all other design considerations. Sweeping the inboard region of the wing further aft ( $\Lambda=10^\circ$ ), and changing the anhedral angle to dihedral (with the same magnitude), produces higher lift coefficients, giving values just below the aft-sweep design. The trend in performance is then followed by the original wing, and the original wing with less

anhedral, the forward-swept wing with the same AR as the original, etc. The worst performance of all in terms of lift coefficient only is by the forward-swept inboard wing with the same wing span as the original wing.

In terms of drag performance, not surprisingly the conventional aft-swept wing results show the highest drag coefficients and the least drag being obtained from the un-swept wing that has the same span as the original W-wing. The original W-wing drag results are very similar to the un-swept wing ones (see Figure 9-22).

Lift-to-drag ratios, plotted in Figure 9-23, show the benefits of employing the forward, sweep or indeed combined sweep design, as the highest lift-to-drag ratios are obtained with these wings. As expected, the forward-swept inboard wing gives the highest L/D ratios, followed closely by the aft swept inboard region of the wing with dihedral, these are then followed by the original wing. The least ratios are observed for the aft-swept wing with the same span as the original. These results show that, on average, the original wing with further aft-sweep on the inboard section of the wing together with dihedral gives the best performance in comparison with the other designs considered herein.

Aside for the other characteristics that define a good wing design one would strive to bring the fundamental principles for the aerodynamically best wing shape. Usually a study of the span wise lift distribution is deemed necessary. Although the elliptical lift distribution is the best lift distribution, sometimes a minor divergence from such distribution may contribute to the overall performance characteristics of the wing such as stability or tip stall delay. Figure 9-25 illustrates the spanwise lift distribution for the above variants.

The aft swept wing design both with the same AR as the original wing and same span length follow the elliptical distribution more than the rest of the designs. Nonetheless, lift coefficients near the tip region for the conventional aft-swept wing are reasonably greater than the rest of the variations. The lift coefficient for the unconventional concept (original and forward swept wings) along the span reveals a distinct maximum at the 20% of the wing span, with low values near the tip region. In general, one would expect that in operating condition with high total lift the

breakdown of the flow would start in this region. However, lift coefficient behavior of such kind is avoided in the tip regions as the highest lift coefficients are usually modified to be shifted near the central regions.

It can be seen that increasing the aft sweep to the original wing to 10 degrees does considerably increase the lift coefficient at the 20% region, whereas the lift coefficients near the tip are the lowest for this design. The unswept leading edge design also produces high lift coefficient near the root region. Forward swept inboard wing does produce similar lift coefficient to the original wing in the inboard and central regions, even so tip lift coefficients are slightly higher than the rest of the variations.

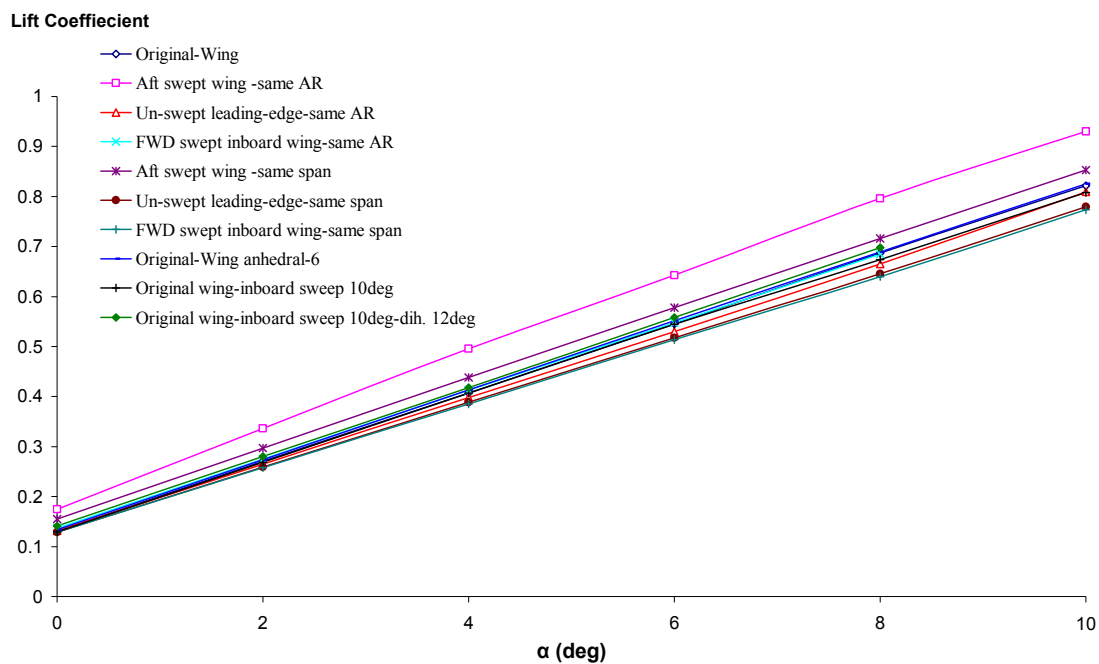


Figure 9-21. Lift coefficient results for a range of design variations to the original wing, at  $M = 0.45$  and  $Re = 3 \times 10^7$ .

**Drag Coefficient**

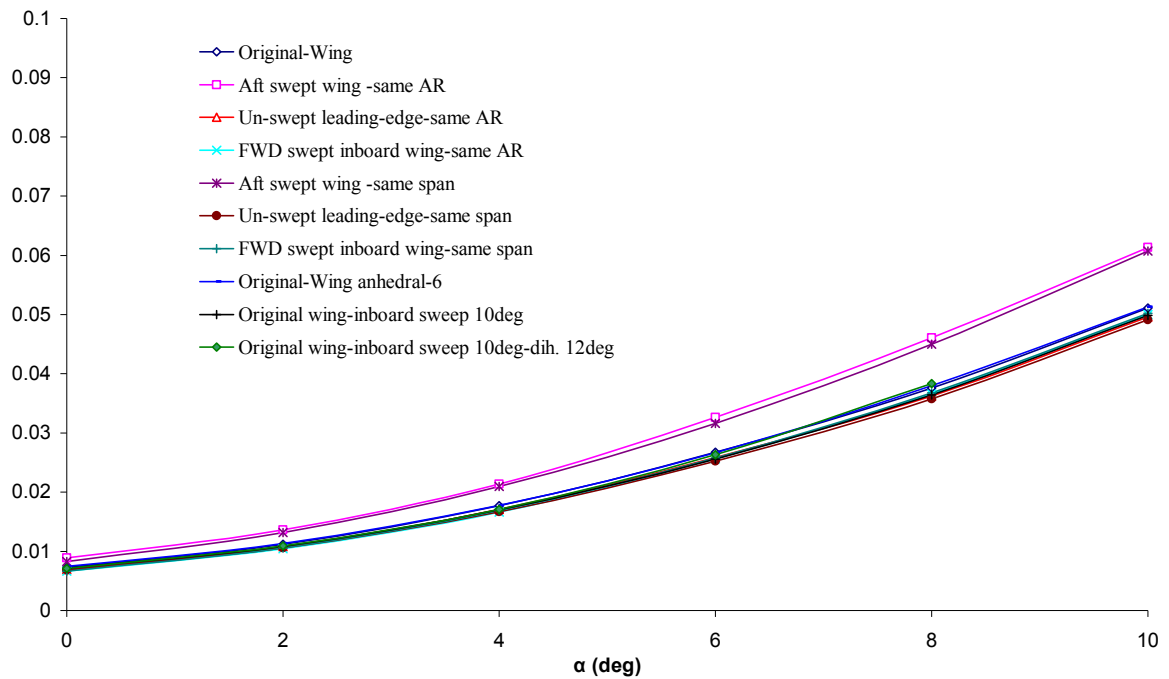


Figure 9-22. Drag coefficient results for a range of design variations to the original wing, at  $M = 0.45$  and  $Re = 3 \times 10^7$ .

**Lift-to-drag ratio**

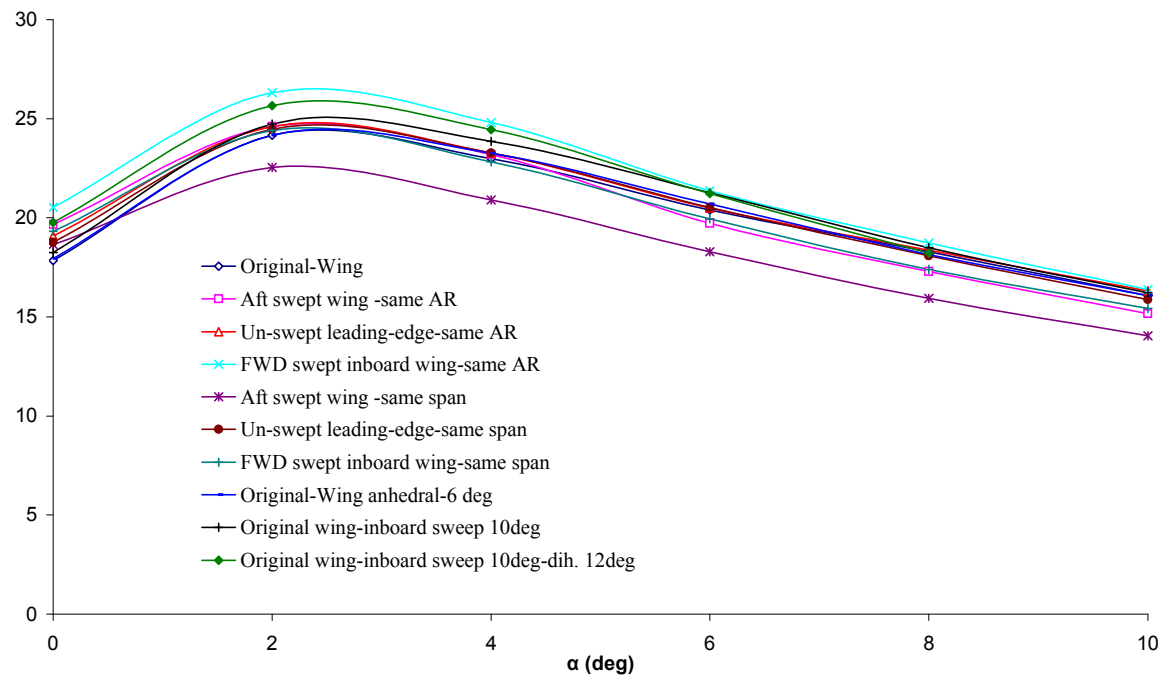


Figure 9-23. Lift-to-drag ratio results for a range of design variations to the original wing, at  $M = 0.45$  and  $Re = 3 \times 10^7$ .

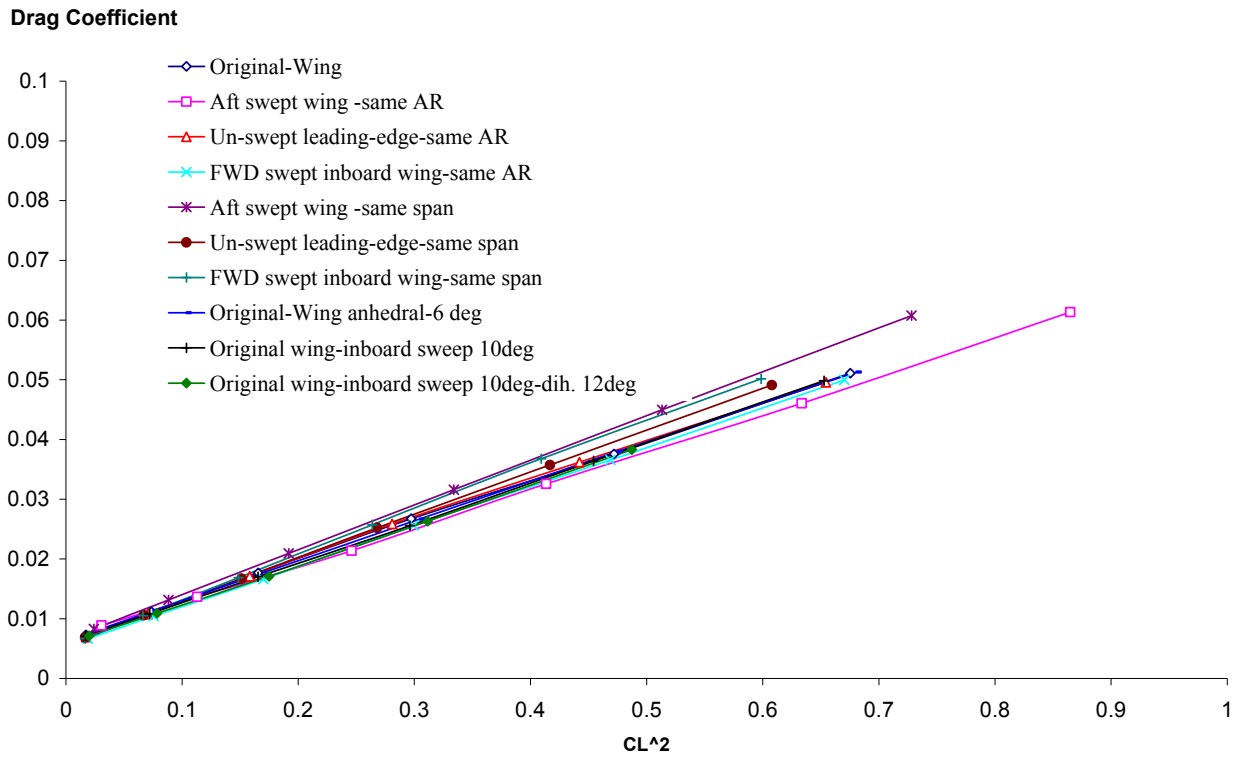


Figure 9-24. Drag Coefficient versus  $C_L^2$  for a range of design variations to the original wing, at  $M = 0.45$  and  $Re = 3 \times 10^7$ .

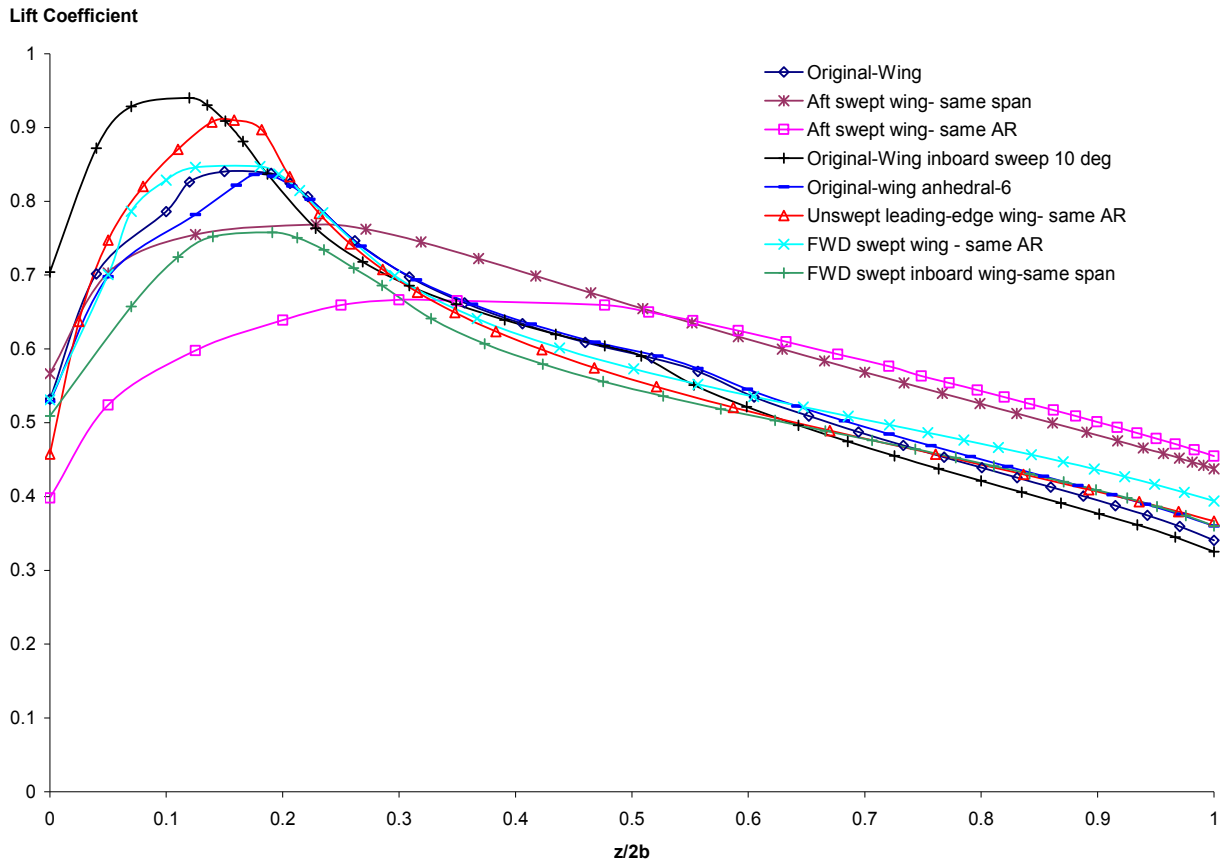


Figure 9-25. Span-wise lift distribution for a range of design variations to the original wing, at  $\alpha = 6^\circ$ ,  $M = 0.45$  and  $Re = 3 \times 10^7$ .

## Summary

In general the results obtained in this section clarify that the separation near the crank region may be associated with the local supersonics pockets, rather than the inboard crank. This would be clarified even more, if various aerofoil sections designed for transonic application are tested against the original wing. Also, by keeping the inboard and central part of the wing un-swept, it has been verified once more that, in the absence of the forward-sweep, the central-wing struggles to maintain attached flow, or indeed prevent further separation on the rest of the wing.

From sweeping the outer-wing forward with the same sweep angle magnitude as the original wing, it was noticed that lift was still being produced by the outboard section of the wing at  $\alpha = 14^\circ$ . This suggested that the effect would delay the stall by approximately  $2^\circ$ . Nevertheless, the off-surface total pressure plots revealed that at  $\alpha = 16^\circ$  and above the forward-swept tip wing was performing slightly worse than the original wing, due to the supersonic pockets being more powerful on the central wing.

Full-potential introductory calculations on various design variations to the original wing showed that the original wing does perform better in terms of lift-to-drag ratio when compared to a conventional swept wing with the same span length. Also, other alternatives, such as increasing the aft-sweep angle for the inboard region of the original wing together with dihedral angle produced noteworthy improvements to performance in terms of lift and lift-to-drag ratio.

The above full-potential results show some potential for further investigations in terms of sweep and dihedral angle. Although, the accuracy of calculating the parasite drag may not be exact, the results are still viable as the same method was used for all designs, and therefore the errors would be proportional.

## 10. Concluding Remarks

The aim of this study was to carry out a thorough aerodynamic analysis of a W-leading-edge reversed delta plan-form wing design. This was done by the use of both numerical and experimental techniques. The tests were carried out to assess the performance of the wing both in cruise and in take-off and landing configurations (i.e. in ground proximity).

The study involved selection of a three-dimensional numerical model which reasonably reflected the physical and geometric conditions of the flow, the design of the appropriate numerical set-up for the high and low-speed investigations, development of an experimental procedure for the flow analyses around a replica scaled (5%) wing model in free-flight and ground effect, detailed numerical and experimental investigation of the full-scale and scaled model of the wing, and lastly, further investigations on possible geometric modifications of the original design to advance the capabilities of the wing. Thus, the problem was divided into four main areas:

1. Low-speed numerical and experimental investigations of the wing in free-flight.
2. High-speed numerical investigations of the wing in cruise conditions.
3. Low-speed numerical and experimental analysis of both the full-scale and scaled wing in ground effect
4. High-speed numerical analyses of geometric variation of the original design in the pursuit of improved performance.

The key observations from these results were:

1. The obtained low-speed results showed a agreement between the two methods employed, which gave some confidence to the employment of the numerical Navier-Stokes/hybrid grid method for full-scale simulations of the W-leading-edge wing. Numerical results gave similar trends to the experimental ones, although exact agreement was not achieved all the results showed consistent trend followed for angles investigated. The results from this section also gave some preliminary insight into the aerodynamic characteristics of the wing, such as the strong inboard vortex observed in the near-wake at higher angles of attack.
2. The key findings from the high-speed predictions were the general indications of the capabilities of the W-wing in cruise. In terms of aerodynamic analyses, the wing exhibits soft stall and good lift-to-drag ratio, as well as statically stable pitching moment response up to stall conditions. Maximum lift was reached at  $14^\circ < \alpha < 16^\circ$ , giving a maximum lift-to-drag ratio of approximately  $L/D = 18$ . Lift coefficient results obtained at cruise conditions do comply with the top level requirements for the current wing design. Static stall onset was noted to initiate from the outboard section of the wing at  $\alpha = 14^\circ$ . Regions of local supersonic flow, which terminated in a shock, were observed to appear at  $\alpha = 10^\circ$  and above. These showed no detrimental effect on the performance of the wing; moreover, the angles where these pockets appeared are less likely to be employed at cruise conditions.

On- and off- surface streamline investigation showed that the wing's inboard and central sections behaved in a similar manner to forward swept wings. These plots revealed the wing's abilities to maintain attached flow at the central section well after stall was reached. The study also implied that careful consideration has to be made when the intersection regions are developed to avoid geometry-induced shortcomings.

An assessment of the origin and direction of the secondary vortex showed that the secondary inboard vortex was a typical static stall behavior of the wing, initiating at the wing tip region. Therefore, a concern was raised with respect to the tailplane positing, as the settings may be dictated by the stall behavior.

3. The general aim of this section was to establish the aerodynamic behaviour of the W-wing in ground effect, by coupled experimental and numerical investigations. It has

been noted that the obtained lift coefficients for take-off and landing configurations do fall within the top level requirements for the current design stated in section 1. A good agreement was achieved between the two methods employed, with greater differences noted in lift coefficients for higher angles of attack. This was due to the employment of the fixed ground board to account for the ground in the experimental tests. Therefore, careful considerations have to be made when the experimental results are considered, because of the fixed ground-board induced shortcomings. No major difference in the drag coefficients was noted as the ground was approached. In general, the results showed a considerable increase of the lift coefficient and lift-to-drag ratio for the W-wing in ground effect. Values of  $L/D = 30$  were achieved for  $h/b = 0.09$ , which is 90% greater than the  $L/D$  ratio in free-flight.

The results also show regions of very low velocity and high pressure underneath the wing, suggesting a very strong “air cushion” effect being induced by the wing. Tip vortices were noticed to move outboard with the decreasing ground height, which indicates an increase of the effective aspect ratio of the wing. Flow separation was more pronounced with the decreasing ground height, and the inboard vortex was noticed to strengthen with ground proximity. This effect signifies delayed vortex breakdown, which could be an undesirable effect for the type of aircraft this wing is envisaged for.

4. The design investigation of variations to the original wing clarified that the in comparison with other conventional designs the original wing does indeed have good performance characteristics. The results also showed that the separation near the crank region is associated with the local supersonic pockets, rather than the inboard crank. This would be better verified if various aerofoil sections designed for transonic application are tested against the original wing. Additionally, by sweeping the outer-wing forward with the same sweep angle magnitude as the original wing, it was noticed that this had the effect of delaying stall by approximately  $2^\circ$ . However, the off-surface total pressure plots revealed that at  $\alpha = 16^\circ$  and above the forward-swept tip wing was performing slightly worse than the original wing.

Full-potential calculations showed that the original wing performed better in terms of lift-to-drag ratio when compared to a conventional swept wing with the same span

length. Similarly, alternative design variations, such as increasing the aft-sweep angle for the inboard region of the original wing and replacing the anhedral with dihedral, showed that the improvement in terms of lift and lift to drag ratio was significant.

## 11. Recommendations for Further Work

The main aspect of this project was to investigate the combined-sweep design of the leading-edge wing in the search for improved aerodynamic performance of a wing, which would potentially be employed for STOL applications. Benefits of the design have been noted, as the wing showed good quality aerodynamic performance in cruise flight and take-off and landing. The use of the interactive numerical and computational investigations reduced the number of investigations; however, the ground-effect analyses showed several variations that led to none of the methods being very reliable. Further progress would be expected if the experimental methods would consider the transient effect of the take-off and landing configurations, where the distance from the ground changes rapidly and this need to be accounted for more rigorously in the computations. Methods such as transient moving geometry with a suitable time step would improve the accuracy of the predicted data and potentially give more realistic values of  $L/D$  ratio at very low ground heights.

The potential benefits of the current design have been noted, however, greater design analyses were limited, due to computer constraints. Therefore, as confidence in numerical analysis is increasing, additional numerical investigations such as twist, anhedral and dihedral would be beneficial. Full-potential investigations showed the prospective benefits of the variations, especially at the inboard region. Nonetheless, for accuracy purposes, and the analysis of the all-important pitching moment variations, Navier-Stokes computations of the more promising designs would be advisable. This includes further Navier-Stokes computations understand the experimental effects such as strut interference and ground board.

Further investigations such as crank geometry, both in terms of aerodynamic and structural aspect are worthwhile. Also analyses of the wing-fuselage analyses would give a more realistic approach on the entire performance of the Jetpod aircraft. Moreover, investigations on the possibility of employing various aerofoil sections for different wing parts, particularly investigation of the best choice for those regions where the highest supersonic pockets are observed, would be advantageous. Other aspect such as adding the benefits of twist would also be worthy for the current wing design.

# References

- “Forward Swept Wing Potential Studied”. *Aviation Week & Space Technology*, **110**(5): pp. 126–127, 1979.
- “Workshop on Computational Turbulence Modelling”. NASA-CP-10130, NASA, 1994.
- Abbott, I.R and Von Doenhoff, A.E *Theory of Wing Sections* Dover Publications New York 1959
- Ahmed, M. R. *et al.*, “Experiments on the Aerodynamics of a Cambered Airfoil in Ground Effect”. In *44th AIAA Aerospace Sciences and Meeting Exhibit*, Reno, NV, 2006.
- Ahn, B. K. and Graham, W. R., “Modelling Unsteady Wall Pressures Beneath Turbulent Boundary Layers”. AIAA Paper 2004-2849, AIAA, 2004.
- Anderson, W. K. and Bonhaus, D. L., “An Implicit Upwind Algorithm for Computing Turbulent Flows on Unstructured Grids”. *Computers and Fluids*, **23**(1): pp. 1–21, 1994.
- Applin, Z. T. *et al.*, “Wing Pressure Distributions from Subsonic Tests of a High-Wing Transport Model”. NASA-TM-4583, NASA, 1995.
- Bagley, J. A., “The Pressure Distribution on Two Dimensional Wings Near Ground”. R & M 3238, Aeronautical Research Council, 1961.
- Baker, M. D. *et al.*, “Numerical Investigation of Slat and Compressibility Effects for a High-Lift Wing”. *Journal of Aircraft*, **39**(5): pp. 876–884, 2002.
- Baker, P. A. *et al.*, “Flight evaluation of Ground Effect on Several Low-Aspect Ratio Airplanes”. NASA TN-D-6053, NASA, 1970.
- Baldwin, B. S. and Lomax, H., “Thin Layer Approximation and Algebraic Model for Separated Turbulent Flows”. AIAA Paper 78-0257, AIAA, 1978.

- Barber, T. J. *et al.*, “Causes for Discrepancies in Ground Effect Analyses”. *Aeronautical Journal*, **106**(1066): pp. 653–667, 2002.
- Barlow, J.B., Rae, W.H., Jr and Pope, A. *Low-speed Wind Tunnel Testing*, 3<sup>rd</sup> Edition Wiley-Interscience 1999
- Bartels, R. E., “A Study of the Grid Resolution, Transition and Turbulence Model Using the Transonic Simple Straked DeltaWing”. NASA, 2001. Available at [http://ntrs.nasa.gov/archive/nasa/casi.ntrs.nasa.gov/20040086474\\_200409%0766.pdf](http://ntrs.nasa.gov/archive/nasa/casi.ntrs.nasa.gov/20040086474_200409%0766.pdf).
- Barth, T. J., “Numerical Aspects of Computing High-Reynolds Number Flows on Unstructured Meshes”. AIAA Paper 1991-721, AIAA, 1991.
- Beall, M. W. *et al.*, “Accessing CAD Geometry for Mesh Generation”. In *12th International Meshing Roundtable*, Santa Fe, NM, 2003.
- Betz, A., *Aerodynamic Theory: Applied Airfoil Theory*. Julius Springer, Berlin, Germany, 1935.
- Bradshaw, P. *An Introduction to Turbulence and its Measurement*, Pergamon Press 1971
- Bowers, P. M., *Unconventional Aircraft*. Tab Books, Blue Ridge Summit, PA, 1990.
- Boyd, D. D., “Navier-Stokes Computations of a Wing-Flap Model with Blowing Normal to the Flap”. NASA-TM-2005-213542, NASA, 2005.
- Bradshaw, P., *An Introduction to Turbulence and its Measurement*. Pergamon Press, New York, NY, 1971.
- Bushnell, D. M., “Fluid Mechanics, Drag Reduction and Advanced Configuration Aeronautics”. NASA-TM-2000-210646, NASA, 2000.
- Bushnell, D. M. *et al.*, “Reynolds Number Influences in Aeronautics”. NASA-TM-107730, NASA, 1993.
- Cabello, J., “Toward Quality Surface Meshing”. In *12th International Meshing Roundtable*, Santa Fe, NM, 2003.
- Campbell, R. L., “Efficient Viscous Design of Realistic Aircraft Configurations”. AIAA Paper 98-2539, AIAA, 1998.
- Capone, F. J. *et al.*, “Recommended Experimental Procedures for Evaluation of Abrupt Wing Stall Characteristics”. In *41st AIAA Aerospace Sciences Meeting and Exhibit*, Reno, NV, 2003.

- Chaffin, M. S. and Pirzadeh, S. Z., "Unstructured Navier-Stokes High-Lift Computations on a Trapezoidal Wing". AIAA Paper 99-1911, AIAA, 1999.
- Chalasan, S. *et al.*, "Assessing Generalized Mesh Quality via CFD Solution Validation". In *43rd AIAA Aerospace Sciences Meeting and Exhibit*, Reno, NV, 2005.
- Chawla, M. D. *et al.*, "Wind-Tunnel Investigation of Wing-in-Ground Effects". *Journal of Aircraft*, **27**(4): pp. 289–293, 1990.
- Chen, Y. S. and Schweikhard, W. G., "Dynamic Ground Effects on a Two-Dimensional Flat Plate". *Journal of Aircraft*, **22**(7): pp. 638–640, 1985.
- Coe, P. L. and Fournier, P. G., "Application of Powered-Lift Concept for Improved Cruise Efficiency of Long-Range Aircraft". NASA-N78-24051, NASA, 1978.
- Coulliete, C. and Plotkin, A., "Airfoil Ground Effect Revisited". *Aeronautical Journal*, **100**(992): pp. 65–74, 1996.
- Curry, R. E. *et al.*, "An In-Flight Investigation of Ground Effect on a Forward-Swept Wing Airplane". NASA-TM-101708, NASA, 1989.
- Davidson, L., "An Introduction to Turbulence Models". 2003. Available at [http://www.tfd.chalmers.se/~lada/postscript files/kompendium turb.pdf](http://www.tfd.chalmers.se/~lada/postscript%20files/kompendium%20turb.pdf).
- Davidson, L. and Stolsic, L., "Implicit Finite-Volume Solver for the k and e Equations on Unstructured Mesh with Arbitrary Control Volumes". CRS4-APPMATH-93-22, CRS4, Cagliari, 1993.
- Demirdzic, I. and Musafirija, S. 1997. "Numerical method for coupled fluid flow, heat transfer and stress analysis using unstructured moving meshes with cells of arbitrary topology", *Comput. Methods Appl. Mech. Eng.*, pp. 1-21.
- Diederich, F.W. and Budiansky, B., "Divergence of Swept Wings". NACA-TN-1680, NACA, 1948.
- Dodbele, S. S., "Three Dimensional Aerodynamic Analysis of a High-Lift Transport Configuration". In *AIAA Applied Aerodynamics*, Monterey, CA, 1993.
- Duquesne, N. *et al.*, "Computation of Turbulent Wake Flows in Variable Pressure Gradient". In *30th AIAA Fluid Dynamic Conference*, Norfolk, VA, 1999.
- Er-El, J. and Weihs, D., "Ground Effect on Slender Wings at Moderate and High Angles of Attack". *Journal of Aircraft*, **25**(3): pp. 357–358, 1986.

- ERCOFTAC “*Best Practice Guidelines in CFD*” January 2000  
“Full-Potential (FP) Method for Three-Dimensional Wings and Wing-Body Combinations–Inviscid Flow (with Amendment A May 2006)”. ESDU Data Item 02014, ESDU, 2006.
- Fink, M. P. and Lastinger, J. L., “Aerodynamic Characteristics of Low-Aspect Ratio Wings in Close Proximity to the Ground”. NASA-TN-D-926, NASA, 1961.
- Flores, J. and Chaderjian, N. M., “Zonal Navier-Stokes Methodology for Flow Simulation About a Complete Aircraft”. *Journal of Aircraft*, **27**(7): pp. 583–590, 1990.
- Fonseca, G. F. *et al.*, “Numerical Simulation of Inviscid Incompressible Two-Dimensional Airfoil-Vortex Interaction in Ground”. *Journal of Aircraft*, **40**(4): pp. 653–661, 2003.
- Frink, N. T. *et al.*, “An Unstructured-Grid Software System for Solving Complex Aerodynamic Problems”. NASA-CP-3291, NASA, 1995.
- Frink, N. T., “Assessment of an Unstructured-Grid Method for Predicting 3-D Turbulent Viscous Flows”. In *34th Aerospace Science Meeting and Exhibit*, Reno, NV, 1996.
- Frink, N. T., “Recent Progress toward Three-Dimensional Unstructured N-S Flow Solver”. AIAA Paper 94-0061, AIAA, 1994.
- Frink, N. T. and Pirzadeh, S. Z., “Tetrahedral Finite-Volume Solutions to the Navier-Stokes Equations on Complex Configurations”. In *10th International Conference on Finite Elements in Fluids*, Tucson, AZ, 1998.
- Furlong, G. C. and McHugh, J. G., “A Summary and Analysis of the Low-Speed Longitudinal Characteristics of Swept Wings at High Reynolds Numbers”. NACA-TR-1339, NACA, 1952.
- Gad-el-Hak, M. and Bushnell, D. M., “Separation Control: Review”. *Journal of Fluids Engineering*, **113**: pp. 5–29, 1991.
- Gatski, T. B., “Prediction of Airfoil Characteristics with Higher Order Turbulence Models”. NASA-TM-96-110246, NASA, 1996.

- Rumsey, C. L. *et al.*, “Turbulence Model Predictions of Extra-Strain Rate Effects in Strongly-Curved Flows”. In *37th Aerospace Sciences Meeting and Exhibit*, Reno, NV, 1999.
- George, A., “Aerodynamic Effects of Shape, Camber, Pitch and Ground on Idealized Ground Vehicle Bodies”. *Journal of Fluid Mechanics*, **103**: pp. 631–638, 1981.
- Ghaffari, F., “Turbulent Vortex-Flow Simulation over a 65° Sharp and Blunt Leading-Edge Delta Wing at Subsonic Speeds”. NASA-TM-2005-213781, NASA, 2005.
- Ghaffari, F., “Unstructured Grid Viscous Flow Simulation Over High-Speed Research Technology Concept Airplane at High-Lift Conditions”. NASA-TP-1999-209718, NASA, 1999.
- Ghaffari, F. *et al.*, “Turbulent Navier-Stokes Flow Analysis of an Advanced Semispan Diamond-Wing Model in Tunnel and Free Air at High-Lift Conditions”. NASA-TP-211779, NASA, 2002.
- Girimaji, S. S., “Pressure-Strain Correlation Modelling of Complex Turbulent Flows”. *Journal of Fluid Mechanics*, **422**: pp. 91–123, 2000.
- Godin, P. Z. *et al.*, “High-Lift Aerodynamic Computations with One- and Two-equation Turbulence Models”. *AIAA Journal*, **35**(2): pp. 237–243, 1997.
- Gooden, J. H. *et al.*, “Experimental Study of the Flow Around Two Scaled 3D Swept Wings”. In *28th AIAA Fluid Dynamics Conference*, Snowmass Village, CO, 1997.
- Graves, S. S., “Investigation of a Technique for Measuring Dynamic Ground Effect in a Subsonic Wind Tunnel”. NASA-CR-209544, NASA, 1999.
- Green, S., *Fluid Vortices*. Kluwer Academic Publishers, Dordrecht, The Netherlands, 1995.
- Guynn, M. D. and Olson, E. D., “Evaluation of an Aircraft Concept with Over-Wing, Hydrogen-Fuelled Engines for Reduced Noise and Emissions”. NASA-TM-2002-211926, NASA, 2002.
- Hamilton, D. W. and Proctor, F. H., “Wake Vortex Transport in Proximity to the Ground”. In *19th Digital Avionics Systems Conference*, Philadelphia, PA, 2000.
- Han, C. and Cho, J., “Unsteady Trailing Vortex Evolution behind a Wing in Ground Effect”. *Journal of Aircraft*, **42**(2): pp. 429–434, 2005.

- Harvey, J. K. and Perry, F. J., “Flow-field Produced by the Trailing Vortices in the Vicinity of the Ground”. *AIAA Journal*, **9**(8): pp. 1659–1660, 1971.
- Hassan, O. *et al.*, “The Numerical Simulation of Viscous Transonic Flows Using Unstructured Grids”. AIAA Paper 94-2346, AIAA, 1994.
- Hayashi, M. and Endo, E., “Measurement of Flow Fields Around an Airfoil Section with Separation”. *Transactions of the Japan Society for Aeronautical and Space Sciences*, **21**(52): pp. 69–75, 1978.
- Hellsten, A., “New Two-Equation Turbulence Model for Aerodynamics Applications”. PhD thesis, Helsinki University of Technology, Finland, 2004.
- Hensch, M., “Statistical Analysis of CFD Solutions from the Drag Prediction Workshop”. In *40th AIAA Aerospace Sciences Meeting and Exhibit*, Reno, NV, 2002.
- Hepperle, M., “Environmental Friendly Transport Aircraft”. *Notes on Numerical Fluid Mechanics and Multidisciplinary Design*, **87**: pp. 26–33, 2004.
- Heyes, A. L. *et al.*, “Wandering of Wing-Tip Vortices”. In *12th International Symposium on Application of Laser Techniques to Fluid Mechanics*, Lisbon, Portugal, 2004.
- Hicks, J. W. and Huckabone, T., “Preliminary Flight-Determined Subsonic Lift and Drag Characteristics of the X-29 Forward-Swept-Wing Airplane”. NASA-TM-100409, NASA, 1989.
- Hoffenberg, R. *et al.*, “Wake Measurement in a Strong Pressure Gradient”. AIAA Paper 95-1912, AIAA, 1995.
- Hooker, S. F., “Twenty-First Century Shipping at Aircraft Speeds”. In *Workshop on Twenty-First Century Flying Ships*, Sydney, Australia, 1995.
- Hsiun, C. H. and Chen, C. K., “Aerodynamic Characteristics of a Two-Dimensional Airfoil with Ground Effect”. *Journal of Aircraft*, **33**(2): pp. 386–392, 1996.
- Huang, R. and Han, L.W., “Effects of Free-stream Turbulence on Wing-Surface Flow and Aerodynamic Performance”. *Journal of Aircraft*, **36**(6): pp. 965–972, 1999.
- Jacobs, E. N. *et al.*, “The Characteristics of 78 Related Airfoil Sections from Tests in the Variable-Density Wind Tunnel”. NACA Report No. 460, NACA, 1933.

- Jameson, A., “CFD for Aerodynamic Design and Optimization: Its Evolution Over the Last Three Decades”. In *16th AIAA CFD Conference*, Orlando, FL, 2003.
- Jameson, A., “Essential Elements of Computational Algorithms for Aerodynamic Analysis and Design”. ICASE Report No. 97-68, Institute for Computer Applications in Science and Engineering, 1997.
- Jing, S. Z. *et al.*, “An Innovative W-Shaped Tailless Aerodynamic Configuration”. *Journal of Northwestern Polytechnical University*, **22**(3): pp. 265–268, 2004.
- Johansson, A. V. and Wallin, S., “An Explicit Algebraic Reynolds Stress Model for Incompressible and Compressible Turbulent Flows”. *Journal of Fluid Mechanics*, **403**: pp. 89–132, 2000.
- Lamar, J. E. *et al.*, “Flight, Wind-Tunnel, and Computational Fluid Dynamics Comparison for Cranked Arrow Wing (F-16XL-1) at Subsonic and Transonic Speeds”. NASA-TP-2001-210629, NASA, 2001.
- Johnson, D. A. *et al.*, “The Status of Turbulence Modelling for External Aerodynamics”. AIAA Paper 94-2226, AIAA, 1994.
- Jones, R. T., “Wing Plan Forms for High-Speed Flight”. NACA Report No. 863, NACA, 1947.
- Joslin, J. R., “Evolution of Stationary Cross-flow Vortices in Boundary Layers on Swept Wings”. *AIAA Journal*, **33**(7): pp. 1279–1285, 1995.
- Kallinderis, Y. *et al.*, “Hybrid Prismatic/Tetrahedral Grid Generation for Viscous Flows Around Complex Geometries”. *AIAA Journal*, **34**(2): pp. 291–298, 1996.
- Kandil, O. A. and El-Hady, N. M., “Development of Disturbances in Swept Wing Flows”. NASA-CR-182675, NASA, 1987.
- Kandil, O. A. *et al.*, “Prediction of Near and Far-Field Vortex-Wake Turbulent Flows”. In *AIAA Atmospheric Flight Mechanics Conference*, Baltimore, MD, 1995.
- Katz, J., “Calculation of the Aerodynamic Forces on Automotive Lifting Surfaces”. *Journal of Fluids Engineering*, **107**(4): pp. 438–443, 1985.
- Kemmerly, G. T. and Paulson, J. W., “Investigation of a Moving-Model Technique For Measuring Ground Effects”. NASA-TM-4080, NASA, 1989.

- Khorrani, M. R. *et al.*, “Computational Simulations of a Three- Dimensional High-Lift Wing”. In *20th AIAA Aerodynamic Conference*, St. Louis, MO, 2002.
- Klausmeyer, S. M. and Lin, J. C., “Comparative Results from a CFD Challenge Over a 2D Three-Element Airfoil”. NASA-TM-112858, NASA, 1997.
- Knight, M. and Noyles, R. W., “Span-Load Distribution as a Factor of Stability in Roll”. NACA Report No. 393, NACA, 1931.
- Kral, L. D., “Recent Experience with Different Turbulence Models Applied to the Calculation of flow Over Aircraft Components”. *Progress in Aerospace Sciences*, **34**(7): pp. 481–541, 1998.
- Kumar, A. K., “Role of Flow Consistent Grid in CFD”. *Computers and Fluids*, **28**(3): pp. 265–280, 1999.
- Lademann, R.W. E., “Development of Tailless and All-Wing Gliders and Airplanes”. NACA-TM-666, NACA, 1932.
- Lamar, J. E., “Part 1 – Vortex Flow and High Angle of Attack”. In *RTO AVT Symposium on Advanced Flow Management*, Loen, Norway, 2001.
- Lange, R. H., “Review of Unconventional Aircraft Design Concepts”. *Journal of Aircraft*, **25**(5): pp. 385–392, 1988.
- Langtry, R. *et al.*, “Drag Prediction of Engine-Airframe Interference Effects with CFX 5”. In *Contribution to the 2nd Drag Prediction Workshop*, Orlando, FL, 2003.
- Leicher, S. *et al.*, “Mesh Generation Strategies for CFD on Complex Configurations”. In *8th International Conference on Numerical Methods in Fluid Dynamics*, Aachen, Germany, 1982.
- Launder, B. and Spalding, D. The Numerical Computation of Turbulent Flows *Computational Methods in Applied Mechanics and Engineering* 3, 269-289 1974
- Lemme, H. G., “Investigation on a Normal Swept-Back Wing, a Blunt Swept Back Wing and an M Wing”. Reports and Translations No. 441, British M.O.S (a), Volkenrode, Editor, 1946.
- Leschnizer, M. A. and Drikakis, D., “Turbulence Modelling and Turbulent-Flow Computation in Aeronautics”. *Aeronautical Journal*, **106**(1061): pp. 349–384, 2002.

Letko, W. and Goodman, A., “Preliminary Wind Tunnel Investigation at Low Speed of Stability and Control Characteristics of Swept Back Wings”. NACA-TN-1046, NACA, 1946.

Lien, F. S. and Leschziner, M. A., “Modelling 2D Separation from a High-Lift Aerofoil with a Non-Linear Eddy-Viscosity Model and Second-Moment Closure”. *Aeronautical Journal*, **99**(984): pp. 125–144, 1995.

Liu, X. *et al.*, “An Experimental Investigation of Wake Development in Arbitrary Pressure Gradients”. In *37th AIAA Aerospace Sciences Meeting and Exhibit*, Reno, NV, 1999.

Lockwood, V. E. and Phillips, W. P., “Measurements of Ground Effect on a Low-Aspect-Ratio Ogee-Wing Airplane Model and Calculations of Landing-Flare Trajectories”. NASA-TN-D-4329, NASA, 1968.

Lohner, R. and Parikh, P., “Generation of Three-Dimensional Unstructured Grids by the Advancing Front Method”. *AIAA Journal*, **34**(1): pp. 43–49, 1988.

Lombardi, G., “Experimental Study on the Aerodynamic Effects of a Forward-Sweep Angle”. *Journal of Aircraft*, **30**(5): pp. 629–635, 1993.

Lombardi, G. and Morelli, M., “Pressure Measurements on a Forward-Swept Wing-Canard Configuration”. *Journal of Aircraft*, **31**(2): pp. 469–472, 1994.

Lombardi, G. *et al.*, “Appraisal of Numerical Methods in Predicting the Aerodynamics of Forward-Swept Wings”. *Journal of Aircraft*, **35**(4): pp. 561–568, 1998.

Lombardi, G. *et al.*, “Boundary Layer Transition on a Forward Swept Wing in Canard Configuration”. *Journal of Aircraft*, **33**(6): pp. 1202–1204, 1998.

Marasli, B. *et al.*, “Effect of Travelling Waves on the Growth of a Plane Turbulent Wake”. *Journal of Fluid Mechanics*, **235**: pp. 511–528, 1992.

Marcum, D., “Generation of Unstructured Grids For Viscous Flow Applications”. In *33rd Aerospace Sciences Meeting and Exhibit*, Reno, NV, 1995.

Marino, L., “Induced-Drag Reduction of Wing-Wings and Wings-Ground Configurations”. *Aeronautical Journal*, **108**(1088): pp. 523–530, 2004.

Marvin, J. G., “Progress and Challenges in Modelling Turbulent Aerodynamic Flows”. NASA-TM-102811, NASA, 1990.

- Marvin, J. G., "Turbulence Modelling for Compressible Flows". NASA-TM-X-73, NASA, 1977.
- Mavriplis, D. J., "Adaptive Meshing Techniques for Viscous Flow Calculations on Mixed Element Unstructured Meshes". ICASE Report No. 97-20, Institute for Computer Applications in Science and Engineering, 1997.
- Mavriplis, D. J., "Unstructured Mesh Generation and Adaptivity". NASA-CR-195069, NASA, 1995.
- Mavriplis, D. J. and Levy, D.W., "Transonic Drag Prediction Using an Unstructured Multi-grid Solver". NASA-CR-2002-211455, NASA, 2002.
- Mavriplis, D. J. and Pirzadeh, S. Z., "Large Scale Parallel Unstructured Mesh Computations for 3D High-Lift Analysis". In *37th AIAA Aerospace Sciences Meeting*, Reno, NV, 1999.
- Mavriplis, D.J. and Valarezo, W.O., Navier-Stokes applications to high-lift airfoil analysis. *Journal of Aircraft*. (23). 457-688, 1999
- McCormack, G. M. and Cook, W. L., "A Study of Stall Phenomena on a 45 Degree Swept-Forward Wing". NACA-TN-1797, NACA, 1949.
- McCormick, D. J., "*An Analysis of Using CFD in Conceptual Aircraft Design*". Master's thesis, Virginia Polytechnic Institute and State University, Blacksburg, VA, 2002.
- Menter, F. R., "Improved Two-Equation k-omega Turbulence Models for Aerodynamic Flows". NASA-TM-103975, NASA, 1993.
- Menter, F. R., "Influence of Free-stream Values on k-w Model Predictions". *AIAA Journal*, **30**(6): pp. 1657–1659, 1992.
- Menter, F. R., "Performance of the Popular Turbulence Models for Attached and Separated Adverse Pressure Gradient Flows". *AIAA Journal*, **30**(8): pp. 2066-2072, 1992.
- Menter, F. R. *et al.*, "CFD Based Simulation of Aerodynamic Flows with a Pressure Based Method". In *24th International Congress of the Aeronautical Sciences*, Yokohama, Japan, 2004.

- Menter, F. R. *et al.*, “Ten Years of Industrial Experience with the SST Turbulence Model”. In *4th International Symposium on Turbulence, Heat and Mass Transfer*, Antalya, Turkey, 2003.
- Merriam, M. L., “An Efficient Advancing Front Algorithm for Delaunay Triangulation”. AIAA paper 91-0792, AIAA, 1991.
- Morishita, E. and Tezuka, K., “Ground Effect Calculation of Two-Dimensional Airfoil”. *Transactions of the Japan Society for Aeronautical and Space Sciences*, **36**(114): pp. 270–280, 1994.
- Morrison, J. H. and Hensch, M. J., “Statistical Analysis of CFD Solutions from the Third AIAA Drag Prediction Workshop”. AIAA Paper 2007-0254, AIAA, 2007.
- Munk, M. M., “Note on the Relative Effect of the Dihedral and the Sweep back of Airplane Wings”. NACA-TN-177, NACA, 1924.
- Nielsen, E. J. and Anderson, W. K., “Recent Improvements in Aerodynamic Design Optimization on Unstructured Meshes”. AIAA Paper 2001-0596, AIAA, 2001.
- Nuhait, A. O., “Unsteady Ground Effect on Aerodynamic Coefficients of Finite Swept Wings with Camber”. *Journal of Aircraft*, **32**(1): pp. 186–192, 1995.
- Nuhait, A. O. and Mook, D. T., “Numerical Simulation of Wings in Steady and Unsteady Ground Effect”. *Journal of Aircraft*, **26**(12): pp. 1081–1089, 1995.
- Nuhait, A. O. and Zedan, M. F., “Numerical Simulation of Unsteady Flow Induced by a Flat Plate Moving Near Ground”. *Journal of Aircraft*, **30**(5): pp. 611–617, 1993.
- Obayashi, S., “Algorithm and Code Development for Unsteady Three-Dimensional N-S Equations”. NASA-CR-192760, NASA, 1993.
- Olson, M. D. and Guynn, E. D., “Evaluation of an Aircraft Concept With Over-Wing, Hydrogen-Fuelled Engines for Reduced Noise and Emissions”. NASA-TM-2002-211926, NASA, 2002.
- Orzechowski, J. A. and Baker, A. J., “An Interaction Algorithm for Prediction of Mean and Fluctuating Velocities in Two-Dimensional Aerodynamic Wake Flows”. NASA-CR-3301, NASA, 1980.
- Owen, S. J., “A Survey of Unstructured Mesh Generation Technology”. In *Proceedings of the 7th International Meshing Roundtable*, Dearborn, MI, 1998.

- Owens, D. B. and Perkins, J. N., “Stability and Control of a Three-Surface, Forward Swept Configuration”. *Journal of Aircraft*, **33**(6): pp. 1206–1208, 1996.
- Pandya, M. J. *et al.*, “Recent Enhancement to USM3D Unstructured Flow Solver for Unsteady Flows”. In *22nd AIAA Applied Aerodynamic Conference and Exhibit*, Providence, RI, 2004.
- Pandya, S. A. *et al.*, “Unsteady Computations of a Jet in Cross-flow with Ground Effect”. In *33rd AIAA Fluid Dynamics Conference and Exhibit*, Orlando, FL, 2003.
- Paulson, J. W., “An Experimental and Theoretical Investigation of Thick Wings at Various Sweep Angles In and Out of Ground Effect”. NASA-TP-2068, NASA, 1982.
- Payne, R., *Stuck on the Drawing Board: Unbuilt British Commercial Aircraft Since 1945*. The History Press Ltd., Gloucestershire, UK, 2004.
- Pirzadeh, S., “An Adaptive Unstructured Grid Method by Grid Subdivision, Local Remeshing, and Grid Movement”. AIAA Paper 99-3255, AIAA, 1999.
- Pirzadeh, S., “Three-Dimensional Viscous Grids by Advancing-Layer Method”. *AIAA Journal*, **34**(1): pp. 43–50, 1994.
- Poll, D. I. A., “On the Effects of Boundary-Layer Transition on a Cylindrical Afterbody at Incidence in Low Speed Flow”. *Aeronautical Journal*, **89**(888): pp. 315–327, 1985.
- Pope, S.B *Turbulent Flows* Cambridge University Press, Cambridge UK 1952
- Proctor, F. H. *et al.*, “Wake Vortex Transport and Decay in Ground Effect: Vortex Linking with the Ground”. In *38th AIAA Aerospace Sciences Meeting and Exhibit*, Reno, NV, 2000.
- Purser, P. E. and Spearman, M. L., “Wind Tunnel Tests at Low Speed of Swept and Yawed Wings Having Various Plan-forms”. NACA-TN-2454, NACA, 1951.
- Putnam, T., “X-29 Flight-Research Program”. NASA-TM-86025, NASA, 1994.
- Rakowitz, M. and Eisfeld, B., “Structured and Unstructured Computations on the DLR-F6 Wing-Body Configuration”. *Journal of Aircraft*, **40**(2): pp. 256–263, 2003.
- Rautaheimo, P. P. *et al.*, “The Importance of Advanced Turbulence Modelling- Examples of Practical Flows”. In *ECCOMAS 2000 Congress*, Barcelona, Spain, 2000.
- Raymond, A., “Ground Influence on Aerofoils”. NACA-TN-67, NACA, 1921.

Redeker, G., “DLR-F4Wing Body Configuration”. *A Selection of Experimental Test Cases for the Validation of CFD Codes*, AGARD, AGARD Report AR-303, 1994.

Redeker, G. and Wichmann, G., “Forward-Sweep: A Favourable Concept for a Laminar Flow Wing”. *Journal of Aircraft*, **28**(1): pp. 97–103, 1991.

Reed, H. L., “Numerical Simulation of Swept-Wing Flows”. NASA-CR-189457, NASA, 1991.

Ricketts, R. H. and Robert, V. D., “Wind-Tunnel Experiments on Divergence of Forward-Swept Wings”. NASA-TP-1685, NASA, 1980.

Rizzeta, D. P. and Visbal, M. R., “Comparative Numerical Study of Two Turbulence Models for Airfoil Static and Dynamic Stall”. *AIAA Journal*, **31**(4): pp. 784–786, 1993.

Rogers, S. E. *et al.*, “Computation of Viscous Flow for a Boeing 777 Aircraft in Landing Configuration”. *Journal of Aircraft*, **38**(6): pp. 1060–1068, 2001.

Rogers, S. E. *et al.*, “CFD Validation of High-Lift Flows with Significant Wind-Tunnel Effects”. AIAA Paper 2000-4218, AIAA, 2000.

Rudnik, R. *et al.*, “Evaluation of CFD Methods for Transport Aircraft High Lift Systems”. *Aeronautical Journal*, **109**(1092): pp. 53–64, 2005.

Rumsey, C. L. and Bedron, R. T., “Computation of Flow over a Drag Prediction Wing/Body Transport Configuration Using CFL3D”. In *19th AIAA Applied Aerodynamics Conference*, Orlando, FL, 2001.

Rumsey, C. L. and Gatski, T. B., “Summary of EASM Turbulence Models in CFL3D with Validation Test Cases”. NASA TM 2003-212431, NASA, 2003.

Rumsey, C. L. *et al.*, “Study of CFD Variation on Transport Configurations from the 2nd Drag-Prediction Workshop”. In *42nd Aerospace Science Meeting and Exhibit*, Reno, NV, 2004.

Rumsey, C. L. and Vatsa, V. N., “Comparison of the Predictive Capabilities of Several Turbulence Models”. *Journal of Aircraft*, **32**(3): pp. 510–514, 1995.

Rumsey, C. L. *et al.*, “Isolating Curvature Effects in Computing Wall-Bounded Turbulent Flows”. In *39th AIAA Aerospace Sciences Meeting and Exhibit*, Reno, NV, 2001.

- Rumsey, C. L. *et al.*, “Prediction of High-Lift Flows Using Turbulent Closure Models”. AIAA Paper 1997-2260, AIAA, 1997.
- Rumsey, C. L. and Gatski, T. B., “Recent Turbulence Model Advances Applied to Multi-element Airfoil Computations”. In *18th Applied Aerodynamics Meeting*, Denver, CO, 2000.
- Rumsey, C. L. *et al.*, “Turbulence model Predictions of Extra-Strain Rate Effects in Strongly Curved Flows”. AIAA Paper 99-0157, AIAA, 1999.
- Saltzman, E. J. and Hicks, J.W., “In-Flight Lift-Drag Characteristics for a Forwards-Swept Wing Aircraft (And Comparison with Contemporary Aircraft)”. NASA-TP-3414, NASA, 1994.
- Schilling, V. K., “Motion and Decay of Trailing Vortices within the Atmospheric Surface Layer”. *Beitrage zur Physik de Atmosphere*, **65**(2): pp. 157–169, 1992.
- Schmitt, V. and Charpin, F., “Pressure Distribution on the Onera M6 Wing at Transonic Mach Numbers”. *Experimental Data Base for Computer Program Assessment: Report of the Fluid Dynamics Panel Working Group 04*, AGARD, AGARD Report AR-138, 1979.
- Sharov, D. and Nakahashi, K. “Direct Surface Triangulation using Advancing Front Method” AIAA Paper 95-1686-CP, 1995
- Shaw, J. A., “Hybrid Grids”. *Handbook of Grid Generation*, CRC Press, Boca Raton, FL, 1998.
- Shen, S. *et al.*, “Numerical Modelling Studies of Wake Vortices: Real Case Simulations”. In *37th AIAA Aerospace Sciences Meeting and Exhibit*, Reno, NV, 1999.
- Shepherd, M. S. and Georges, M. K., “Automatic Three-Dimensional Mesh Generation by the Finite Octree Technique”. *International Journal for Numerical Methods in Engineering*, **32**(4): pp. 709–749, 1991.
- Shih, T. H. *et al.*, “A New k-epsilon Eddy Viscosity Model for High Reynolds Number Turbulent Flows - Model Development and Validation”. NASA-TM-106721, NASA, 1994.
- Shevell, R.S *Fundamentals of Flight* Prentice Hall 2<sup>nd</sup> Edition, New Jersey 1998
- Slooff, J. W., “Subsonic Transport Aircraft - New Challenges and Opportunities

for Aerodynamic Research”. NLR-TP-2002-376, National Aerospace Laboratory of the Netherlands, 2002.

Smith, J. H. B., “Vortex Flows in Aerodynamics”. *Annual Review of Fluid Mechanics*, **18**: pp. 221–242, 1986.

Smith, S. C., “A Computational and Experimental Study of Nonlinear Aspects of Induced Drag”. NASA-TP-3598, NASA, 1996.

Sowdon, A. and Hori, T., “An Experimental Technique for Accurate Simulation of Flow Field for Wing-in-Surface-effect Craft”. *Aeronautical Journal*, **100**(996): pp. 215–222, 1996.

Spacht, G., “The Forward Swept Wing: A Unique Design Challenge”. In *AIAA Aircraft Systems Meeting*, Anaheim, CA, 1980.

Spaid, F. W., “Experimental Study of the Turbulent Boundary Layer on a Transport Wing in Subsonic Flow”. *Journal of Aircraft*, **27**(7): pp. 591–598, 1990.

Spalart, P., “Airplane Trailing Vortices”. *Annual Review of Fluid Mechanics*, **30**: pp. 107–138, 1998.

Spalart, P. R. and Allmaras, S. R., “A One-Equation Turbulence Model for Aerodynamic Flows”. *La Recherche Aeronautique*, **1**: pp. 5–21, 1994.

Spreeman, K. P., “Effects of Ground Proximity on the thrust of a Simple Downward-Directed Jet beneath a Flat Surface”. NACA-TN-4407, NACA, 1958.

Spreeman, K. P., “Investigation of Interference of a Deflected Jet with Free Stream and Ground on Aerodynamic Characteristics of a Semi-span delta-Wing Model”. NASA-TN D-915, NASA, 1961.

Staufenbiel, R. W. and Schlichting, U. J., “Stability of Airplanes in Ground Effect”. *Journal of Aircraft*, **25**(4): pp. 289–294, 1988.

Steinbach, D., “Aerodynamic Characteristics of a Two-Dimensional Airfoil with Ground Effect”. *AIAA Journal*, **34**(3): pp. 455–456, 1997.

Suh, Y. B. and Ostowari, C., “Drag Reduction Factor Due to Ground Effect”. *Journal of Aircraft*, **25**(11): pp. 1071–1073, 1988.

Sullivan, J. P. *et al.*, “High Lift Wake Investigation”. NASA-CR-200256, NASA, 1996.

- Thomas, J. L. *et al.*, “Powered Low-Aspect -Ratio Wing in Ground Effect (WIG) Aerodynamic Characteristics”. NASA-TM-78793, NASA, 1979.
- Tobak, M. and Peake, D.J “Topology of Three-dimensional Separated Flows” *Annual Review of Fluid Mechanics*, **14**: pp.61-85 1982
- Tombazis, N. and Bearman, P. W., “A Study of Three-Dimensional Aspects of Vortex Shedding from a Bluff Body with a Mild Geometric Disturbance”. *Journal of Fluid Mechanics*, **330**: pp. 85–112, 1997.
- Tseng, J. B. and Lan, C. E., “Calculation of Aerodynamic Characteristics of Airplane Configurations at High Angles of Attack”. NASA-CR-4182, NASA, 1998.
- Tuck, K., “Nonlinear Extreme Ground Effects on Thin Wings of Arbitrary Aspect Ratio”. *Journal of Fluid Mechanics*, **136**: pp. 73–84, 1983.
- Tuncer, I. H. and Platzer, M. F., “Computation Study of Subsonic Flow Over a Delta Canard-Wing-Body Configuration”. *Journal of Aircraft*, **35**(4): pp. 554–560, 1998.
- Turner, T. R., “Endless-belt Technique for Ground Simulation”. NASA-SP-116, NASA, 1966.
- Dam, C. P. *et al.*, “Drag Prediction at Subsonic and Transonic Speeds Using Euler Methods”. *Journal of Aircraft*, **32**(4): pp. 839–852, 1995.
- Versteeg, H. K and Malalasekera W. *Introduction to Computational Fluid Dynamics: The Finite Volume Method* Pearson Education Ltd , Essex ,UK 1995
- Viegas, J. R. *et al.*, “On the Use of Wall Functions as Boundary Conditions for Two-Dimensional Separated Compressible Flows”. AIAA Paper 85-0180, AIAA, 1985.
- Vogler, R. D., “Wind Tunnel Investigation of Internally Blows Jet-Flap STOL Airplane Model”. NASA-TN-D-8309, NASA, 1976.
- Wang, C. R., “Navier-Stokes Computations with One-Equation Turbulence Model for Flows along Concave Wall Surfaces”. NASA-TM-2005-213830, NASA, 2005.
- Wang, Q. *et al.*, “Solving Navier-Stokes Equations with Advanced Turbulence Models on Three-Dimensional Unstructured Grids”. AIAA 99-0156, AIAA, 1999.
- Ward, S. and Kallinderis, Y., “Hybrid Prismatic/Tetrahedral Grid Generation for Complex 3D Geometries”. AIAA Paper 93-0669, AIAA, 1993.

Weatherill, N. P. and Hassan, O., “Efficient 3D Grid Generation using the Delaunay Triangulation”. In *1st European CFD Conference*, Amsterdam, The Netherlands, 1992.

Weiss, J. M. and Smith, V. A., “Preconditioning Applied to Variable and Constant Density Flows”. *AIAA Journal*, **33**(11): pp. 2050–2057, 1995.

Wetmore, J. W. and Turner, L. I., “Determination of Ground Effect from Tests of a Glider in Towed Flight”. NACA-TR-695, NACA, 1940.

Wieselsberger, C., “Wing Resistance Near the Ground”. NACA-TM-77, NACA, 1922.

Wilcox, D. C., *Turbulence Modelling for CFD*. DCW Industries Inc., La Canada, California, 1993.

Williams, J. C., “Three-Dimensional Boundary Layers Approaching Separation”. NASA-TR-1976-0101, NASA, 1976.

Wu, C. K. and Rozhdestvensky, K. V., “Computation of Lift-to-Drag Ratio for Flow Past a Wing in Ground Effect”. *Transactions of the Aeronautical and Astronautical Society of the Republic of China*, **37**(3): pp. 261–267, 2005.

Yamamoto, K. *et al.*, “CFD Sensitivity of Drag Prediction on DLR-F6 Configuration by Structured Method and Unstructured Method”. In *42nd AIAA Aerospace Sciences and Meeting Exhibit*, Reno, NV, 2004.

Yaros, S. F. *et al.*, “Synergistic Airframe-Propulsion Interactions and Integrations”. NASA-TM-1998-207644, NASA, 1998.

Zheng, Z. C. and Robert, L. A., “Study of Aircraft Wake Vortex Behaviour Near the Ground”. *AIAA Journal*, **34**(3): pp. 580–589, 1996.

Zhu, K. and Takami, H., “Effect of Ground on Wake Roll-up Behind a Lifting Surface”. In *37th Japan National Congress for Applied Mechanics*, Tokyo, Japan, 1987.

[www.shortlist.com](http://www.shortlist.com) (Peake 2007)

# Appendix

The method described below was employed to obtain the parasite drag for the full-potential studies, as the drag coefficient obtained with the full-potential numerical method corresponds to the vortex drag only.

## Parasite Drag Calculations

The two major contributions to the parasitic drag are the skin friction drag, which is evaluated from knowledge of the wetted area and the skin friction coefficient, and the pressure form drag. The parasite drag is calculated as the summated profile drag of the principal elements; i.e. wing, horizontal stabiliser, fin, engines and nacelles.

The skin friction drag is generated by the resolved components due to the shear stresses acting on the surface of the body. To determine the skin friction drag for the all the wing design studies with full-potential, involved computing the Reynolds Number, for the wing the Reynolds Number calculated was based on the mean aerodynamic chord. Where

$$m.a.c = \frac{2}{3} \left( Cr + Ct - \frac{CrCt}{Cr + Ct} \right) \quad (A1)$$

Where  $Cr$  is the root chord and  $Ct$  is the tip chord.

The parasite drag coefficient for all components was calculated from the following

$$C_{Dp} = \sum_i \frac{K_i C_{fi} Swet_i}{Sref} \quad (A2)$$

Where  $K$  is the correction factor for pressure drag and increased local velocities,  $C_{fi}$  is skin friction coefficient,  $Sref$  is the reference area (usually the wing area) and  $Swet$

is the wetted area, is the actual area in contact with air. A 2% correction factor is typically introduced due to airfoil curvature. Thus

$$S_{wet} = 1.02(2S_{exposed}) \quad (A3)$$

The skin friction coefficient was estimated from the turbulent boundary layer Schlichting formula (A4); it can also be obtained from typical aircraft roughness from Figure 11.2 in (Shevell, 1989).

$$C_f = \frac{0.455}{(\log_{10} Re)^{2.58}} \quad (A4)$$

The aerodynamic surface factor K was obtained from Figure 11.3 (Shevell, 1989). The form factor K, can be obtained for different thickness to chord ratio and sweep angle.

The procedure was carried out using the Excel program, which also makes it easier for any changes in geometry, for example, to be implemented into updating the program with no additional time required.